Improving models of Earth structure in Greenland

by

Parviz Ajourlou

Thesis submitted to the University of Ottawa
in partial Fulfillment of the requirements for the

Doctor of Philosophy

at the

Department of Earth and Environmental Sciences
Faculty of Science
University of Ottawa

November 2024

Abstract

The work presented in this thesis aims to enhance our knowledge of Earth structure and composition beneath Greenland and the surrounding region. Improving Earth structure and composition constraints are important to understand and separate the evolution of ice sheet change and solid Earth response signals. In addition, it provides valuable information about the tectonic evolution and mantle dynamics of this region.

We generated a new, regional, high-resolution Rayleigh wave phase velocity model for Greenland and the surrounding region using the teleseismic two-station interferometry technique. The new phase velocity map improved the constraints on the velocity structure of the crust and the shallow upper mantle. The azimuthal anisotropy analysis also provided valuable insight into the geologic evolution and lattice-preferred orientation (LPO)/mantle flow. Significant heterogeneity was observed in our results, and we found a strong correlation between inferred geological features and isotropic and anisotropic velocities.

While the thermal properties are usually inferred only from seismic data, we constrained the thermochemical properties of the shallow upper mantle beneath Greenland and surrounding regions via multiple geophysical data sets. We adopted the LitMod software, which applies the Bayesian probabilistic approach to invert for the radial thermochemical structure of the lithosphere and shallow mantle. We combined the inferred seismic data with other geophysical data sets to perform a joint inversion for temperature and composition, from which properties such as viscosity can be determined. Our results indicate large LAB-depth variations across Greenland, reflecting multiple geologic structures and thermal processes. Our LAB-depth result supports the W-E passage of the Iceland hotspot with the inferred thin lithosphere in the mid-section of Greenland.

We examined the impact of lateral variations in Earth viscosity on the GIA model fits to paleo RSL and VLM data. We used the inferred regional temperature models to generate structures of the lithosphere and upper mantle in Greenland. We used a machine learning technique to emulate the 3D GIA models to examine a wide range of parameter sets (UMV-LMV-LT). We generated 50 Earth model realizations from inferred temperature profiles to quantify the uncertainty corresponding to the Earth viscosity structure. Our 3D model indicates the significant influence of laterally variable viscosity on RSL and VLM predictions compared to 1D model results. Overall, the 3D model fits the paleo RSL and contemporary VLM rates data better than the 1D model. Incorporating recent and short-term changes in ice loading with the Huy3 deglacial model improved the VLM data-model fit greatly. Uncertainty in modelled RSL and VLM rates data originating from the Earth viscosity structures was significant and could accommodate the residuals at many sites.

Acknowledgements

I would like to express my deepest gratitude to those who have supported and guided me throughout the process of completing this thesis.

First and foremost, I would like to extend my sincere thanks to my supervisor, Professor Glenn Milne, for his patience, unwavering support, invaluable guidance, and constant encouragement throughout this research. I have been so lucky to work with him, who considered and shaped my ideas and helped me to be coming the researcher I am today. Your expertise and insightful feedback have been instrumental in shaping this work, and I am deeply grateful for your mentorship.

I am deeply thankful to my collaborators, Professor Pascal Audet, Fiona Darbyshire, and Juan Afonso. Your partnership and intellectual contributions have enriched this research, and I have greatly valued the opportunity to work alongside you. Our collaborative efforts have been a vital part of this thesis, and I am sincerely grateful for your dedication and teamwork. I am also thankful to Professor Konstantin Latychev, who has spent a generous time testing and fixing many codes that were essential for the final chapter. I would also like to thank Dr. Ryan Love for his support and help with Linux inquiries when I encountered various compiler or package installation issues on the group's clusters and the Digital Research Alliance of Canada (the Alliance) HPC.

I would also like to acknowledge my examination committee Drs Douglas A. Wiens, Pascal Audet, Claire Perry, and Maurice Lamontagne for volunteering to read and evaluate this thesis. Your comments and suggestions significantly enhance the quality of this thesis, and I appreciate the time and effort you dedicate to reviewing my work.

I am incredibly fortunate to have a supportive circle of family and friends whose encouragement has been a constant source of strength. To my family, thank you for your unconditional love, patience, and belief in my abilities. Your support has been my anchor through this journey. To my friends, thank you for being there in moments of stress and celebration alike. Your understanding, humor, and encouragement have helped me stay grounded and focused throughout this process.

This thesis would not have been possible without the collective support of all these individuals, and I am deeply grateful for their contributions.

Author Contribution

The submitted thesis consists of five chapters, three of which (2-4) describe original research contributions. In the following I outline my contributions to these chapters.

Chapter 2: Structure of the crust and upper mantle in Greenland and northeastern Canada: Insights from anisotropic Rayleigh wave tomography

This work was done in collaboration with Dr. Fiona Darbyshire, Dr. Pascal Audet, and Dr. Glenn Milne. Dr. Andrew Schaeffer was involved in the early stages of this work. This study was initially conceptualized by Drs Audet, Schaeffer, and Milne. Under the guidance of Drs Audet and Schaeffer, I chose the seismic stations to be used for the analysis. I downloaded the data from these stations for use in the two-station interferometry technique that Dr. Audet's group had already developed (and coded in the 2stnPV software package). I processed the teleseismic data while getting feedback from Dr Audet on each step. Once the phase velocity dispersion curves were determined for each station pair, Dr. Darbyshire was invited to join the team given her expertise on the Greenland region. She provided software and guided me in performing resolution tests. Dr. Darbyshire acted as my primary supervisor through the process of data interpretation. I led the writing with detailed feedback from Dr. Darbyshire. Drs Audet and Milne also contributed to reading and giving feedback on the content. This paper is published in Geophysical Journal International.

Chapter 3: Thermochemical State of the Upper Mantle Beneath Greenland and Northeastern Canada From Multi-Observable Probabilistic Inversion

This work was done in collaboration with Dr. Juan Carlos Afonso, Dr. Farshad Salajegheh, and Dr. Glenn Milne. Drs Afonso and Milne originally conceptualized this study. Dr. Afonso provided the inversion software (LitMod) and he, and his PhD student (Dr. Salajegheh), provided guidance on how the software (required input files and parameter choices) works. With guidance from Drs Afonso and Milne, I defined the model grid (column array) and compiled the necessary data constraints for each column. I performed a number of trial inversions to optimise parameter choices under the guidance of Dr. Afonso. I performed all of the inversions using the Digital Alliance of Canada (formerly Compute Canada) hardware resources. I led the interpretation of the results under the guidance of Drs Afonso and Milne. I led the writing of this chapter with primary feedback from Dr. Milne. Dr. Afonso provided input once a complete draft was available. The thermal model resulting from this work, alongside the results of Chapter 4, will shortly be submitted to the journal Nature for publication.

Chapter 4: The Influence of Lateral Earth Structure on Glacial Isostatic Adjustment in Greenland

This work was done under the guidance of Drs Glenn Milne, Ryan Love and Konstantin Latychev. Drs Sarah Woodroffe and Kristian Kjeldsen provided data and model input, respectively. Dr. Milne had the original idea for this study. I ran the 3D numerical GIA model developed by Dr. Latychev using hardware at the University of Ottawa and provided by the Digital Alliance of Canada. I also used the 1D GIA modeling developed by Dr. Milne. I learned these software packages with guidance from Drs Milne and Love and regularly met with them to ensure reliable results. Dr. Love also showed me how to run the 3D GIA models on hardware hosted by the Digital Alliance of Canada. He also assisted me in emulating output from the 3D GIA model using a software package he recently created. Dr. Latychev provided important information on how to patch a regional (Greenland) viscosity model into global viscosity model. I generated all of the 3D Earth models described in this Chapter and ran all of the simulations based on these models. I led the interpretation of the results under the guidance of Dr. Milne. I wrote Chapter 4 with detailed feedback from Dr. Milne. The result of this chapter, including the thermal model determined in Chapter 3, will shortly be submitted to the journal Nature.

Table of Contents

List of Tables

List of Figures

Abbreviations

ASL absolute sea level 17

CMB core-mantle boundary 16

DRAM Delayed Rejection Adaptive Metropolis 74

GIA glacial isostatic adjustment 2

GNSS global navigation satellite system 21

GPS ground positioning system 2

GrIS Greenland ice sheet 1

InSAR interferometric synthetic aperture radar 21

LAB lithosphere-asthenosphere boundary 46

LGM last glacial maximum 13

LIA Little Ice Age 117

LPO lattice preferred orientation 4

LT lithospheric thickness 121

MCMC Markov chain Monte Carlo 73

NAIP North Atlantic igneous Province 41

PDF probability density function 11

PDFs probability distribution functions 4

PG peripheral glaciers 125

PVDCs phase velocity dispersion curves 4

RHP radioactive heat production 75

RSL relative sea level 2

SHF surface heat flow 10

SLIPs sea-level index points 20

THO Trans-Hudson orogen 27

UMV upper mantle viscosity 116

VLM vertical land motion 2

Chapter 1

Introduction

1.1 Overview

Global sea-level change is one of the climate warming effects that has had and will have significant socio-economic impacts (Dodman et al., 2022). Global sea levels change due to many geophysical and climatological processes with different spatial and temporal scales (Pörtner et al., 2022). In most areas, the contributions from ocean warming and land ice melting will be dominant (Constable et al., 2022). Among all the ice reservoirs on the Earth, the two major ice sheets (Antarctica and Greenland) will dominate the land ice contribution over the coming decades (Pörtner et al., 2022) and so projections of future sea-level rise depend strongly on the contribution of the Greenland ice sheet (GrIS) (Pattyn et al., 2018; Hanna et al., 2020). Mass loss of the GrIS increased by 0.65-0.73 mm/yr of mean sea-level rise equivalent between 2000-2012 (IMBIE, 2019; Pattyn et al., 2018). This acceleration in mass loss is expected to continue through the 21st century.

Projections of GrIS mass loss are limited in accuracy due to the incomplete knowledge of processes and properties that influence the mass balance of the ice sheet. For example, projections strongly depend on the accuracy of the models applied which are dependent on several factors such as the boundary conditions, parameter values, and ensuring that the governing processes are suitably captured. For the GrIS, the most important boundary conditions are those associated with the upper surface (i.e., the atmospheric/climate forcing). However, the lower surface is also important as a source of heat flux that influences the basal conditions (e.g., whether the ice is frozen or grounded to the bed) and the rate and amplitude of the isostatic response, which impacts surface mass balance and can influence ice sheet dynamics (Zeitz et al., 2022). The PhD project presented here contributes to enhancing knowledge about solid Earth properties in the Greenland region, which will result in more accurate simulations of the solid Earth - ice boundary (i.e., the isostatic response) and its influence on ice sheet evolution.

The GrIS underwent a major evolution during the recent glacial to interglacial transition (approximately 20-10 kyr before present, Funder and Hansen 1996). During this transition, the ice sheet lost around 40% of its volume, resulting in land/sea floor uplift in areas that experienced ice retreat or thinning (Lecavalier et al., 2014). This 'rebound' process, formally termed glacial isostatic adjustment (GIA), continues to this day and has implications for interpreting geodetic observations to constrain contemporary ice mass loss – an important 'initial condition' for making accurate future projections of GrIS mass changes. Data such as gravimetry, vertical land motion (VLM) determined using satellite positioning systems, and radar altimetry have frequently been used to determine contemporary ice mass loss, and a 'correction' must be applied to remove the signal associated with ongoing isostatic changes (Shepherd et al., 2012; Wouters et al., 2013). In particular, the gravimetry and VLM observations contain a large signal associated with past loading changes and so provide information on both past ice evolution and contemporary change. Accurate interpretation of these observations thus requires separation of these two signals, which is difficult due to uncertainty in both the past ice sheet evolution and properties of the solid Earth that govern the isostatic response. Therefore, by placing improved constraints on the structure of the solid Earth, the results of this thesis will provide information that is relevant to separating these two signals.

GIA-type studies have provided useful information on how the ice sheet has responded to past climate changes over millennial timescales (Tarasov and Peltier, 2004; Lecavalier et al., 2014). GIA model simulations output Earth deformation, gravity, and relative sea level (RSL) by using a global ice loading history and model of solid Earth structure (Farrell and Clark, 1976; Milne and Mitrovica, 1998, see Sec. 1.5). As noted above, one critical data set that provides constraints on past ice-sheet changes is ground positioning system (GPS)-based estimates of contemporary ground motion. Another key data set used to constrain GIA models is geological records of postglacial RSL, which provides a record of the GIA response immediately after ice retreat in coastal areas (Engelhart, 2009; Milne and Shennan, 2013). Predictions from GIA models tuned to fit the GPS constraints are very different from those adjusted to fit the RSL data (Khan et al., 2016; Milne et al., 2018). This difference is a problem that motivates current research into Greenland GIA, including the research presented in this thesis. Possible hypotheses to explain this dilemma include a transient signal in the isostatic response (Adhikari et al., 2021; Paxman et al., 2023) and lateral variations in Earth structure (rheology); testing the latter hypothesis is a primary motivation of this thesis.

Accurate and improved knowledge of Earth structure and composition beneath Greenland and the surrounding region is important not only for understanding how the ice-sheet has responded to past climate change and our ability to accurately predict its future evolution (Shepherd et al., 2012; Wouters et al., 2013), but also because it provides valuable information about the tectonic history of this region (Artemieva, 2019; Darbyshire, 2003; Darbyshire et al., 2017; Pourpoint et al., 2018b; Schaeffer and Lebedev, 2014; Schiffer et al., 2022; Toyokuni et al., 2020) and mantle dynamics (e.g., Afonso et al., 2019; Lebedev et al., 2018; Schaeffer et al., 2016; Steffen et al., 2018). Other than at a small selection of deep ice core sites, the thick interior ice ($\sim$3 km at center) prevents direct access to the solid Earth surface except for ice-free areas around the periphery of Greenland. Therefore, for most of the Greenland region, solid Earth properties are inferred from indirect methods (e.g., Bamber et al., 2001; Brooks, 2011; Dawes, 2009; van Gool et al., 2002) or geophysical modelling (e.g., Artemieva, 2019; Darbyshire et al., 2017; Mordret, 2018; Pourpoint et al., 2018b; Rogozhina et al., 2016; Steffen et al., 2017, 2018).

The key Earth model parameters for understanding GIA and ice sheet evolution are viscosity and density structure (Whitehouse et al., 2012), which are governed by temperature, pressure and compositional variations. A number of studies have inferred 1D (depth-dependent) viscosity structure beneath Greenland using forward modelling approaches (e.g., Lecavalier et al., 2014). However, this approach provides a crude estimate of the 1D viscosity structure due to low depth resolving power and the assumption that lateral variations are of second order. Constraining more realistic 3D Earth structure requires greater observational control. An alternative approach, known as inverse modelling, can also give an estimate of Earth structure (e.g., density, temperature, lithosphere thickness) based on different types of geophysical observations such as gravity, topography, heat flow, seismic tomography (e.g., Darbyshire et al., 2017; Lebedev et al., 2018; Martos et al., 2018; Mordret, 2018; Rogozhina et al., 2016; Steffen et al., 2018; Steinberger et al., 2019). The traditional inversion method generally considers one type of data to infer model parameters relating to Earth structure. A growing number of studies are considering multiple data types within a probabilistic framework (Afonso et al., 2013a,b; Fullea et al., 2009). In these so-called "joint inversion" methods, the Earth structure parameters and their corresponding uncertainties are estimated using the combination various geophysical and geochemical data types with complementary sensitivities (Afonso et al., 2016, 2019, 2022; Tork Qashqai et al., 2016, 2018; Shan et al., 2014; Yang et al., 2021). The results of these inversions are often heavily dependent on the input seismic data set. Therefore, producing high-quality results requires an accurate regional, high-resolution seismic data set to more accurately constrain Earth structure.

1.2 Thesis Aims and Outline

My thesis research aims to determine an improved estimate of 3D Earth properties in the Greenland region for the purpose of better fitting RSL and VLM data, improving boundary conditions for coupled ice-sheet-solid Earth simulations, and enhancing our knowledge of the tectonic history and mantle dynamics of the region. To achieve these aims, I took a series of steps, which are detailed in the following chapters. These steps are linked together in a way that the output of each step (chapter) is used as an input to the next step (chapter). I generated a new regional high-resolution seismic data set, incorporated this alongside other available geophysical data into a joint inversion framework to improve constraints and estimation of Earth properties, and, as a final contribution, utilized the inferred Earth properties to model GIA-related RSL and VLM to investigate the aims mentioned above.

In Chapter 2, a new, regional, high-resolution Rayleigh wave phase velocity model is generated for the Greenland and surrounding region. The motivation for this aim is to provide regional, high-resolution phase velocity dispersion curves (PVDCs) to constrain the velocity structure of the crust and the shallow upper mantle. A new Rayleigh wave phase velocity model is inferred from 48 permanent seismograph stations with seismic records spanning over two decades in Greenland (on/offshore), northeastern Canada, and western Europe to produce Earth structure constraints. More than 454 phase velocity dispersion curves were generated using the two-station interferometry technique (Sec. 1.3.3). The PVDCs were inverted for phase velocity maps in 25-185 s periods over a $1^{\circ}\times1^{\circ}$ grid. Another product of this seismic analysis is the estimation of azimuthal anisotropy that provides valuable insight into geologic evolution (shorter periods) and lattice preferred orientation (LPO)/mantle flow (longer periods). The inferred PVDCs used in the joint inversion are the most important dataset to constrain the thermochemical structure of the crust and shallow mantle because of the high sensitivity of these data to this structure and the improved spatial resolution compared to other data sets.

In Chapter 3, the main aim is to infer the thermal structure of the upper mantle (to $\sim$400 km depth). The regional, high-resolution surface wave data is combined with various other data sets to perform a joint inversion for temperature and composition, from which properties such as viscosity can be determined. Specifically, the LitMod software (Afonso et al., 2013a,b), which applies the Bayesian probabilistic approach, is used to invert for radial thermochemical structure of the lithosphere and shallow mantle. In short, we define $\sim$500 grid points (or columns) over Greenland, Baffin Bay, and northeastern Canada, in which we solve for radial thermochemical properties by performing 300,000 simulations (forward modelling). On average, 25-30 % of these simulations are accepted to form the posterior probability distribution functions (PDFs) for different Earth properties (such as temperature). Among LitMod's many outputs, we use only mantle temperature for our GIA analysis. The other results, including crustal or compositional properties, could be used for a variety of purposes, such as investigating the geological evolution of the crust.

In Chapter 4, the main aim is to calculate RSL and VLM using the new 3D temperature model developed in Chapter 3 to determine if considering lateral variations in Earth viscosity structure can provide improved fits to these data sets (and fit both simultaneously). The temperature model was used to determine a regional 3D viscosity model to depths of 400 km. Since accurate GIA simulations require solution of the sea-level equation (Sec 1.5.1), a global model of mantle viscosity is required. Therefore, we incorporated the regional Greenland viscosity and lithospheric thickness model into a global model. To efficiently search the parameter space of the global viscosity model (different upper/lower mantle viscosity and lithospheric thickness), we applied a recently developed machine learning technique to emulate the 3D GIA simulation (Love et al., 2024). To quantify uncertainty in GIA model output originating from the 3D Earth models, a sub-ensemble of inferred temperature profiles from Chapter 3 was adopted. We picked 25 temperature profiles for each grid node such that the mean and variance were representative of the full ensemble for that node. With these 25 temperature profiles, 50 Earth viscosity models were generated using two different values to scale temperature to viscosity. These viscosity models were used with a small set of ice loading models to generate model output of RSL and VLM and the corresponding uncertainty.

1.3 Seismic wave tomography

Seismic tomography is a technique used to create three-dimensional models of the Earth's interior velocity structure. The resulting velocity models have many applications in various fields, such as earthquake studies (e.g., source location, fault modelling), oil and gas exploration, and understanding the Earth's internal structure, dynamics, and evolution. Seismic waves propagate through the Earth's interior at different depths and are generated by earthquakes, explosions, or controlled sources. The arrival times are measured, and the paths of seismic waves are inferred from various receivers (seismometers) around the Earth's surface. The concept of seismic tomography is based on the fact that seismic waves travel at different speeds through different materials, which enables scientists to infer the properties of the materials through which the waves have passed.

The seismic energy received at seismometers is a combination of body and surface waves. Body waves, which are classed into primary (P) and secondary (S), travel through the Earth's interior. In contrast, surface waves, which are classed into Rayleigh and Love waves, travel near Earth's surface. P waves propagate by causing the host material to move back and forth in a direction aligned with wave propagation (1.1-A). In contrast, S waves propagate by causing the host material to move perpendicular to the direction of wave propagation (Fig. 1.1-B). P and S waves travel at different velocities due to the way each wave type deforms the material it is propagating through. Based on Eq. 1.1, the velocity of P waves (Vp) depends on density (ρ), bulk modulus (κ), and shear modulus (μ), while S wave velocity (Vs) depends only on the density and shear modulus. Therefore, since the bulk and shear moduli are both positive, Vp is faster than Vs.

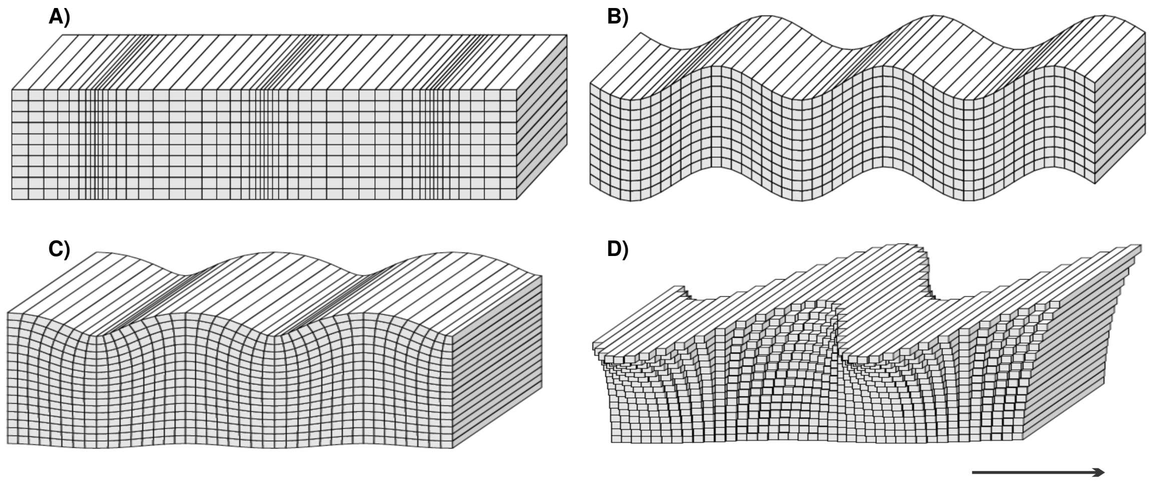

Figure 1.1: Displacement caused by **A)** P waves, **B)** S waves, **C)** Rayleigh waves, **D)** Love waves moving left to right across the page. P waves change the shape and volume of the material, while S waves change only the shape. It should be noted that the displacement is exaggerated for these plots. (Modified from Figs. 3.2 & 8.3 in Shearer (2019).)

Vp and Vs are essential parameters in seismology and geophysics because they provide valuable information about the elastic properties and density of the materials they travel through.

$$V_p = \sqrt{\frac{\kappa + 4/3\mu}{\rho}}, \qquad\qquad V_s = \sqrt{\frac{\mu}{\rho}}\ . \tag{1.1}$$

Surface waves are the result of P and S waves interacting with the Earth's surface. Rayleigh waves, which are a combination of P and SV (vertically polarized shear waves) motions, cause particles in the ground to move in elliptical paths, with particle motion decreasing exponentially with depth (Fig. 1.1-C). Love waves resulting from SH (horizontal polarized shear waves) cause shearing of the ground perpendicular to the direction of wave propagation. Unlike Rayleigh waves, Love waves have a side-to-side motion that occurs perpendicular to the direction of wave propagation, and they are faster than Rayleigh waves (Fig. 1.1-D). One of the essential features of surface waves is dispersion, which means that waves with different periods travel at different velocities. Therefore, the wave energy spreads along the direction of propagation as the longer period waves, which sample deeper (faster) Earth material, pull away from the shorter period waves.

The choice of seismic wave type for a seismic tomography study depends on multiple factors, such as the depth of the target area/volume, the distribution and density of available seismic stations, etc. Body waves are commonly used for regional seismic tomography, but this requires a relatively dense seismometer network and provides limited sensitivity to shallow subsurface structure (Toyokuni et al., 2020). Because the Greenland ice sheet covers most of Greenland, it is not possible to have a long-term, dense seismic network. Therefore, most of the regional seismic tomography investigations, including the one in this thesis, considered surface waves. Numerous surface wave tomography studies in the past two decades have investigated shallow subsurface to sub-lithospheric mantle structure using Rayleigh waves (Darbyshire et al., 2004, 2017; Pourpoint et al., 2018b,a; Mordret, 2018).

1.3.1 Rayleigh waves

To describe Rayleigh waves, which are the combination of P and SV waves, we use potentials for waves propagating in the x direction as follows:

$$
\begin{aligned}
\phi &= A \exp(i(\omega t - k_x x - k_x r_\alpha z)) \\
\psi &= B \exp(i(\omega t - k_x x - k_x r_\beta z)),
\end{aligned}
\tag{1.2}
$$

where ω is the angular velocity, t is time, k_x is the wave number, A and B are potentials amplitudes, and r_α, r_β are scaling factors defined to keep the energy trapped near the surface (Stein and Wysession, 1991):

$$
\begin{aligned}
r_\alpha &= -i(1 - c_x^2/\alpha^2)^{1/2} \\
r_\beta &= -i(1 - c_x^2/\beta^2)^{1/2},
\end{aligned}
\tag{1.3}
$$

where c_x is the apparent velocity and needs to be less than the shear velocity (β) (c_x =0.92β, more details in Stein and Wysession (1991)). By following calculations in Sec. 2.7 from Stein and Wysession (1991), the displacement from Rayleigh waves at depth z=0 is:

$$
\begin{aligned}
u_x &= 0.42\, A k_x \sin(\omega t - k_x x), \\
u_z &= 0.62\, A k_x \cos(\omega t - k_x x).
\end{aligned}
\tag{1.4}
$$

Based on equations Eq. 1.4, Rayleigh wave displacements are proportional to its horizontal wave number (inversely proportional to wavelength). At t=0 and x=0, u_x=0 and u_z is maximum, and as time increases, u_x and u_z sum to define a retrograde motion (as depicted in Fig. 1.1-C). For a homogeneous body, the maximum vertical displacement at the surface is $\sim$1.5 times greater than the horizontal displacement. Commonly, Rayleigh waves exist in non-homogeneous bodies,

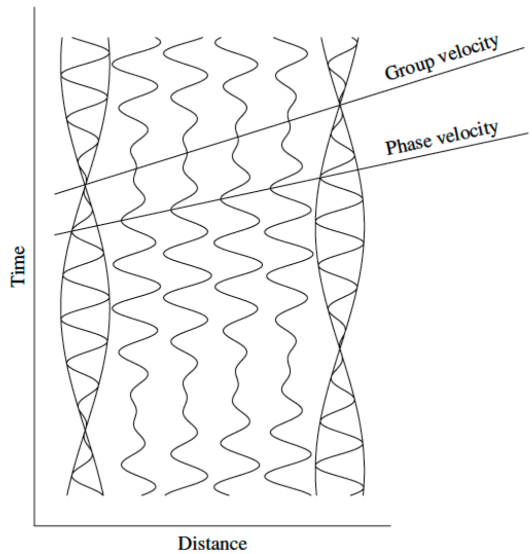

Figure 1.2: The inference of two non-destructive waves. The phase velocity is defined by the propagation of the higher frequency/shorter period peaks, whereas the group velocity is defined by the propagation of the lower frequency/longer period wave packets. (Fig. 8.5 from Shearer (2019))

and the apparent velocity (c_x) is not constant and is a function of frequency, leading to energy dispersion as noted above.

The wave pulse shape changes when the velocity varies with frequency due to interference effects. This can be illustrated by considering two harmonic waves with different frequency and wave number. Non-destructive inference would be as follows:

$$u(x,t) = \cos(\omega_1 t - k_1 x) + \cos(\omega_2 t - k_2 x). \tag{1.5}$$

By rewriting Eq. 1.5 relative to an average ω ($\omega_{1,2} = \omega \pm \delta\omega$) and wave number k ($k_{1,2} = k \pm \delta k$), we obtain:

$$u(x,t) = 2\cos(\omega t - kx)\cos(\delta kx - \delta\omega t). \tag{1.6}$$

The inferred waveform from Eq. 1.6 is a signal with average frequency ω and velocity ω/k, which is known as the phase velocity (c), whose amplitude is modulated by a lower frequency $\delta\omega$ that travels at velocity $\delta\omega/\delta k$, known as group velocity (U) (Fig. 1.2). In Chapter 3, we present a seismic tomography analysis based on Rayleigh wave PVDCs and the method known as "two-station interferometry" (Sec. 1.3.3).

1.3.2 Seismic anisotropy

In an anisotropic medium, the elastic behavior depends on the direction in which seismic waves travel. The elastic tensor (μ_{ijkl}) is defined via Hooke's law to relate strain (ϵ_{kl}) and stress (σ_{ij}) tensors as follows:

$$\sigma_{ij} = \mu_{ijkl}\, \epsilon_{kl}. \tag{1.7}$$

In an isotropic medium, the elastic constants are independent of orientation and so the elastic tensor involves only three independent parameters. However, for an anisotropic material, the elastic tensor includes 21 independent components. As a result, seismic waves may travel at different velocities through an anisotropic medium depending on the propagation direction.

Seismic anisotropy can result from several mechanisms at different depths, from crust to mantle. In the mantle, the source of seismic anisotropy can be caused by mantle flow. Mantle flow and lattice-preferred orientation or the orientation of intrinsically anisotropic minerals such as olivine may be responsible for seismic anisotropy (Nicolas and Christensen, 1987). In the crust, several isotropic, horizontally layered rocks (sediments) can introduce anisotropy, also known as shape-preferred orientation anisotropy. Seismic waves traveling perpendicular to the layering may experience anisotropy and, therefore, a change in the velocity. The magnitude and orientation of crustal anisotropy are often highly correlated with regional geological structures and so inferences of seismic anisotropy provides valuable/complementary insights about the tectonic/geological evolution in a given region (Darbyshire et al., 2017; Bagherpur Mojaver and Darbyshire, 2022; Petrescu et al., 2017).

1.3.3 Two-station interferometry

We use the well-established two-station interferometry technique (Meier et al., 2004; Darbyshire and Lebedev, 2009) to calculate a phase velocity map from fundamental Rayleigh wave dispersion curves (a curve made of phase velocities at different periods). This technique identifies surface waves traveling between station pairs from the cross-correlation of the signals measured at the two stations (Meier et al., 2004; Darbyshire and Eaton, 2010). PVDCs, inferred from the cross-correlation, reflect depth-averaged variations in velocity structure between each station pair. Therefore, these averaged velocities between station pairs must be inverted in a predefined grid to make velocity profiles.

The generated PVDCs from the cross-correlation are inverted to make azimuthally anisotropic phase velocity maps using procedures described in Darbyshire and Lebedev (2009). The phase velocity anomaly model to be solved for is:

$$\delta C(\theta,\phi) = \delta C_{iso}(\theta,\phi) + \delta C_{2\psi}(\theta,\phi) + \delta C_{4\psi}(\theta,\phi), \tag{1.8}$$

where ϕ, θ denote latitude and longitude, and $(\delta C_{iso}), (\delta C_{2\psi}), (\delta C_{4\psi})$ indicate the isotropic, 2ψ, and 4ψ phase velocity variations, respectively. In this project, the 4ψ component is neglected due to the low sensitivity of Rayleigh waves to this component (Darbyshire et al., 2017).

In seismic tomography studies, Rayleigh phase velocity maps are commonly inverted for 1D velocity profiles. In this step, the PVDCs are inverted to estimate the 1D shear velocity profiles with depth using the method outlined in Lebedev and Van Der Hilst (2008). The inversion is solved using the Levenberg-Marquardt gradient search, which is suitable for a highly non-linear equation, with the non-linear least-squares method to minimize the difference between synthetic velocities (computed using the MINEOS normal mode code) and the original data. Due to the non-uniqueness associated with shear velocity structure determination from Rayleigh dispersion curves, *a priori* information about the crustal structure and Moho depth is required to add additional constraints to the problem Lebedev and Van Der Hilst (2008). However, we skip the 1D shear velocity profiles inversion and invert the phase velocity maps using a joint inversion method (Sec. 1.4). This technique is capable of using several datasets in a self-consistent framework to invert for Earth properties.

1.4 Joint Inversion of Regional Geophysical Data

The PVDCs determined in Chapter 2 are used in Chapter 3, alongside other data (e.g., free-air gravity anomaly, geoid, elevation, and surface heat flow (SHF)) to infer the composition and temperature beneath the Greenland region using a joint-inversion algorithm (Afonso et al., 2013a,b). The advantages of this joint-inversion approach is discussed in the methodology section of Chapter 3. In short, using different data sets brings, ideally, complementary information to the problem to enhance sensitivity to Earth structure, thus permitting more accurate inferences of this structure to be made. The inferred compositional and thermal structure will be used to estimate the viscosity structure which is a required input for GIA modelling (Sec. 1.5 and Chapter 4). Also, the joint-inversion software used in Chapter 3 (known as LitMod, Afonso et al. (2013a,b)) is couched within a Bayesian framework which provides estimates of uncertainty in the inferred quantities.

1.4.1 Bayesian framework

In a Bayesian formulation, unknowns are considered as random variables and are defined via probability distributions. Bayes' theorem defines the probability of an event if there is prior knowledge and the corresponding conditions to the event (Joyce, 2021), and it is formulated as:

$$P(A|B) = \frac{P(A).P(B|A)}{P(B)}, \tag{1.9}$$

where $P(A|B)$ is a conditional probability (i.e., the probability of event A occurring if B is true), $P(B|A)$ is the probability of B occurring if A is true (also known as the likelihood); $P(A)$ and $P(B)$ are the probabilities of occurrence of each event, A or B, without any conditions. In geophysical modelling, we can substitute A and B with, respectively, input data (**d**) and unknown model parameters (**m**) and re-define $P(A|B)$ as the posterior probability density function (PDF):

$$P(\mathbf{m}|\mathbf{d}, f) = \frac{P(\mathbf{m}|f)\, P(\mathbf{d}|\mathbf{m}, f)}{P(\mathbf{d}|f)}, \tag{1.10}$$

where $P(\mathbf{m}|\mathbf{d}, f)$ is the posterior PDF. $P(\mathbf{m}|f)$ describes prior parameter information relating to the model, $P(\mathbf{d}|\mathbf{m}, f)$ provides the likelihood of observational data (**d**) given specific parameters (**m**), and $P(\mathbf{d}|f)$ (called the "Bayesian evidence" which normalizes the parameter space) is the probability of the observed data (**d**) given a specific model (f) .

In the Bayesian approach to joint inversion, prior information for the data and model parameters is used in a joint probability density function known as ρ(**d**,**m**), and, similarly, initial knowledge about relationships between data and unknown model parameters (i.e., the forward model (f)) is given by the PDF known as Θ(**d**,**m**). The general solution to the inverse problem is represented by a multi-dimensional PDF from the conjunction of given states of information over the parameter space, known as the posterior PDF (Tarantola, 2005),

$$\sigma(\mathbf{d}, \mathbf{m}) \propto \rho(\mathbf{d}, \mathbf{m})\ \Theta(\mathbf{d}, \mathbf{m}). \tag{1.11}$$

By integrating over the data space to achieve the marginal PDF in the parameter space (Afonso et al., 2013a; Tarantola, 2005), Eq. 1.11 can be restructured as follows,

$$\sigma(\mathbf{m}) \propto \rho(\mathbf{m})\ L(\mathbf{m}), \tag{1.12}$$

with

$$L(\mathbf{m}) \propto \int \rho(\mathbf{d})\ \theta(\mathbf{d} \mid \mathbf{m})\ d\mathbf{d}, \tag{1.13}$$

where the $\rho(\mathbf{m})$ describes the *a priori* information about the parameters independently from the data ($\mathbf{d}$), $L(\mathbf{m})$ is the *Liklihood function*, which describes the probability of the similarity between observation and a model prediction based on a specific parameter set, $\rho(\mathbf{d})$ is the *a priori* PDF of data uncertainties, and $\theta(\mathbf{d} \mid \mathbf{m})$ is the conditional probabilities related to the uncertainties of the predictions from the forward model.

1.4.2 LitMod framework

The LitMod software takes geophysical and geochemical data and uses them in a self-consistent inverse framework (Afonso et al., 2013a,b). Self-consistency means that a unique physiochemical model should link together physical and chemical observations. Probabilistic formulations (statistical inferences) of this kind of inversion provide a practical means to deal with data and model uncertainties. In this method, the solution is represented by a series of PDFs (one for each parameter) rather than a single parameter vector (Tarantola, 2005; Congdon, 2002; Biegler et al., 2011).

In general, there are no formal mathematical expressions to calculate $\rho(\mathbf{m})$ and/or $\sigma(\mathbf{m})$, so a sampling scheme, for example based on a Monte Carlo analysis, is necessary (Tarantola, 2005). However, due to the large number of parameters required to estimate a full 3D model, and the much greater amount of samples for which the 3D forward problem needs to be solved in order to get reliable estimates of the posteriori $\sigma(\mathbf{m})$, this approach is impractical. In order to overcome this issue, the inversion is divided into two stages (Fig. 1.3).

In the first stage, which is a 1D inversion (with depth), the 3D model space is subdivided into an array 1D rectangular vertical columns (Fig. 1.4). Then, a subset of the data vector associated with each column is inverted individually. Each column has three discretization scales: the finest discretization scale (defining the *computation nodes*) is used in the numerical solution of the forward problem (Sec. 3.2.5), the intermediate discretization scale (defining the *thermodynamic nodes*) is used to solve the Gibbs free energy minimization problem, and the third and most crude discretization scale (*compositional layers*) refers to the actual number of independent compositional layers assigned in the model (Afonso et al., 2013b). The result of each column-by-column inversion will be used as the first estimation of the marginal PDFs describing the 1D thermochemical structure that is compatible with the 1D data. These PDFs will be utilized as *a priori* information in the second stage, the so-called "refinement stage," in which the full 3D problem is addressed. In the second stage, additional data are incorporated to the framework to spatially 'tie together' the 1D results. Data such as gravity gradients are used to generate a more spatially coherent 3D thermochemical models. However, since the second stage of the inversion generally results in relatively minor revisions to the results of the first stage, we perform only

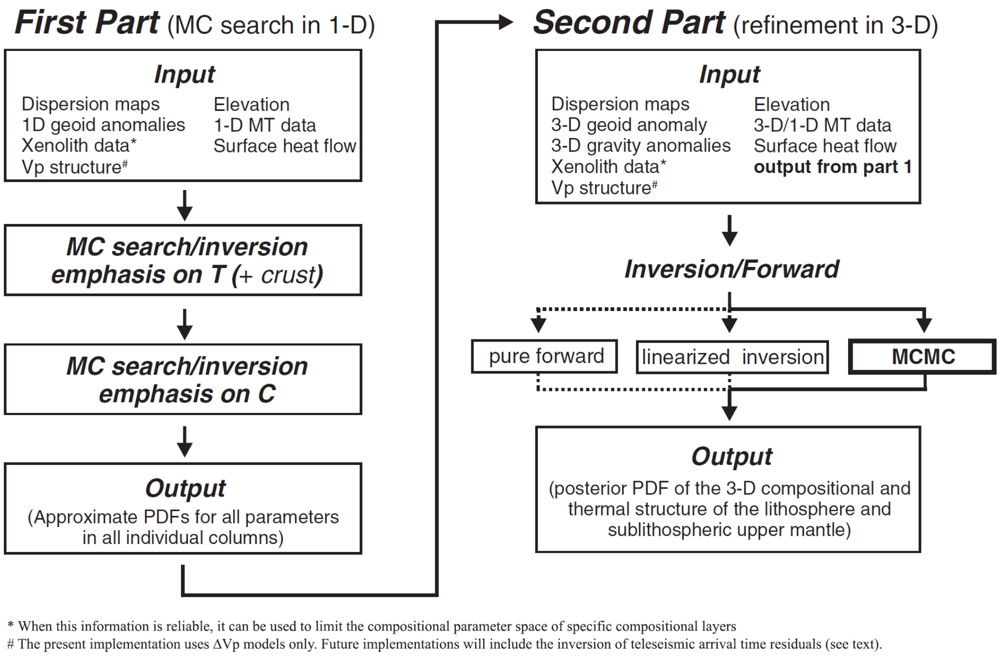

Figure 1.3: Flow chart illustrating the two-part inversion approach applied in a LitMod analysis . T refers to temperature and C refers to composition. (Figure from Afonso et al. (2013b)).

the 1D inversion in this study (more details on the 3D refinement methodology can be found in Afonso et al. (2013b, 2016)).

1.5 Glacial Isostatic Adjustment

The Earth experienced glaciation and deglaciation during the Quaternary ($\sim$2.6 Ma to the present) with quasi-periodic variations in ice extent (Shackleton and Opdyke, 1973). The latest glacial maximum occurred around 21 kyr and is referred to as the last glacial maximum (LGM). During this period, three major ice sheets existed in north America (Laurentian, Innuitian, and Cordillerran) and four in Eurasia (British-Irish, Fennoscandian, Barents, and Kara), along with substantially more extensive ice in Antarctica and Greenland (compared to that at present). The accumulation and ablation of these ice sheets reflects the major mass redistribution between land ice and oceans that has existed on Earth for many glacial cycles. This repeating mass redistribution caused deformation of the solid Earth, changes in gravity and Earth rotation, and changes in

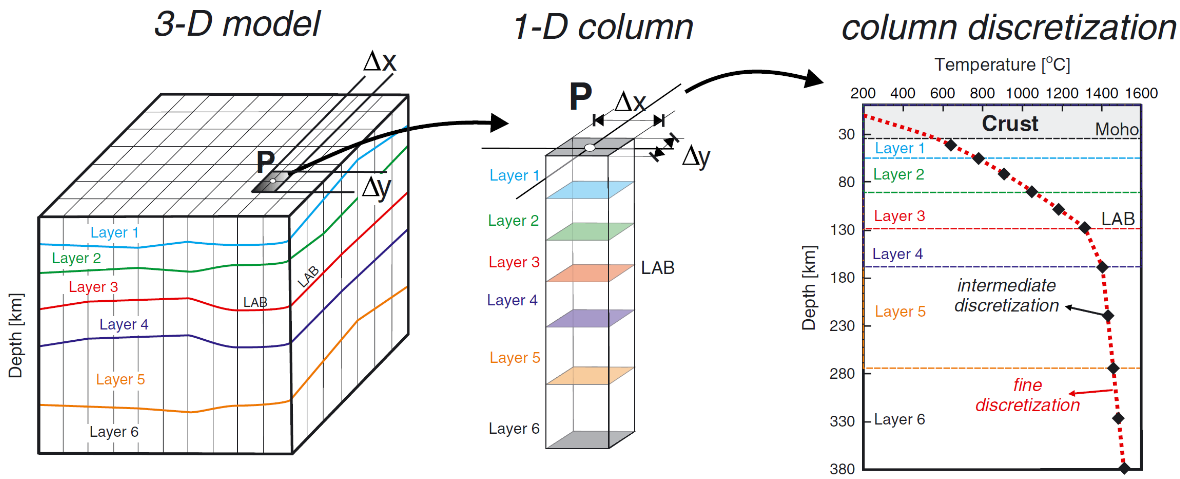

Figure 1.4: Discretization length scales used in the LitMod inversion software. A 3D model can be divided into a collection of 1D columns. Each column is discretized in different layers and nodes for determining the compositional and thermal parameters. The number of layers and nodes can vary spatially, mainly due to the different Earth structures. (figure from Afonso et al. (2013b))

global sea levels (e.g., Whitehouse (2018).

The following provides a conceptual overview of the GIA process in near-field regions (those close to the ice sheets). During ice sheet growth, ice covered regions experienced subsidence while the surrounding areas experienced an uplift, leading to the formation of so-called "peripheral bulges" (Fig. 1.5-A). In addition to the solid Earth deformation, gravitational changes are caused by both the increase in ice mass, resulting in an increase of RSL in the vicinity of the growing ice sheet (Fig. 1.5-B) (which also influences the gravitational changes), and the resulting Earth deformation. Finally, the surface (ice-ocean) and internal (deformation) mass redistribution changes the Earth's inertia tensor, resulting in changes to the Earth's rotation vector. This, in turn, also causes changes in gravity and solid Earth deformation at the global scale (e.g., Mitrovica and Wahr, 2011).

During deglaciation, all of the above-mentioned processes are reversed. The shrinking ice sheet causes mantle mass to flow back under the deglaciating ice sheet. Consequently, the solid Earth rises in areas once covered by ice and subsides in peripheral regions (Fig. 1.5-C). The resulting melt water is redistributed back to the oceans in a non-uniform spatial pattern that is governed by the deformational, gravitational, and rotational changes (Fig. 1.5-D). The resulting sea-level changes also act as an important surface load in the GIA problem. In the following sections, further information is provided on the nature of the solid Earth response and how it is

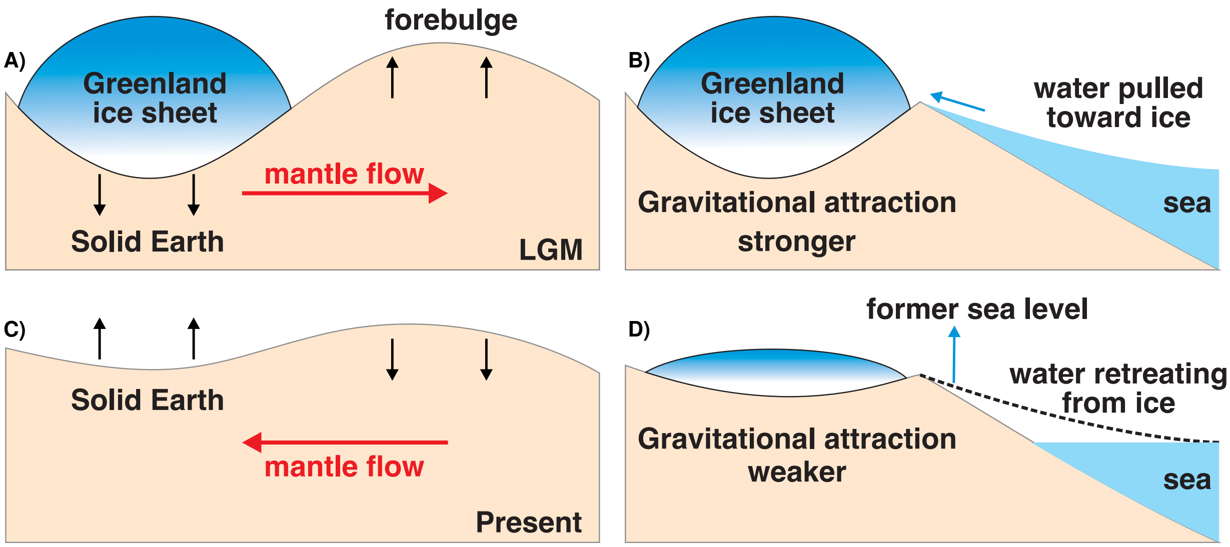

Figure 1.5: Schematic diagram illustrating the loading (A and B) and unloading (C and D) effect on solid Earth deformation and sea level change (modified from Ipcc4 AR5 (Oppenheimer et al., 2019)).

modelled (Sec. 1.5.1) and how global sea-level changes (and thus the ocean load) is determined (Sec. 1.5.2).

1.5.1 Earth Rheology

Solid Earth rheology depends on lattice and grain scale mechanisms that are active on different timescales and at different depths. Depth variation controls the environmental conditions in which deformation mechanisms are active (Ranalli, 1995). For example, shallow crustal deformation is mostly elastic and brittle due to the relatively cold temperatures and low pressures. At greater depths, ductile deformation becomes important, and Earth deformation is mainly elastic and viscous. As pointed out previously, Eq. 1.7 represents an elastic rheology, in which the strain response is instantaneous and fully recoverable. This model is suitable for describing the solid Earth response to short-term stress changes that do not exceed the yield stress of the material (e.g., seismic wave propagation and isostatic response to ice mass changes on annual to decadal time scales). On the other hand, at longer timescales, viscous flow becomes significant in the mantle. For long timescales ($\geq$ 100 kyr), the elastic strain is negligible in comparison to the viscous strain and so viscous models are used to model mantle flow, as follows:

$$\dot{\epsilon} = \frac{\sigma}{2\eta}, \tag{1.14}$$

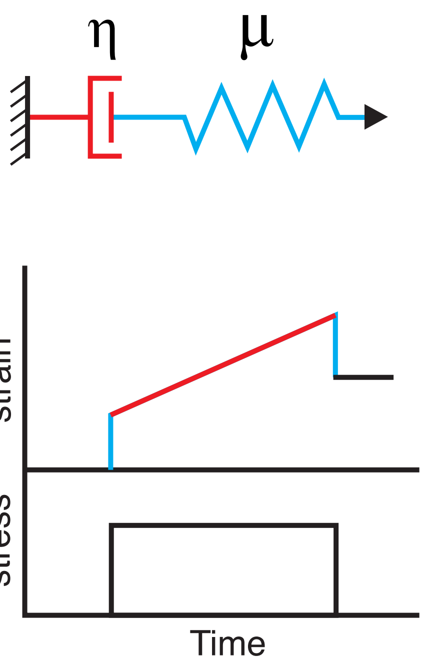

Figure 1.6: Schematic diagram of the Maxwell rheology. The top panel shows a spring (blue) attached to a dashpot (red) representing elastic and viscus components of deformation, respectively. The bottom panel shows the strain (deformation) based on the applied stress at different times. The blue color corresponds to elastic and red color to viscous deformation.

where $\dot{\epsilon}$ is strain rate, σ is the applied deviatoric stress, and η is mantle viscosity. Mantle depth is $\sim$2800 km and, despite being relatively homogeneous in composition, its viscosity varies by 1-2 orders of magnitude from the asthenosphere to the core-mantle boundary (CMB) (e.g., Ranalli, 1995). The mantle can also exhibit large lateral variations in viscosity, particularly near plate boundaries and hot spots.

The advance and retreat of ice sheet margins may take several hundreds to thousands of years and results in a significant load change at the Earth's surface. The solid Earth response to these changes comprises both an elastic and viscous response. The Maxwell model (Fig. 1.6) combines a spring and dashpot in series to simulate the elastic and viscous components of deformation. In this model, when stress is applied, the spring deforms first, causing an instantaneous change in strain. As the stress is applied for a longer time, the dashpot contributes a growing component of the deformation. When the stress is removed, there is a sharp change in deformation corresponding to the recovery of elastic strain with the non-recoverable viscous component resulting in the net deformation. The strain accumulated between times t_0 and t_1 can be represented as follows:

$$\epsilon = \frac{\sigma}{2\mu} + \int_{t_0}^{t_1} \frac{\sigma}{2\eta}\, dt. \tag{1.15}$$

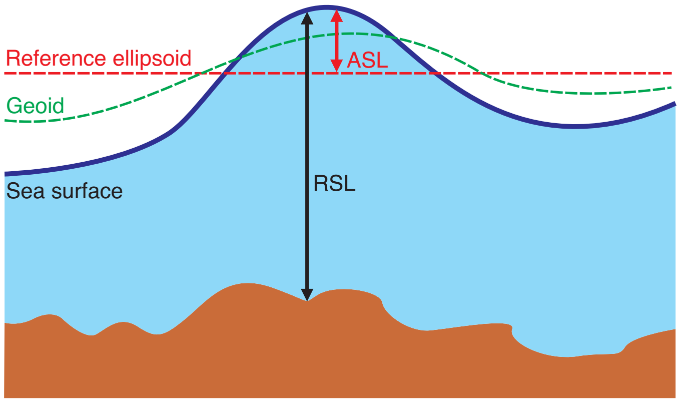

Figure 1.7: Schematic diagram of RSL and absolute sea level (ASL) as the vertical distance from sea floor to sea surface and reference ellipsoid to sea surface, respectively. The geoid is the average height of the sea surface over decades, and approximates an equipotential of the gravity field.

1.5.2 Relative Sea Level

Relative sea level is the vertical distance from the solid Earth (sea floor) to the ocean surface (Fig. 1.7). A change in RSL can, therefore, be related to one or both of sea surface height change and solid Earth vertical movements. RSL change is time-dependent including long-time scale (millennia) changes related to solid Earth deformation or gravitational attraction between ice and ocean mass, and short-time scale (daily) changes due to tides (Fig. 1.7).

Farrell and Clark (1976) first developed a theory for calculating the sea level change due to surface mass redistribution on a visco-elastic, non-rotating, model Earth. Subsequently, this theory was extended to include time-varying shoreline positions and Earth rotation (e.g., Mitrovica and Milne, 2002; Milne and Mitrovica, 1998; Milne et al., 1999). Farrell and Clark (1976) formulated change in RSL at geographical location θ, λ (co-latitude and east longitude, respectively), and time t as follows:

$$
\begin{aligned}
SG(\theta, \lambda, t) &= G(\theta, \lambda, t) - R(\theta, \lambda, t), \\
S(\theta, \lambda, t) &= C(\theta, \lambda)\, SG(\theta, \lambda, t),
\end{aligned}
\tag{1.16}
$$

where G is the geoid height change (or absolute sea level change), R is the solid Earth radial displacement (or height change of the sea floor), S is the sea level change, and C is the so-called ocean function ($C = 1$ in ocean areas, and $C = 0$ in land areas).

Absolute sea level (or sea surface height change) is the combination of spatially uniform, $E(t)$, and spatially variable, $\Phi/g(\theta, \lambda, t)$, components. The uniform sea surface height change is comprised of two parts: barystatic, $E_b(t)$, and syphoning, $E_s(t)$, and ensures ice-water mass conservation between ice sheets and the oceans (Farrell and Clark, 1976). Using this information, Eq. 1.16, including spatially variable and uniform sea height change, can be written as:

$$SG(\theta,\lambda,t) = \left[\Phi/g(\theta,\lambda,t) + E(t)\right] - R(\theta,\lambda,t), \tag{1.17}$$

where

$$\begin{aligned} E(t) &= E_b(t) + E_s(t), \\ E_b(t) &= -\frac{1}{A_o}\frac{\rho_I}{\rho_w}\iint_{\Omega} \Delta I(\theta',\lambda',t)d\Omega, \\ E_s(t) &= -\frac{1}{A_o}\left\langle\left[\Phi/g(\theta,\lambda,t) - R(\theta,\lambda,t)\right]\right\rangle_o, \end{aligned} \tag{1.18}$$

where ρ_I and ρ_w are the density of ice and water, A_o is the ocean area, ΔI is ice thickness change, $d\Omega$ is spherical polar differential elements (or $sin\theta' d\theta' d\lambda'$), Φ is the perturbation to the gravitational potential, g is gravitational acceleration, and $\langle\cdot,\cdot\rangle_o$ is the inner product for calculating spatial integration over ocean area. As mentioned above, the radial displacement and gravitational potential changes are caused by ice and loading. Green functions G_R and G_Φ are used, respectively, to project the effect of surface mass load (L) on R and Φ between loading point and time (θ', λ', t') and fingerprint point and time (θ, λ, t), as follows:

$$\begin{aligned} R(\theta,\lambda,t) &= \int_{t'}\iint_{\Omega} L(\theta',\lambda',t')\, G_R(\psi, t-t')\, r^2\, d\Omega\, dt', \\ \Phi(\theta,\lambda,t) &= \int_{t'}\iint_{\Omega} L(\theta',\lambda',t')\, G_\Phi(\psi, t-t')\, r^2\, d\Omega\, dt', \end{aligned} \tag{1.19}$$

where ψ is angular distance, r is Earth's radius, and

$$\begin{aligned} L(\theta',\lambda',t') &= \rho_w\, S(\theta',\lambda',t') + \rho_I \Delta I(\theta',\lambda',t'), \\ G_R(\psi,t) &= \frac{r}{M_E}\sum_{n=0}^{\infty}\left[h_n^V(t) + h_n^E\delta(t)\right] P_n(cos\psi), \\ G_\Phi(\psi,t) &= \frac{rg}{M_E}\sum_{n=0}^{\infty}\left[\delta(t) + k_n^V(t) + k_n^E\delta(t)\right] P_n(cos\psi), \end{aligned} \tag{1.20}$$

where M_E is the Earth's mass, $(h,k)_n^{E,V}$ are surface load Love numbers corresponding to, respectively, the elastic and viscus components; δ is the impulse function (= 0 or 1), and P_n are the Legendre polynomials. Using the relationships in Eqs. 1.19 and 1.20, the sea level equation is obtained as follows ($\otimes$ denotes convolution in time and space):

$$
\begin{aligned}
SG(\theta,\lambda,t) = &\frac{G_R}{g} \otimes L + \frac{G_\Phi}{g} \otimes L + \\
&\underbrace{-\frac{M_I(t)}{A_o \rho_w} - \frac{1}{A_o} \Big\langle \frac{G_R}{g} \otimes L + \frac{G_\Phi}{g} \otimes L \Big\rangle_o}_{C_{SL}(t)},
\end{aligned}
\tag{1.21}
$$

where relative sea level change (SG) is a function of itself, and the general approach to solving such a problem is iterative (e.g., Mitrovica and Peltier, 1991).

1.5.3 GIA modelling

In the late 20th century, contemporary GIA modelling developed with the first theoretical sea level change formulation (Sec. 1.5.2). In Eq. 1.19-1.20, ice loading (ΔI) and Earth properties (embodied in Love numbers, k and h) for a visco-elastic Earth (Maxwell rheology) are the two primary components. Therefore, GIA analyses often contribute to Earth rheology and ice evolution constraints, as described below.

Conventionally, the forward modelling approach is used to solve sea level equation by providing parameter sets of Earth model realizations (e.g., lithosphere elastic thickness and upper and lower mantle viscosities) and ice model history. Once these are defined, various observables can be generated and compared to observations (Fig. 1.8). The model parameter set with the lowest data-model misfit is accepted as the final, optimum, result. However, multiple parameter sets often lead to similar data-model misfits due to non-uniqueness issues. In addition, Earth rheology variation is often considered only with depth, and so lateral variations are ignored. Despite 1D Earth models being unrealistic, this class of models have generally provided acceptable regional fits to RSLs. A growing number of studies have considered Earth models with 3D viscosity structure (e.g., Li et al., 2018). However, in most of these studies, the 3D models provided only equivalent or poorer fits to the observations. Ice history models are often developed based on a spherically symmetric (1D) Earth model (e.g., Tarasov et al., 2012; Peltier et al., 2015; Lambeck et al., 2017; Simon et al., 2016), which makes them incompatible with 3D Earth models.

As mentioned above, the 1D linear Maxwell rheology can provide a good fit to RSL data. However, laboratory experiments have shown that a non-linear (power law) component of the viscous response is commonly observed for mantle materials and conditions (Karato et al., 2008), and so both should be considered when simulating GIA observables (Wouters et al., 2013). Another recent attempt to explain data-model residuals has considered transient rheology, which means the viscosity varies with the frequency of the surface loading (Lau and Holtzman, 2019).

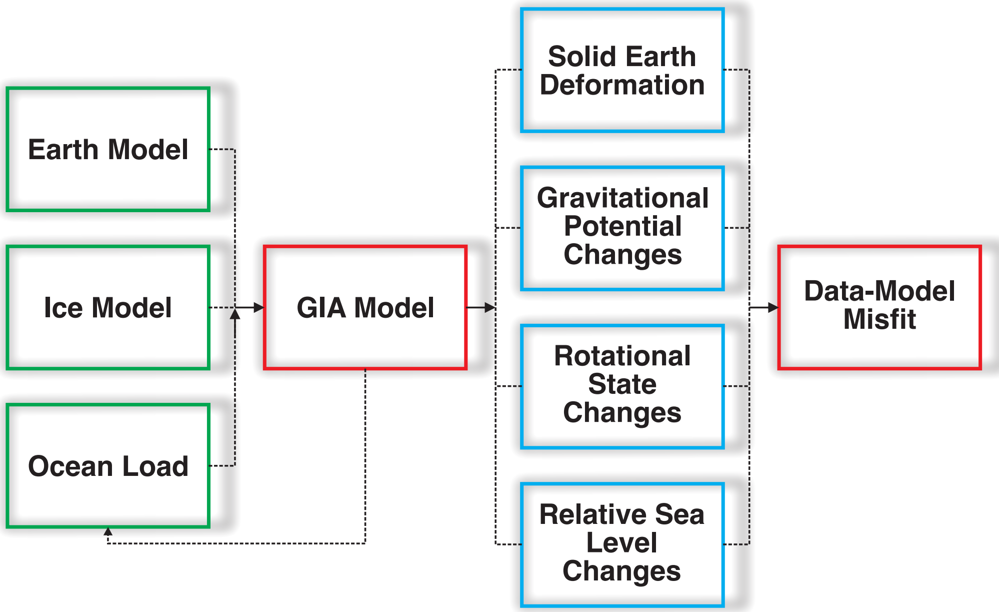

Figure 1.8: Schematic of GIA model components and modelling procedure. The main GIA model inputs (green boxes) are the Earth, and ice models. Solving the sea level equation (Eq. 1.21) generates the ocean load which, along with the ice and Earth model, are used to generate the listed model outputs (blue boxes). The outputs are compared to observations to calculate the data-model misfit and to find the optimum model parameter set.

Frequency-dependent viscosity has been proposed to explain some differences in viscosity inferred using different data sets (e.g., Adhikari et al., 2021; Paxman et al., 2023). These more complex Earth models - with 3D structure and more complex rheology - will play an important role in explaining data-model residuals as the quality and quantity of observational control improves. A wide range of observables capture the GIA signal (Fig. 1.8). The two that are most commonly used RSL reconstructions spanning many millennia and geodetic determinations of land motion (vertical and horizontal) over the past few years to decades.

Paleo RSL is reconstructed from sea-level index points (SLIPs), which constrain ancient RSL in height and time, and limiting data points, which provide only an upper or lower bound on RSL at some past time (Fig. 1.9). SLIPs are determined from the analysis of microfossils (e.g., foraminifera, pollen, diatoms) from in situ sediment cores or features (e.g., morphological/archeological) that can be used to place an accurate constraint on paleo sea level (Shennan, 2015). Limiting data points are also obtained through different proxy types. For example, limiting data points reconstructed from plant macrofossils that could have lived only in fresh water

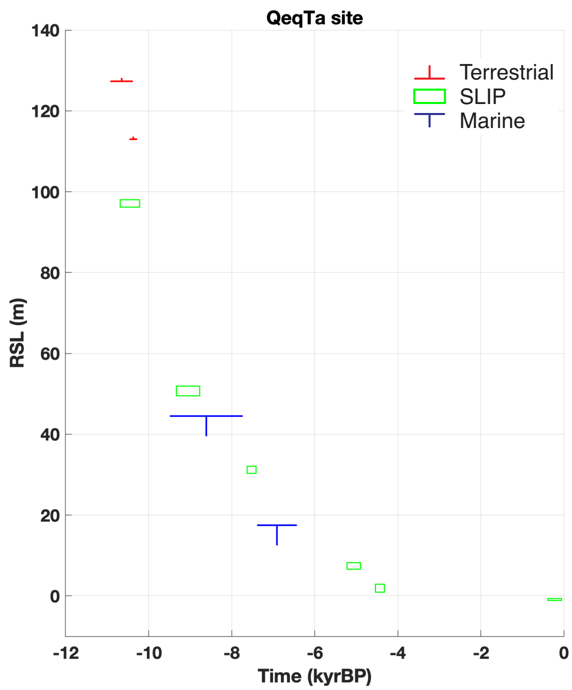

Figure 1.9: Example of paleo RSL data types (see key) used in Chapter 4 (site location is shown in Fig. 4.1-A).

conditions, indicate sea level was lower than the measured RSL height. On the other hand, corals could have lived only in salt-water conditions, indicating that sea level was above the height of the fossil coral when it was alive.

Geodetic data, including global navigation satellite system (GNSS) and interferometric synthetic aperture radar (InSAR), have been used for VLM studies in specific regions (Khan et al., 2016; Berg et al., 2024; Wang et al., 2024; Cao et al., 2023). There have been growing GPS networks in some areas of interest, such as Greenland and Antarctica. However, our knowledge of the present VLM in Greenland is limited to the margins because the precision required involves the installation of continuously operating receivers that are coupled to the bedrock. VLM time series determined from GPS capture both of the ongoing viscous deformation caused by past ice and ocean loading, as well as the elastic deformation associated with ice thickness changes during the monitoring period. Therefore, the VLM data, measured from GPS, have to be corrected for elastic deformation to be suitable for GIA modelling (Khan et al., 2022; Berg et al., 2024).

Chapter 2

Structure of the crust and upper mantle in Greenland and northeastern Canada: Insights from anisotropic Rayleigh wave tomography

2.1 Introduction

Greenland is covered by the second-largest ice sheet in the world, whose volume is equivalent to about 7 m of global mean sea level rise (Haines, 2003). Due to the thick interior ice ($\sim$3 km at center), other than at a small selection of deep ice core sites, direct access to the solid Earth surface is only possible beyond the ice margin. Consequently, much of the Earth's structure beneath the ice sheet and its surroundings is inferred from indirect methods (e.g., Bamber et al., 2001; Brooks, 2011; Dawes, 2009; van Gool et al., 2002) or geophysical modelling (e.g., Artemieva, 2019; Darbyshire et al., 2017; Mordret, 2018; Pourpoint et al., 2018b; Rogozhina et al., 2016; Steffen et al., 2017, 2018; Voss and Jokat, 2007; Voss et al., 2009). As a result, there is limited knowledge of geological and geophysical properties (e.g., rock type, heat flow, lithospheric thickness) and their spatial distribution beneath most of Greenland and peripheral regions. Improving our knowledge of the subsurface structure would provide valuable insights into the tectonic history (Artemieva, 2019; Darbyshire, 2003; Darbyshire et al., 2017; Pourpoint et al., 2018b; Schaeffer and Lebedev, 2014; Schiffer et al., 2022; Toyokuni et al., 2020) and related mantle dynamics (e.g., Afonso et al., 2019; Lebedev et al., 2018; Schaeffer et al., 2016; Steffen et al., 2018). In addition, more accurate velocity constraints will lead to improved models of the density and rheology (e.g., Artemieva, 2019; Afonso et al., 2013a,b; Lebedev et al., 2018; Mordret, 2018), both of which govern the isostatic response. A better understanding of this response will lead to improved model reconstructions of the past and future evolution of the ice sheet (e.g., Lecavalier et al., 2014; Wake et al., 2016; Edwards et al., 2021) and its impact on global and regional sea-level changes (e.g., Lecavalier et al., 2014; Wake et al., 2016; Faure, 2022) and regional land motion (e.g., Khan et al., 2016; Adhikari et al., 2021).

A primary motivation for this study is to improve upon the geographic extent and resolution of past studies. Over the past 10-15 years, several new seismograph stations have been progressively installed, notably in Greenland's central and southern parts and northeastern Canada. In addition, we have broadened the aperture of the network used in our study by adding stations from beyond these regions, leading to improvements in regional data coverage and resolution around the coast, the continental shelves, and the far north of the Greenland/Arctic region. We consider Greenland, northeastern Canada, and Baffin Bay as our main study regions and so generate a model of lithospheric and upper-mantle seismic velocity structures for these regions using data from fundamental-mode Rayleigh wave phase velocities. Teleseismic data and associated two-station cross-correlation techniques are used to estimate isotropic and anisotropic phase velocity maps, which adds insight into lithospheric structure and fabric that can help constrain the regional geologic, tectonic, and geodynamic history.

2.1.1 Geology and Tectonic Background

Much of Greenland is commonly assumed to be underlain by Precambrian Shield altered by several orogenic and rifting events. These events divide the landmass into several blocks, including several Proterozoic mobile belts and an Archean craton in the south (Dawes, 2009; Henriksen et al., 2008, 2009). Tectonic models suggest that during the Early Proterozoic era, most of Greenland's original Archean structure was modified by orogenic activities (Fig. 2.1).

The only significant unaltered Archean basement is located in the southern part of Greenland (Fig. 2.1). This Archean block, part of the North Atlantic craton, is bounded to the south by the Ketilidian mobile belt, which is largely composed of juvenile Paleoproterozoic rocks. To the north, the craton is bounded by the Nagssugtoqidian mobile belt in the west and the Ammassalik mobile belt in the southeast. The Rinkian mobile belt extends northwards from the Nagssugtoqidian mobile belt towards the Inglefield mobile belt, though the boundaries between these orogenic belts are not well defined (e.g., St-Onge et al., 2009). The Nagssugtoqidian, Ammassalik, and Rinkian mobile belts are largely composed of reworked Archean rocks, whereas the Inglefield mobile belt is dominated by juvenile Paleoproterozoic assemblages. Both the main Archean block and the mobile belts can be correlated with units in northeastern Canada, such as the Rae craton and structures related to the Trans-Hudson Orogen (Henriksen et al., 2008, 2009; St-Onge et al., 2009; van Gool et al., 2002).

The formation of the Paleoproterozoic fold belts led to the establishment of the stable Greenland basement around 1,750 million years ago. Subsequently, the Greenland craton experienced only minor tectonic events, such as local rift formation and limited block uplift and subsidence (Henriksen et al., 2008, 2009). Later tectonic activity occurred along the craton margins, including Late Proterozoic sedimentary basin formation in the north-northeast of Greenland and Paleozoic orogeny, resulting in the formation of the Ellesmerian fold belt in the north and the Caledonian orogenic belt in the east (Henriksen et al., 2008, 2009; Schmidt-Aursch and Jokat, 2005).

During the Paleozoic to Mesozoic periods, rift basin formation and sediment deposition took place in the north, east, and west of Greenland's margins. These events were followed by continental breakup and sea-floor spreading of the Labrador Sea about 62 million years ago, and the opening of the North Atlantic around 56 million years ago that led to the separation of Greenland and northern Europe (Chalmers and Pulvertaft, 2001; Torsvik et al., 2002). The breakup and sea-floor spreading coincided with the passage of the Icelandic hotspot beneath Greenland approximately 100 to 50 million years ago, leading to increased volcanic activity in western, eastern, and offshore southern Greenland, eventually resulting in the formation of the western and eastern Tertiary flood basalt provinces (Brooks, 2011; Holbrook et al., 2001; Hopper et al., 2003; Voss et al., 2009; Voss and Jokat, 2007). More detailed information about Greenland's geology and tectonic history is given by Henriksen et al. (2008, 2009).

Much of northeastern Canada is underlain by rocks of the eastern Canadian Shield, comprising Archean crust of the Superior, North Atlantic, and Rae cratons. The Archean domains are welded by Paleoproterozoic collisional belts, in particular the northeastern Trans-Hudson orogen, which crosses through southern Baffin Island (e.g., St-Onge et al., 2006, 2009). These terranes are overlain in parts of Baffin Island and the Queen Elizabeth Islands by Mesoproterozoic-Devonian sedimentary sequences, including the Franklinian basin which is exposed on eastern Ellesmere Island. The northernmost Canadian Arctic was affected by several Paleozoic tectonic events, including the Ellesmerian (or Innuitian) orogeny in the Devonian - Early Cretaceous, the accretion of exotic terranes to northern Ellesmere Island, and the development of the post-Ellesmerian Sverdrup Basin (Oakey and Stephenson, 2008).

2.1.2 Previous Seismic Studies

Seismic velocity models play an important role in constraining Earth properties in Greenland and northeastern Canada (Paxman et al., 2023). The lithospheric and crustal structure of Greenland

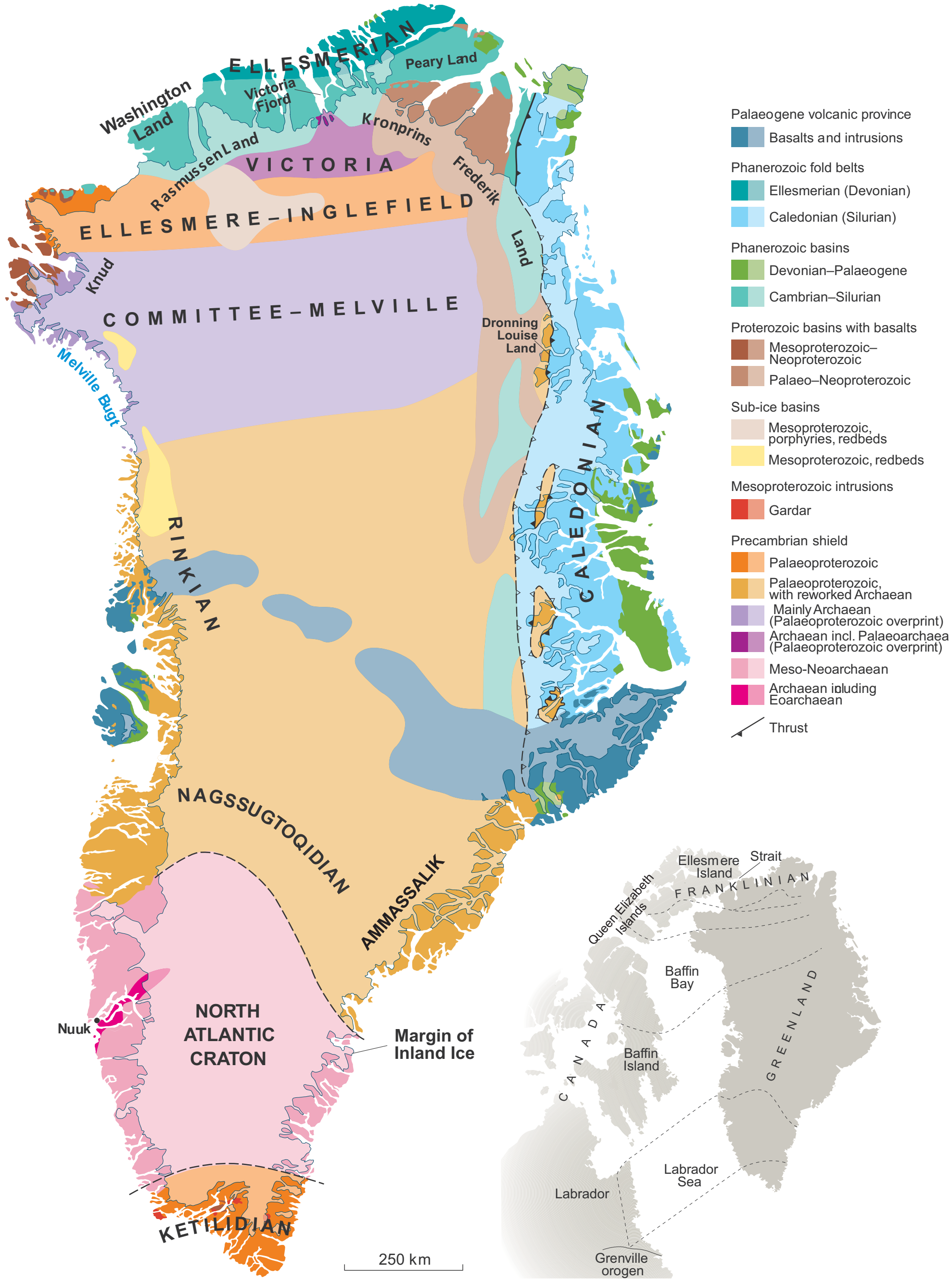

Figure 2.1: Geological map of Greenland including inferences of sub-ice bedrock units. Modified from Dawes (2009). The inset map (bottom-right) shows the extension of tectonic boundaries from Greenland to eastern and northeastern Canada.

and northeastern Canada has been studied with seismic tomography, receiver function analysis, ambient noise, and shear-wave splitting for decades (e.g., Levshin et al., 2001; Dahl-Jensen et al., 2003; Rickers et al., 2013; Darbyshire et al., 2017; Mordret, 2018; Toyokuni et al., 2020; Nathan et al., 2021). However, seismic data collection in these regions is challenging due to the difficulties involved in installing and maintaining seismic equipment on the ice sheet. As a result, most velocity models for this region are relatively low-resolution or do not cover the entire region (for example, northern Greenland and northeastern Canada are poorly resolved compared to central and southern Greenland). With the advancement of station coverage and more earthquake recordings, several high-resolution models of Greenland's lithospheric and crustal structure have been published. However, data coverage in northeastern Canada and northern Greenland is still sparse.

Global tomographic models (e.g., Ekström, 2011; Larson and Ekström, 2001; Ritzwoller et al., 2001, 2002; Schaeffer and Lebedev, 2013) provide some insights into Greenland's lithospheric structure. These models indicate that the lithosphere beneath Greenland can be divided roughly into two zones: a high seismic velocity region to the north-northwest and a low seismic velocity region to the south-southeast. However, these global studies have inherent limitations in lateral resolution, typically ranging from approximately 500 to 1,000 kilometers. Consequently, they cannot accurately capture important smaller-scale seismic velocity variations that may exist in the region. Regional seismic tomography studies, using surface waves and ambient noise tomography (Levshin et al., 2001; Darbyshire et al., 2004; Darbyshire, 2005; Darbyshire et al., 2017; Mordret, 2018; Pourpoint et al., 2018b,a), full-waveform S-wave / surface-wave tomography (Rickers et al., 2013; Lebedev et al., 2018) or P-wave arrival time tomography (Toyokuni et al., 2020; Toyokuni and Zhao, 2021), have provided insights into Greenland's geologic and tectonic structure by generating higher-resolution constraints of its subsurface. However, these studies have important limitations: either they do not resolve the deep lithospheric structure, or the coverage does not include the continental shelves or margins, or they have not been updated with information from recently installed seismograph stations.

Seismic anisotropy has been studied in Greenland and northeastern Canada using permanent and temporary stations (Darbyshire et al., 2017; Dube et al., 2020; Evans et al., 2006; Nathan et al., 2021; Ucisik et al., 2008). Shear-wave splitting studies are limited in their ability to resolve the source depth of the anisotropy, though some constraints are possible by considering lateral variations between nearby stations. Ucisik et al. (2008) measured splitting at stations across Greenland, assuming a single layer of anisotropy, and interpreted the results in the context of potential lithospheric deformation and/or asthenospheric flow. With a larger dataset, Nathan et al. (2021) considered backazimuthal variation in splitting measurements at stations across Greenland to model two-layered anisotropy, interpreted as lithospheric deformation in the shallow layer and either asthenospheric shearing or underthrust lithospheric layering in the deeper layer.

Both Nathan et al. (2021) and Dube et al. (2020) measured splitting for northernmost Ellesmere Island, also finding backazimuthal variations consistent with layered anisotropy. A more direct depth constraint on seismic azimuthal anisotropy is possible through surface wave tomography. Estimations of mantle anisotropy beneath Greenland and its surroundings have been made in global and large-scale regional studies (Levshin et al., 2001; Pilidou et al., 2004; Schaeffer et al., 2016) but the relatively low lateral resolution and the data coverage of the older models limits detailed interpretation. Darbyshire et al. (2017) investigated anisotropy beneath Greenland and its surroundings at much higher resolution using regional group velocity tomography, but their study is restricted to the crust and uppermost mantle (to $\sim$80 km depth), thus limiting direct comparisons with splitting and other previous measurements. In this study, the period range of the surface waves allows constraint on azimuthal anisotropy in the lower crust and upper mantle, with the possibility of resolving the apparent discrepancies in previous studies that arise from the differences in methodology used.

The assembly of eastern Laurentia has been extensively studied in northern Canada, using seismographs distributed around the Hudson Bay region and Baffin Island. SKS splitting measurements were carried out by Bastow et al. (2011); Snyder et al. (2013); Liddell et al. (2017), and anisotropic surface wave tomography by Darbyshire et al. (2013). Bastow et al. (2011) and Liddell et al. (2017) observed significant variations in SKS splitting parameters over short spatial scales, as well as evidence for complex multi-layered and/or dipping anisotropy. They attributed these features entirely to plate-scale lithospheric deformation associated with the Paleoproterozoic assembly of Laurentia. In contrast, Snyder et al. (2013) suggested a component of present-day plate motion to explain their splitting measurements. Darbyshire et al. (2013) inferred two cores of high seismic wavespeeds in the upper lithospheric mantle, associated with the Archean Churchill and Superior cratons, with a subvertical zone of lower wavespeeds in between, consistent with juvenile Proterozoic material being preserved in the Trans-Hudson orogen (THO). The lower lithosphere exhibited more uniform wavespeeds but a distinct pattern of anisotropy mirroring the near-surface expression of the THO. These findings in northern Canada were interpreted as evidence for modern-style plate tectonics in the Paleoproterozoic, and a multi-stage formation process for the Laurentian keel. Similar signatures of Precambrian tectonic processes may be expected beneath much of the Greenland shield region (e.g., St-Onge et al., 2009), except for areas overprinted by later tectonic activity.

2.2 Data and Methods

2.2.1 Seismograph Network and Waveform Data

We calculate the Rayleigh-wave phase velocity structure across Greenland and northeastern Canada. To do so, we use a broad distribution of stations consisting of 48 permanent broadband seismic stations belonging to various networks, including the Canadian National Seismograph Network (Natural Resources Canada, 1975) , Danish National Seismograph Network (Danish Seismological Network, 1976), Geoscope (Institut de physique du globe de Paris (IPGP), & École et Observatoire des Sciences de la Terre de Strasbourg (EOST), 1982), Korea Polar Seismic Network (Won Sang Lee, 2013), Norwegian National Data Center (Norsar, 1971; University of Bergen, 1982), Global Seismograph Network (GSN, Scripps Institution of Oceanography, 1986; Albuquerque Seismological Laboratory/USGS, 2014), and some individual stations (X5, GE, GB, GG, Stephen, 2005; Sokos, 2015; Marianne Karplus, 2017; Fletcher, 2018; GEOFON Data Centre, 1993; British Geological Survey, 1970; IRIS HQ (DC), 2012) located in Greenland, eastern Canada, Norway, Svalbard, and Iceland (Fig. 2.2 and Table A2.1 in the Appendix section). We mostly used permanent stations for their extended temporal recording to obtain high-quality seismic data and measure fundamental mode Rayleigh wave phase dispersion (i.e., surface wave propagation speed changes as a function of frequency) from teleseismic earthquakes.

2.2.2 Teleseismic Two-station Surface Wave Dispersion

In this study, we generate two-station measurements using seismic records from the vertical component of teleseismic events with a magnitude (Mw) greater than 5.8 and epicentral distance of $\geq 20°$ that occurred between 1989 and 2022. To minimize the off-path propagation effect, we specifically select station pairs with an inter-station distance greater than 300 km, for which the difference in back azimuth between the station-event great circle path and station pairs is less than 5 degrees. In addition, for each station pair, we ensure that the earthquake dataset includes events from a range of epicentral distances and from both directions (i.e., station A$\rightarrow$B and B$\rightarrow$A) to minimize any potential bias associated with off-great-circle propagation and angular deviations from a great circle path at short periods (e.g., Foster et al., 2014; Meier et al., 2004; Pedersen, 2006; Pedersen et al., 2015).

The selected waveforms are detrended, resampled to 1 Hz, and low-pass filtered with a corner frequency of 0.5 Hz to improve the signal-to-noise ratio. We remove instrument response such that the signals are expressed in terms of displacement. Following these processing steps, we employ a two-station measurement method to eliminate the effects of the earthquake source

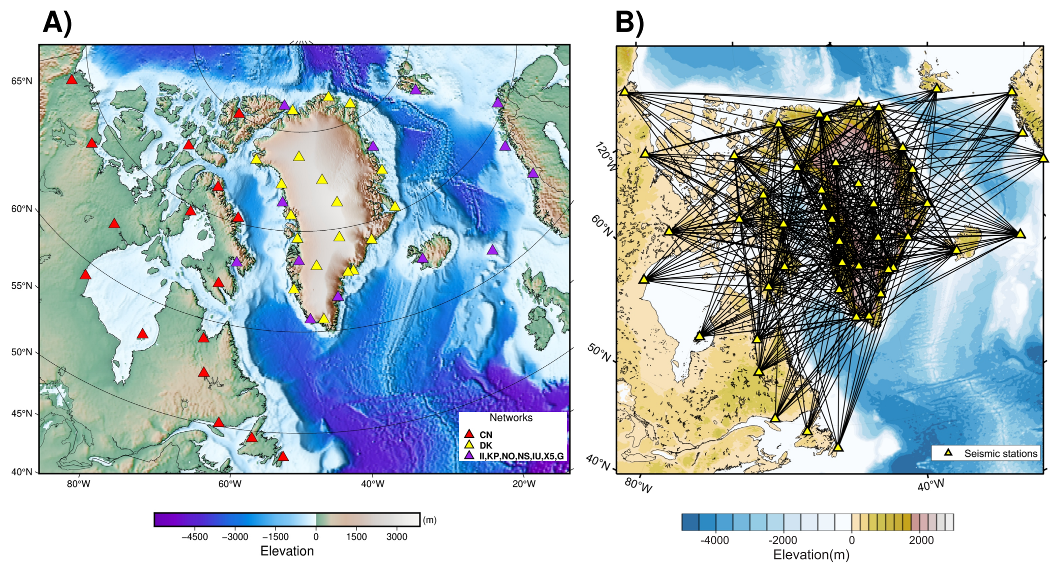

Figure 2.2: **A)** Location of all stations used in this study. The color of the symbols indicates specific networks (see Table A2.1). **B)** All possible station pairs and corresponding ray paths for the station distribution shown in (A).

and teleseismic paths. This method calculates the cross-correlation between the two vertical components and converts it into the frequency domain to estimate the phase velocity c(ω) from the complex phase spectrum. Fig. 2.3 -A&B shows the vertical displacement waveforms and their corresponding spectrograms for a pair of seismograph stations. This visualization helps us identify the potential frequency range suitable for analyzing Rayleigh waves using the two-station method. Near-surface scattering significantly impacts frequencies between 0.1 and 0.6 Hz; therefore, we restrict our analysis to frequencies lower than this range. Figure 2.3-C illustrates the cross-correlation time series, its spectrogram, and the corresponding phase spectrum.

Phase wrapping introduces ambiguity in determining the integer number of cycles. Consequently, different cycle numbers lead to a range of possible solutions for phase velocity, as depicted in Fig. 2.3-D. To address this, we employ a reference model (specifically, the AK135 global model of Kennett et al. (1995)) as a guide to identifying the phase velocity curves that visually match the reference model. We select only the smooth parts of the dispersion curve that lie close to the reference model to ensure a reliable range of measurements. The final dispersion curve is obtained by averaging the selected solutions for all available earthquakes that align with the pair of seismic stations. This estimated dispersion curve represents the average Rayleigh-wave phase velocity between the two stations. Using this technique, we calculate 454 inter-station dispersion curves (as shown in Fig. 2.2-B) for periods ranging from 25 to 185 seconds across 48 seismograph stations. We further refine the selected dispersion curves by remov-

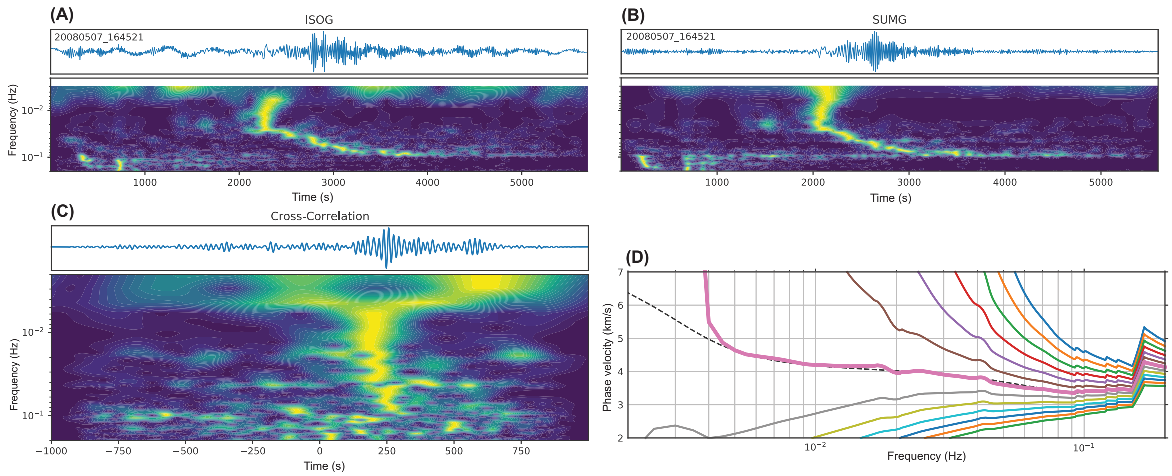

Figure 2.3: Example of the interactive cross-correlation technique for phase velocity dispersion curve selection as applied in this study. **A-B)** vertical displacement seismograms and spectrograms of an earthquake recorded by stations ISOG and SUMG, **C)** the cross-correlation seismogram and spectrogram of the two signals, and **D)** Rayleigh wave phase velocity solutions given the $2n\pi$ ambiguity. The black dashed line in (D) is the theoretical dispersion curve based on the AK135 model that we used as a guide to pick the closest dispersion curve.

ing unstable results or significant outliers based on the standard deviation of the averaged phase velocity. These averaged two-station phase velocity dispersion measurements serve as input for the tomographic inversion to obtain phase velocity maps. Further examples of dispersion curve measurements are shown in supplementary material (text and Fig. A2.8).

2.2.3 Seismic Tomography Inversion: Phase Velocity Maps

Each averaged two-station dispersion curve represents the integrated structure along the path between the stations. The inferred phase velocities are then inverted for azimuthally anisotropic phase velocity maps as a function of period, based on the methodology described in past work (Darbyshire and Lebedev, 2009; Deschamps et al., 2008). The total phase velocity anomaly $\delta\bar{c}_i$ can be described as the integration of local anomalies $\delta c(\omega, \phi, \theta)$ at a discrete set of frequencies (ω), and at each grid knot of longitude (θ) and latitude (ϕ) along the corresponding inter-station path i:

$$\delta\bar{c}_i(\omega, \phi, \theta) = \int\int k_i(\omega, \phi, \theta) d\phi d\theta \tag{2.1}$$

where i describes the path for which we calculate the anomaly, and the kernel $k_i(\omega, \phi, \theta)$ refers to the Rayleigh waveform sensitivity area that regulates the weight of each grid point along the path i (Lebedev and Van Der Hilst, 2008). For each frequency, the local phase velocity anomaly (Eq. 2.1) at each grid knot is decomposed into isotropic and anisotropic components by applying a Fourier series expansion based on azimuth (Smith and Dahlen, 1973; Deschamps et al., 2008):

$$\begin{aligned} \delta c(\omega) = \delta c_{iso}(\omega) + A_1(\omega)\cos(2\psi) + A_2(\omega)\sin(2\psi) \\ + A_3(\omega)\cos(4\psi) + A_4(\omega)\sin(4\psi) \end{aligned} \tag{2.2}$$

where δc_{iso} is the isotropic component, A_1 and A_2 denote the 2ψ anisotropic components and A_3 and A_4 refer to the 4ψ anisotropic components, respectively. These five parameters are the unknown coefficients to solve for. We develop a linear system of equations for each period and path, based on Eq. 2.2, by projecting the dispersion curve intersections onto a model grid. The system of equations is solved separately at each period using the least squares technique (Paige and Saunders, 1982). We solve for isotropic and anisotropic $(2\psi, 4\psi)$ phase velocities (Paige and Saunders, 1982). However, it is worth noting that Rayleigh waves exhibit weak sensitivity to the 4ψ component in the upper mantle (Montagner and Anderson, 1989). As a result, although these components exist in our model, we exclude them from our interpretation. Further reference to anisotropic parameters (amplitude, orientation) in this paper thus refers exclusively to the 2ψ parameters. Since the technique employed does not provide a covariance matrix for uncertainty quantification, we regularize the model using norm damping, lateral smoothing, and lateral gradient adjustments at each period. These adjustments help reduce fitting errors, prevent overfitting, and maintain a reasonable model norm. Moreover, we perform resolution and leakage tests to evaluate the reliability of the inversion results in resolving synthetic velocity structures (Sec. 2.2.5).

2.2.4 Model Parameterization, Regularization, and Data Fit

We adopt a spherically-tessellated triangular grid with a knot spacing of 150 km, specifically designed for the region under investigation (Wang and Dahlen, 1995). This grid configuration ensures that the inter-knot spacing is approximately equal throughout. Such an approach is particularly suitable for smoothing and damping effects, especially in higher latitudes (e.g., 58° to 88°). The functional model vector ($\vec{m}$) is solved by minimizing the cost function:

$$|\mathbf{A}\vec{m} - \vec{d}| + \alpha|\boldsymbol{I}\vec{m}| + \lambda|\Lambda\vec{m}| + \gamma|\Gamma\vec{m}| \tag{2.3}$$

where $\mathbf{A}$ is the design (kernel) matrix, $\vec{d}$ is the observation vector, $\vec{m}$ contains our unknown

Table 2.1: Final inversion parameters.

Period	Smoothing parameters		Damping Parameters	
	Isotropic	Anisotropic	Isotropic	Anisotropic
(s)		(2ψ & 4ψ)		(2ψ & 4ψ)
25-185	0.3	0.6	0.1	0.15

model parameters, α, λ, and γ are the norm damping, lateral smoothing, and gradient damping coefficients, respectively, $\boldsymbol{I}$ is an identity matrix, and Λ and Γ are the the lateral smoothing and gradient operators, respectively. Gradient damping reduces the first derivative of the phase velocity anomaly distribution, whereas smoothing penalizes the second spatial derivative and propagates the local anomaly peaks into the final phase velocity distribution (Darbyshire and Lebedev, 2009). In this study, we fix the gradient damping to a small value for both isotropic and anisotropic heterogeneity and focus mainly on norm damping and lateral smoothing for the inversion. The selection of these parameters is subjected to several tests. These tests are mainly applied at three periods (short - 25 s, intermediate - 61 s, long - 151 s) since variations in ray path coverage with period could differ and affect the inversion results.

Tests carried out to obtain the optimum smoothing parameters are applied with a fixed low damping value of 0.5. We investigate the effect of different isotropic and anisotropic smoothing values on roughness versus remaining variance curves. The trade-off curve between roughness and variance for both isotropic and anisotropic models enables us to pick the best value at the "knee" part of the L-curve shape. Then, we narrow our parameter search space around the chosen value, inspect the phase velocity maps visually, and find the best approximate smoothing value for isotropic and anisotropic components. A similar approach is performed to find damping values by fixing a low smoothing parameter (0.1 and 0.2 for isotropic and anisotropic inversion, respectively). The final test is run to find the balance between the chosen smoothing and damping parameters for both components. Final parameter selection was made after examining model results at the three mentioned periods. Due to approximately constant ray paths at different periods (Fig. A2.1), the best parameters didn't show significant changes, and so we selected one set of parameters to be used for all periods (Table 2.1). The reliability of the selected parameters is then inspected by carrying out a resolution test analysis (Sec. 2.2.5).

We perform a linearized inversion for phase velocity variations, which outputs a best-fitting model based on the data points, without incorporating input data uncertainties. Therefore, no output statistics for model uncertainties are estimated. To mitigate the limitations of linearized inversions, we use the input data uncertainties in the outlier-exclusion process prior to the final inversion, where inter-station measurements that cannot be fit within their uncertainties are excluded from further analysis. Outliers cause artifacts in the phase velocity maps by producing sharp and non-realistic phase velocity jumps. These artifacts generally occur in regions with low path density where the inversion performs poorly. Another possible reason for these artifacts may be station-specific issues, such as data noise, timing problems, or response problems. This kind of artifact shows up as a strong (bright) anomaly at the location of the faulty stations compared to the surrounding regions. Removing outliers reduces the overall variance of the model. We perform this test by setting outlier thresholds of 75%, 85%, and 95% (see Schaeffer and Lebedev, 2013, for details). Lower threshold values result in fewer paths, leading to faster convergence and lower variance. Based on a visual inspection of phase velocity maps and remaining variance, we use a threshold value of 95%, consistently across all periods. The final phase velocity maps are generated by inversion following the outlier removal.

2.2.5 Model Resolution

We perform a series of resolution tests to assess the reliability and sensitivity of the inverted phase velocity maps at intermediate (61 s) and long (151 s) periods. All tests use the same framework: producing synthetic phase velocity measurements with a synthetic model, adding 0.02 km/s of random Gaussian noise uniformly to the synthetic data, and inverting the measurements for an anisotropic phase velocity model based on the great circle ray propagation and zero-width ray assumptions. In these steps, the inversion parameters and ray path coverage are the same as those used for the observed data. In this section, we present the results of model resolution from two different test types: synthetic tests (using regular and irregular geometric shapes) and leakage tests (see Figs. 2.4 & 2.5, and Fig. A2.2).

We design a pseudo-checkerboard model to estimate the phase velocity resolution (Fig. 2.4). The pseudo-checkerboards are generated in different shapes and sizes (200 km to 400 km) by setting the velocity variation at model grid points (150 km spacing) to $\pm 3\%$ and then interpolating onto a finer grid. This synthetic analysis was applied in previous studies (e.g., Deschamps et al. (2008); Darbyshire and Lebedev (2009); Foster et al. (2020)). We note that instead of the conventional Cartesian framework (e.g., Nolet, 1993; Boyce et al., 2016), a triangular geometry is used for the tomography model grid. Therefore, the anomaly shapes in Fig. 2.4 are based on triangles and hexagons rather than the more commonly used squares and rectangles.

Based on Fig. 2.4, $\sim$200 km wide anomalies (first row) are recovered well over Greenland, the Labrador Sea, and northeastern Canada, although the model anomalies fade out in northern Greenland and the Queen Elizabeth Islands. The $\sim$400 km anomalies (second row) are better recovered than the smaller anomalies over Greenland and northeastern Canada, representing a greater resolution for structures of this scale. Since the main objective of this study is to study

Greenland and northeastern Canada, and the initial network design was based on this purpose, the synthetic signal recovery in other regions like Iceland, the Atlantic Ocean, and the western side of Baffin Island is poor, and the synthetic anomalies are not recovered well. Poor magnitude recovery originates from low inter-station path density and low path cross-cutting (especially at the edges of our study region). Therefore, we focus our interpretation on Greenland, northeastern Canada (Baffin Island, Baffin Bay, and the Queen Elizabeth Islands), and the Labrador Sea regions. At intermediate to long periods (61 s-151 s), the differences in the number of paths ($\sim$450), cross-cutting geometry, and directional variation are negligible, which makes the model recovery similar for the entire period range (Fig. A2.2).

We create synthetic input models that broadly simulate the spatial distribution of continental lithosphere and oceanic upper mantle to investigate the model's ability to resolve these two features (Fig. 2.4, last row). The synthetic model consists of fast velocity anomalies in Greenland, northeastern Canada, Svalbard (continental lithosphere), and Iceland, with slow anomalies in the Labrador Sea, Atlantic Ocean, and Baffin Bay. At 61 s period, fast anomalies are well recovered over Greenland, Baffin, and the Queen Elizabeth Islands. However, the recovery over Iceland and Svalbard is poor. Slow anomalies are well recovered in the Labrador Sea and Baffin Bay, whereas the anomalies are smeared in other regions. The longer period (151 s) map also shows similar patterns, and the recovered boundaries between fast and slow anomalies in the continent and ocean are accurate except for some smearing at the edges. Spurious anisotropy is minimal and mostly appears in northeastern Canada at shorter periods and southeast Greenland at longer periods, associated with sharp velocity gradients.

Spurious velocity anomalies can leak between the inverted isotropic and anisotropic components during the inversion procedure (i.e., isotropic parameters are mapped as anisotropic components and vice versa). To examine the impact of such numerical artifacts, we perform three separate resolution tests in which we invert each component individually: (a) isolated isotropic velocity (to investigate leakage into anisotropy), (b) isolated anisotropic velocity (to investigate leakage into isotropic velocity), and (c) a combination that includes rotated anisotropy (by 90°). Fig. 2.5 shows the recovery of these synthetic models and the numerical artifacts that appear on the other components at periods 61 s and 151 s.

In all three cases, the magnitudes of the leaked isotropic or anisotropic anomalies are similar for the two periods. In the isolated isotropic model, a mean anisotropy anomaly amplitude of 0.2% leaks into the 2ψ component, with a few regions showing spurious anisotropy anomalies of up to $\sim$0.5% (central and southeast Greenland). Isotropic velocity patterns are well recovered with slightly reduced amplitudes (-0.5%) in northwest Greenland and eastern Canada at 61 s and increased values (+0.5%) at 151 s in the Labrador Sea and eastern Greenland. In the isolated anisotropic model (here, only 2ψ), there is negligible leakage into the isotropic component (mean isotropic phase velocity leakage of $\pm$0.2%). The azimuthal anisotropy amplitudes and directions

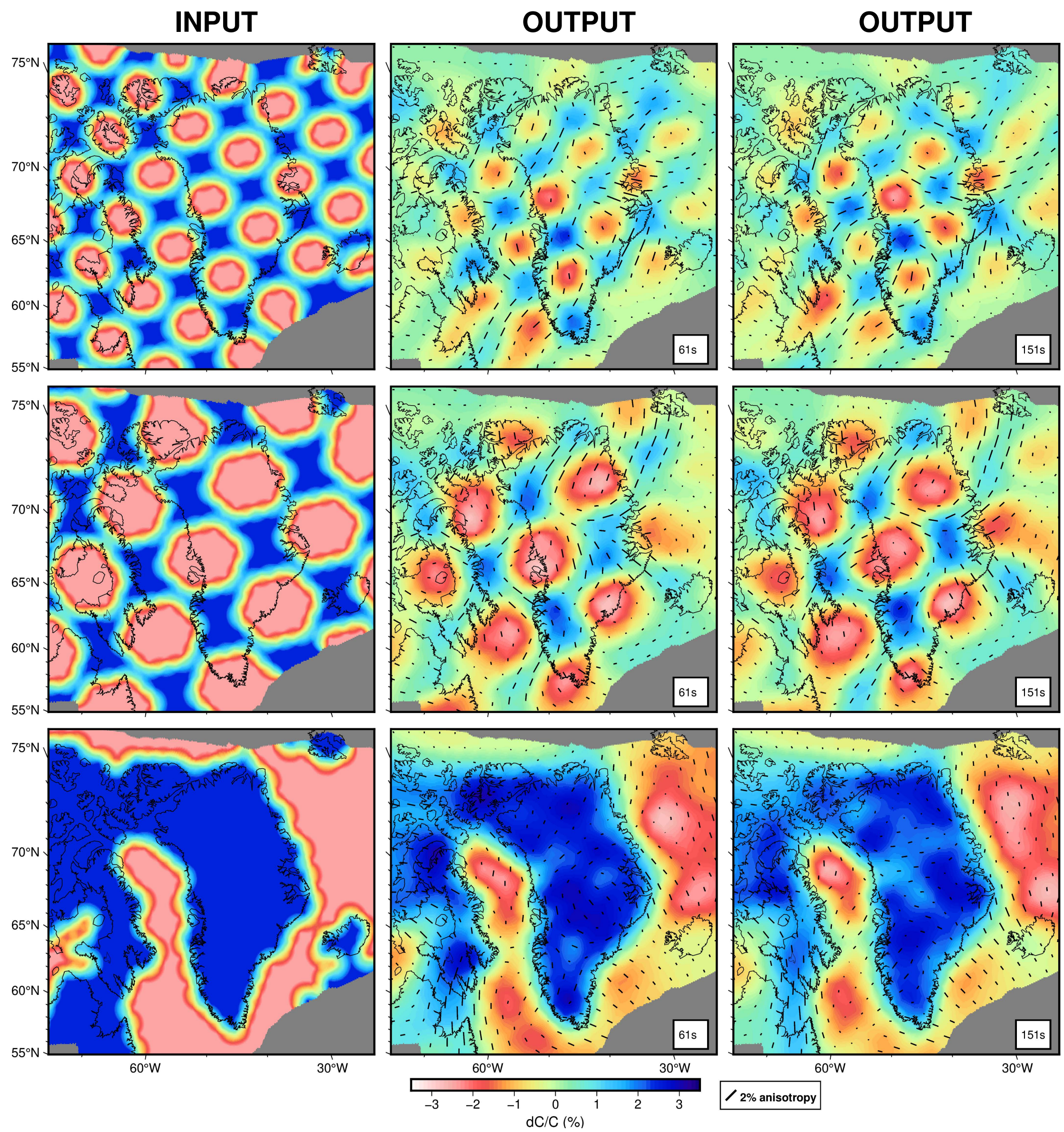

Figure 2.4: Two checkerboard patterns of different lateral scales (first and middle rows) and one structural pattern (continent vs. ocean; bottom row) form the basis of the resolution tests. The first column shows input models (isotropic), and the second and third columns are recovered velocity models (isotropic plus 2ψ) for, respectively, intermediate (61s) and long (151s) periods. Further resolution tests are provided in Appendix section (Fig. A2.1).

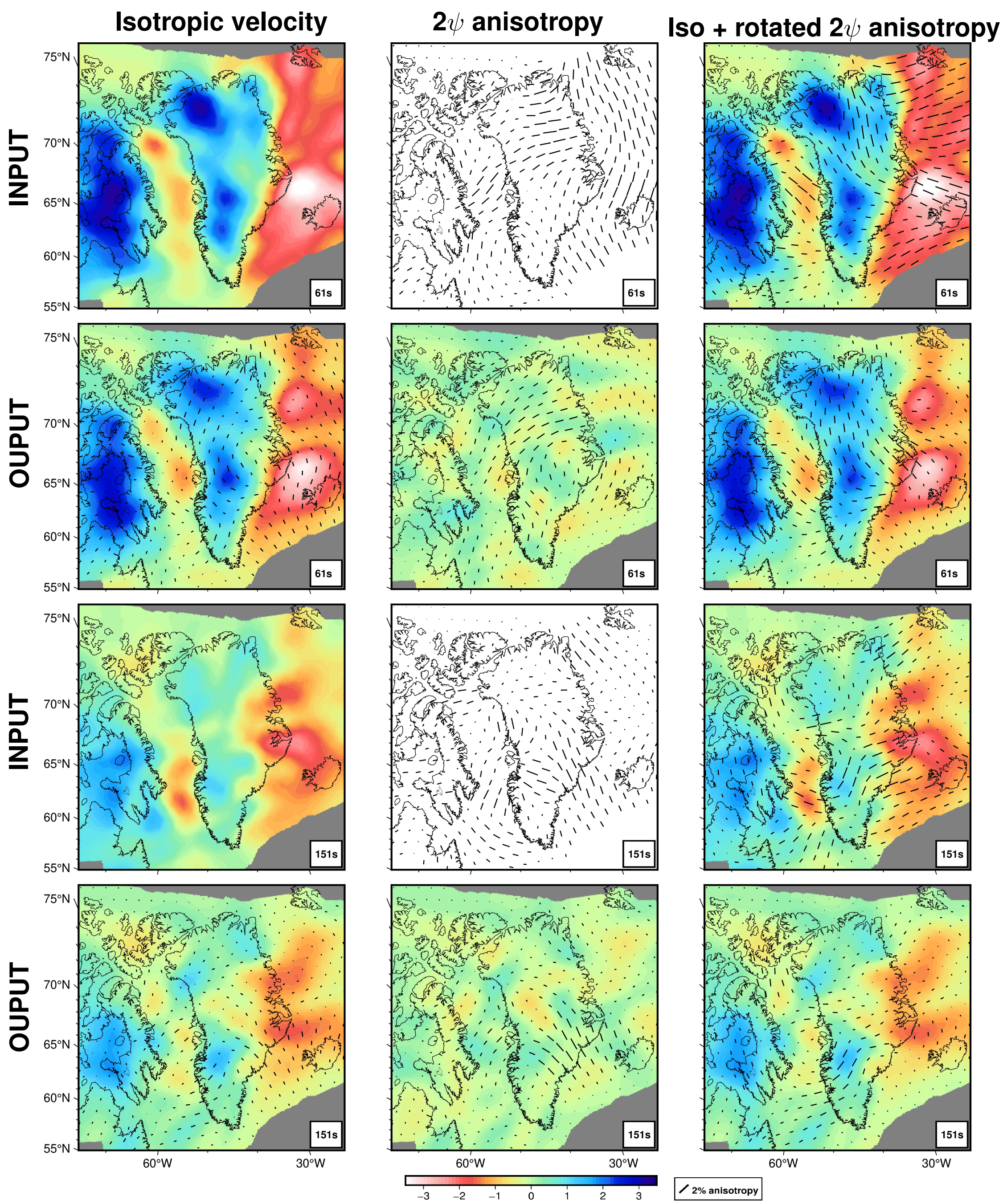

Figure 2.5: Three leakage tests at periods of 61 s and 151 s. In the left column, the input model is the isotropic component of the preliminary data inversion, and in the middle column, the input model is the 2ψ anisotropic component. In the right column, the input model includes both isotropic and 2ψ components, but with the anisotropy fast orientations rotated through 90° from the original inversion.

are well recovered over Greenland and northeastern Canada, with an average anomaly reduction of $\sim$0.1% and a mean azimuthal deviation from the input values of $\sim$10°, whereas areas like the Atlantic Ocean and northern Labrador Sea show much-reduced anisotropy amplitude. At the longer period (151 s), the recovered anisotropy amplitudes are the same over Greenland and northeastern Canada as the shorter period, whereas the amplitude is significantly reduced in the Labrador Sea.

In the third test, we invert for a model that involves a combination of both isotropic and anisotropic components at 61 s and 151 s. The anisotropy directions are rotated by 90° to test for bias in the recovered azimuthal distribution. Fig. 2.5 shows that the rotated anisotropy directions are well recovered, with high azimuthal deviations occurring only in eastern Greenland. Isotropic velocity patterns are well recovered with slightly reduced amplitudes (-0.5%) in northwest Greenland and eastern Canada at 61 s and increased values (+0.5%) at 151 s in the Labrador Sea and eastern Greenland. In summary, the above resolution and leakage tests indicate that the inversion method, as applied to our data set, is able to generate valid tomographic models without significantly distorting each component or inducing significant numerical artifacts that could bias the interpretation in the main study area.

2.3 Results: Phase Velocity Maps

Isotropic velocity anomalies are presented for selected periods between 25 and 185 s in Fig. 2.6 as the perturbation from the mean velocity over the entire region at each selected period. As mentioned previously, we invert for isotropic, 2ψ, and 4ψ anisotropy; however, we do not interpret 4ψ signals because Rayleigh-wave sensitivity to 4ψ anisotropy is low in the mantle (Montagner and Anderson, 1989). To aid the interpretation of phase velocity maps, we include sensitivity kernels (Fig. 2.7) for the corresponding periods because phase velocity represents a depth-integrated measure of shear wave velocity structure. Based on the resolution tests discussed in Sec 2.2.5, we limit our interpretation to Greenland and northeastern Canada.

At short periods ($\sim$25 s), Rayleigh waves are mostly sensitive to the shear wave velocity structure in the 20-70 km depth range. At these periods, based on Fig. 2.6 with respect to the average velocity, we observe isotropic anomalies of up to $\pm$2%, with the most prominent negative anomalies over central, northwest, and northeast Greenland, the Queen Elizabeth Islands, and positive anomalies in Baffin Bay and the Labrador Sea. The anisotropic signals are variable, with amplitudes typically less than 2%. They are primarily oriented N-S in northeastern and central Greenland but more NW-SE in northwest and southeast Greenland. The fast orientation in the Labrador Sea is E-W and rotates to NE-SW in the area between southeast Greenland and Iceland.

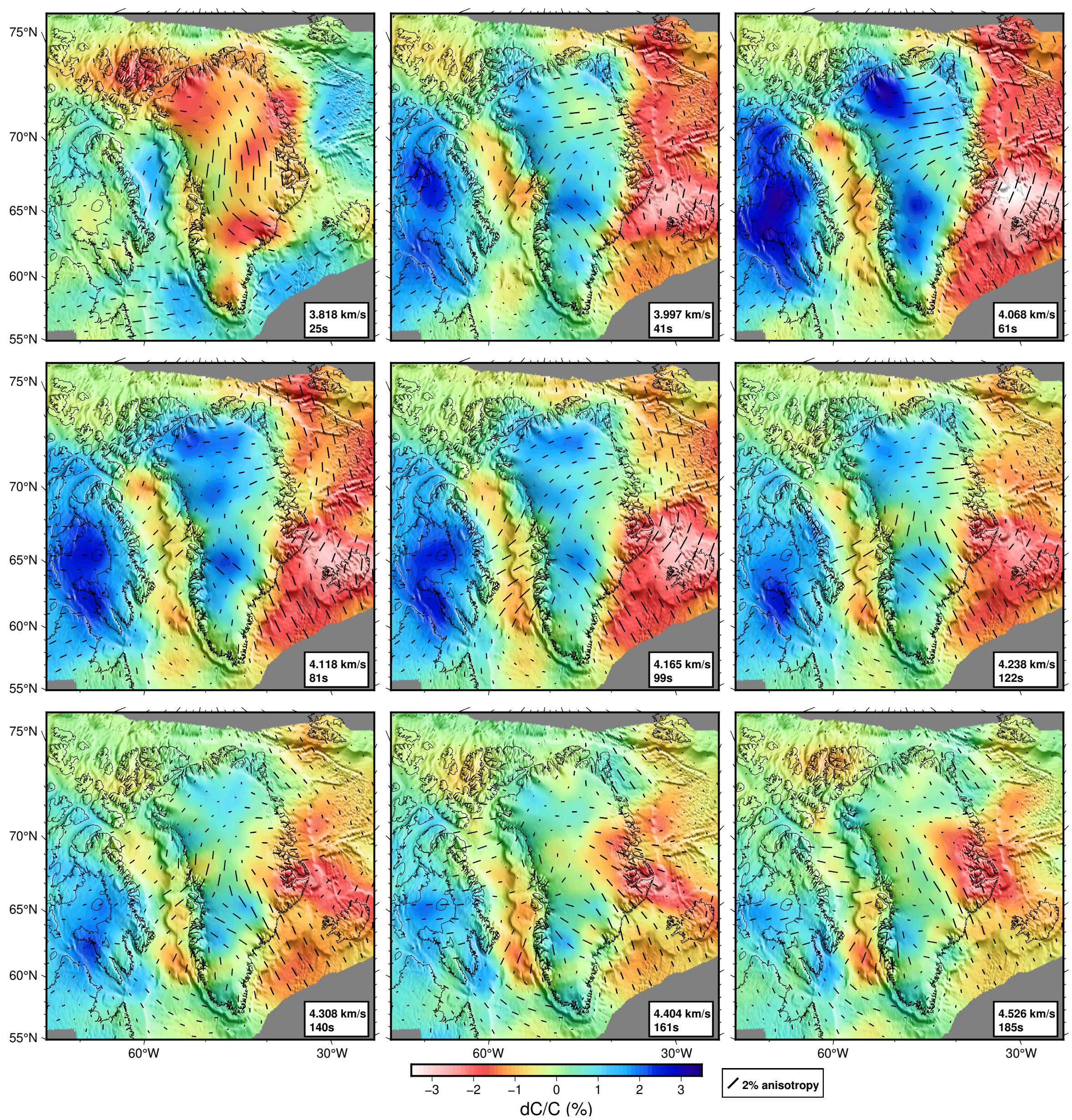

Figure 2.6: Rayleigh wave phase velocity anomaly (isotropic and azimuthal anisotropy) maps of Greenland and northeastern Canada at periods ranging from 25 to 185 s. The velocity given in the white box at the bottom right is the regional reference (average) in km/s for each period. Grey areas represent no path coverage.

At intermediate periods (41-61 s), the depth sensitivity to shear wave velocity ranges from $\sim$40-130 km. At these periods, isotropic phase velocities vary up to $\pm 3.5\%$ from the regional average velocity. In contrast to shorter periods, the fastest velocity anomalies are located beneath the continents, notably northwest and central Greenland and Baffin Island. Lower-velocity anomalies are observed in central-eastern Greenland, Baffin Bay, and the Labrador Sea. The amplitudes of these anomalies increase with increasing period. Compared to shorter periods, the anisotropy orientations are rotated by $\sim 90°$ in northern Greenland to an E-W orientation. There is weak $\sim$N-S anisotropy in northern Baffin Bay, stronger NE-SW anisotropy in southern Baffin Bay ($\sim$ 2%), N-S to NW-SE orientations in southeast Greenland, and NNW-SSE to N-S in southern Greenland.

At longer periods (81-122 s), the Rayleigh waves are most sensitive to structure in the $\sim$80-250 km depth range. Isotropic phase velocity anomalies vary up to $\pm 2.5\%$ from the regional average velocity. High velocities continue to be observed for northern and central Greenland and northeastern Canada, although their amplitude decreases with increasing period. Low-velocity anomalies observed for east Greenland, the Labrador Sea, and Baffin Bay maintain their amplitude as periods increase. At these periods, compared to intermediate periods, the anisotropy in northern Greenland has the same orientation with a lower amplitude, whereas the amplitude increases in southern Greenland and Baffin Bay. We observe stronger NW-SE anisotropy in southeastern Greenland and NE-SW in southwest Greenland.

At periods greater than 140 s, the structural sensitivity of Rayleigh waves extends deeper into the $\sim$200-350 km depth range. The variation of phase velocity anomalies drops to $\pm 1\%$ over Greenland except for eastern Greenland (-2%). Positive velocity anomalies in Greenland decrease considerably as periods increase beyond 140 s. At these longer periods, the highest velocity anomaly is located beneath southern Baffin Island. The observed low-velocity anomaly in eastern Greenland is persistent in this depth range and extends northwards and westwards as periods increase. Also, weak low-velocity anomalies in the Davis Strait and southern Baffin Bay are present. Compared to shorter periods, the anisotropy is weaker in northern and southeastern Greenland, but the orientation is broadly similar; also, the anisotropy in northern Baffin Bay is stronger and has an E-W orientation. In eastern Greenland, the low-velocity anomaly is accompanied by NW-SE-trending anisotropy that becomes increasingly coherent with increasing period.

2.4 Discussion

Our phase velocity maps are sensitive to structure ranging from the lowermost continental crust and oceanic mantle lithosphere ($\sim$20-30 km depth) through to depth ranges that primarily sample

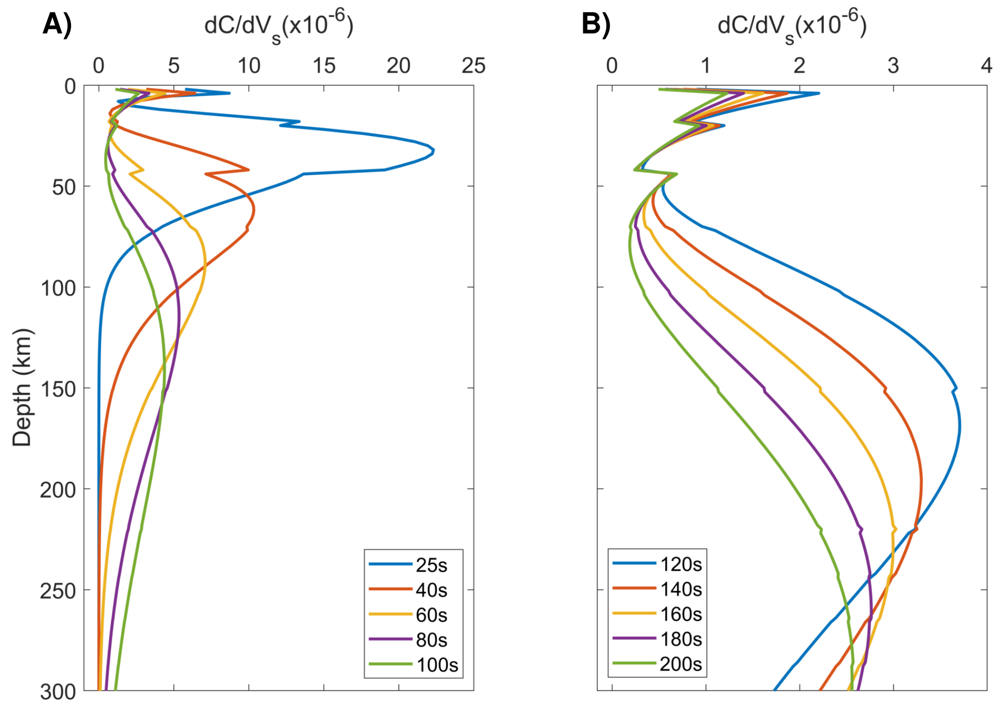

Figure 2.7: Fundamental mode Rayleigh wave depth sensitivity kernels for period range 25 s to 100 s (**A**) and 120s to 200s (**B**) (Keilis-Borok et al., 2012).

sublithospheric structure even beneath thick cratonic keels ($\geq$250 km depth). We examine the patterns of phase velocity anomalies and azimuthal anisotropy (Fig. 2.6) in the context of the assembly and evolution of Precambrian Greenland, Paleozoic and younger orogenic episodes, rifting and ocean basin formation, and the past and present-day influence of the Iceland plume.

2.4.1 Isotropic Crust and Mantle Structure

In contrast to northern Canada, where tectonic boundaries are clearly visible in surface geology or potential field maps (e.g., St-Onge et al., 2009; Eaton and Darbyshire, 2010), direct correlation between seismic tomography results and tectonics is challenging on mainland Greenland due to the presence of the ice sheet. Direct geological sampling is limited to coastal regions and isolated drill sites or nunataks inland. Potential-field data, previous crustal tomographic studies and sub-ice geomorphology add some additional constraint, but interpolation is also used to infer tectonic subdivisions (Dawes, 2009; MacGregor et al., 2024). There is good consensus on tectonic subdivisions in southern Greenland (North Atlantic craton, Ketilidian and Nagssugtoqidian orogens), as well as the younger Caledonian and Ellesmerian/Franklinian fold belts in the east and north respectively. The tectonic subdivisions of Precambrian central-northern Greenland are more uncertain; Dawes (2009) suggests a set of east-west-trending belts, whereas MacGregor et al. (2024) infer a more north-south trend, including central regions of unknown affinity. A further outstanding question is whether the volcanic rocks of the North Atlantic igneous Province (NAIP), exposed in west and east Greenland, also continue beneath central Greenland, as suggested by Dawes (2009). Fig. 2.8 provides an overview of the main tectonic boundaries inferred by Dawes (2009); St-Onge et al. (2009); MacGregor et al. (2024), superimposed on four selected phase velocity maps, to facilitate our interpretations.

2.4.1.1 Southern Greenland

At periods most sensitive to the crust and uppermost mantle (25-30 s), we observe relatively lower velocities beneath the Nagssugtoqidian and Ketilidian orogens compared to the North Atlantic craton, consistent with the thickened crust reported in these areas (Dahl-Jensen et al., 2003; Darbyshire et al., 2017; Mordret, 2018; Pourpoint et al., 2018b) and with observations in the Canadian Shield where Proterozoic mobile belts are typically associated with thicker crust than Archean cratons (e.g., Gilligan et al., 2016; Vervaet and Darbyshire, 2022).

At longer periods, where the Rayleigh waves are largely sampling upper-mantle structure, we observe the development of a prominent series of high-velocity anomalies beneath much of southern Greenland, with the exception of the Ketilidian belt in the far south and the east coast Ammassalik belt, where our phase velocity maps are likely affected by the continental edge. Previous seismic studies (e.g., Lebedev et al., 2018; Mordret, 2018; Pourpoint et al., 2018a; Celli et al., 2021) have also imaged high velocities beneath this region, but our resolution allows us to identify internal heterogeneities in this anomaly for the first time. The position of the highest velocity anomalies changes with period, but their main extent covers the region from the central North Atlantic craton to the inferred (Dawes, 2009) trace of the NAIP beneath central Greenland. At 40-50 s period, the highest velocities are observed north of the Nagssugtoqidian orogen, within the southern Rae craton, with a much weaker anomaly beneath the North Atlantic craton. Between $\sim$55 and 70 s period, high velocities almost equal to the Rae signature are observed beneath the northern North Atlantic craton, with the Nagssugtoqidian orogen forming a band of relatively lower velocity between them. At 75 s period, the two cores appear to coalesce, forming a high-velocity anomaly that persists to $\sim$140 s period, for which the amplitude gradually diminishes with increasing period.

We speculate that the Nagssugtoqidian orogen exhibits a signature of tectonic reworking related to the collision between the North Atlantic and Rae cratons, but that this feature is largely

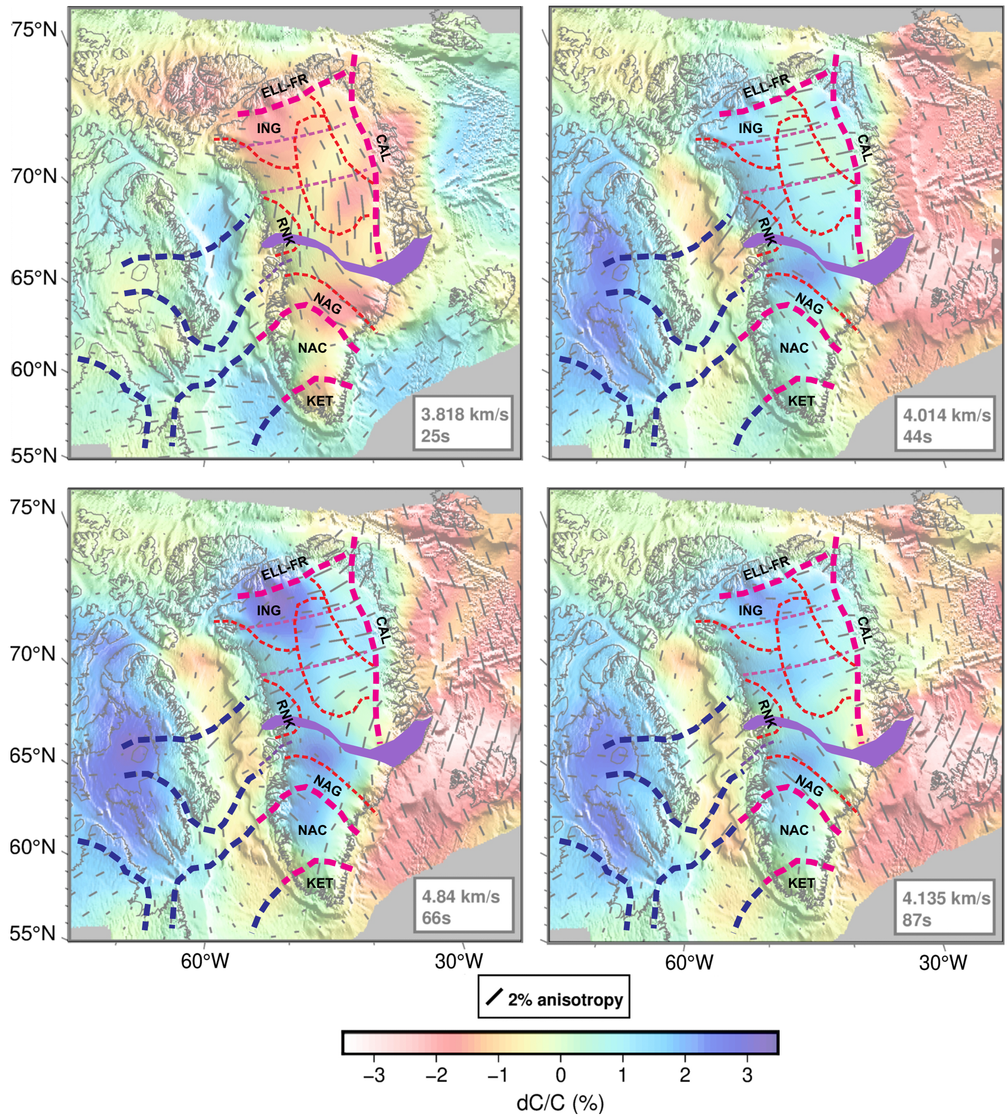

Figure 2.8: Phase velocity maps at four selected periods with main inferred tectonic boundaries overlaid, redrawn from St-Onge et al. (2009), Dawes (2009) and MacGregor et al. (2024). On mainland Greenland: wide magenta lines are high-confidence boundaries common to all interpretations, pink-purple lines are inferences from Dawes (2009), red lines are inferences from MacGregor et al. (2024), the mauve band is the proposed trace of the North Atlantic Igneous Province beneath Greenland (Dawes, 2009). Offshore and in northern Canada, dark blue lines are redrawn from St-Onge et al. (2009). ELL-FR: Ellesmerian-Franklinian foldbelt, ING: Inglefield mobile belt, CAL: Caledonian orogen, RNK: Rinkian mobile belt, NAG: Nassugtoqidian orogen, NAC: North Atlantic craton, KET: Ketilidian orogen.

confined to the upper lithospheric mantle and likely pinches out at depth. Similar lowered velocities are observed beneath a section of the THO beneath Hudson Bay (e.g., Darbyshire et al., 2013), though they are a more persistent feature with depth, perhaps along large-scale thrust-faulting systems. Although the Nagssugtoqidian is considered to be part of the THO system (e.g., St-Onge et al., 2009), it is a much smaller-scale feature, and not related to preserved juvenile Proterozoic material, which may explain its more limited depth extent.

2.4.1.2 Central Greenland

North of the Nagssugtoqidian orogen, extending to the inferred northern boundary of the Rinkian orogen in the west (MacGregor et al., 2024) and to the contact between the Paleozoic Caledonidan belt and NAIP in the east (Dawes, 2009; MacGregor et al., 2024), we observe a transition from slightly below-average phase velocities at 25-30 s period to slightly above-average phase velocities at 40-60 s period. The area closest to Iceland, where the NAIP outcrops, is a notable exception, exhibiting a significant low-velocity anomaly at all periods greater than $\sim$30 s. Relatively high velocities, likely associated with cratonic lithosphere, persist in the western half of central Greenland to $\sim$75 s period. There is no clear signature associated with the Rinkian orogenic belt, suggesting that its extent into mainland Greenland is limited, as suggested by St-Onge et al. (2009); MacGregor et al. (2024).

At periods of $\sim$80-130 s, central Greenland is dominated by a band of average to low phase velocities, where the amplitude of the negative anomaly increases with increasing period. This anomaly lies slightly to the north of the inferred trace of the NAIP (e.g., Dawes, 2009) but, nevertheless, it likely represents a trace of the interaction between the Iceland plume and the Greenland cratonic lithosphere, which could have been locally eroded or metasomatized as a result of the plume's passage beneath the keel. The corridor of lowered phase velocities diverges from the plume track proposed by Martos et al. (2018) in western Greenland, but aligns with the hotspot trajectory proposed by Rogozhina et al. (2016).

Low phase velocities in eastern-central Greenland become increasingly prominent as periods increase beyond $\sim$140 s. The anomaly spreads northwestwards from its centre beneath the eastern outcrops of the NAIP, eventually extending beneath much of central and central-northern Greenland. At these periods, present-day asthenospheric structure likely dominates the phase velocity maps, with peak depth sensitivities exceeding $\sim$150 km (Fig. 2.7), so this prominent anomaly most likely represents warm sublithospheric mantle extending outwards from the present-day Iceland hotspot.

2.4.1.3 Northern Greenland

North of the inferred NAIP track, the phase velocity maps at 25-30 s period are dominated by two large low-velocity anomalies, with the northwestern anomaly also extending into the Queen Elizabeth Islands. The northeastern part of the eastern anomaly is most likely related to thick sedimentary sequences in the Danmarkshavn-Thetis basin (Henriksen et al., 2009), where basin thicknesses are estimated to be ~15-18 km (Laske et al., 2013; Petrov et al., 2016). The low-velocity anomalies further inland broadly correlate with a region of high surface heat flow (Rogozhina et al., 2016), which is thought to be causing enhanced basal melting of the northeast Greenland ice stream.

As periods increase, low-velocity anomalies are replaced by high velocities consistent with cratonic lithosphere. Detailed tectonic interpretations of the nature of the Precambrian lithosphere in inland northern Greenland are challenging due to the lack of consensus regarding tectonic boundaries, but certain features stand out due to the resolution possible from our path coverage (Figs. 2.2 and 2.4). In the far northeast, high-velocity anomalies extend beyond the Greenland coastline, almost to the edge of the continent-ocean transition, in contrast to regions further south where average-to-low velocities extend into eastern Greenland from the Greenland Sea. Between 57 and 75 s period, the phase velocity maps are dominated by the strongest high-velocity anomaly in the entire Greenland landmass. The anomaly is spatially correlated with the Inglefield orogenic belt, but also extends beneath much of the Ellesmerian-Franklinian belt, suggesting that this fold-and-thrust structure may be a relatively thin-skinned feature, confined to the crust and underlain by Precambrian lithospheric mantle.

At ~80-100 s period, the amplitude of the Inglefield anomaly decreases, and the northern Greenland lithosphere is divided into two broad high-velocity belts with relatively lower velocities between them. The transition correlates approximately with the southern boundary of the Inglefield mobile belt as inferred by MacGregor et al. (2024). The geometry of the high-velocity anomalies is consistent with the hypothesis that Greenland was assembled by a series of north-to-south accretions between cratonic blocks, but more detailed inferences are challenging without direct information on tectonic boundaries. The high-velocity anomalies become more localized again for periods >110 s, and gradually fade with increasing period.

We do not see any clear signature in the phase velocity maps that correlates with the surface extent of the Caledonian orogenic belt in eastern and northeastern Greenland. It is possible that, similar to our interpretation of the Ellesmerian-Franklinian belt, the Caledonides are a predominantly crustal feature onshore, as suggested by Hodges (2016), and underlain by cratonic mantle lithosphere all the way to the continent-ocean transition. An alternative interpretation might be that the belt extends deeper, but is too narrow onshore Greenland to be distinguished between the strong cratonic signatures to the west and the strong oceanic signatures to the east, at the resolution possible from our path coverage.

2.4.1.4 Northeast Canadian Shield

Baffin Island and the Foxe Basin immediately to the west of the island exhibit low seismic velocities compared to the neighbouring oceanic regions at 25 s period, consistent with the presence of continental crust, but this signature rapidly changes to a pervasive high-velocity anomaly consistent with Canadian Shield cratonic lithosphere. The highest velocities are generally located beneath western Baffin Island and the Foxe Basin, and persist to periods >160 s. The surface geology of Baffin Island is broadly divided into Rae craton rocks in the north and foldbelts, batholiths and continental fragments associated with the Trans-Hudson orogen in the south (e.g., St-Onge et al., 2009). We do not observe any clear coherent distinction between these units in our phase velocity maps, though this may in part be due to a gradual loss of resolution in the west of our study region.

2.4.1.5 Oceanic lithosphere and asthenosphere

At 25 s period, where Rayleigh waves are most sensitive to the ∼20-50 km depth range, we observe a clear distinction between continental and oceanic regions, where the latter exhibit consistently higher phase velocity. Exceptions are slightly lowered velocity beneath Davis Strait and a stronger signature of lowered velocity beneath the Greenland-Iceland Ridge, both regions being associated with thickened crust (e.g., Holbrook et al., 2001; Suckro et al., 2013). Above 35 s period (North Atlantic and Greenland Sea) or 40 s period (Baffin Bay, Labrador Sea), this pattern reverses, and the oceanic regions are characterised by low-velocity anomalies. In the west, the strongest contrast between continental and oceanic signatures is observed at ∼45-60 s period. The North Atlantic and Greenland Sea are characterised by the lowest-velocity signatures (up to -3%), which are pervasive across the entire resolved oceanic region between ∼45 and 65 s period. At longer periods, the Greenland Sea anomaly moderates, and the lowest velocities are concentrated beneath Iceland, and between Iceland and Greenland, until periods ≥150 s, where the anomaly migrates further north and west towards the Greenland coast and interior.

2.4.1.6 Implications for lithospheric thickness and plume-lithosphere interaction

The positive velocity anomalies across Greenland and northeastern Canada are consistent with the signature of cratonic lithosphere, and their persistence to long periods suggests that the lithosphere in these regions is thick. Previous seismic (e.g., Darbyshire et al., 2004; Schaeffer and

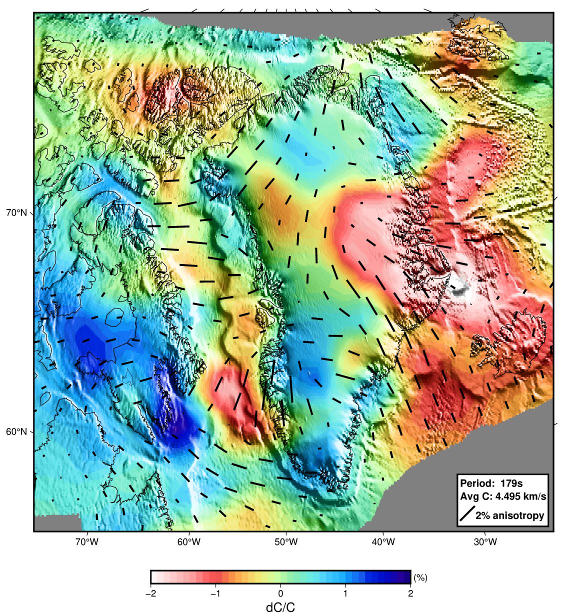

Figure 2.9: Rayleigh wave phase velocity anomaly (isotropic and azimuthal anisotropy) map of Greenland and northeastern Canada at period 179 s, highlighting the spread of low phase velocities from the North Atlantic across eastern and central Greenland.

Lebedev, 2013; Lebedev et al., 2018) and other geophysical (Artemieva, 2019; Steinberger et al., 2019; Steffen et al., 2018) studies show similar patterns of lithospheric thickness. Artemieva (2019) estimated lithosphere-asthenosphere boundary (LAB) depth based on a thermal isostasy method using gravity, heat flow, and seismic datasets. The resulting models suggest a deep LAB in central-southern Greenland and a shallower LAB in eastern Greenland extending to the northwest. Our findings agree well with most aspects of this study, except for their shallow LAB in northwest Greenland where our phase velocity maps suggest a thick cratonic keel in this region. In Steinberger et al. (2019), the LAB depth interpretation is based on an Arctic tomography model, AMISvArc (Lebedeva-Ivanova et al., 2019). Their model suggests that the thickest lithosphere is located in the far northeast, the far northwest and the central-southern regions of Greenland, along with northeastern Canada, with the thinnest lithosphere beneath eastern Greenland, Baffin Bay and the Labrador Sea. Our results are in broad agreement, except for northeast Greenland where we do not observe strong positive velocity anomalies persisting to long periods. The model of Steffen et al. (2018) infers effective elastic thickness using gravity and (rock-equivalent) topography, and suggests that the thickest lithosphere is located in northwestern Greenland and the thinnest in central-eastern Greenland. They do not, however, infer thick lithosphere in central-southern Greenland, unlike our results that show persistent positive phase velocity anomalies in this area.

Iceland plume influence in Greenland can be inferred by a variety of seismic signatures on our phase velocity maps. At periods associated with the lower crust, the low-velocity anomalies in central and northwest Greenland (Fig. 2.6) correlate spatially with regions of anomalously high heat flux inferred at the base of the ice sheet by Rogozhina et al. (2016) and Martos et al. (2018). These authors suggest that the heightened heat flow is linked to the interaction of the Icelandic mantle plume with the Rinkian and north Greenland block between $\sim$50 and $\sim$100 million years ago. The plume may have caused lithospheric heating, erosion and partial melting, including emplacement of magmatic material at the base of the crust. Between $\sim$57 and 130 s period, the highest velocity anomalies are broadly divided into a northern and southern section, with a corridor of lowered velocities in between, becoming more prominent with increasing period. As discussed above, the alignment of this feature with the coastal signatures of the NAIP suggests that this feature can be attributed to lithospheric erosion and/or modification related to interaction between the Iceland plume and the Greenland lithospheric keel, similar to the lithospheric modification associated with other regions of hotspot-lithosphere interaction. At the longest periods, where asthenospheric signals likely dominate the phase velocity maps, the prominent low-velocity anomaly extending from Iceland northwestwards into Greenland (Fig. 2.9) is consistent with the signature of a present-day mantle temperature anomaly. The centre of the anomaly appears to migrate northwestwards with increasing period, which would be consistent with the suggestion of a tilted Iceland plume by Celli et al. (2021), though the wide depth range sampled by our longest periods precludes a more detailed interpretation of plume geometry.

2.4.2 Seismic Anisotropy

Seismic azimuthal anisotropy and its depth variation are related to crust, lithospheric mantle, and sublithospheric fabrics. These may arise from structural alignments such as dykes and cracks, mineral alignments associated with tectonic stresses, or mantle convective flow. In the lower crust, the preferred alignment of anisotropic minerals, such as amphiboles and micas, is primarily attributed to the deformation of metamorphic rocks, resulting in foliation and lineation (e.g., Brocher and Christensen, 1990; Meltzer and Christensen, 2001). Depending on the intricacies of crustal deformation, these alignments can exhibit predominantly 2ψ symmetry or include a 4ψ component. Within the lithospheric mantle, deformation processes can lead to a lattice-preferred orientation (LPO) of olivine (e.g., Silver and Chan, 1988, 1991; Vauchez and Nicolas, 1991; Karato et al., 2008), where the a-axes align with the direction of deformation, resulting in a distinctive anisotropic fabric that manifests a 2ψ symmetry in Rayleigh waves. In the asthenosphere, ongoing mantle convection is believed to be responsible for the mineral alignment of olivine, and thus, the observed fast orientations are indicative of present-day (or relatively recent) strain.

2.4.2.1 Southern Greenland

At periods sensitive to the crust and uppermost mantle (~25-35 s), anisotropy appears relatively weak and incoherent beneath the North Atlantic craton. In contrast, beneath the Nagssugtoqidian orogenic belt, and extending almost as far north as the suggested trace of the NAIP, we observe high amplitudes and a consistent NW-SE fast orientation, trending roughly parallel to the orogenic belt. As periods increase (~40-70 s), the strong anisotropy in this region becomes progressively weaker, whereas anisotropy increases beneath the North Atlantic craton. Initially, in this period range, fast orientations are uniformly ~NNW-SSE, but they become more variable, with a NW-SE to NNE-SSW trend in different parts of the craton. Above 75 s period, anisotropy largely weakens again beneath the North Atlantic craton, while strengthening and becoming more coherent further north, with a NW-SE trend, until the longest periods when the anisotropy weakens again. Based on the variations in anisotropy with period, we suggest that the North Atlantic craton has weak anisotropic fabric in the lower crust, but a more anisotropic, and likely stratified, lithosphere, as suggested for cratonic regions of northeast Canada.

2.4.2.2 Central Greenland

Anisotropic fast orientations around the inferred NAIP track appear to create a transitional zone between fabrics in the south and north of Greenland. Between 25 and 35 s period, anisotropy rotates from NW-SE to N-S as latitude increases, with high amplitudes at the shortest periods. From ~40-100 s period, this region is predominantly characterized by N-S to NE-SW fabric, with moderate amplitudes except for a much weaker signal in the centre-east at ~87-100 s period. At longer periods, we observe a shift to a NNW-SSE orientation which becomes increasingly pervasive across both central and northern Greenland. In particular, a strong NW-SE to NNW-SSE signature begins to develop beneath central-eastern Greenland and spreads further north and west beneath the mainland as periods increase. At these periods, sensitivity kernels (Fig. 2.7) suggest that the Rayleigh waves are predominantly sampling depths in excess of 120 km, therefore we interpret this fabric as LPO arising from present-day asthenospheric flow.

2.4.2.3 Northern Greenland

At the shortest period in our study (25 s), central and northern Greenland exhibit strong anisotropy with a N-S to NW-SE trend. However, this pattern rapidly changes to a pervasive E-W trend, with weak anisotropy at 29-35 s that strengthens significantly and then persists to ~120 s period. This orientation rotates gradually to a more NE-SW orientation in the vicinity of the Rinkian mobile belt. Beyond ~120 s, anisotropy in northern Greenland becomes less spatially coherent, with variable amplitudes and fast orientations. These anisotropy patterns suggest that the lower crust of northern Greenland may have a fabric completely distinct from that of the lithospheric mantle with its pervasive E-W fabric. The broadly N-S fabric observed at 25 s period has some consistency with the strike of the tectonic boundaries interpreted by MacGregor et al. (2024), whereas E-W fabric in the lithospheric mantle is more consistent with a broad-scale north-to-south tectonic assembly of Precambrian northern Greenland as suggested by Henriksen et al. (2009). Magnetic anomaly patterns, which may be expected to reflect crustal fabric, are strong but not particularly coherent in northern Greenland (Meyer et al., 2017), with the exception of a strong WNW-ESE trending lineament beneath the Inglefield mobile belt, consistent with short-period anisotropic orientations in this region. The persistence of the E-W trend from $\sim$40 to almost 130 s period suggests that the northern Greenland lithosphere has an almost uniform deformational fabric, with little stratification. This character contrasts with many regions of the Canadian Shield to the west and south (e.g., Darbyshire et al., 2013; Petrescu et al., 2017), but is also observed beneath the western Superior craton (e.g., Foster et al., 2020), where the pervasive anisotropy is thought to be the result of north-south accretion of Archean terranes.

The E-W fast orientation persists all the way to the east coast, and directional changes do not correlate spatially with the surface expression of the Caledonian orogenic belt. Instead, N-S trending anisotropy is visible beneath the northeast Greenland continental shelf, with the coastline marking this abrupt change in orientation. Within the limits imposed by path coverage and model resolution, we speculate that this observation provides further evidence that the Caledonian orogenic belt onshore is a thin-skinned crustal feature (e.g., Hodges, 2016). In this scenario, lithospheric-scale orogen-parallel fabrics are only prevalent in the coastal and offshore areas, where Schiffer et al. (2014) interpreted an eastward-dipping structure persisting to $\sim$100 km depth as a relict of subduction associated with the Caledonian-Appalachian orogeny.

2.4.2.4 Baffin Bay, Labrador Sea and Baffin Island region

At periods below $\sim$140 s, anisotropic fast orientations in northern Baffin Bay range from NNW-SSE to NE-SW, with variable coherence and amplitude. For most of this period range, they are distinct from the stronger, more coherent NE-SW trending anisotropy beneath southern Baffin Bay, the Davis Strait and central Baffin Island. Even at short periods, we do not observe any clear evidence for spreading-parallel fabrics in these northern rifted regions between Canada and Greenland. Beyond $\sim$140 s period, anisotropy is strong across Baffin Bay and western Baffin Island, with a predominantly E-W to ESE-WNW orientation. In the northern Labrador Sea, anisotropy trends E-W at the shortest periods, which could tentatively be interpreted as preserved spreading-parallel fabric. From $\sim$40-50 s period, Labrador Sea anisotropy is weak and incoherent, but reorganises to a pervasive NW-SE to NNW-SSE fast orientation that persists through to the longest periods in this study.

2.4.2.5 The North Atlantic and Greenland Sea

Although our path coverage is less dense in this region than beneath Greenland, the rotated-anisotropy resolution test (Fig. 2.5) suggests that the large-scale anisotropy orientations are robust for Iceland and the Greenland Sea. Azimuthal path coverage is poor south of Iceland, however, and as a result we do not interpret the observed anisotropy patterns. Anisotropy is weak at the shortest periods but strengthens significantly as periods increase, consistent with the strong low-velocity anomalies observed on the isotropic component. N-S fast orientations dominate at most periods from ∼40 to 140 s in the Greenland Sea, rotating to NE-SW beneath Iceland and the Greenland-Iceland Ridge. At the longest periods, the anisotropic signal beneath much of the Greenland Sea and Iceland becomes weaker and less coherent. Instead, the area northwest of Iceland appears to become the origin point for the strong NW-SE trending anisotropy that penetrates beneath central-eastern Greenland.

2.4.2.6 Comparison with previous studies

In contrast to the isotropic structure, where different surface wave and ambient noise tomographic studies show many common features within the limits imposed by data coverage and differences in methodology, agreement between inferences of anisotropic structure remains elusive. Our results have partial agreement with those of previous regional-scale studies (e.g., Levshin et al., 2001; Pilidou et al., 2004; Darbyshire et al., 2017), but there are also some significant differences, such as the strong E-W fast orientations in northern Greenland, and the ridge-parallel anisotropy in the Greenland Sea. Seismic anisotropy inferences beneath mainland Greenland can also be compared with the SKS splitting studies of Ucisik et al. (2005, 2008) and Nathan et al. (2021). Direct comparison is challenging due to the depth resolution of the two methods, where SKS splitting measurements represent a cumulative effect from wave propagation through the entire mantle; however, both sets of studies suggest depth-dependent anisotropy beneath Greenland, with both 'fossil' lithospheric fabric and present-day mantle flow playing a role. Dominant SKS splitting orientations display significant spatial variability across Greenland, which is consistent with a lithospheric component to the anisotropy. We observe partial agreement between our anisotropy orientations and those inferred by the SKS splitting studies; however, we note that there is also significant disagreement between the SKS studies. Using their larger dataset, Nathan et al. (2021) observed back-azimuthal variation at most of the stations on Greenland. They compiled the results to model dipping two-layered anisotropy across Greenland, with a NE-SW trend for the shallower layer and a NW-SE trend for the deeper layer, interpreted as lithospheric and asthenospheric fabric, respectively. We resolve more spatial variability than this approach, but we note that the NW-SE orientation also dominates our phase velocity maps at long periods, where direct comparisons between the studies are likely more valid due to the large depth range sampled by Rayleigh waves at these periods (Fig. 2.7). Multiple and/or dipping anisotropic layers are also inferred for northern Canada by SKS splitting (e.g., Bastow et al., 2011; Snyder et al., 2013; Liddell et al., 2017) and surface wave tomography (Darbyshire et al., 2013) studies. The observed anisotropy was interpreted in the context of Precambrian plate-tectonic processes, notably those associated with the Trans-Hudson orogen and the related interactions between the Superior and Churchill plates as well as juvenile Paleoproterozoic material and Archean cratonic fragments preserved within the collision zone.

2.4.2.7 Implications for Lithospheric Structure and Mantle Flow

One of the main challenges in interpreting anisotropy in our study region is due to the significant changes in lithospheric thickness between the modern-day North Atlantic / Greenland Sea, the oceanic lithosphere above the failed rifts in Baffin Bay / Labrador Sea, and different parts of the Greenland landmass where cratonic lithosphere appears thick and well-preserved in the north and south, but eroded in central Greenland. These large variations mean that, at a given period, the proportion of 'frozen' lithospheric anisotropy versus fabric associated with active mantle flow varies significantly across the region. In regions where the lithospheric keel is best preserved, only the longest periods in our study are capable of sampling anisotropy that arises purely from asthenospheric flow. In addition, variations in lithospheric thickness can have a significant effect on patterns of mantle flow, leading to localised perturbations such as those inferred around the "divot" in the lithospheric keel in southeast Canada (Eaton et al., 2004; Fouch et al., 2000; Fouch and Rondenay, 2006; Frederiksen et al., 2006), or to the development of significant edge-driven convection associated with suboceanic mantle flow meeting an abrupt lithospheric step at a continental edge (e.g., Brunsvik et al., 2021). Plume-ridge and plume-lithosphere interaction also both likely play an important role in developing sublithospheric flow and associated anisotropic fabric (Brunsvik et al., 2021).

Lithospheric Fabric

At periods primarily sensitive to lithospheric depths beneath Greenland and northeast Canada, seismic anisotropy patterns preserve a record of past deformation processes associated with the assembly and subsequent tectonic evolution of the Laurentian continent. The preserved fabric is likely associated with the most recent tectonic event to have affected the lithosphere, with older deformation fabrics partially or entirely overprinted. Unlike some of the SKS splitting studies carried out across our study region (e.g., Liddell et al., 2017; Nathan et al., 2021), we cannot resolve dipping anisotropic layers, but the orientations of azimuthal anisotropy provide insight into the horizontal component of lithospheric deformation.

Precambrian Greenland, like North America, is dominated by collisional tectonics. In general, anisotropic fabric follows lithospheric deformational structures in orogenic belts which, at the surface, are characterised by fold-and-thrust belts, shear zones and evidence of pervasive reworking. On Greenland, these features are directly observed where the orogenic belts are exposed at the coasts (e.g., van Gool et al., 2002; Henriksen et al., 2009), and further evidence is visible via magnetic anomaly patterns associated with the Nagssugtoqidian and Inglefield mobile belts (Meyer et al., 2017). E-W trending anisotropy in northern Greenland, under a regime of modern-style plate tectonics, would be consistent with north-south subduction, collision and terrane accretion episodes. The anisotropy resolved on Baffin Island is relatively weak compared to Greenland. Nevertheless, at lithospheric depths, changes in fast orientation appear to correlate with known tectonic subdivisions, including a significant difference between the Rae craton in northern Baffin and the central-southern foldbelts which have previously been interpreted (e.g., Snyder et al., 2013; Liddell et al., 2017) as plate-scale collisional features related to the Trans-Hudson orogen. Orogen-parallel fabrics would also be expected for the east Greenland Caledonides and for the Ellesmerian-Franklinian foldbelt in the far north. Since the strike of the northern foldbelt is parallel to the anisotropic fabric beneath Precambrian northern Greenland, we cannot distinguish the two structures by an anisotropic signature. As discussed in Sec. 2.4.2.3, our anisotropy results are only consistent with the north-south trend of the Caledonian belt offshore northeast Greenland, suggesting that the surface expression of the orogen is not a lithospheric-scale feature onshore.

The most recent tectonic events to play a role in our study region are the rifting and sea floor spreading that gave rise to Baffin Bay, the Davis Strait and the Labrador Sea, as well as the arrival of the Iceland plume beneath Greenland, leading to magmatism, lithospheric erosion and North Atlantic breakup. Clear evidence of anisotropic fabric directly associated with Canada-Greenland breakup remains elusive. Assuming a lithospheric thickness of $\sim$50-60 km beneath central Baffin Bay and $\sim$120 km beneath Davis Strait (Steinberger et al., 2019) and considering Rayleigh wave sensitivity kernels, a component of the coherent NE-SW anisotropy could be associated with rifting. This orientation is, however, also parallel to Precambrian orogenic belts correlated across the Davis Strait from southern Baffin Island to southwest Greenland, so a partial rift-related overprint of an existing Precambrian fabric could also explain our observations. Beneath central Greenland, the corridor of relatively low phase velocities between the northern and southern cratonic cores is also accompanied by anisotropic orientations that are distinct from those to the north and south. While not the only potential explanation, perturbation of older anisotropic fabric by plume-related lithospheric erosion and modification is a plausible source for this observation.

Mantle Flow and Influence of the Iceland Plume

In our study region, at a large scale, mantle flow is likely dominated by a combination of (i) divergence related to mid-ocean ridge dynamics and (ii) the effect of the Iceland mantle plume. Global geodynamic models (e.g., Marquart et al., 2007; Simmons et al., 2010; Colli et al., 2018; Lu et al., 2020) provide a lower spatial resolution than this study, and inferences of regional-scale flow fields have a strong dependence on assumptions about the viscosity structure of the mantle, with most models based on 1D viscosity profiles. Nevertheless, a common feature of such models is a strong horizontal component of mantle flow radiating outwards from the centre of the Iceland hotspot, which produces a northwestward flow direction extending from Iceland and penetrating beneath Greenland. We observe similar orientations in long-period anisotropy for this region, suggesting that mantle flow related to the Iceland plume is a major contributor to seismic anisotropy at depth beneath Greenland. Further away from the Iceland hotspot, direct comparison of anisotropy orientations with mantle flow patterns becomes less clear. Notably, the strong NW-SE anisotropy gives way to more variable trends and weaker amplitudes at the longest periods beneath northern Greenland. This change in character may be explained in part by the perturbation of the plume-related mantle flow by its interaction with the thick northern Greenland lithospheric keel, as suggested by Nathan et al. (2021).

At a wide range of periods beneath the Greenland Sea, we observe anisotropic fast orientations that are parallel to the strike of the Mid-Atlantic Ridge. Although our model resolution diminishes in this region compared to mainland Greenland and the Baffin region, our resolution tests (Fig. 2.5) suggest that this feature is robust at a large scale. Globally, seismic anisotropy is typically observed with a spreading-parallel (ridge-perpendicular) orientation near mid-ocean ridges (e.g., Schaeffer et al., 2016). However, this flow direction may be significantly perturbed in the presence of a mantle plume, especially if the plume viscosity is low and the spreading rate is slow. In these cases, a significant component of along-ridge channelling of mantle flow is inferred, resulting in ridge-parallel anisotropy (e.g., Albers and Christensen, 2001; Ito et al., 2003, 2014), as observed here.

2.5 Conclusion

In this study, we generate new high-resolution Rayleigh-wave phase-velocity maps encompassing Greenland and northeastern Canada by processing over three decades of teleseismic earthquake records and incorporating recently added stations in Greenland and Arctic Canada. Our maps are sensitive to depths from the lower crust down to the sub-lithospheric mantle and show significant lateral variations at all periods (25-185 s).

Our findings reveal the presence of significant heterogeneity and a strong correlation of isotropic and anisotropic velocities with known and inferred geological structures. At short periods ($\sim$25 s), sensitive to the lower continental crust, we observe marked velocity and anisotropy variations across Greenland. In the south, there is a clear tectonic correlation, where the North Atlantic craton shows higher velocities and weaker anisotropy than the Nagssugtoqidian and Ketilidian orogenic belts. The Nagssugtoqidian belt exhibits strong orogen-parallel anisotropy, which also persists to periods sensitive to the continental lithospheric mantle. In northern Greenland, we observe two zones of lowered phase velocity, one beneath the Inglefield mobile belt in the northwest, and the other extending inland from the deep sedimentary basins offshore to a zone characterized by high heat flow. In the regions surrounding Greenland, there is clear distinction between the high phase velocities of the oceanic upper mantle and lower velocities in zones of thickened crust such as the Greenland-Iceland Ridge and the Davis Strait.

At periods sensitive to continental upper mantle depths, we identify two zones of high-velocity anomalies beneath Greenland, one in the south and one in the north, likely indicating the thick, cold, depleted cratonic root. Between these two zones lies a corridor of reduced phase velocities which correlates spatially with the proposed interaction between the Iceland mantle plume and the Greenland lithosphere $\sim$100-50 Ma ago, and the outcrops of Paleogene volcanics on the east and west coasts. We interpret this feature as the signature of lithospheric erosion and modification due to the passage of the plume and associated upwelling of hot asthenospheric material beneath the Greenland keel. Lower velocities underly the Baffin Bay / Labrador Sea region, where Greenland rifted off from the rest of Laurentia in the early Paleogene. The lowest velocities are found beneath Iceland, the North Atlantic and the Greenland Sea. At these periods, the Iceland / Greenland Sea region also exhibits strong anisotropy consistent with the channelling of plume flow along the Mid-Atlantic Ridge.

Within the cratonic keel, we infer subdivisions that provide new clues to the tectonic history of Greenland. Our high-resolution model results in a detailed image of the internal structure of both the southern and northern portions of the keel. In the south, the Nagssugtoqidian orogenic belt exhibits slightly lower velocities than those of the cratonic cores (North Atlantic and Rae) on either side. However, this feature is only visible until $\sim$75 s period, suggesting that the lithospheric expression of the orogen may pinch out at depth, with a full terminal collision between the two Archean cores in the lower lithosphere. The North Atlantic also shows variations in anisotropic fast orientation with period, suggesting lithospheric stratification. In the north, a large, localized zone of high velocities is dominant at $\sim$57-75 s period, but this gives way to a north-south division into two high-velocity anomalies that span the width of Greenland, visible to $\geq$100 s period. At all periods from $\sim$40 to 120 s, the entire northern part of Greenland exhibits persistent E-W trending anisotropy. This orientation is broadly consistent with the notion of the Greenland shield being assembled through a series of north-south collisions and terrane accretions. Intriguingly, the progression of anisotropic fast orientations in northern Greenland from N-S in the lower crust to E-W in the mantle suggests that the crust and the lithospheric mantle may be decoupled in terms of structural fabric and deformation, contrasting with Canadian cratonic regions, in which anisotropy has largely been interpreted as a coherent plate-scale process.

We do not observe a clear distinction in isotropic or anisotropic signature between the cratonic lithosphere and the Phanerozoic fold belts in northern and eastern Greenland. The Ellesmerian-Franklinian fold belt does exhibit orogen-parallel anisotropy, but this is difficult to separate from the broader-scale E-W trend across the northern Greenland keel. In the east, the change in anisotropic fast orientation from E-W (perpendicular to the Caledonian orogen) to N-S (orogen-parallel) occurs at the Greenland coast instead of following the onshore expression of the fold belt. We speculate that these fold belts are characterized by thin-skinned tectonics onshore, with a more significant lithospheric-scale signature for the Caledonian orogen being restricted to the continental margin offshore.

From $\sim$35 to 130 s period, the lowest phase velocities in our study region are centered beneath Iceland, consistent with the influence of the Iceland hotspot. As periods increase, the centre of the low-velocity anomaly shifts northward and extends northwestward to underly large areas of eastern Greenland. The low velocities are also accompanied by strong NW-SE trending anisotropy. Since periods of $>$140 s are predominantly sensitive to depths greater than the inferred extent of the Greenland lithospheric keel, particularly in the east and centre of the landmass, this feature is likely due to present-day mantle flow associated with a possibly tilted Iceland plume. High temperature asthenospheric material appears to flow outward from the plume centre, extending predominantly beneath regions where the Greenland lithosphere had already been eroded by past plume activity. Mantle flow patterns beneath our study region are, however, likely more complicated than either a simple radial flow from the plume or a simple divergence outward from the mid-ocean ridge, as variations in lithospheric thickness can create localized perturbations in mantle flow and small-scale convection. More detailed analysis based on depth-dependence of anisotropy and geodynamic models incorporating lateral viscosity variations will be necessary to resolve these phenomena.

2.6 Acknowledgments

PAd and PAu acknowledge funding from the University of Ottawa. FD, GAM, and PAu are supported by the Natural Sciences and Engineering Research Council of Canada through the

Discovery Grant program. We thank Andrew Schaeffer for providing software and guidance during the early stages of this work. Plots were generated using the PyGMT package (Uieda et al., 2023). Finally, we thank the editor and reviewers for their helpful comments that improved the manuscript.

2.7 Data Availability

All seismic waveform data used in this study are available from IRIS Data Management Center and the Canadian National Data Center (CNDC). See Table A2.1 in Appendix section for details of the seismograph networks used. Also, the Rayleigh wave phase velocity model data is available from here.

2.8 Appendix A2

This supplementary material presents additional information to support the primary text, such as the seismograph stations utilized and the coverage of ray paths connecting these stations across the regions of Greenland and eastern Canada. As an illustrative example, we present one of the final dispersion curves depicting the average seismic phase velocity between stations FRB and POIN. Four other examples are also shown to illustrate regional variability. We show tests made to select the optimal resolution parameters for the inversion, which are chosen based on the best compromise between model roughness and variance reduction. In addition, we provide visual representations of the corresponding isotropic and anisotropic phase velocity models resulting from this parameter selection. To comprehensively evaluate the robustness of our approach, we undertake additional resolution tests on various geological structures. These tests are performed to assess the accuracy of the generated models for different synthetic structures. Finally, we present a comprehensive array of phase velocity maps spanning the range from 25 to 185 seconds of periods. These maps serve as a reference, encapsulating the results of our analysis across this spectrum of wave periods.

- Text and Table A2.1. List of seismograph stations used in this study
- Text and Fig. A2.1. Maps of ray path coverage for short, intermediate, and long periods
- Text and Fig. A2.2. Measured dispersion curves between stations FRB and POIN
- Text and Fig. A2.3. Various measured dispersion curves

- Text and Fig. A2.4. The trade-off between data fit and model roughness
- Text and Fig. A2.5. Effect of regularization parameters on isotropic phase velocity
- Text and Fig. A2.6. Effect of regularization parameters on anisotropic phase velocity
- Text and Fig. A2.7. Resolution tests with different patterns
- Text and Fig. A2.8. Phase velocity maps with 2ψ anisotropy

Text A2.1 (Table). This table provides a short overview of the seismograph stations used in this study. It contains information about the geographical location, the operation time, and the network.

Text A2.1 (Figure). Phase velocity dispersion curves (PVDC) can be measured at a given station pair for any earthquake on a common great-circle path with respect to the two stations. Depending on the earthquake-station distance, the frequency content of the surface wavetrain can vary, with closer earthquakes yielding shorter-period signals and more distant earthquakes dominated by longer periods. Given the heterogeneous distribution of both stations in the study area and earthquakes worldwide, care must be taken to ensure that the final dataset contains a wide range of wave periods and that surface wave period limits are similar for the different station pairs. Azimuthal bias can be introduced if multiple station pairs sample very similar structures due to their location, so the dataset is chosen to reduce such duplication. In addition, we avoid inter-station or earthquake-station distances that are too short or too long to respect the approximations used in the inversion (e.g., the great-circle ray approximation). Careful selection of events leads to a PVDC dataset with similar inter-station ray path coverage at all periods, allowing us to use the same regularization parameters and resulting in similar inversion accuracy and model resolution. The figure shows path coverage at periods of 25, 61, 122 and 185 s, all with similar numbers of ray paths.

Text A2.2. The PVDC is generated from the cross-correlation of the recorded seismic waves at the two stations, and the dispersion characteristics are related to the average structure along the inter-station path. For each station pair, phase velocity measurements are made for all individual earthquakes that meet the great-circle path criterion, resulting in a few tens of curves with different but overlapping period ranges. The individual curves are averaged to estimate a single representative PVDC for the station pair, as shown in Fig. A2.2-a. However, some individual curves may have errors and kinks related to spectral instabilities, resulting in artifacts in the initial averaged curve, so subsequent quality control is carried out in which spurious curves are removed in order to refine and smooth the final PVDC (Fig. A2.2-b).

Text A2.3. The generated PVDC from the cross-correlation of the recorded seismic waves is highly dependent on the location and the distance between stations, and the path seismic waves travel through. Fig. A2.3 represents four different station pairs PVDC for A) from western Europe (NSS) to central Greenland (SUMG) going through the mid-oceanic ridge, B) a long distance from the North Sea (SOFL) to Ellesmere (EUNU), C) a long distance from eastern Canada (BLKN) to central Greenland (ICESG), and D) for path through eastern Ellesmere (ALE) to southwestern Greenland (NUUK). In Fig. A2.3-A), due to the long distance and going through

MOR, only a few PVDCs were generated. Although the final averaged PVDC (the red line) is smooth and continuous, the reliability of this PVDC is low due to low samples. In Fig. A2.3-B), which is the longest pair, the generated PVDCs are noisier and represent higher variability. In this case, although the averaged PVDC is a smooth curve, the uncertainty of the final PVDC is higher. In Fig. A2.3-C), like (A), the number of PVDC samples is low due to the long distance and location of the ICESG station on the thickest ice in Greenland. In Fig. A2.3-D), enough samples of PVDC generate a reliable PVDC in western Greenland. All of these four PVDC pairs capture only intermediate and long periods and short periods are removed due to low SNR. In fact, the short periods in these paths are provided by complimentary short-distance pairs overlapping long-distance pairs to generate short to long-period PVDCs after inversion.

Text A2.4, A2.5, A2.6. Selecting regularization parameters (damping and smoothing) is a subjective matter. This process is a trade-off between the model's capability to explain the data, which is usually interpreted as the variance reduction or the output roughness, and how much of this variation is geologically explainable. We address this subject in two steps: first, find approximate values for smoothing and damping based on the trade-off L_curve. Then, choose the final values by investigating the phase velocity maps visually. Fig. A2.4 shows the trade-off curves by keeping the gradient damping constant and varying smoothing and norm damping for isotropic and anisotropic components at 60 s period. Fig. A2.5 and A2.6 illustrate the isotropic and anisotropic components of the phase velocity models after the first regularization parameter selection. The smoothing parameter in these figures varies vertically, whereas the damping parameter varies horizontally. It is observed that there are higher variations in isotropic and anisotropic components with lower smoothing and damping (top-left corner), and the variations decrease with higher smoothing and damping (bottom-right corner). Here, we need to select damping and smoothing parameters carefully in order to find the best compromise between model fit and realistic resolution of structure.

Text A2.7. Resolution tests assess the ability of the model to resolve structures with different shapes and sizes. In the main text, synthetic structures with small, medium, and large sizes are provided, and here we add structures with different shapes and sizes and test the model for intermediate and long periods (61s and 151s). In Fig. A2.7, we observe that the model is unable to resolve small structures, especially in the northeast (first row). For the second row, the recovered signal correlates with synthetic input, and the model can recover it, although the recovered shape is not exact. The stripes are well recovered in the last row except for the Queen Elizabeth Islands, where the ray path density is insufficient.

Text A2.8. We provide a set of 18 isotropic phase velocity maps for periods from 25 to 185 seconds to illustrate in more detail the transitions in structure with depth (i.e., with an increasing period).

Table A2.1: List of seismograph stations used in this study. Channels HH, BH, and LH represent seismograph sampling rate and stand for High broad band, Broad band, and Long period.

Network	Station Code	Channel	Latitude	Longitude	Elevation (m)	Operation
CN	CLRN	HH	70.4743	-68.5871	10	2019-present
CN	EUNU	BH	80.0532	-86.4158	620	2008-2019
CN	FRB	BH	63.7469	-68.5451	30	1992-present
CN	ILON	HH	69.3712	-81.8243	50	2018-present
CN	KUQ	HH	58.109	-68.4113	50	2018-present
CN	POIN	HH	72.7012	-77.962	20	2018-present
CN	RES	BH	74.6892	-94.8962	20	1992-present
CN	SAKN	HH	56.5359	-79.2324	0	2014-present
CN	FCC	HH	58.7592	-94.0884	20	2019-present
CN	BLKN	HH	64.3185	-96.0024	40	2017-present
CN	KUKN	HH	67.8227	-115.0897	50	2018-present
CN	SCHQ	BH	54.8324	-66.8332	500	1994-present
CN	INK	BH	68.3065	-133.5254	40	1992-present
CN	NATG	HH	50.2872	-62.8102	0	2005-2017
CN	DRLN	BH	49.2562	-57.5032	240	1993-present
CN	SJNN	HH	47.5951	-52.678	140	2005-present
DK	ANGG	BH	65.6163	-37.6371	10	2010-present
DK	DBG	HH	74.3071	-20.2193	0	2010-present
DK	DY2G	HH	66.4796	-46.3094	2130	2011-present
DK	ICESG	HH	69.0922	-39.6474	2930	2011-present
DK	ILULI	HH	69.2121	-51.1048	50	2009-present
DK	KULLO	HH	74.5805	-57.2201	40	2009-present
DK	NOR	HH	81.6	-16.6833	40	2002-present
DK	NRS	HH	61.1595	-45.4188	80	2009-present
DK	NUUG	HH	71.5384	-53.1996	40	2010-present
DK	NUUK	HH	64.1838	-51.6679	110	2010-present
DK	SCO	HH	70.4833	-21.95	70	1999-present
DK	SOEG	HH	68.2035	-31.3755	180	2011-present
DK	TULEG	HH	76.5374	-68.8238	40	2000-present
DK	ISOG	BH	65.548	-38.9754	10	2007-present
DK	FFBG	BH	82.1294	-56.0338	30	2004-2006
DK	CFJ	BH	83.0835	-28.3208	60	2004-2007
DK	SUMG	BH	72.5763	-38.4539	3240	2000-present
DK	NGR	BH	75.001	-42.3148	2960	2000-2003
GE	DAG	BH	76.7713	-18.655	20	1999-present
GB	SOFL	HH	62.0685	-6.9658	720	2007-present
GG	SE1	BH	63.2485	-42.0349	20	2016-present
II	ALE	BH	82.5033	-62.35	60	1990-present
II	BORG	BH	64.7474	-21.3268	110	1994-present
KP	UPNV	HH	72.7829	-56.1395	40	2013-present
NO	BRBA	HH	78.0588	14.2191	310	2010-present
NS	LOF	HH	68.1325	13.5398	310	2011-present
NS	HAMF	HH	70.6425	23.6841	310	2010-present
NS	NSS	HH	64.5303	11.9658	310	2009-present
IU	SFJD	BH	66.9961	-50.6208	330	2005-present
X5	PNGN	BH	66.1435	-65.7115	30	2007-2011
G	IVI	LH	61.2058	-48.1712	10	2011-present

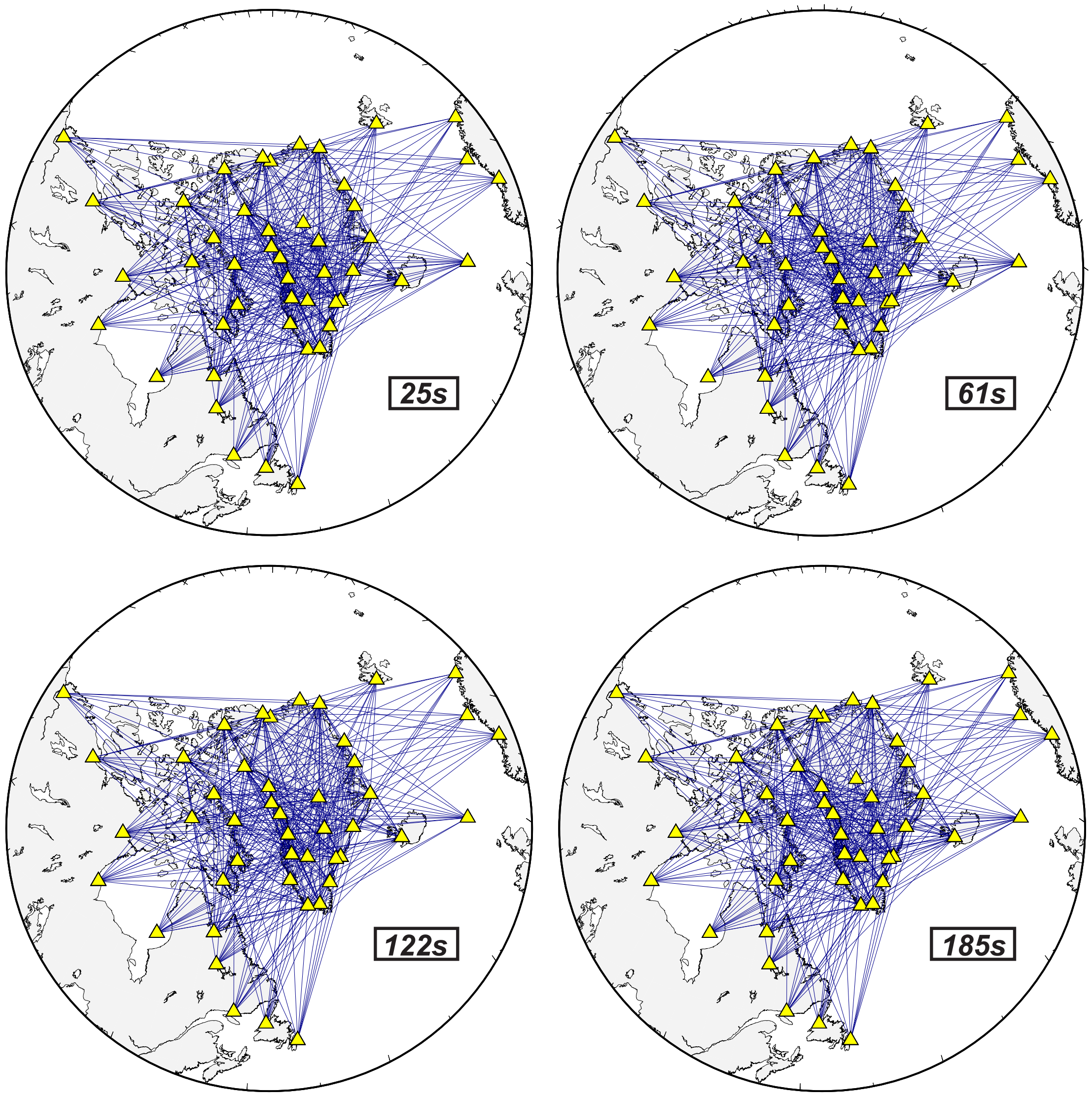

Figure A2.1: Maps of ray path coverage for short, intermediate, and long periods. Blue lines show the ray paths and yellow triangles show seismograph stations. The ray path numbers are 438, 432, 430, and 420, respectively, after removing the outliers.

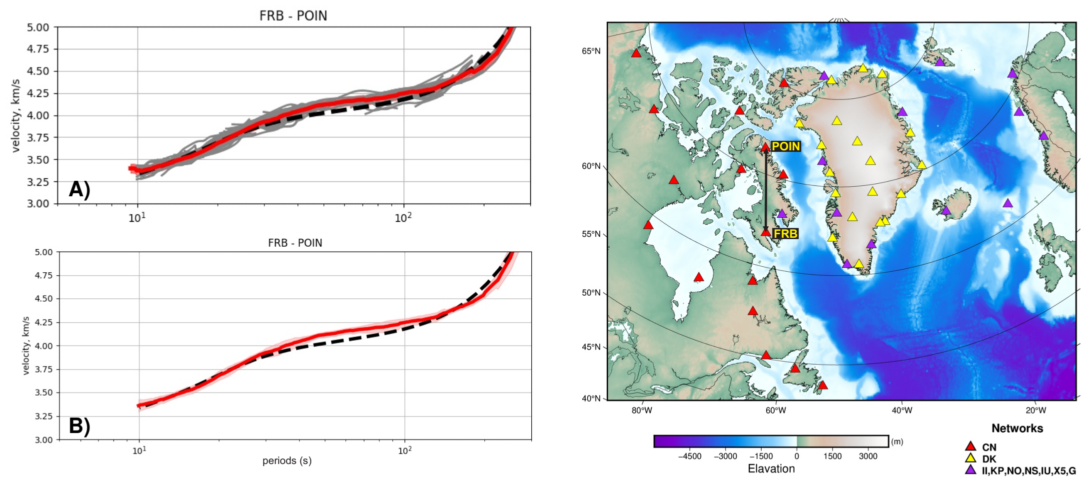

Figure A2.2: Phase velocity dispersion curve measured between stations FRB and POIN. **A)** Gray lines are the calculated phase velocities between FRB and POIN (the path is shown in the right panel) for different earthquakes, and the red line is the average of these PVDCs. **B)** The red line and pale red shading show the refined averaged PVDC and its uncertainty overlaid on the reference model dispersion curve (black dashed line).

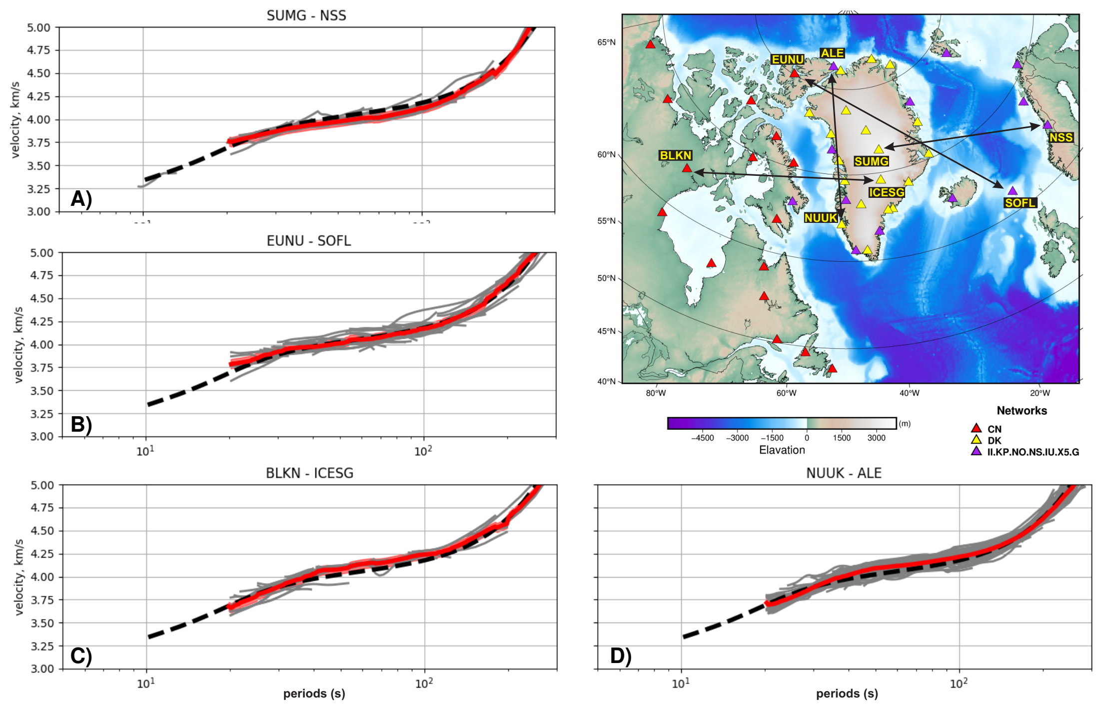

Figure A2.3: Phase velocity dispersion curve measured between four stations with various distances. Gray lines are the calculated phase velocities between stations (the path is shown in the top-right panel) for different earthquakes, and the red line is the average of these PVDCs overlaid on the reference model dispersion curve (black dashed line).

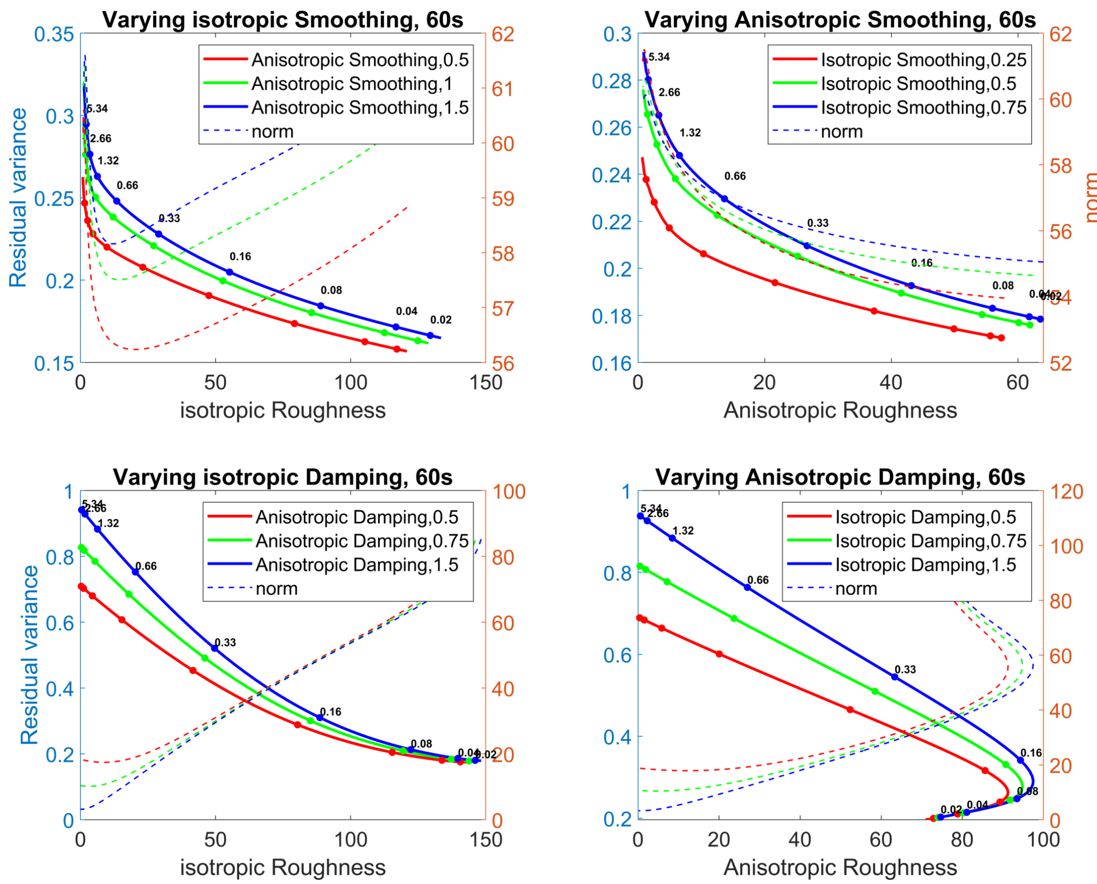

Figure A2.4: Trade-off between data fit and model roughness at 60 s period. Solid lines represent residual variance, and dashed lines show the model norm. Left panels correspond to the isotropic component, whereas the right panels relate to the anisotropic component. The first approximate regularization parameters are selected in the knee of the L_curves.

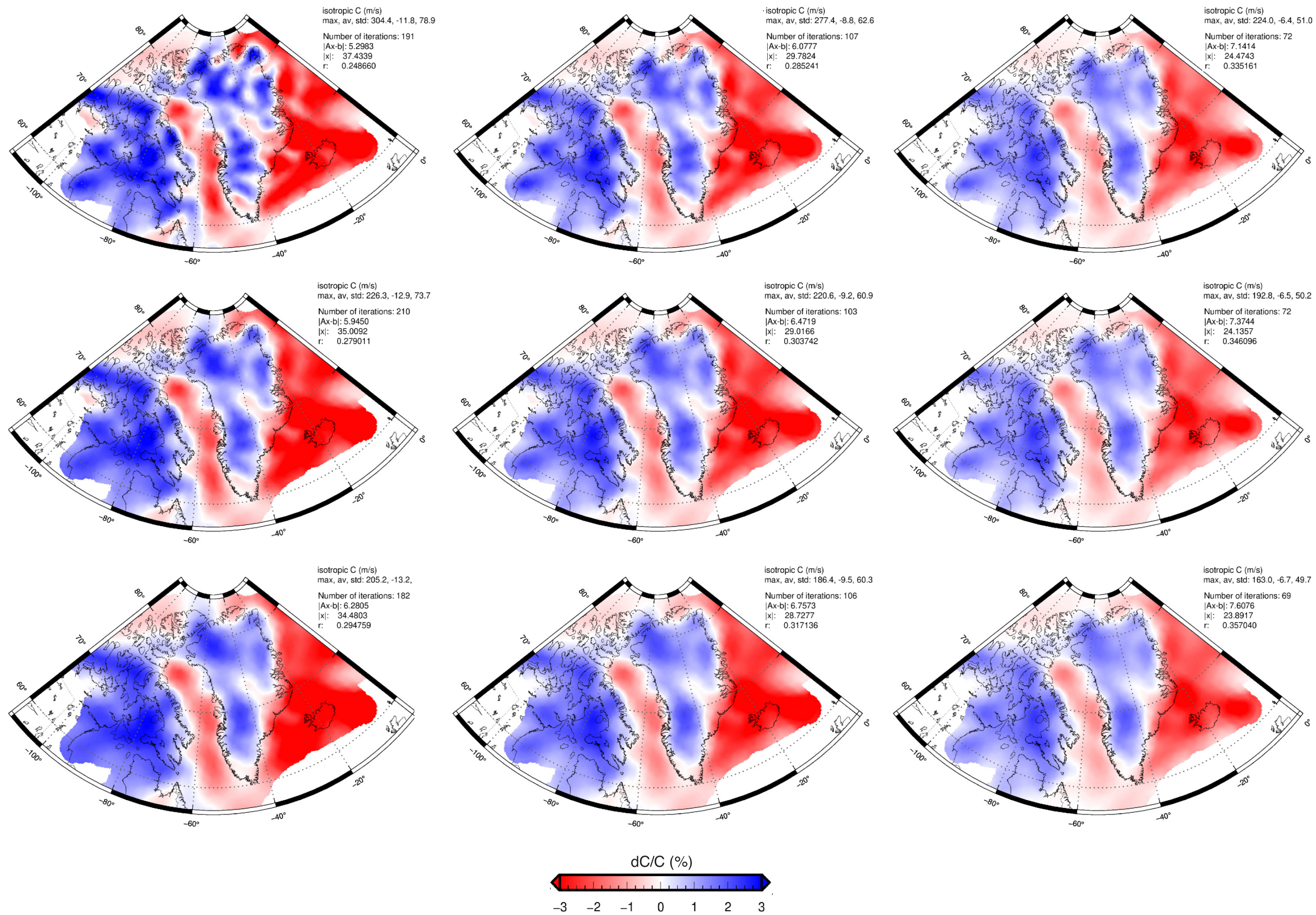

Figure A2.5: Isotropic phase velocity maps based on the first approximate regularization parameters for period 60s. From left to right (each row), the damping parameter changes from 0.1 to 0.3 with 0.1 step, and from top to bottom, the smoothing parameter varies from 0.05 to 0.65 with 0.3 step.

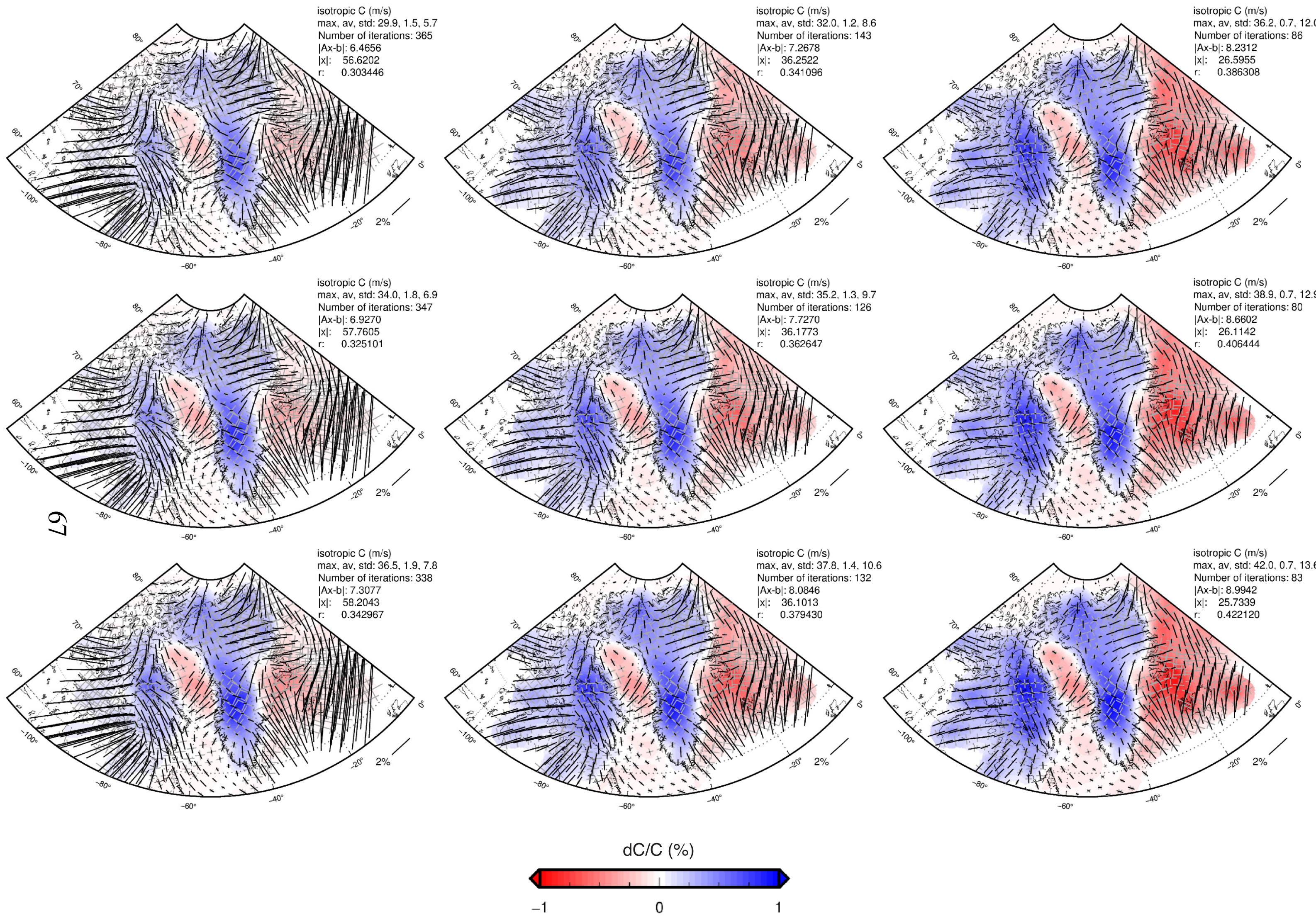

Figure A2.6: Anisotropic phase velocity maps based on the first approximate regularization parameters for period 60s. From left to right (each row) the damping parameter changes from 0.05 to 0.25 with 0.1 step, and from top to bottom the smoothing parameter varies from 0.45 to 0.85 with 0.2 step.

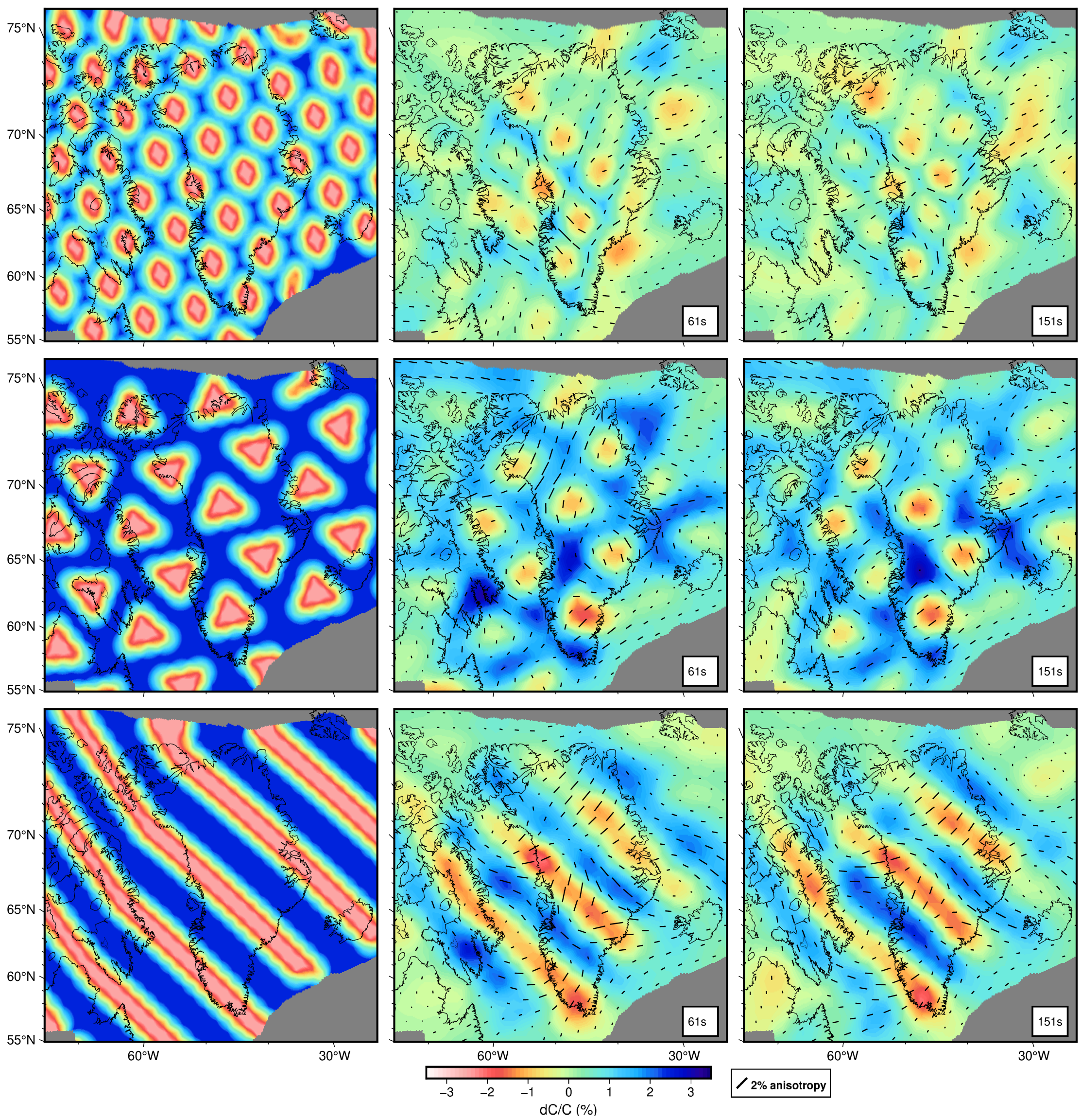

Figure A2.7: Resolution test with small to large synthetic patterns. Left: input model, middle: resolved patterns at 61 s period, right: resolved patterns at 151 s period.

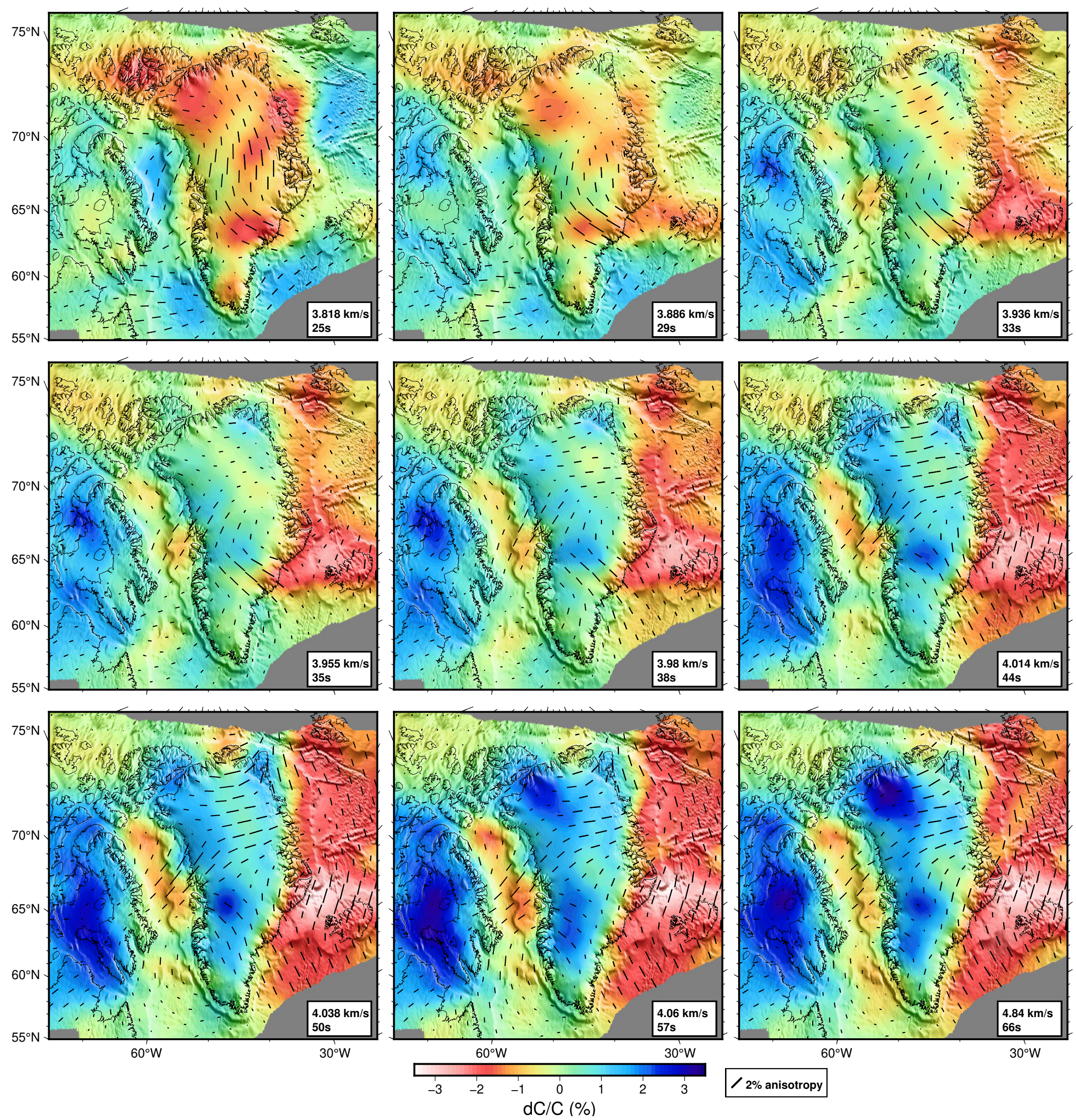
75°N
70°N
65°N
60°N
55°N
3.818 km/s
25s
3.886 km/s
29s
3.936 km/s
33s
3.955 km/s
35s
3.98 km/s
38s
4.014 km/s
44s
4.038 km/s
50s
4.06 km/s
57s
4.84 km/s
66s
60°W
30°W
−3 −2 −1 0 1 2 3
dC/C (%)
2% anisotropy

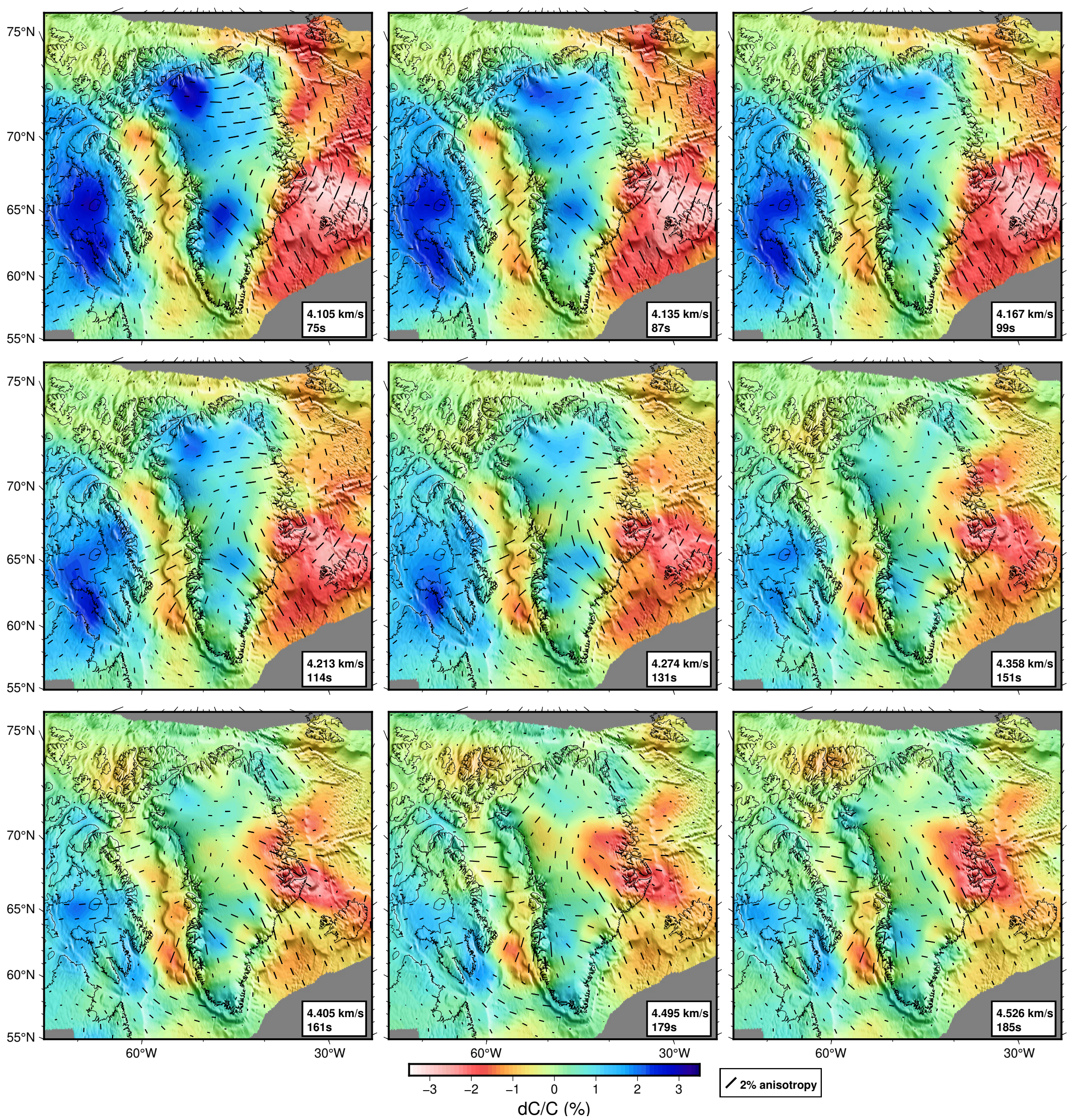

Figure A2.8: Phase velocity maps for periods between 25 and 185s with 2ψ anisotropy. The phase velocity perturbation is expressed relative to the average phase velocity in each period mentioned in the white box.

Chapter 3

Thermochemical State of the Upper Mantle Beneath Greenland and Northeastern Canada From Multi-Observable Probabilistic Inversion

3.1 Introduction

Our knowledge of solid Earth properties in the Greenland region is limited due to the fact that the majority of the island is covered by an ice sheet reaching $\sim$3 km thick in central regions. Therefore, other than a few locations where the ice sheet has been drilled through to the underlying rock, only the ice-free coastal regions can be accessed directly. Consequently, current knowledge of Earth structure in Greenland is inferred by indirect methods and geophysical modelling (e.g., Bamber et al., 2001; Brooks, 2011; Dawes, 2009; van Gool et al., 2002; Artemieva, 2019; Darbyshire et al., 2017; Mordret, 2018; Pourpoint et al., 2018b; Rogozhina et al., 2016; Steffen et al., 2017, 2018; Voss and Jokat, 2007; Voss et al., 2009). Improving our knowledge of subsurface structure in northeastern Canada and Greenland would provide valuable insight to the tectonic history (Artemieva, 2019; Darbyshire, 2003; Darbyshire et al., 2017; Pourpoint et al., 2018b; Schaeffer and Lebedev, 2014; Schiffer et al., 2022; Toyokuni et al., 2020) and related mantle dynamics (e.g., Afonso et al., 2019; Lebedev et al., 2018; Schaeffer et al., 2016; Steffen et al., 2018). Furthermore, improved estimates of Earth properties such as density and temperature will result in better models of Earth rheology (e.g., Wouters et al., 2013) and more accurate calculations of the isostatic response. This will enable improved reconstructions/simulations of past/future ice sheet evolution (Wake et al., 2016; Edwards et al., 2021) and, consequently, improved determinations of past and future sea-level changes (Zeitz et al., 2022; Lecavalier et al., 2014; Wake et al., 2016).

Earth structure in Greenland have been studied from different perspectives such as seismic tomography, surface heat flow (SHF), gravity, and joint inversion of multiple geophysical data sets. These methods have unique sensitivities to Earth structure and provide complimentary realizations. Despite the importance of each method and data in providing helpful information about Earth properties, they have limitations due to their inherent methodologies or the difficulty of application related to the study region. One of the above-mentioned methods that has been pivotal in constraining Earth structure in Greenland is seismic-related studies. As detailed below, seismic tomography, ambient noise, receiver function analysis, and shear wave splitting have been performed for decades to gain knowledge about the lithospheric and crustal structure of Greenland and northeastern Canada. However, despite the harsh environment in Greenland, installing and maintaining seismic equipment is challenging and hampers data collection and future modelling. Consequently, the resulting seismic models often have low resolution (global models) or gaps in specific regions (regional models). There are several global tomography models (e.g., Ekström, 2011; Larson and Ekström, 2001; Ritzwoller et al., 2001, 2002; Schaeffer and Lebedev, 2013; Schaeffer et al., 2016; Simmons et al., 2010) that provide information about Greenland's lithospheric and mantle structure. Still, the inability to capture variations at scales of a few 100 km due to the low resolution limits the utility of these models. On the other hand, regional studies (Darbyshire et al., 2004, 2017; Lebedev et al., 2018; Levshin et al., 2001; Mordret, 2018; Pourpoint et al., 2018a,b; Toyokuni et al., 2020) provided higher resolution information with more spatial variability, but these studies often don't cover the entire region (especially in northern Greenland).

Recent seismic studies (e.g., Ajourlou et al., 2023; Celli et al., 2021; Lebedev et al., 2018; Schaeffer and Lebedev, 2013; Toyokuni et al., 2020; Mordret, 2018; Pourpoint et al., 2018b; Darbyshire et al., 2017) have provided high quality data sets with similarities in the distribution of velocity anomalies beneath Greenland, adding confidence to the robustness of the first-order results and interpretations. Yet, they have also demonstrated significant discrepancies that remain unexplained (Sec. 2.4.1.6). Differences in interpretation become more apparent when comparing Earth structure resulting from seismic studies to those inferred using other methods such as SHF, gravity, etc. These differences originate from the data quality and inherent sensitivity of the data to Earth properties. One route to reducing these differences is to consider multiple data sets. Studies such as Rogozhina et al. (2016); Steffen et al. (2018); Steinberger et al. (2019) used gravity and topography to estimate SHF, elastic thickness, and lithosphere-asthenosphere boundary (LAB) depth, respectively. Although the results of using different methods and data are generally different, they show correlations in some regions and so can result in more robust inferences.

In this work, we expand on these analyses via the application of a joint inversion method that utilizes multiple geophysical data sets in a self-consistent framework (Afonso et al., 2013a,b). This technique has been used in many regions (e.g., Afonso et al., 2016, 2022; Tork Qashqai et al., 2016, 2018; Yang et al., 2021; Gradmann et al., 2013) to provide valuable thermochemical information on lithosphere and upper mantle properties. Specifically, this study uses the new local high-resolution seismic data set presented in Chapter 2 (Ajourlou et al., 2023) and multiple complementary geophysical observables to infer a range of Earth properties (e.g., temperature, density) through the joint inversion method applied in the LitMod software (Afonso et al., 2013a,b). The results of this inversion are then used in Chapter 4 to determine improved models of regional viscosity structure for a glacial isostatic adjustment (GIA) modelling analysis.

3.2 Data and Methodology

3.2.1 Inversion method: Multi observable probabilistic inversion

In this study, we adopt the multi-observable probabilistic inversion approach of Afonso et al. (2013a,b, 2016) to jointly invert multiple geophysical datasets for the thermochemical structure of the lithosphere. This approach uses a Bayesian formulation and Markov chain Monte Carlo (MCMC) techniques to solve the inverse problem. Following Bayes' theorem, all prior information on both observable data (d) and model parameters (m) are encoded into 'prior' probability distributions and combined with information from observed data and physical models (i.e., the forward problems) to define a multidimensional probability density function (PDF) over the parameter space, referred to as the posterior PDF (σ(m); (Tarantola, 2005)). The latter can be defined as,

$$\sigma(\mathbf{m}) \propto \rho(\mathbf{m})\, L(\mathbf{m}), \tag{3.1}$$

where $\rho(\mathbf{m})$ is the prior over $\mathbf{m}$ (describing all known information about the model parameters independently from the data), and $L(\mathbf{m})$ is the so-called likelihood function, a measure of how well the model explains the data. Assuming that all errors afecting the data and model parameters can be considered normally distributed, $L(\mathbf{m})$ can be written as

$$L(\mathbf{m}) \propto \exp\left[-\frac{1}{2}\sum_j \Phi(\mathbf{m})_j\right], \tag{3.2}$$

where

$$\Phi(\mathbf{m})_j = w_j \sum_i \left[\frac{\mathbf{d}_i^{\text{obs}} - g_i(\mathbf{m})}{\sigma_i} \right]_j^2, \tag{3.3}$$

and $\Phi(\mathbf{m})_j$ is known as the misfit function. The index j refers to data type (e.g., seismic, SHF, geoid anomaly), i is the total number of data points per grid node (30 in this study) used to sample logarithmically the Rayleigh and Love wave PVDCs at specific periods, σ_i denote data uncertainty for each data type (we have assumed that there is no correlation between data and so variances are independent (Tarantola, 2005)), w_j are arbitrary weights allocated for each data type, and $g_i(\mathbf{m})$ are the synthetic data computed by model $\mathbf{m}$. The weights control the impact of each data type on the total misfit function ($\Phi(\mathbf{m})_j$), and thus, the final inversion results. The numerical value ascribed to the weights depends not only on the type of data set but also on the goals of the inversion. In our case, we seek to obtain models that fit the seismic data as well as possible while being simultaneously consistent with, but not dominated by, non-seismic data. This choice is based on previous work that indicated that seismic data provides better sensitivity to the first-order thermal structure compared to the other input data sets, which are needed as supplementary information to increase the sensitivity to the compositional structure (Afonso et al., 2013a, 2016). We used the same scaling (weighting) factors used in Afonso et al. (2016), and for non-seismic data, we use only the associated uncertainties (i.e., $w_j = 1$). For an acceptable result, $\Phi(\mathbf{m})$ for non-seismic input data in Eq. 3.3 needs to be ≤ 1, and for surface wave PVDCs, $\Phi(\mathbf{m})$ needs to be ≤ 4 (Tork Qashqai et al., 2016).

The posterior PDF in Eq. 3.1 has no closed-form solution due to the complex priors used in the inversion. Therefore, sampling techniques like MCMC have been employed to estimate the $\sigma(\mathbf{m})$ posterior PDF. Among the several approaches in the MCMC method, we employed the Delayed Rejection Adaptive Metropolis (DRAM) due to its high accuracy and efficiency (Haario et al., 2006). The DRAM algorithm is an improved delayed rejection (DR) algorithm with efficient sampling that reduces rejected samples and focuses on high posterior probability sampling (adaptive metropolis (AM) algorithm). Basically, the AM algorithm updates/adapts the proposal distribution made of the prior PDFs with the previously accepted models to be utilized for model parameter sampling (Mira, 2001). The chain covariance matrix after N iterations is used to generate an N-dimensional Gaussian proposal distribution. In the adaptation step, the posterior distribution for each proposal distribution is estimated (Haario et al., 2006; Mira, 2001). Based on previous studies (Tork Qashqai et al., 2016, 2018; Shan et al., 2014; Zhang et al., 2019; Yang et al., 2021), 4-7 adaption steps generate a stationary chain after $\sim 10^5$ iterations. However, the optimum number of samples for each adaptation and the number of samples needed between each adaptation depends strongly on the problem (Chen and Niu, 2016; Guo et al., 2016; Haario et al., 2006). Based on previous studies and several tests (Afonso et al., 2016; Chen and Niu, 2016; Guo et al., 2016; Tork Qashqai et al., 2016; Shan et al., 2014), we adopt five adaptations and 30,000 samples between adaptations. We also start with 150,000 simulations in the initial non-adaptation stage, which makes, in total, 300,000 simulations for each grid point to estimate the Earth properties with depth, and the same number of simulations is required for all grid points (more information on the grid points in the following sections).

3.2.2 Model parameterization and prior information

A full set of crust and mantle parameterization is described in previous studies (Afonso et al., 2013a,b, 2016; Tork Qashqai et al., 2016; Shan et al., 2014), and so here we focus only on defining parameter values that are specific to our region (and so depart from those used in previous studies). In this study, the 3D volume of Greenland and northeastern Canada consists of 446 non-overlapping columns in a $1^\circ \times 1^\circ$ grid (Fig. 3.1). Each 1D column is defined by three crustal layers (i.e., sediment/ice, upper, and lower crust) over two lithospheric and sub-lithospheric mantle layers. In an area covered with ice, the first layer is considered as ice, and the sediment (which is generally negligible in these areas) is ignored. For glaciers in the Canadian Arctic, only major glaciated areas with spatial extent larger than $\sim 0.5^\circ$ are considered. In areas with no ice, the first layer is considered as a sedimentary layer.

Each crustal layer is characterized by seven parameters: thickness perturbation (Δh), coefficient of thermal expansion (α), bulk density at surface pressure-temperature (P-T) conditions [$\rho(P_0, T_0)$], thermal conductivity (κ), compressibility (β), V_p/V_s, and radioactive heat production (RHP). Since the inversion results are heavily affected by variations in RHP, ρ, Δh, and V_p/V_s (Afonso et al., 2016), these parameters are considered unknown to within a defined range (Table. 3.1) and solved for in the inversion, whereas the other properties (α, κ, β) are treated as constant within each layer (Table. 3.2; Sec. 3.2.6).

Similar to previous studies (Afonso et al., 2013a, 2016; Guo et al., 2016; Shan et al., 2014), we discretize the 1D column (crust and upper-mantle) with a 2 km finite-difference mesh (red dots in Fig. 3.2-right panel) to solve for elevation, lithospheric geotherms, and geoid height with forward modelling. Also, the upper mantle is discretized into 15 thermodynamic nodes (black circles in Fig. 3.2-right panel) to calculate equilibrium mineral assemblages and corresponding thermo-physical properties (e.g., Vp, Vs, rho) via a Gibbs free-energy minimization problem. The number of thermodynamic nodes within the two mantle domains depends on the lithospheric thickness. In ocean areas, where the lithosphere is thin, we use eight thermodynamic nodes in the lithosphere and seven in the sublithospheric mantle. In contrast, in continental areas, we use ten thermodynamic nodes in the lithosphere and five below the lithosphere.

Based on the strong correlation between temperature and rock strength (Afonso et al., 2016), the

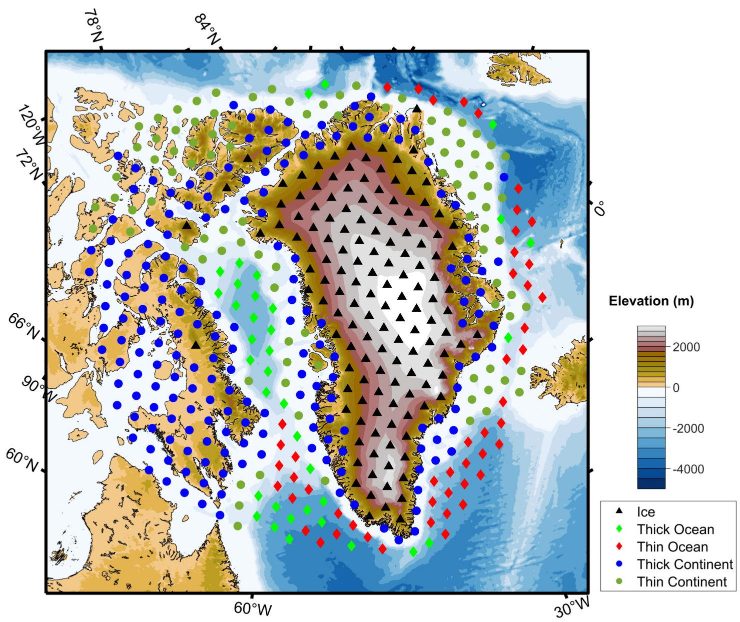

Figure 3.1: Distribution of grid points over Greenland and northeastern Canada. The grid is divided into different zones based on the first crustal layer and whether it is located in a continental or oceanic area (see key). Outside of ice-covered areas, the sub-classification of "thick" or "thin" corresponds to the sediment thickness and a threshold of 2 km.

1250 °C isotherm (T_{1250}) is considered the bottom of the thermal lithosphere and so defines the depth of the LAB. This correlates with the numerical results of upper mantle convection with realistic viscosities (Afonso et al., 2008; Afonso and Zlotnik, 2011; Ballmer et al., 2011; Gerya, 2010; van Wijk et al., 2010; S. Zlotnik and Fernández, 2008). The sub-lithospheric isotherm is constructed with three unknown parameters, T_{buffer}, T_{inter}, and T_{bottom} (in Fig. 3.2-right panel) at different depths Afonso et al. (2008, 2010, 2013a,b).

Lithospheric thickness (i.e., the depth to the LAB) and the bulk composition of the mantle layers within the CFMAS system (CaO, FeO, MgO, Al2O3, and SiO2) complete the vector of model parameters to invert for. The mantle compositional layers and the crustal layers are inverted on the coarsest grid in the framework (Afonso et al., 2013b). Since the LAB depth is not a well-constrained parameter, the depth of the thermodynamic nodes (and compositional layers) changes in each MCMC inversion iteration.

3.2.3 Prior information: Seismic data

The surface wave data set shown in Fig. 3.3 includes Rayleigh and Love wave PVDCs for 30 periods ranging from 25 to 185 seconds. Rayleigh wave PVDCs were extracted from a Greenland and northeastern Canada phase velocity model (Ajourlou et al., 2023), which was generated using the teleseismic two-station interferometry technique (Meier et al., 2004). The Love wave PVDCs

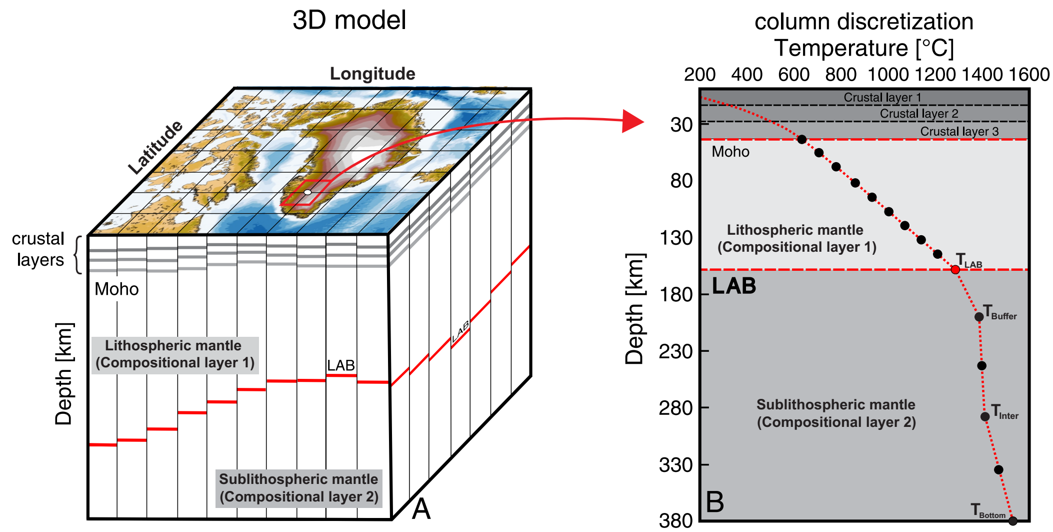

Figure 3.2: Model discretization and parameterization. **A)** Schematic illustration showing discretization of the 3D volume into its 1D columns (see Fig.3.1 for a more accurate representation of the spatial distribution of columns). **B)** Example depth discretization of a 1D column (modified from Afonso et al., 2013a). Three different discretizations are used: the coarse grid consists of three layers in the crust (ice or sediment in the first crustal layer) and two layers in the upper mantle; the intermediate grid (black circles) defines the thermodynamic nodes; the fine grid (red dots) is used for computing surface values such as elevation and SHF.

were calculated from this Rayleigh wave velocity model and the radial anisotropy extracted from a recent global shear wave velocity model (Celli et al., 2021). These PVDCs are sensitive to velocity structure from the lower crust (∼40 km) down to the sub-lithospheric mantle (∼400 km) (Ajourlou et al., 2023). Since the uncertainty of the surface wave inversion increases with depth, we allocate an uncertainty that linearly increases from one percent at 30 s to two percent at 185 seconds based on previous analyses (e.g. Tork Qashqai et al., 2016; Afonso et al., 2022) and preliminary tests. To mitigate the slight perturbations in long period phase velocities caused by truncating our numerical model to the depth of 400 km, we extended the velocity model to a depth of 1000 km by incorporating the GypSum model (Simmons et al., 2010).

3.2.4 Prior information: Non-seismic data

Elevation data (Fig. 3.4-A) is taken from the international GEBCO bathymetry dataset. This is a global terrain model for ocean and land, providing elevation data in meters on a 15 arc-second interval grid. Total geoid height (Fig. 3.4-B) is extracted from the Gravity field model, XGM2016

Table 3.1: List of all variable parameters and their associated initial prior ranges.

Parameters	Continental	Oceanic	Ice
Crust			
STP density1 (first crustal layer, g/cm^3)	1.7 - 2.8	1.915 - 2.6	0.915 - 0.945
STP density2 (second crustal layer, g/cm^3)	2.5 - 3	2 - 2.98	2.5 - 3
STP density3 (third crustal layer, g/cm^3)	2.65 - 3.15	2.8 - 3.15	2.8 - 3.15
V_p / V_s 1 (first crustal layer)	1.65 - 4.1	1.6 - 2.6	1.6 - 2.0
V_p / V_s 2 (second crustal layer)	1.65 - 1.95	1.6 - 1.95	1.5 - 2.0
V_p / V_s 3 (third crustal layer)	1.65 - 1.95	1.6 - 1.95	1.45 - 2.0
Δh1-Thin (first crustal layer, km)	-0.5 - 0.5	-0.5 - 0.5	-1 - 1
Δh1-Thick (first crustal layer, km)	-2 - 2	-1.5 - 1.5	-1 - 1
Δh2 (second crustal layer, km)	-4.0 - 4.0	-2.0 - 2.0	-5.0 - 5.0
Δh3 (third crustal layer, km)	-5.0 - 5.0	-3.0 - 3.0	-4.0 - 5.0
RHP (μWm^{-3})	1.0 - 3.6	0.1 - 4.0	0.1 - 3.8
Mantle			
LAB (km)	110 - 300	60 - 170	80 - 360
Al_2O_3 (in lithosphere, wt %)	0.5 - 4.0	0.2 - 4.0	0.2 - 4.0
FeO (in lithosphere, wt %)	6 - 9	6 - 9.2	6 - 9.5
MgO (in lithosphere, wt %)	34 - 50	34 - 55	34 - 55
CaO (in lithosphere, wt %)	0.5 - 4	0.15 - 4.5	0.15 - 5.0
Al_2O_3 (in sub-lithosphere, wt %)	1.5 - 4.3	1.5 - 4.5	1.5 - 4.8
FeO (in sub-lithosphere, wt %)	6 - 9.0	6 - 9.2	6 - 9.5
MgO (in sub-lithosphere, wt %)	34 - 50	34 - 55	34 - 55
CaO (in sub-lithosphere, wt %)	0.5 - 4.0	0.5 - 4.5	0.5 - 5.2
T_{Buffer} (°C)	1250 - 1500	1240 - 1470	1240 - 1470
T_{Inter} (°C)	1300 - 1700	1230 - 1650	1300 - 1650
T_{Bottom} (°C)	1350 - 1750	1400 - 1680	1400 - 1680

Mean RHP for the continental crust is as mentioned above, and for the lower crust, RHP/100 is used.

(Pail et al., 2018), which contains spherical harmonic coefficients up to degree and order 5399. Although this dataset is more sensitive to variations in the LAB depth than gravity anomalies (Afonso et al., 2008, 2013a), it often includes a large contribution from deep ($\geq$400 km) mantle density anomalies that are not of interest here. Therefore, the total geoid height data are filtered with a band-pass filter using the tapering approach of Horowitz et al. (2021) to suppress

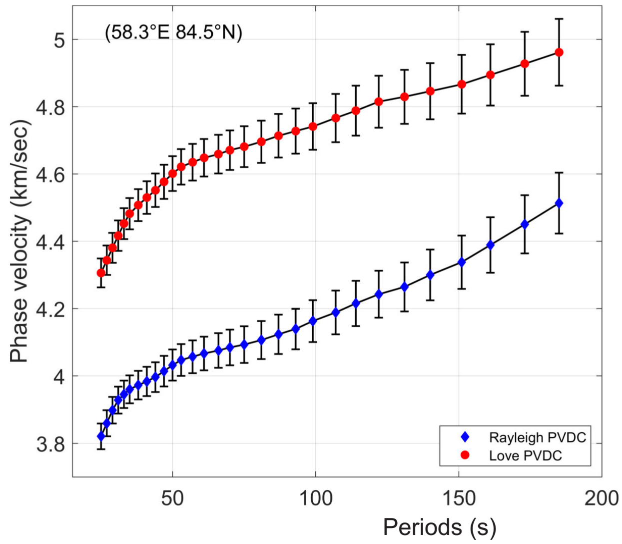

Figure 3.3: An example pair of Rayleigh (blue) and Love (red) wave PVDCs from 25 to 185 s with estimated 1-σ uncertainties at the location 58°E 84.5°N.

contributions from density structure deeper than ~400 km. Based on previous analyses (e.g., Chase, 1985; Doin et al., 1996; Chase et al., 2010; Afonso et al., 2019) and preliminary tests, we set spherical harmonic coefficients for degrees ≤ 5 to zero and roll off spherical harmonic coefficients between degrees 5 and 9 using a cosine tapering function.

The SHF data set (Fig. 3.4-C) is a combination of data over Greenland (including the continental shelves) from Martos et al. (2018), which were generated using a Curie depth analysis and, for the rest of our study region, data from Lucazeau (2019), which are based on direct, in-situ measurements and modelling. Since these two models are the results of different methods applied at different spatial scales, they have significant differences. Therefore, we applied spatial smoothing (using moving average with a Gaussian kernel) to prevent sharp and unrealistic changes at the boundaries between these data sets. SHF uncertainty values in Martos et al. (2018) are ten times smaller than those in Lucazeau (2019), which reflects the different approaches used in each study. However, since these data were not combined (one or the other was used for a given grid point), this difference is only evident in greater model parameter uncertainty for locations where the Lucazeau data were used.

The mean and the corresponding uncertainty values for elevation, geoid, and SHF were calculated on a $1^\circ \times 1^\circ$ grid from their original high-resolution data sets. To account for measurement variability as well as theoretical modelling errors in the elevation data, we follow previous studies and assigned the standard deviation in a given $1^\circ \times 1^\circ$ grid as uncertainty to the elevation (~150 m) (e.g., Afonso et al., 2013a; Guo et al., 2016; Shan et al., 2014; Zhang et al., 2019; Tork Qashqai et al., 2018). The mean values, as well as the corresponding uncertainties, were used to make the prior PDFs required in the Bayesian framework (Sec. 3.2.1). Random samples

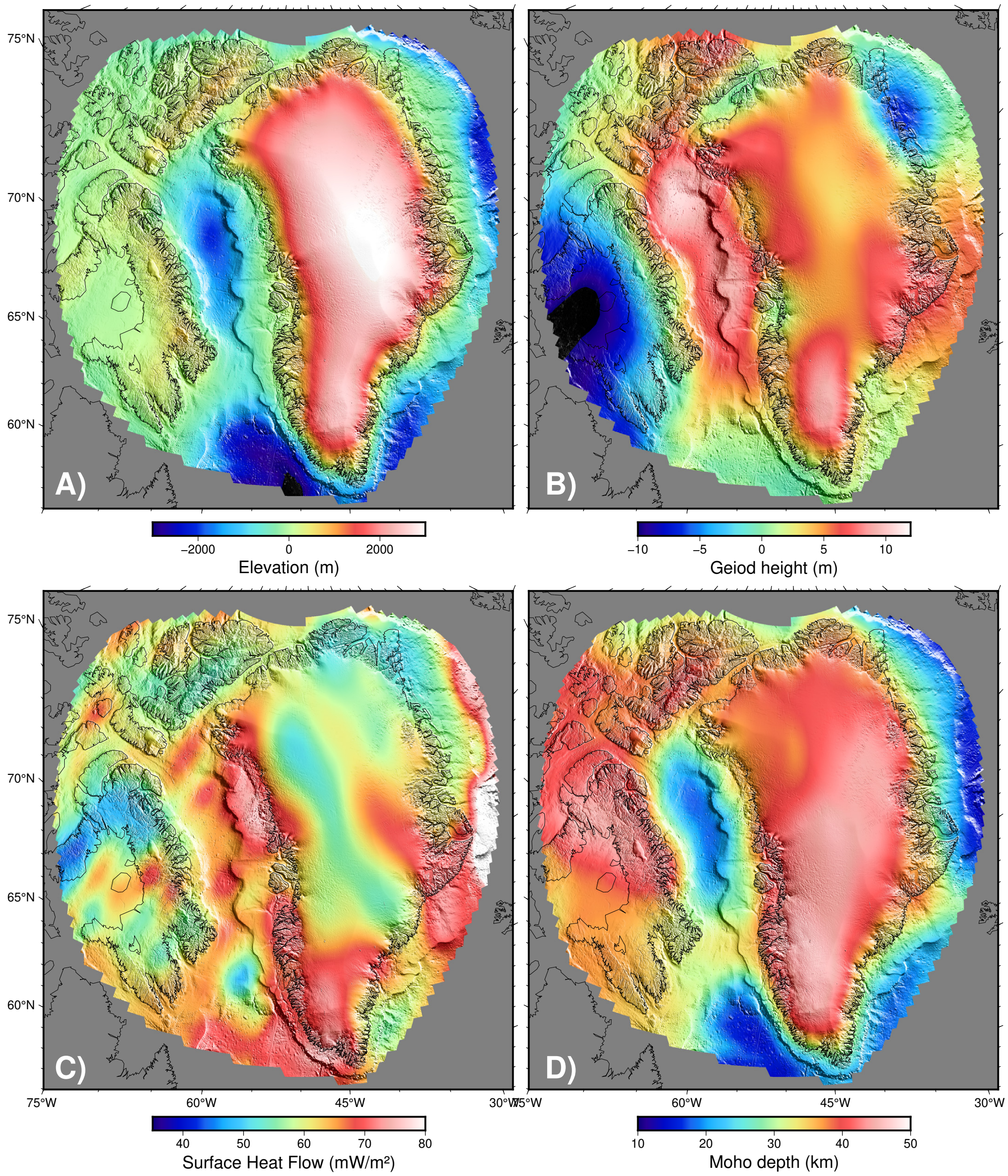

Figure 3.4: Initial input non-seismic data used in the joint inversion. **A)** Elevation (GEBCO), **B)** Geoid height (Pail et al., 2018), **C)** Surface Heat Flow (SHF) (Lucazeau, 2019; Martos et al., 2018), **D)** Moho depth (Laske et al., 2013).

of these prior input PDFs were used in thousands of simulations, and compatible samples with other data and parameters were considered. Therefore, the posterior input data used to find the Earth structure parameters may be slightly different from the mean values used at the beginning (more information in Sec. 3.3.1).

3.2.5 Prior information: Crustal data

Information about the initial crustal model, including layer thicknesses, Moho depth, and what lies above it (e.g., sediment, ice), is required for the inversion. Information from several local and global products was used to provide this information for our study region. For crustal information and Moho depth (Fig. 3.4-D), we incorporated information from the NAGTEC crustal thickness grid (Funck et al., 2017), the ArcCrust model for the Arctic region (Lebedeva-Ivanova et al., 2019), and the global model of Szwillus et al. (2019). The resulting initial crustal model comprises information on, for example, the thickness, velocity, and density of each layer (at a given grid point).

As for the crustal information, the input sedimentary thickness is an assemblage of regional (NAGTEC sedimentary thickness model and the TEMAR model for the Arctic region including the land areas from Petrov et al. (2016)) and global (marine sedimentary thickness from Straume et al. (2019) and the remaining from CRUST1.0 (Laske et al., 2013)) models. The ice thickness information was obtained by considering IceBridge BedMachine (Morlighem, 2022) for Greenland and the results from Farinotti et al. (2019) for the Canadian Arctic.

It should be noted that an inversion for crustal properties is not the main aim of this study, and the inverted data sets are not strongly sensitive to shallow crustal structure. As a result of this insensitivity, the posterior PDFs of the crustal information mostly have a uniform shape (i.e., they strongly reflect the uniform prior distributions (Table,3.1)). As in previous studies (Afonso et al., 2016, 2022; Fullea et al., 2009; Yang et al., 2021; Zhang et al., 2021), to avoid long processing times (due to lack of convergence), we define a relatively small range for plausible crustal properties (Table. 3.1).

3.2.6 Forward models

The forward models used in determining the posterior PDFs of output variables are described in this section. For more detail, the reader is referred to previous papers (e.g., Afonso et al., 2013a,b, 2016; Fullea et al., 2009; Kumar et al., 2020). Lithosphere geotherms are calculated from the steady-state conductive heat transfer equation on the finite-difference mesh (Fig. 3.2-B (intermediate grid)) subject to Dirichlet boundary conditions at the Earth's surface (T_S = 10

°C) and at the LAB (T_{LAB} = 1250 °C). Beneath the lithosphere, we assume a constant thermal conductivity (κ = 3.4 $Wm^{-1}{}^{\circ}C^{-1}$) with no internal radioactive heat production. In contrast to the common assumption of considering a uniform, adiabatic gradient in the upper mantle, which can be inaccurate in areas with local convective dynamics, we control the temperature structure with three temperature values specified at the thermodynamics nodes defined in Fig. 3.2-B (T_{buffer}, T_{inter}, and T_{bottom}). Specifically, temperature isotherms in the sub-lithospheric mantle are constructed by linear interpolation between these three nodes (Afonso et al., 2016; Shan et al., 2014). The possibility of mantle dynamic effects on inverted isotherms in the eastern parts of our study region is high due to proximity to the Iceland hotspot, and so results in this region could be inaccurate.

The thicknesses of crustal layers are obtained by randomly perturbing an initial crustal model based on the given prior ranges (Δh values) in Table. 3.2. The P-T-dependent densities (Afonso et al., 2016) for each crustal layer at computation nodes are calculated on the finest grid (red dots in Fig. 3.2-B) using a lithostatic pressure profile, the computed geotherm and α and β of the corresponding layer via the following equation:

$$\rho(P,T) = \rho(P_0,T_0)\big[1 - \alpha(T - T_0) + \beta(P - P_0)\big] \tag{3.4}$$

where $\rho(P_0,T_0)$ is a free parameter sampled from its prior distribution during the inversion in each crustal layer. At each finite-difference node within the crust, lithostatic pressure is calculated at each depth by integrating the weight of the overlying material. Since the pressure and density are directly connected, the obtained pressure is then used in eq. 3.4 to get the density at any node (e.g., Afonso et al., 2013a; Fullea et al., 2009). The inferred density is then used to update the pressure at the next (deeper) node point.

By assuming Birch's law of correspondent states as an approximation (Karato et al., 2008), and the determined density within each crustal layer, the corresponding V_p is calculated via:

$$V_P = 39.128\rho - 63.064\rho^2 + 37.083\rho^3 - 9.1819\rho^4 + 0.8215\rho^5 \tag{3.5}$$

where this equation is a modified version of that proposed by Brocher (2005) to produce more accurate velocity values for mafic rocks (Afonso et al., 2016). The associated Vs values are then obtained for each layer from the computed V_p using the relation $V_s = \frac{V_p}{V_p/V_s}$ and the Vp/Vs parameter sampled by the MCMC algorithm.

The stable mantle mineral assemblages within the CFMAS system (CaO-FeO-MgO-Al_2O_3-SiO2), and their associated physical properties (e.g., density, velocities, an-harmonic elastic moduli) are obtained using components of the software package Perple X (Connolly, 2005) to

Table 3.2: Constant crustal parameters

Parameters	Continental	Oceanic	Ice
$\alpha 1$ (first crustal layer, 1/°C)	2.7×10^{-5}	2.3×10^{-5}	7.1×10^{-5}
$\alpha 2$ (second crustal layer, 1/°C)	2.6×10^{-5}	2.3×10^{-5}	2.6×10^{-5}
$\alpha 3$ (third crustal layer, 1/°C)	2.3×10^{-5}	2.5×10^{-5}	2.3×10^{-5}
$\kappa 1$ (first crustal layer, $\mathrm{Wm^{-1}{}^{\circ}C^{-1}}$)	2.8	2	2.21
$\kappa 2$ (second crustal layer, $\mathrm{Wm^{-1}{}^{\circ}C^{-1}}$)	2.6	2.6	2.7
$\kappa 3$ (third crustal layer, $\mathrm{Wm^{-1}{}^{\circ}C^{-1}}$)	2.3	2.4	2.3
$\beta 1$ (first crustal layer, 1/Pa)	5.0×10^{-11}	2.5×10^{-11}	1.5×10^{-11}
$\beta 2$ (second crustal layer, 1/Pa)	1.4×10^{-11}	1.2×10^{-11}	3.2×10^{-11}
$\beta 3$ (third crustal layer, 1/Pa)	1.1×10^{-11}	1.2×10^{-11}	1.1×10^{-11}

Note: α = coefficient of thermal expansion, κ = thermal conductivity, and β =compressibility

solve the Gibbs free-energy minimization problem, and the thermodynamic database of Stixrude and Lithgow-Bertelloni (2011). The CFMAS system includes $\gtrapprox$98 wt.% of the mantle's mass, and so it is an appropriate compositional representative for phase assemblage modelling of the mantle. More detailed information about compositional priors, associated correlations in MCMC sampling, and forward problems related to elevation and geoid height can be found in previous studies (Appendix A, Afonso et al., 2013a, 2016).

By estimating bulk properties such as density, seismic velocities, etc., in the crust and upper mantle, we are able to calculate Rayleigh and Love wave dispersion curves using a modified version of the program disp96 (Herrmann, 2013), based on the Thompson-Haskell eigenvalue problem (Haskell, 1953) and the frequency-dependent attenuation model of Jackson and Faul (2010).

3.3 Results

3.3.1 Data Fit

Before focusing on the main results, we first describe data-model misfits and posterior PDFs. Inspection of Fig. 3.5 shows that the quality of the simultaneous fit to all input datasets (Rayleigh

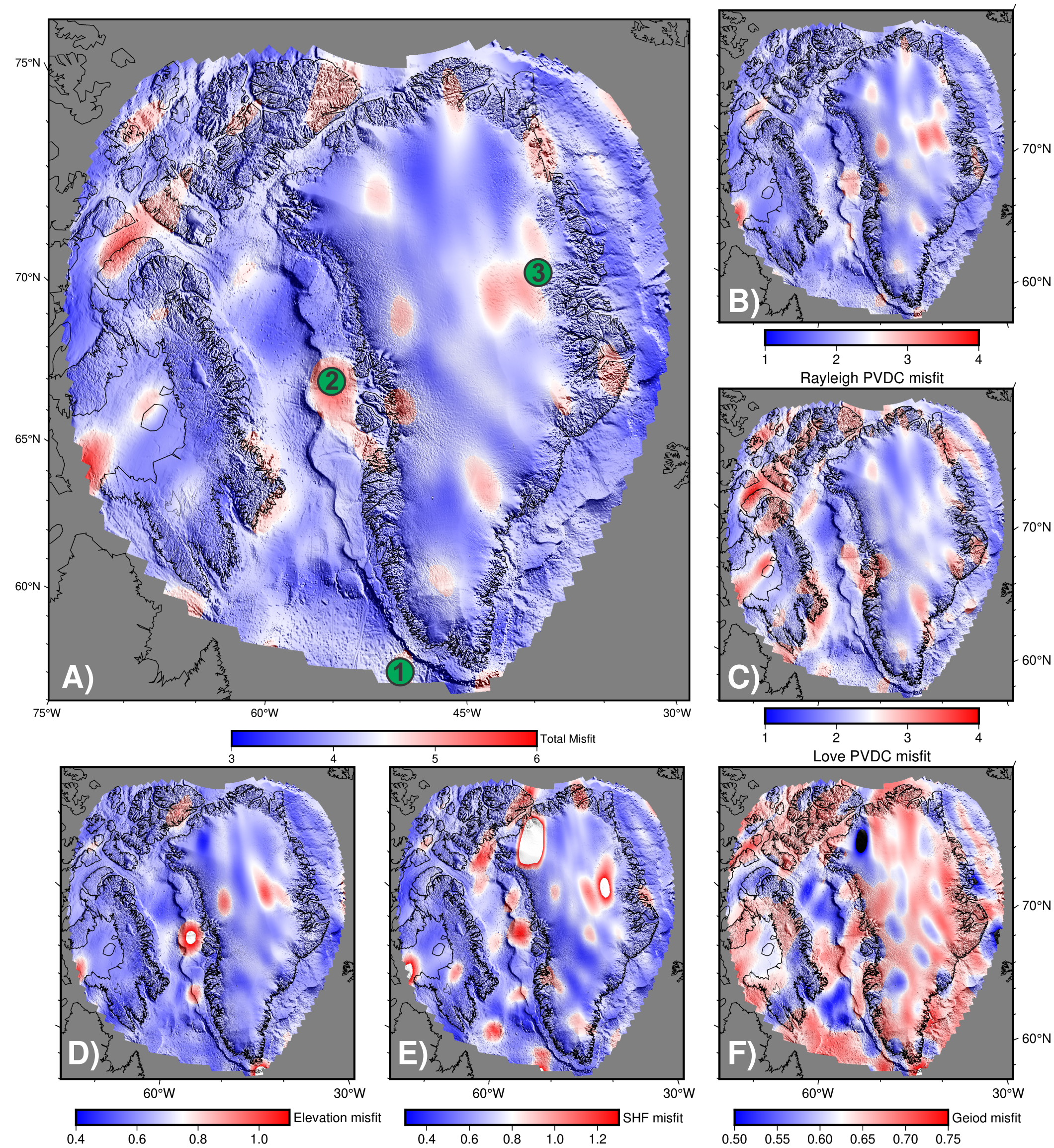

Figure 3.5: **A)** Total misfit calculated using all data sets (Eq.3.3). Three circled numbers show the locations corresponding to the three examples of the full posterior PDF shown in Fig. 3.6. Misfit results are also provided for Rayleigh (B) and Love (C) PVDCs, elevation (D), surface heat flow (SHF) (E), and geoid height (F). Note that scale bar ranges vary from plot to plot.

and Love wave PVDCs, surface heat flow, geoid, and absolute elevation) varies spatially. Fig. 3.5-A represents the misfit values when all data are considered (Eq. 3.3), hereafter referred to as the total misfit. Since the inversion at each grid point is 1D, with no spatial correlation between each grid node, the results can show high variability in the total and individual misfits between grid points. For example, there are high misfit values in eastern and western Greenland and northern Baffin Island. Examination of the individual misfit maps (Fig. 3.5-B&F) indicates that surface wave PVDCs tend to be the highest contributor to total misfits. This primarily occurs due to spatial irregularities in the PVDCs associated with the inversion technique and edge effects. For example, these data are less accurate in areas with low surface wave path densities, such as in northern Greenland and at grid margins, due to insufficient seismic station density (Ajourlou et al., 2023). Although the Love wave PVDCs are based on the Rayleigh wave PVDCs, there is a notable difference in the data-model misfits for these two constraining datasets. High misfits for the Love wave PVDCs occur mainly in northeastern Canada and in several locations in Greenland, while the Rayleigh wave misfits are generally smaller, with the largest values in Greenland. This could reflect the effect of anisotropy and variations of this quantity across the study region. Also, as evident in comparing results in frames B-F in Fig. 3.5, the PVDC data set results in greater spatial variations in misfit compared to other data sets. However, exceptions exist in some data sets. For example, SHF results show a high local misfit in NW Greenland, which has greater misfit compared to the seismic data. However, regardless of the large misfit at this location, the mean SHF values are within the adopted uncertainties (Fig. 3.6). Based on the information given in Sec. 3.2.1, the misfit values are lower than the adopted thresholds and so indicate high-quality inversion results.

To further illustrate and investigate data misfit characteristics of the model, we chose three points with high total misfits (as numbered in Fig. 3.5-A) in different zones (i.e., ocean (1), continent (2), and ice (3)). Fig. 3.6 illustrates the posterior PDFs for Rayleigh and Love PVDCs, SHF, geoid, and absolute elevation in these three locations, which are plotted alongside the input data. The means of the respective posteriors are used to show the predicted data (unless mentioned otherwise). However, note that for some data types, the PDFs are non-Gaussian and skewed toward larger misfit values. The predicted Rayleigh and Love PVDCs fit the input data to within one standard deviation at the three chosen grid points and for all periods (Fig. 3.6, first column), except for shorter period (≤ 30 s) Love waves. The same is true for the distributions of predicted elevation, geoid, and SHF (Fig. 3.6, last three columns). Since the results in Fig. 3.6 are for locations where misfits are anomalously large, it follows that, for most grid points, the predicted data is within 1σ of the input data.

We also investigate the three designated high total misfit grid points (Fig. 3.5) for other model parameters. Fig. 3.7 illustrates the inversion results for various parameters at the ice grid point (location 3 in Fig. 3.5-A; results for continent and ocean locations are presented in Appendix 3, Figs. A3.2 and A3.3). These results correspond to a location in eastern Greenland with 1.5 km of ice and a $\sim$38% parameter search success rate (38% of the total simulations were accepted).

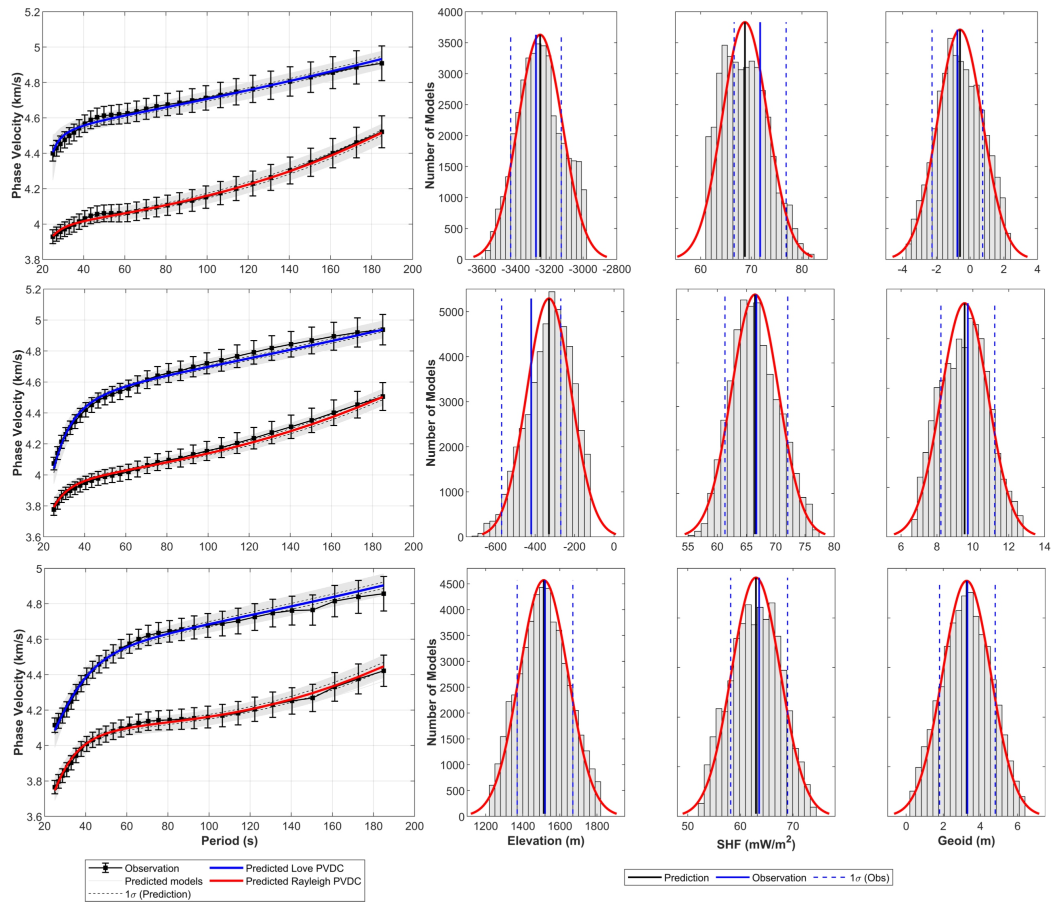

Figure 3.6: Data-model fits and posterior histograms for Rayleigh and Love wave PVDCs, elevation, SHF, and geoid height for three locations (see numbered green circles in Fig 3.5-A): 1) ocean the first row, 2) continent in the second row, and 3) ice in the third row. For surface waves (first column), gray lines are the accepted models, black lines and the bars are the input data and corresponding uncertainty, blue lines are the mean of predicted posterior PDF for the Love PVDC, red lines are the mean of predicted posterior PDF for the Rayleigh PVDC, and black dashed lines are the predicted uncertainty. In the histogram plots, gray bars indicate output from the accepted models, solid and dashed blue lines are the input data and corresponding uncertainty (1σ), black lines are the mean of the predicted posterior PDFs, and the red lines are the best-fitting Gaussian distributions.

Except for the mineral volume results (Fig. 3.7-G), accepted models are indicated by the grey lines, black lines are the mean of the posterior distribution, and the dashed blue lines are the 1σ uncertainties. The quality of the final inversion depends on the input data, the corresponding sensitivity to model parameters, and the adopted prior bounds for each parameter. That is, the

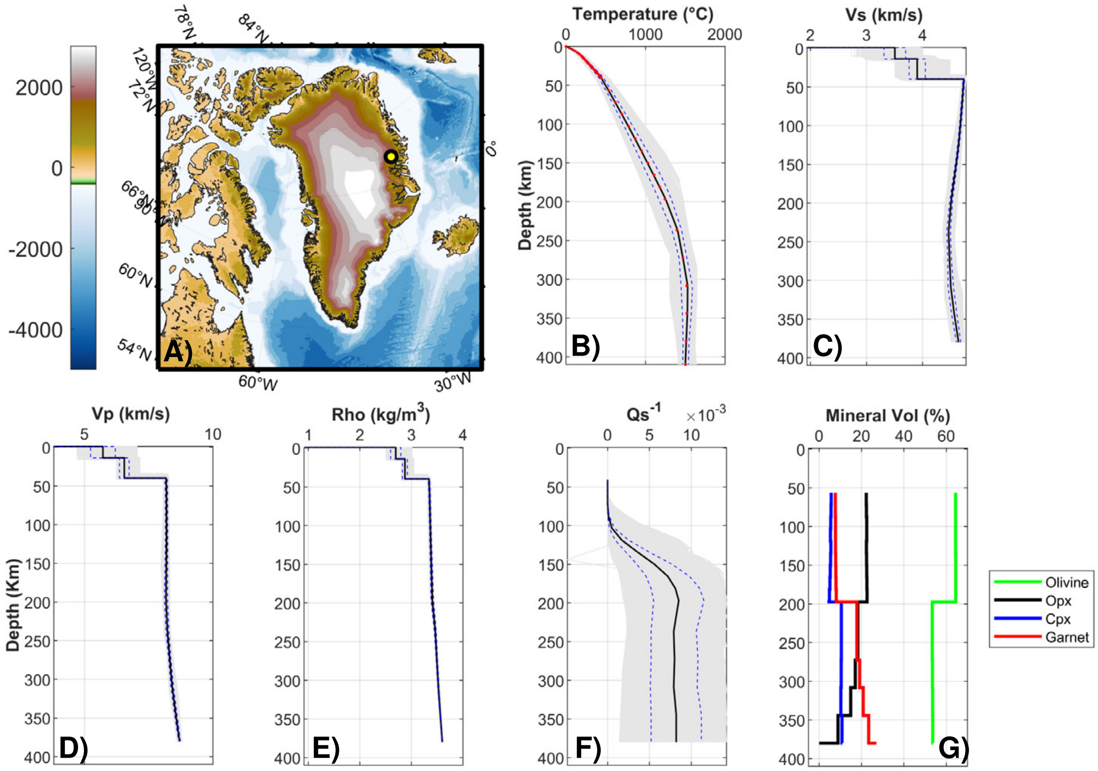

Figure 3.7: A) Location map of the grid point in eastern Greenland with high total misfit (location labeled as '3' in Fig. 5). **B-F)** Posterior distributions of temperature, Vs, Vp, bulk density, and seismic attenuation. Gray lines denote the accepted models, black lines are the mean of the posterior distribution, and the dashed blue lines are the 1σ uncertainties. **G)** Inferred volume profiles of four dominant mantle minerals. opx and cpx are abbreviations for orthopyroxene and clinopyroxene, respectively.

distributions of accepted models vary with each quantity shown and with depth. For example, the applied, high-resolution Rayleigh wave data set is sensitive to Earth structure over the depth range of $\sim$50 to 400 km, and so the inversion quality is high (tight PDFs) within this range. In general, the quality of the inversion results is high, and the uncertainty is less than 10% of the estimated mean predicted value for most of the model parameters. The mineral volume at this location is dominated by olivine ($\sim$50-60%), and the rest is occupied with garnet and pyroxene ($\sim$0-20%). The abrupt increase in mineral volumes at depth $\sim$200 km correlates with the LAB depth estimation, where a boundary is placed in the model.

3.3.2 Crustal structure

Maps of depth-averaged crustal properties are provided in Fig. 3.8. Based on Fig. 3.8-A, higher-density material is found in north Baffin Island, Baffin Bay, southern-west Greenland, and the

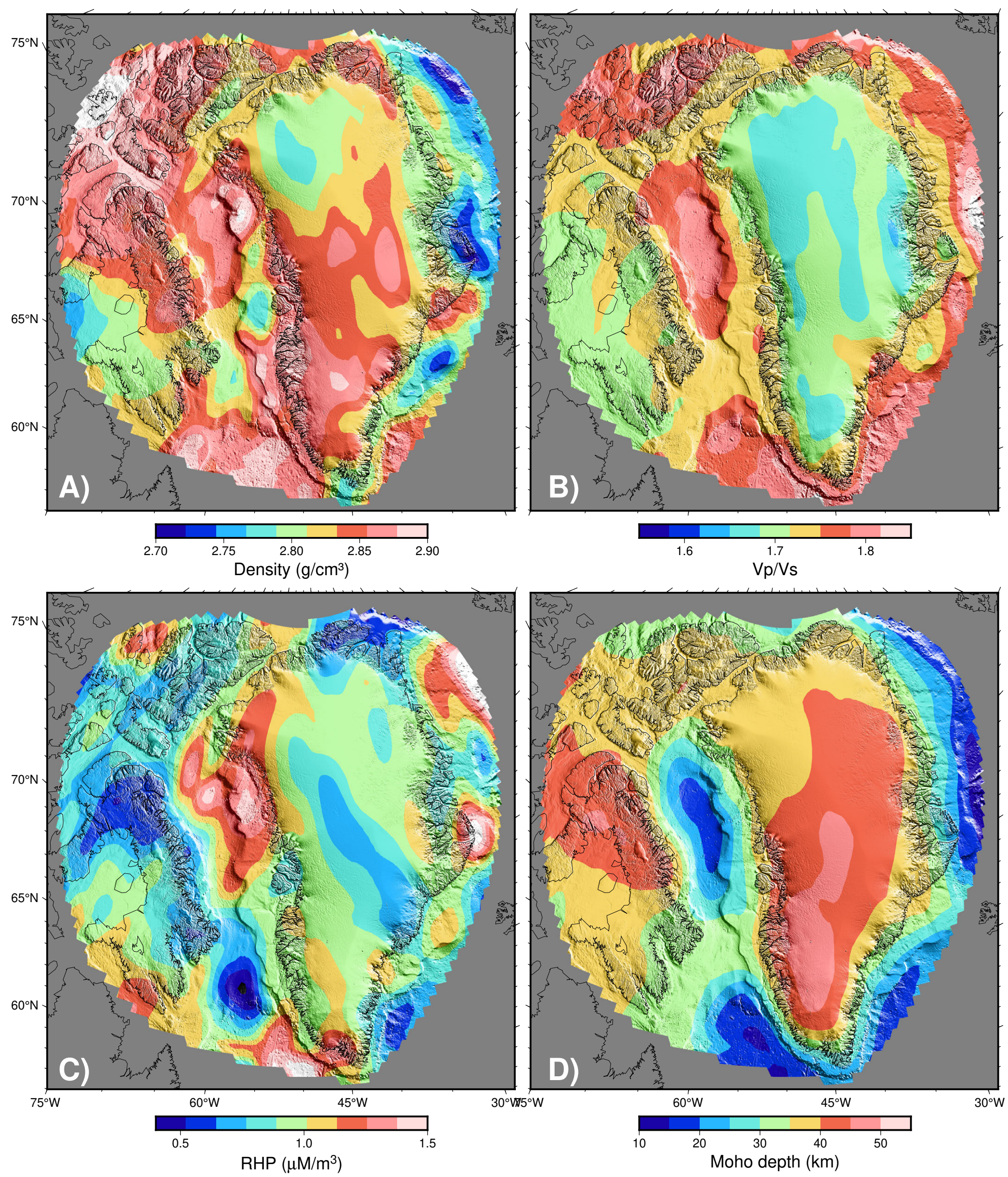

Figure 3.8: Crustal properties resulting from the inversion. **A-C)** depict the depth-averaged density, Vp/Vs ratio, and RHP, respectively, and **D)** shows the Moho depth.

Labrador Sea, whereas lower-density material is found in Eastern and northwestern Greenland. In Fig. 3.8-B, there is a clear distinction in eastern Greenland between oceanic and continental crystalline layers, which depicts Vp/Vs $\geq$1.75 corresponding to mafic rocks in the oceanic domain (Mjelde et al., 2002). The lowest Vp/Vs ratios, typically representative of continental crust, are found in Greenland; this is consistent with the results of previous ambient noise studies (e.g., Kumar et al., 2007). Based on Fig. 3.8-C, the highest RHP ($\geq$1.5 μWm^{-3}) exists in eastern, northeastern, southern, and western Greenland, as well as Baffin Bay and the Labrador Sea. Also, the lowest RHP ($\leq$0.5 μWm^{-3}) values are found in the Labrador Sea, north Baffin Islands and northeastern Greenland. Most of the high RHP values are located in continental shelves around Greenland (where thick sedimentary deposits are located), whereas inland Greenland has less variation in RHP values. In the Labrador Sea offshore southern Greenland, the RHP values are considerably higher than normal oceanic crust RHP ($\leq$1 μWm^{-3}). The excessive RHP values might be related to un-modeled shallow thermal process (e.g., past rifting, volcanism, sedimentation) that has not been included, and higher RHP values (though unrealistic) are required to compensate for these processes. Although the RHP values in this localized region are not robust, the upper-mantle isotherms are not significantly affected. The Moho depth inversion results (Fig. 3.8-D) show no significant change compared to the input data (Fig. 3.4-D); it is thickest ($\sim$50 km) in southern Greenland and northern Baffin Island, and thinnest ($\sim$15 km) in oceanic regions. More detailed information on the crustal inversion results is provided in Appendix (Fig. A3.4).

3.3.3 LAB depth and compositional structure of the lithosphere

The thermal LAB depth (depth to 1250 °C isotherm) and the corresponding uncertainty of the posterior PDF are illustrated in Fig. 3.9-A&B. Based on Fig. 3.9-A, the LAB is deepest ($\geq$250 km) to the west of Baffin Island, northwestern and central-south Greenland. In comparison, shallow LAB depths ($\leq$ 100 km) are located in Baffin Bay, the Labrador Sea, and central-eastern Greenland. There is a clear region of thinner lithosphere separating the thicker regions in northwestern and central-south Greenland. Uncertainty (1σ) corresponding to the LAB depth inversion in Fig. 3.9-B indicates that, for a given location (grid point), the results are well resolved as the uncertainty is generally less than 10%. The estimated uncertainty over Greenland ($\sim$10-30 km) is also about 10% of the inferred variation in this quantity ($\sim$200 km). At large spatial scales, the uncertainty increases as LAB depth increases, with cratonic regions exhibiting the greatest uncertainty and oceanic regions the smallest. This is mainly due to the decrease in depth resolution of the input data with depth. For example, the depth resolution of surface wave PVDCs reduces with the increasing period (Fig. 2.7). Notably, this correlation does not hold to the west of Baffin Island, where the thick lithosphere is associated with relatively low uncertainty.

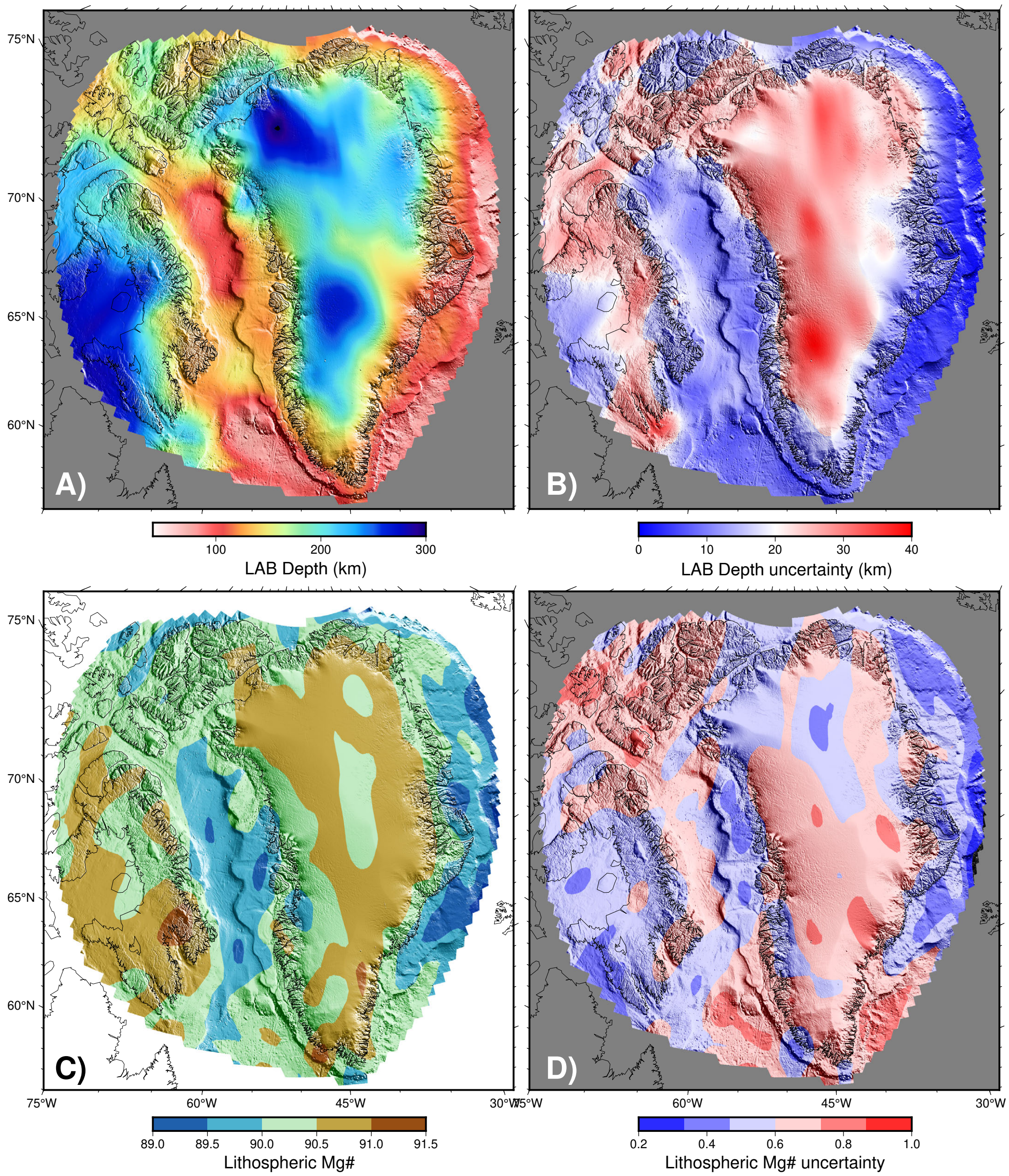

Figure 3.9: **A)** Mean value of the depth to the 1250 °C isotherm, which we take to define the lithosphere-asthenosphere boundary (LAB), from the posterior PDF, and **B)** the corresponding 1σ uncertainty. **C)** Depth-average of the lithospheric Mg#, and **D)** the corresponding 1σ uncertainty.

The data sets included in the joint inversion provide some sensitivity to the average bulk composition of mantle material (Afonso et al., 2013a,b). The magnesium number (Mg#) of the mantle is often used as a proxy to identify compositional anomalies and distinguish mantle domains by assessing the fertile and depleted character. This is justified given the strong correlation between Mg# and relevant bulk physical properties of peridotites (e.g. Afonso et al., 2010, 2013a). Since bulk composition is the least well-constrained aspect of the inversion (Fig. 3.9-D, Afonso et al., 2013a; Zhang et al., 2019), instead of considering absolute values, we will focus our description on the largest (spatial) contrasts in Mg# only (Fig. 3.9-C). More detailed compositional information (CFMAS system) is provided in Appendix (Fig. A3.6).

Despite the large compositional priors used for the inversion (to span the broad compositional range observed in nature; Table. 3.1), the results reveal distinct compositional domains in oceanic and continental regions. In oceanic areas, the average composition becomes more fertile at locations removed from spreading ridges (e.g., eastern Greenland). The average composition where the LAB is shallow (i.e., near a mid oceanic ridge) reflects mostly the depleted shallow layer produced during decompression melting of passively upwelling mantle material. With ocean floor spreading and plate thickening, the average composition comprises more fertile mantle material from the asthenosphere, which leads to the Mg# decrease. Also, the average composition observed in Baffin Bay and the Davis Strait suggests a fertile mantle in these regions. The oceanic lithosphere generally shows lower Mg# and a more fertile mantle, whereas the continental regions present higher Mg#, representing a more depleted mantle. The largest contrasts in Mg# are located in southern, southeastern, and central Greenland, as well as southern Baffin Island, and several local high values in eastern, northeastern, and northwestern Greenland. Although the Mg# uncertainty (1σ) in Fig. 3.9-D is $\leq$1% of the Mg# amplitude, it is relatively large (up to $\sim$50%) compared to the spatial variation ($\sim$2) across the study region.

3.3.4 Mantle structure

The inferred mantle structures and corresponding uncertainties are summarized as depth slices in Fig. 3.10 and Fig. A3.5, showing the mean of posterior PDFs and 1σ uncertainty, respectively. Lithospheric temperature variations in Fig. 3.10 (first column) show that the hottest areas are generally in oceanic regions and, more specifically, east of Greenland and in the Labrador Sea. Beneath Greenland, a relatively thick and cold lithosphere is bisected by a higher temperature channel aligned approximately NW-SE across all depths except for 350 km. This pattern is also present in the LAB map in Fig. 3.9-A and correlates with the trace of the Iceland plume track proposed in previous studies based on different analyses (Ajourlou et al., 2023; Lebedev et al., 2018; Martos et al., 2018; Rogozhina et al., 2016; Steinberger et al., 2019). Also, a high-temperature anomaly continues to exist in the sub-lithospheric mantle beneath the southwestern

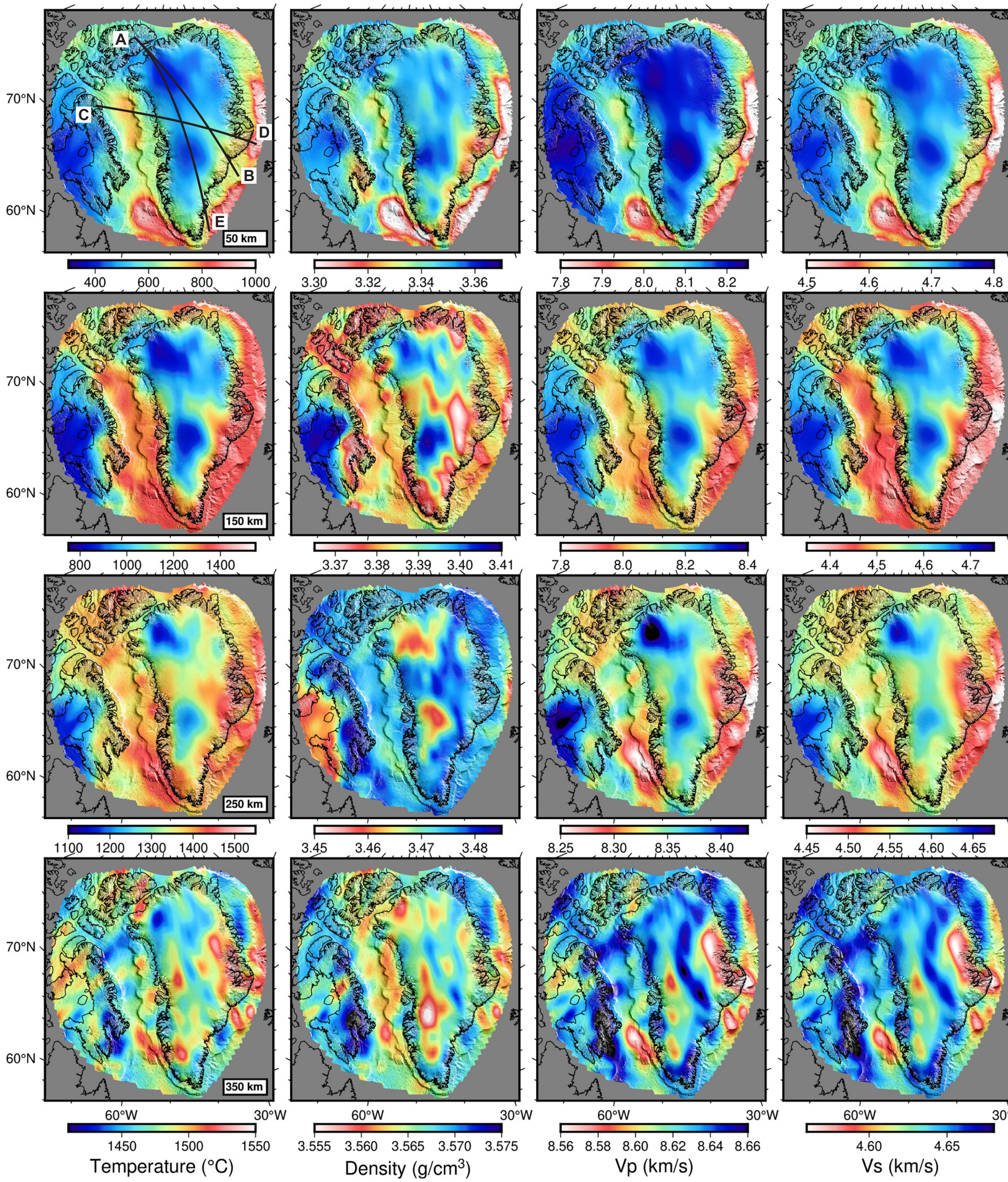

Figure 3.10: Depth slices of shallow mantle properties. Left to right: temperature, density, Vp, and Vs. Top to bottom: properties at depths 50 km, 150 km, 250 km, and 350 km.

and the central-eastern coasts of Greenland. The high-temperature anomaly in central-eastern Greenland has recently been identified based on local and global surface wave seismic tomography(Ajourlou et al., 2023; Celli et al., 2021; Rogozhina et al., 2016). Our results show that the temperature difference over Greenland is $\sim$350 to 700 °C at depth 50 km, $\sim$800 to 1400 °C at 150 km, $\sim$1100 to 1500 °C at 250 km, and $\sim$1400 to 1550 °C at depth 350 km. Thus, the lateral temperature variations are largest within the 150-250 km depth range. Based on Fig. A3.5, although the temperature uncertainty is small relative to absolute values ($\leq$10%), it is more significant relative to the spatial variations noted above, and increases with depth. The uncertainty correlates with temperature, and so is generally lower in colder regions such as western Baffin Island, northwestern, and central-southern Greenland. However, we note that this pattern becomes reversed at $\sim$350 km depth, where the relative uncertainty is greater in colder regions (Sec. 3.4.1).

The density structure in Fig. 3.10 (second column) is due to variations in temperature and bulk composition. The density varies from 3.3 g/cm^3 in oceanic regions, such as eastern Greenland and the Labrador Sea, at 50 km depth to 3.58 g/cm^3 in continental regions such as northeastern Greenland and Baffin Island at 350 km depth. At a depth of 50 km, density is lowest in oceanic regions like offshore and inland eastern Greenland, southern Baffin Islands, and the Labrador Sea, and it is highest in central-southern and northeastern Canada. At this depth, the density variations correlate well with temperature changes except for northeastern Greenland, suggesting significant compositional changes in this region (Sec. 3.3.3). Based on Fig. A3.5, the density uncertainty (second column) at this depth is relatively large ($\sim$30% of the spatial variation in density). In contrast to temperature, the uncertainty doesn't necessarily correlate with density magnitude. At 150 km depth, the lower density material is evident in eastern, southern, and northeastern Greenland as well as the Queen Elizabeth Island and southern Baffin Islands. In comparison, the higher density material is located in central south and northeastern Canada. At this depth, the density variations correlate well with temperature changes except for northeastern Canada and the Queen Elizabeth Island. Based on Fig. A3.5, the density uncertainty at this depth is significant and represents $\sim$75% of the density spatial variation. Most of Greenland and the Queen Elizabeth Island have the highest uncertainty and oceanic regions and northeastern Canada have the lowest, representing the composition and thermal variability.

At 250 km depth, the pattern of density variations changes dramatically with areas showing relatively high density at shallower depths (northwestern and central-southern Greenland and west of Baffin Island) now showing relatively low values. This pattern contrasts with the temperature structure at this depth. In eastern and southwestern Greenland, temperature and density variations show poor correlation (more details in Sec. 3.4.1). The uncertainty maps in Fig. A3.5 represent an inverse relationship between density magnitude and uncertainty, in which the lowest density has the highest uncertainty and vice versa, except for western Baffin Island. The uncertainty is significant at ∼90% of the density spatial variation. At 350 km depth, the lateral density variations decrease, with only some relatively small and localized variations. At this depth slice, the lowest density is located in the central southwest and highest in southern Baffin Island. Density and temperature at this depth correlate strongly except for the central southwest, northwest, and eastern Greenland. The corresponding uncertainty at this depth (Fig. A3.5) is ∼75% of the density variation, and it is highest in western Baffin Island, northwestern, and central south Greenland.

Seismic wave velocities (Vp and Vs; Fig. 3.10, third and fourth columns) present very similar patterns with high velocities in continental areas, specifically northern, central southern Greenland, and northeastern Canada, and low velocities in oceanic areas, specifically in the Atlantic Ocean and the Labrador Sea. Low seismic velocities in eastern Greenland are persistent across all depths, similar to the temperature results. At 50 km depth, Vp varies from 7.8 km/s in offshore eastern Greenland to 8.2 km/s in northwestern, and central southern Greenland and in northeastern Canada. At 150 km depth, Vp shows similar variations to those at 50 km in pattern and amplitude (from 7.8 to 8.4 km/s). At this depth, the high velocities in Greenland are more localized in northwestern and central-southern areas, while low velocities appear in central-eastern Greenland. Vp varies from 8.25 to 8.45 km/s with, again, a similar pattern at 250 km depth. At 350 km, the variation in Vp is small (∼100 m/s) across the whole region, with the lowest values of 8.56 km/s in eastern Greenland and the Labrador Sea and the highest values of 8.66 km/s in Baffin Island, southern and northern Greenland. Vs across all depth slices follows the same pattern as Vp. Vp and Vs correlate well with temperature structure across all the depth slices and with density to 150 km depth. Beyond 150 km, seismic velocity and density do not correlate, and so we infer that compositional effects become the primary control at these depths.

The seismic velocity uncertainties (Fig. A3.5) reflect different inversion qualities with depth. The geographic variation in uncertainty is similar for Vp and Vs, and has a similar pattern across all depths. The correlation between uncertainty and velocity changes with depth. At 50 km, high-velocity regions have the lowest uncertainty, and the slower regions have relatively high uncertainty (more details in Sec. 3.4.1). Also, the uncertainty accounts for ≤10% of the spatial variation in seismic wave velocity. At 150 km, the geographic pattern in velocity and the uncertainty are similar to those at 50 km except for Vp in northern Greenland and the Queen Elizabeth Island, which has high uncertainty despite the fast seismic velocities. At greater depths, the uncertainty variations increase due to lower data resolution and higher input uncertainty (i.e., PVDCs). At 250 km, high uncertainties are located in high-velocity regions except for western Baffin Island, where we see high velocities and low uncertainty; and in the Queen Elizabeth Island, where there is low Vs and high uncertainty. The uncertainties at this depth are a significant fraction of the lateral velocity variations: more than ∼50% for Vp and ∼20% for Vs. At 350 km, the correlation between uncertainty and seismic velocity is lower, and the geographic range in velocities is higher. The highest uncertainties exist in northeastern, and central south Greenland and in western Baffin Bay. Also, the lowest uncertainties are located in oceanic regions, the Queen Elizabeth Island, and Eastern Greenland. The uncertainties at this depth reach ∼90% of the velocity variations, and so the inferred velocity variations are poorly resolved.

3.4 Discussion

3.4.1 Thermochemical variations in lithospheric mantle

The lithospheric mantle temperatures illustrated in Fig. 3.10 show significant geographic and depth-dependent variations over Greenland and northeastern Canada. While these results are broadly compatible with those in previous studies (e.g., Lebedev et al., 2018; Mordret, 2018), there are some notable differences due to the improved spatial resolution (Lebedev et al., 2018) and coverage in northern Greenland (Mordret, 2018). Our model shows cold material in northwestern and central-south Greenland relative to other regions in Greenland, while Lebedev et al. (2018) suggest a broader cold region spanning much of northern Greenland. Another key difference is in central Greenland, where, our results show that the cold material in northwestern and central south Greenland are connected by a thin N-S, 'arm' of relatively cold material down to ∼250 km. Another notable feature in the temperature map is the relatively high temperatures in the southeast that extend into central Greenland - most apparent at depth slices 150 and 250 km. This feature has also been identified in previous studies (e.g., Mordret, 2018; Lebedev et al., 2018). The Lebedev et al. (2018) study place this temperature anomaly at a higher latitude with an E-W orientation compared to our results and those of Mordret (2018), in which the anomaly is further south in eastern Greenland (south of Scoresby Sund), with a more SE-NW orientation that extends only to central Greenland.

Density heterogeneity in the shallow upper mantle is produced by both temperature and compositional variations (Fig. 3.10 and Fig. A3.7). As expected, the thermal signature in the cratonic regions is of high density due to decreased temperatures, while the compositional signature is of low density due to the depletion of basaltic components. However, the compositional effects in the cratonic regions produce far lower amplitude density variations in the cratons overall relative to the purely thermally-induced density field, as evident in the strong negative correlation between temperature and density at depths shallower than 250 km (Fig. 3.10). However, the influence of density variations appears to dominate at depths ≥250 km, where temperature and density directly correlate, and relatively cold cratonic regions in northwestern and central south Greenland, and northeastern Canada reflect lower density material. The density is high in areas with high temperatures, such as eastern and southern Greenland, David Strait, and the Labrador

Sea. The density variations at these depths must, therefore, reflect compositional changes. This is supported by the pattern visible in bulk composition variations shown in Fig. A3.7 at depths $\geq$250 km. In northwestern and central south Greenland, and northeastern Canada, garnet and cpx concentrations are relatively low, and olivine and opx are relatively high.

Compositional density anomalies related to the spatial variation in major-element composition (or Mg#) are small relative to thermally driven density variations throughout most of the non-cratonic mantle (Simmons et al., 2010; Shulgin and Artemieva, 2019) and account for $<$2%–3% variations in seismic velocity (Schutt and Lesher, 2010). Therefore, the model results at depths $\leq$150 km in eastern and southern Greenland, Labrador Sea, and Queen Elizabeth Island support earlier conclusions (e.g., Lebedev et al. (2018); Schaeffer and Lebedev (2013); Schaeffer et al. (2016)) that the density variations caused by composition are of second-order compared to the thermal contribution.Based on Fig. A3.7, in regions such as central, eastern, and northeastern Greenland at depths $\geq$250 km, the amount of olivine and opx has decreased, and the proportion of garnet and cpx has increased compared to shallower depths. This change in mineral concentrations at these depths can explain the change in the relation between density and temperature, with composition becoming a more dominant control on density. This change in mineral concentrations is most likely related to changes in environmental conditions, such as temperature and pressure, which favor one mineral distribution over another.

The inverse relationship between temperature and density is most visible in the shallow upper mantle around 50-150 km (Fig. 3.10). Because of the temperature dependence of seismic attenuation, the thermal variations have a higher impact on velocities in seismically fast (cold) regions than in slow (hot) regions (Simmons et al., 2010). Based on the results in Fig. 3.10, the seismic velocities in the lithosphere correlate directly to LAB depth variations (temperature change). Basically, areas with lower temperature have higher lithosphere average velocities. Based on Fig. 3.10, at depths $\geq$250 km, temperature inversely correlates with seismic velocity, in contrast to being directly correlated with density.

To investigate the relationships between the Earth properties in Fig.3.10 in more detail and determine if the captured variations are robust, three cross-sections along profiles with high variability in temperature, density, and Vs were made (Fig. 3.10 (top left frame) shows the profiles and cross-sections are in Fig. 3.11). Profiles A-B and A-E go through at least one of the cold anomalies in northwestern and central south Greenland, which, by definition, correspond to the locations of the deepest LAB (Fig. 3.11). These cross sections (Fig. 3.11-top and bottom rows) also capture higher velocities in deep cratonic regions and the direct inverse correlation between temperature and seismic velocity. Based on Fig. 3.11 (second column), at shallower depths, the density increases with deeper LAB (i.e., temperature and density are inversely correlated). For example, along A-B at depth 150 km, density goes from light red to dark red when the LAB gets deeper (lower temperature) and close to location B where the LAB is thinnest (higher tempera-

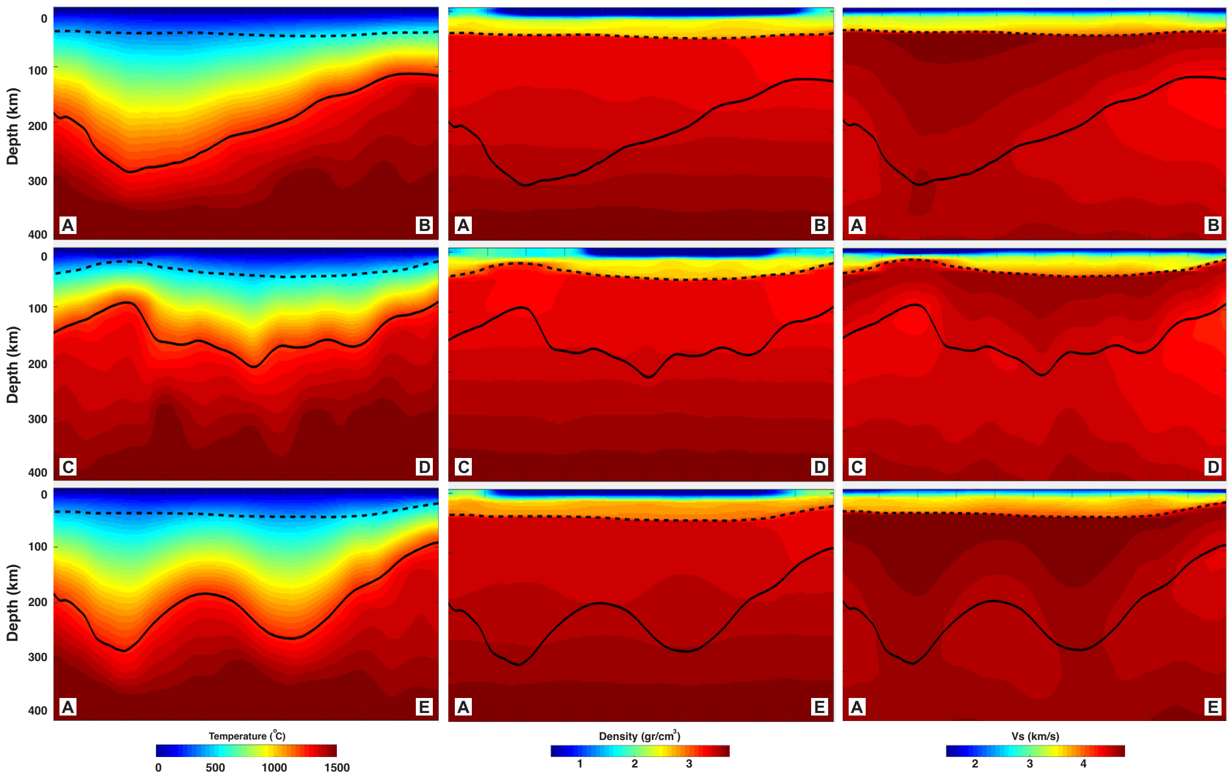

Figure 3.11: Vertical cross-sections showing temperature (left column), density (middle column), and Vs (right column) along profiles A-B (top row), C-D (middle row), A-E (bottom row) shown in Fig. 3.10 (top left frame). Solid and dashed black lines represent the LAB and Moho, respectively.

ture), density is lowest. This pattern is reversed at depth ∼300 km where deeper LAB correlates with lower density. This can be observed in profiles A-B and A-E where cross-sections sample regions with the the deepest LAB. It is noticeable that in areas with a deep LAB, the temperature gradient is greater below the LAB compared to locations with a thinner LAB, while the density gradient does not vary between regions with contrasting LAB depth. The gradient difference and lateral variations in temperature and density below the LAB reflects the contribution of the composition effect discussed above.

Vertical stratification of the Mg# is limited in the lithosphere and asthenosphere due to the model parameterization and the input petrological data, thus making a robust interpretation difficult (Griffin et al., 2004; O'Reilly and Griffin, 2006). Therefore, we investigate the lateral compositional heterogeneity in terms of the depth-averaged Mg# in the entire lithospheric mantle (Fig. 3.9-C). We infer a highly depleted mantle with large values of Mg# (90.5-91) in much of Greenland with values exceeding 91 in the southeast. Southern Baffin Islands are also characterized by a relatively high Mg#. Previous studies have reported high Mg# for Archean cratonic lithospheric mantle (Griffin et al., 2004; O'Reilly and Griffin, 2006). We note that the inferred Mg# values for depleted regions are lower than commonly reported, and this is most likely a result of the model parameterization and inversion method (e.g., Afonso et al., 2019, 2013a,b; Yang et al., 2021). The Mg# uncertainties are highest in central and southern Greenland and the Queen Elizabeth Island (Fig. 3.9-D). The amplitude of these uncertainties can reach ∼50% of the spatial variations (Fig. 3.9-C) and so are important to consider when interpreting the results.

Given that the majority of Greenland and eastern Canada have Mg# values in the range 90-91, it follows that these areas are believed to be relatively unaffected by large-scale magmatic events. On the other hand, we infer fertile mantle with Mg# values ∼89 in oceanic areas, with some of the most fertile mantle in localised areas of eastern and western Greenland, and in Baffin Bay. These areas coincide with the locations of basaltic lavas (Tegner et al., 2011; Larsen and Pedersen, 2009) and relatively thin lithosphere, which supports the hypothesis of active volcanism and lithosphere thinning producing relatively small Mg numbers.

3.4.2 Comparison of lithosphere thickness estimates

In the comparisons provided below, it is important to be aware that lithospheric thickness estimates based on these different methods are not comparable in the absolute sense as they provide different measures of this quantity (Eaton et al., 2009). However, the geographic pattern of thickness variation between the different estimates should be broadly comparable.

The LAB depth results from Steinberger et al. (2019), illustrated in Fig. 3.12-B are based on the Arctic tomography model AMISvArc (Lebedeva-Ivanova et al., 2019). In this LAB model, thick (>250 km) regions exist in northeast, northwest, and central southern Greenland, as well as northeastern Canada. The thinnest lithosphere (∼40 km) exists in central eastern Greenland, Baffin Bay, and the Labrador Sea. The LAB depth inference from Artemieva (2019) (Fig. 3.12-C) is based on the thermal isostasy method using seismic, heat flow, and gravity data sets (Model 1 out of two proposed models is shown here). In this model, a thick lithosphere (∼250 km) is evident in south and southwest Greenland and a zone of thin lithosphere (∼50-100 km) is evident near Scoresby Sund in east Greenland that extends to the northwest of Greenland. A regional study using gravity and (rock-equivalent) topography (Steffen et al., 2018) estimated elastic thickness in the Greenland region (Fig. 3.12-D), finding relatively large values of up to ∼90 km under northwestern Greenland, and low values (20-30 km) for southeastern Greenland and Baffin Bay.

All four models depicted in Fig. 3.12 show significant differences in the spatial pattern of lithosphere thickness variations. This reflects the different methods and data sets used in each case.

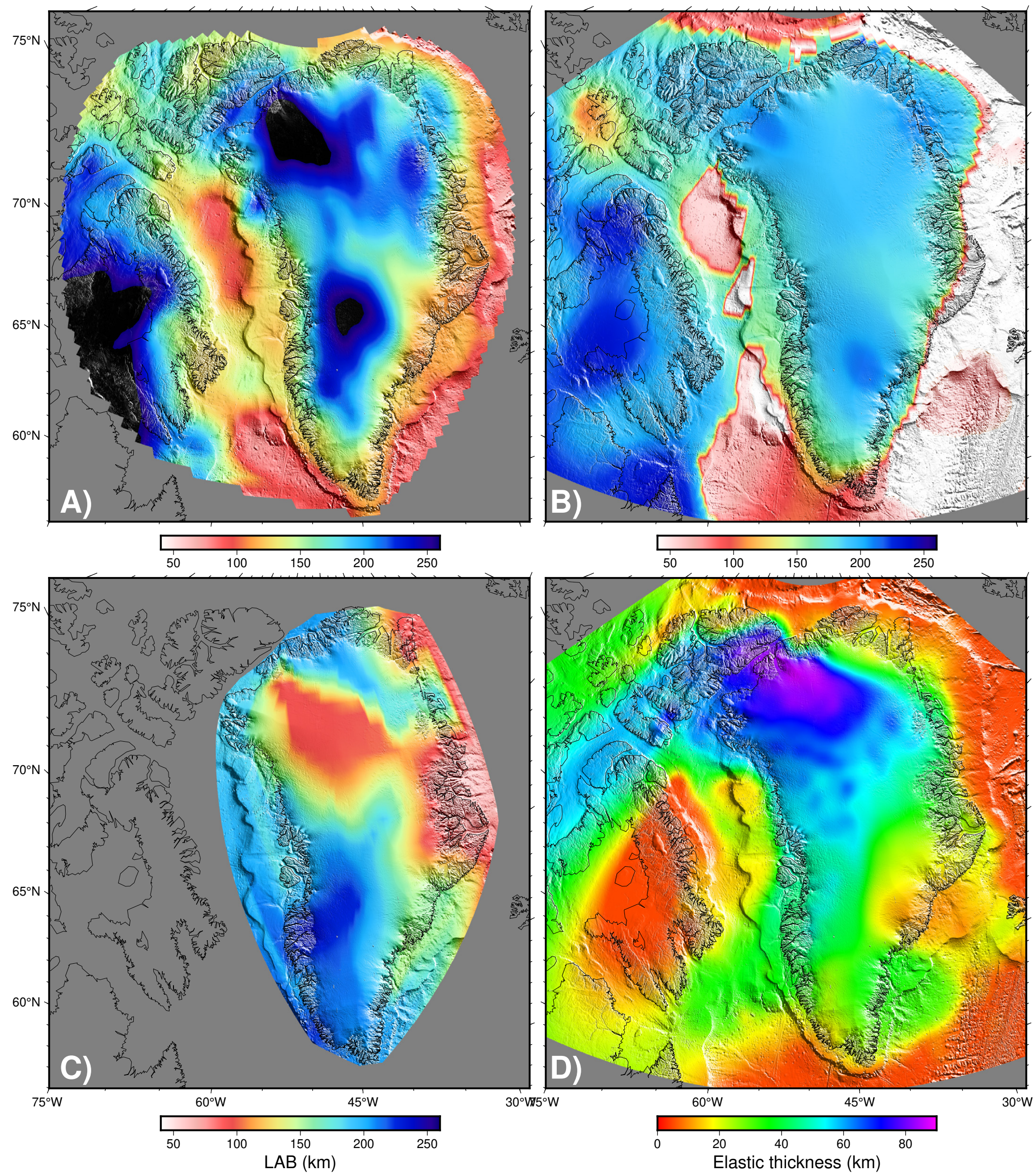

Figure 3.12: A) Mean value of the depth to the 1250 °C isotherm inferred in this study, and **B)** LAB depth from Steinberger et al. (2019) using AMISvArc seismic data from Lebedev et al. (2018), **C)** LAB depth (first model) from Artemieva (2019), and **D)** elastic thickness from Steffen et al. (2018). It should be noted that the color bar scales for depth to the LAB and elastic thickness are different since the absolute values are not compatible and variations are more of interest.

While there are some broad similarities - relatively thick lithosphere in the north and thin lithosphere in the central east - the differences are considerable. Compared to Steinberger et al. (2019), our results don't show a well-defined region of thicker lithosphere in northeastern Greenland, and the region of thinner LAB values in central eastern Greenland shows a much smoother gradient (moving westwards from the coast). Our model shows much greater variation in LAB-depth across most of Greenland compared to the model of Steinberger et al. (2019). Comparing our model to that of Artemieva (2019), the main differences are that the region of thicker lithosphere in southern Greenland in our model does not extend to coastal areas and that we do not infer a region of relatively thin lithosphere in northwestern Greenland (our model indicates a relatively thick lithosphere in this area). Furthermore, the location of the thinner lithosphere in eastern central Greenland is located further to the north in Artemieva (2019). In Steffen et al. (2018), the estimated elastic thickness is approximately uniform in central south Greenland, while our results suggest more variation. The spatial pattern of our result is consistent with the model of Steffen et al. (2018) except for the well-defined region of the thicker lithosphere in central south Greenland in our model.

The general agreement of deep LAB in northwestern Greenland and shallow LAB in eastern Greenland indicates that these features are the most robust. As noted, there are significant differences in the spatial extent and location of these features. The existence of a deep lithospheric root in southern Greenland is evident in three of the four models (Fig. 3.12-A&C). However, the spatial extent and location of this feature is markedly different between these three models. The differences can be ascribed primarily to the limited sensitivity of the input data and the assigned approaches to determine lithosphere thickness. The majority of seismic velocity-based methods have shown limited sensitivity in thick lithosphere environments (Eaton et al., 2009). Regarding this approach, the vertical resolution of a shear wave velocity model derived from surface wave (Rayleigh wave) data is limited, with a vertical resolution typically in the range of 20–50 km for the upper mantle (e.g., Celli et al., 2021; Darbyshire et al., 2004, 2017), and significant uncertainties remain in the velocity-temperature conversion due to the neglect of factors such as composition, anelasticity, melt and the presence of other fluids (e.g., Darbyshire et al., 2004, 2017; Lebedev et al., 2018; Schaeffer and Lebedev, 2013).

3.4.3 Implications for constraining the Iceland hotspot track beneath Greenland

Here, we discuss some of our results and their implications for constraining the hotspot track in light of past work. Fig. 3.13 shows our estimates of LAB-depth (left) and lithospheric Mg# (right) with previously proposed hotspot tracks superimposed.

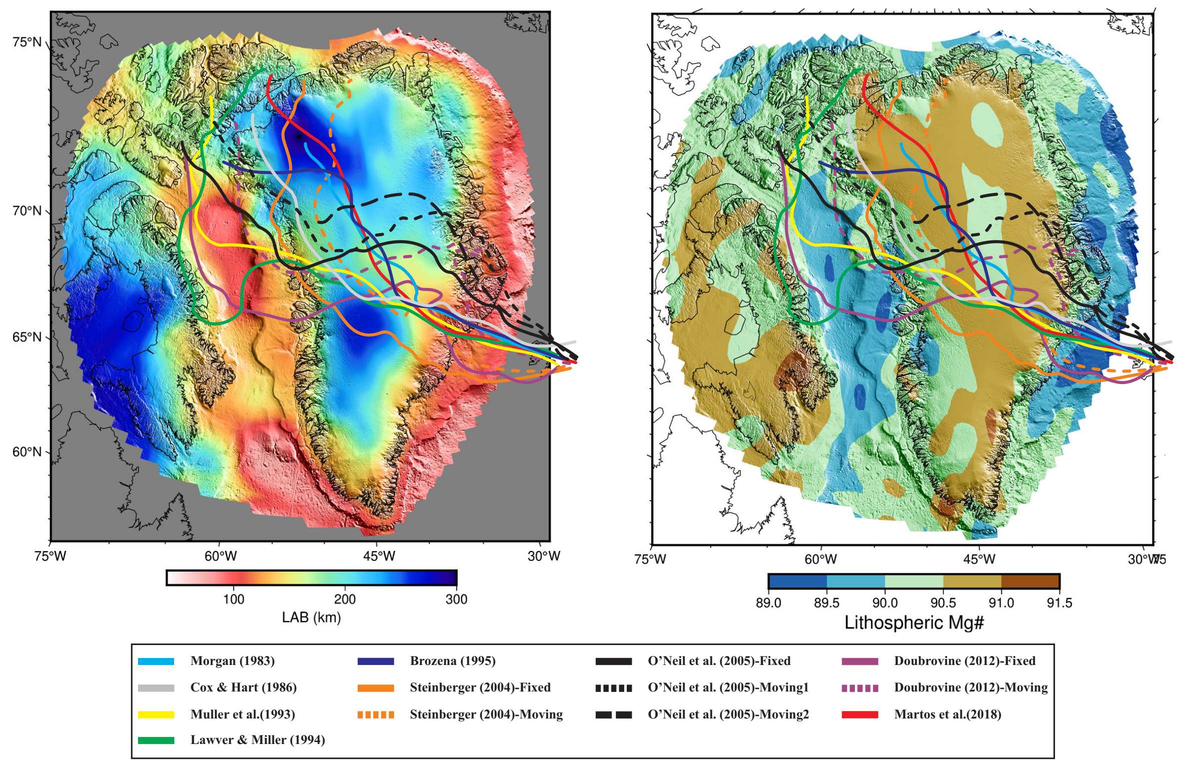

Figure 3.13: LAB depth (left) and Mg# (right) overlaid by reconstructed Iceland hotspot tracks from previous studies (see legend). Different colors represent results from various studies as indicated in the legend. The legend also indicates whether each reconstruction is based on assuming a fixed or moving hotspot.

The inferred LAB-depth variations in Greenland are expected to reflect thermal erosion (or thinning of the lithosphere) and significant underplating by dense mafic material - both a common consequence of plume passage (Steinberger et al., 2004). During the underplating process, the heat source from the plume would have moved the LAB isotherm to shallower depths and increased the concentration of radiogenic heat-producing material due to partial melting, which may have acted to prolong the heat flux along the plume track. These observations agree with Martos et al. (2018) in eastern and offshore northwestern Greenland, who infer a shallower Curie depth and elevated heat flux along the postulated plume track with a NW-SE orientation within Greenland. On the other hand, Rogozhina et al. (2016) infer a hotspot track from SHF analysis that is oriented more west to east, with an eastern location that is further north compared to the results of this analysis and those in Martos et al. (2018).

Although we used the surface heat flow data from Martos et al. (2018), which is reflected in our crustal RHP result, the LAB depth doesn't follow this pattern completely: it differs substantially in central to northwestern Greenland. Instead, it correlates more with previous studies (Doubrovine et al., 2012; Lawver and Muller, 1994; Muller et al., 1993; Mordret, 2018; ONeill et al., 2005; Rogozhina et al., 2016; Steinberger et al., 2019) that suggested a possible W-E Iceland plume track through Greenland after passing from Ellesmere Island and Baffin Bay. Also, as suggested by some previous studies (e.g., Doubrovine et al., 2012; Lawver and Muller, 1994; Muller et al., 1993; Steinberger et al., 2004), the Iceland plume may have been responsible for the opening of Baffin Bay and the associated magmatism in eastern and western Greenland, which is supported by a shallow LAB in these regions. The exposed volcanic rocks of the North Atlantic igneous Province (NAIP) in east and west Greenland, which is thought to extend beneath central Greenland (Dawes, 2009) follow the same W-E direction. This interpretation is also supported by the inferred change in mineral composition at 250 km depth and below (Fig. A3.7), where the proportion of garnet and cpx increases from west to east. The high Mg# values (90.5-91) in the interior of Greenland (Fig. 3.13-right), reflect the effect of a hotspot in depleting the mantle and altering the rocks during the underplating process. However, due to high uncertainty and the average Mg# estimation in lithosphere, the hotspot track is not clearly captured in the Mg# values.

Based on the above discussion, we conclude that, our results don't overlap with previous studies suggesting a NW-SE path (e.g., Martos et al., 2018; Steinberger et al., 2004; Jason Morgan, 1983; Cox and Hart, 1986), and we conclude that a W-E Iceland plume track over Greenland seems the most likely scenario based on current constraints.

3.5 Conclusion

We present state-of-the-art constraints on the thermochemical properties of the lithosphere and sublithospheric upper mantle beneath Greenland and surrounding regions. This study combined multiple geophysical data such as new high-resolution Rayleigh wave PVDCs, geoid height, surface heat flow, and absolute elevation data to constrain thermodynamic structure using a Bayesian joint inversion method. Our main results and their implications are summarized in the following.

- Our inference of thermal structure extends previous results in terms of the spatial resolution and geographic coverage and indicates large variations in LAB-depth across Greenland. In northwestern and southern Greenland, the LAB is located at depths ∼250-300 km correlating with cratonic regions. Whereas, in the east, the depth to the LAB is much shallower (∼100 km). Despite some agreement between our LAB depth estimation and previous studies (Steinberger et al., 2019; Steffen et al., 2017; Lebedev et al., 2018), significant differences exist in northwestern and southern Greenland, indicating the importance of considering a range of input data (e.g., seismic, geoid height, topography).

- Our LAB-depth inference supports the hypothesis of a major lithospheric erosion event caused by passage of the Iceland hotspot through Greenland's interior. Despite the effect of plume passage on RHP concentration and, therefore, SHF, we do not observe any correlation between SHF and LAB-depth in northwestern Greenland. The inferred thin lithosphere in the mid-section of Greenland is in agreement with reconstructions suggesting a possible W-E Iceland plume track beneath Greenland after passing beneath Ellesmere Island and Baffin Bay. The exposed volcanic rocks of the NAIP in east and west Greenland, which is inferred to extend beneath central Greenland, follow the same W-E path. This interpretation is also supported by the inferred change in mineral composition at 250 km depth and below.

- Thermochemical uncertainty estimation indicates that the quality of the inversion result is depth-dependent and spatially variable for each parameter. Inversion reliability is strongly dependent on the input data quality and the sensitivity of model output to the parameters being inverted. Our inference of physical structure (e.g., temperature, density) is more robust than that of chemical structure, partly due to the different quality in the input data sets. Furthermore, spatial resolution (depth and geographically) is strongly dependent on the adopted PVDC data set (e.g., constraints in the crust and below 300 km are relatively poor).

Our 3D temperature and compositional model offers implications for several geodynamic processes. Our results complement and expand past work that indicates large variations in the thermal structure of the Greenland lithosphere and shallow mantle. Comparing our results to previous studies emphasizes the importance of combining different data sets with complementary sensitivities to investigate thermochemical estimates of the lithosphere and upper mantle. Despite overall high-quality inversion results, there are several recommended paths to extend the work presented here. One that affects the geothermal reconstruction significantly is not considering the shallow local thermal processes such as volcanism and deep thermal processes such as heat transfer by advection. Ignoring these processes can advective heat transfer result in overestimation of other parameters such as crustal RHP (e.g., offshore southern Greenland) and lithospheric geotherms (e.g., offshore eastern Greenland in the proximity of Iceland). In terms of new data constraints, adding different forms of seismic data such as Vp, Vs, and receiver functions will strengthen the inversion quality. The addition of new (e.g., magnetorelluric Bedrosian, 2007; Takam Takougang et al., 2015) and improved data sets (e.g., petrological) will enhance resolution and enable more robust interpretation, allowing the community to move towards a more highly resolved and accurate lithosphere model for the Greenland region.

3.6 Appendix A3

This supplementary material presents additional information to support the primary text.

- Text and Fig. A3.1. Rayleigh wave PVDC data-model difference
- Text and Fig. A3.2. 1D inversion results in southern-offshore Greenland
- Text and Fig. A3.3. 1D inversion results in western-offshore Greenland
- Text and Fig. A3.4. Inversion results for crustal properties
- Text and Fig. A3.5. Uncertainties for various shallow mantle properties at different depths
- Text and Fig. A3.6. Major element distributions
- Text and Fig. A3.7. Mantle minerals distributions
- Text and Fig. A3.8. Input data-model and the differences.

Text A3.1. The input seismic wave dataset (Rayleigh wave PVDC here) and corresponding model calculated values may differ in some locations. For example, Fig. A3.1 illustrates the differences between input and inverted Rayleigh wave PVDCs for various periods. Although the spatial variation at each period is about $\sim$10 m/s, variability is different between periods. Based on this figure, the model velocities are generally faster for short periods and slower for longer periods. Note that, the mean value of the PDFs was used to generate these differences and so model uncertainty might be larger than some of the differences shown.

Text A3.2. Inverted thermochemical parameters for the example high total misfit location in southern-offshore Greenland (located in Fig. 3.5). At this location, the acceptance ratio of the simulation is 36% and, like results at the example ice covered location (Fig. 3.7), based on the distributions of the parameters, the inversion quality differs with depth for each quantity. In general, the quality of the inversion results is high, as the uncertainties are less than 10% of the estimated mean predicted value for most of the thermo-chemical parameters. We note that the uncertainties for some properties, such as temperature and seismic velocity, are lower than those determined for the example ice-covered location. The mineral volumes follow the same pattern as for the ice-covered location. Olivine is the dominant mineral and garnet volume increases with depth and becomes the second dominant mineral.

Text A3.3. As a final example, we also investigated a location of relatively high total misfit at a continental location. Based on the 1D inversion results shown in Fig. A3.3, the quality of the inversion is high as the uncertainties are less than 10% with 32% acceptance ratio for the simulations. For the ocean location example (Fig. and text A3.2), the inversion quality is higher compared to the ice-covered location due to lower uncertainties. In contrast to the ice-covered and oceanic regions, olivine in the continent increases with depth and becomes more than 60% of the mantle below the LAB.

Text A3.4. The crustal analysis is not of interest to this study as the main aim is to infer Earth structure in the upper mantle. However, crustal parameter settings are important as they can influence the inferred mantle parameters. For example, there are important boundary conditions like SHF and Moho depth that are key to the inversion problem. Since the input datasets are generally less sensitive to crustal properties, the inversion quality for crustal parameters is is poorer compared to that for mantle properties, and crustal properties often have uniform posterior distributions. Crustal inversion properties are divided into three different layers in Fig. A3.4. The first layer generally considers what is above the Earth's surface, such as ice in Greenland and sediment in continent and ocean regions. Based on panels in the first row (Fig. A3.4), the thickest first crustal layer is located in Baffin Bay, Queen Elizabeth Island, and northeast Greenland, corresponding to substantial sediment packages. The density in sediment-covered regions is fairly constant and is higher than ice-covered regions. Also, the seismic velocity in sediment-covered regions is higher than ice-covered regions, where the sediment thickness is large. The thickness in the second layer varies from $\sim$15 km in continents to $\sim$5 km in oceans. The density variation is low except for a few areas in the NW, western, and southeastern Greenland. The seismic velocities are low in a few areas like NW Greenland and ocean areas and are high in some locations such as the Queen Elizabeth Island, southern Baffin Island, and a few areas in Greenland. In the third crustal layer (Fig. A3.4-third row), continental regions are thicker than the oceanic plate with the thickest parts in southern Greenland and northern Baffin Island and thinnest parts in Baffin Bay and oceanic regions. Density is higher in northern Baffin Island, the Queen Elizabeth Island, Baffin Bay, and the Labrador Sea, and there are a few low-density zones in eastern and northeastern-offshore Greenland. The seismic velocity variations are high in northern Baffin Bay, Queen Elizabeth Island, and southern Greenland. As mentioned above, since the distribution of crustal properties is close to a uniform distribution, the mean of PDF (shown here) may not be accurate.

Text A3.5. Uncertainty in our inference of mantle properties enables us to interpret the inversion quality and determine how well spatial variations are captured in these properties. Although the absolute uncertainty magnitudes are generally small, they can be significant compared to the captured spatial variations in inverted properties. The inversion uncertainties vary spatially and with depth. Also, the magnitude and variations differ for each property, reflecting the model sensitivity to various input geophysical data sets. The main text thoroughly discusses the effect of uncertainties on inverted properties.

Text A3.6. The distributions of major elements in the mantle vary with geographical location and depth. The four most common elements in the mantle are shown in Fig. A3.6. MgO is the most abundant element compared to others and, in the lithosphere, it is dominant in continental regions such as Greenland and the Baffin Islands. In the asthenosphere, this element is depleted in the continent and is found more in oceanic regions like Baffin Bay, Labrador Sea, and eastern-offshore Greenland. The second abundant element is FeO which is dominant in oceanic lithosphere such as Baffin Bay, and continental asthenosphere like northeastern Canada. Surprisingly, Greenland doesn't exhibit the same pattern, and the FeO volume decreases with depth. Based on the last two columns of Fig. A3.6, Al_2O_3 and CaO correlate laterally and with depth. Both of these elements are at their highest in the oceanic lithosphere such as Baffin Bay and eastern-offshore Greenland and continental asthenosphere such as Greenland. Al_2O_3 and CaO increase with depth mostly in eastern Greenland. Based on Fig. A3.6, MgO inversely correlates with other elements except for FeO in the Greenland asthenosphere. It should be noted that the geographic and depth variations of FeO, Al_2O_3, and CaO are insignificant and these estimations are not constrained well.

Text A3.7. Mineral distributions vary significantly with depth and location. Olivine is the most abundant mineral in the mantle with a volume of $\sim$60%-65%. At different depths, olivine is dominant mostly in oceanic regions (and southern Baffin Island) at depths of 50 km. It is more abundant in continents such as Greenland and northeastern Canada at depths $\sim$50-250 km. Garnet is the second dominant mineral in the mantle with a volume of $\sim$20-25%. This mineral is dominant in oceanic regions at shallower depths ($\sim$100 km) and in continents at, generally, greater depths ($\geq$50 km; except for two thick cratonic regions in northwestern and central south Greenland). Based on the last two columns in Fig. A3.7, opx correlates directly with olivine variations, whereas cpx directly correlates with garnet variations. The connection between mineral distributions and thermal structure is discussed in the main text.

Text A3.8. In Fig. A3.8, the data-model differences are illustrated over our entire study region. The differences for elevation and geoid height are less than 4%, but reach 40% for SHF in eastern Greenland close to Iceland and in the Davis Strait (the ocean area between Baffin Bay and western Greenland). It is worth noting that although the SHF differences over Greenland are small ($\leq$ 20%), they are larger elsewhere, particularly in marine areas, which could indicate large model structural error (not considering convective heat flow), or input data inaccuracy. As mentioned in Sec. 3.2.4, the input SHF values are a combination of two datasets: one of higher resolution with low uncertainty over Greenland (Martos et al., 2018), and the other a global data set with large uncertainties in other areas (Lucazeau, 2019). In the latter case, the larger input uncertainties result in a wider distribution of possible values in the inversion procedure, leading to an increase in the width of the posterior PDF (or a decrease in the precision of the inversion). However, it should be noted that the mean values of the posterior PDFs are considered for comparisons, and so the large differences do not necessarily imply lower accuracy. As long as the predicted data is in the range of input uncertainty, the predicted models are acceptable (accurate) (e.g., SHF for the ocean grid point (location 1 in Fig. 3.5-A) in Fig. 3.6). The seismic data-model differences are also negligible, as illustrated in Fig. A3.1.

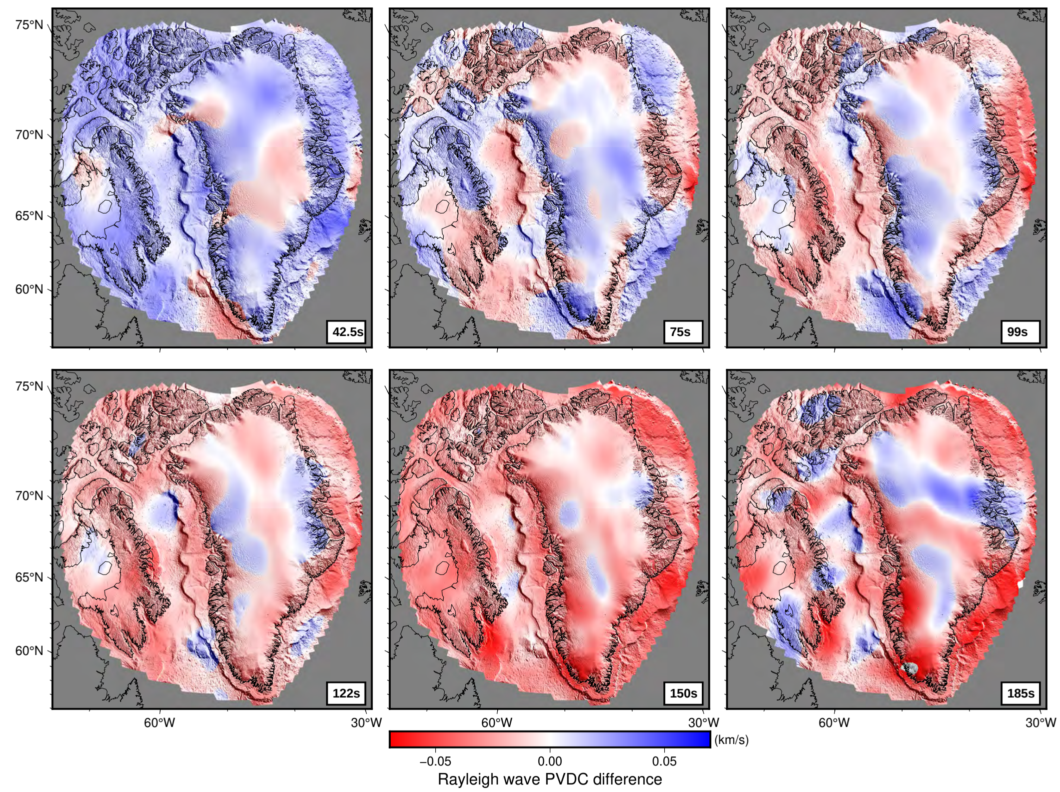

Figure A3.1: Difference between input and modelled (mean value of the posterior PDF) for Rayleigh wave phase velocity for short to long periods.

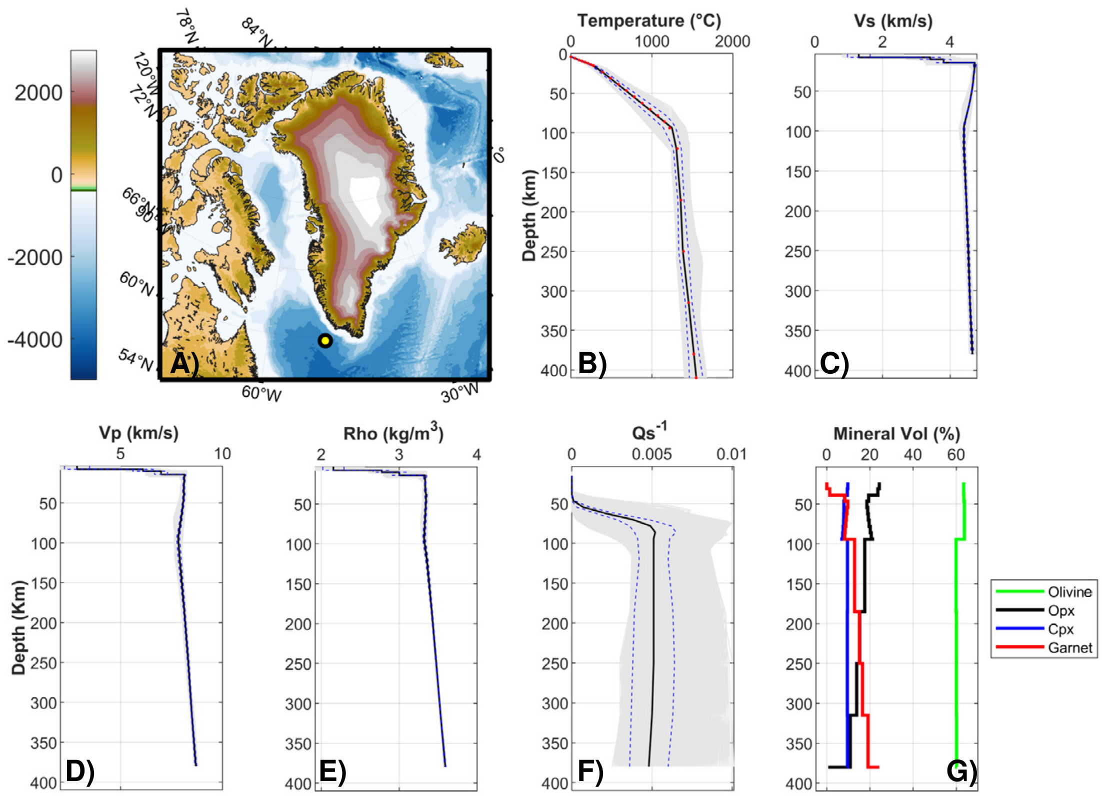

Figure A3.2: A) Location map of the grid point in southern-offshore Greenland with high total misfit (location labeled as '1' in Fig. 3.5). **B-F)** Posterior distributions of temperature, Vs, Vp, bulk density, attenuation. Gray lines denote the accepted models, black lines are the mean of the posterior distribution, and the dashed blue lines are the 1σ uncertainties. **G)** Inferred volume profiles of four dominant mantle minerals.

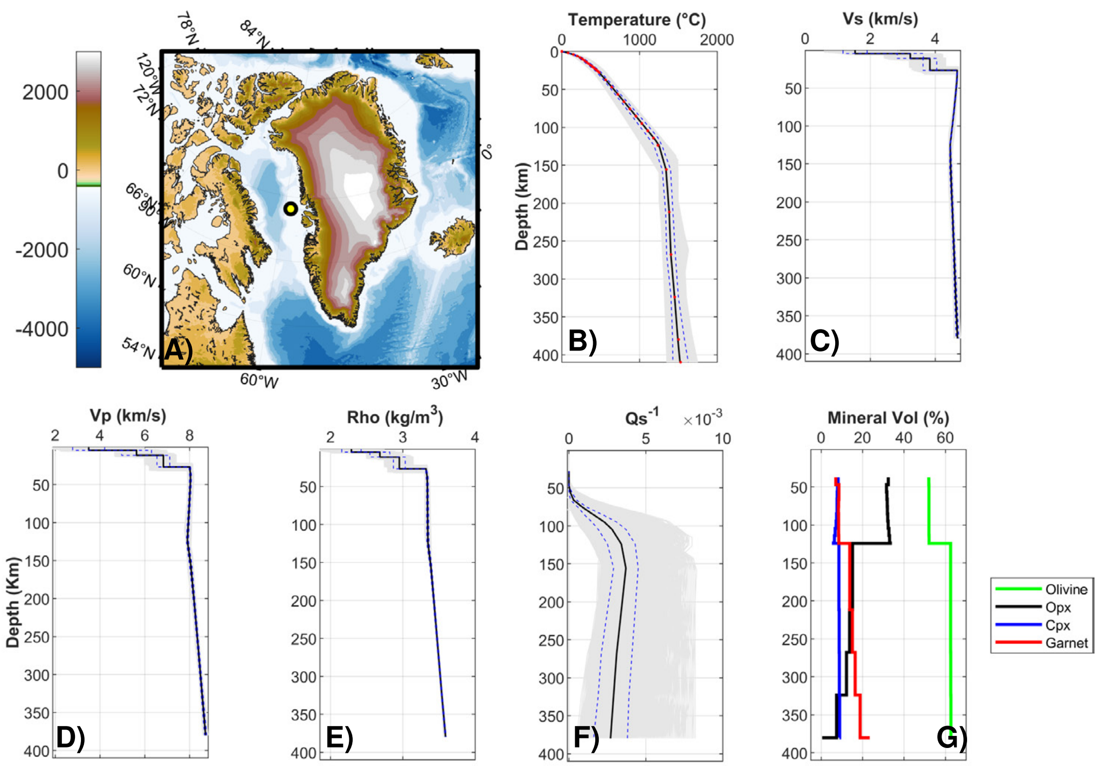

Figure A3.3: **A)** Location map of the grid point in western-offshore Greenland with high total misfit (location labeled as '2' in Fig. 3.5). **B-F)** Posterior distributions of temperature, Vs, Vp, bulk density, attenuation. Gray lines denote the accepted models, black lines are the mean of the posterior distribution, and the dashed blue lines are the 1σ uncertainties. **G)** Inferred volume profiles of four dominant mantle minerals.

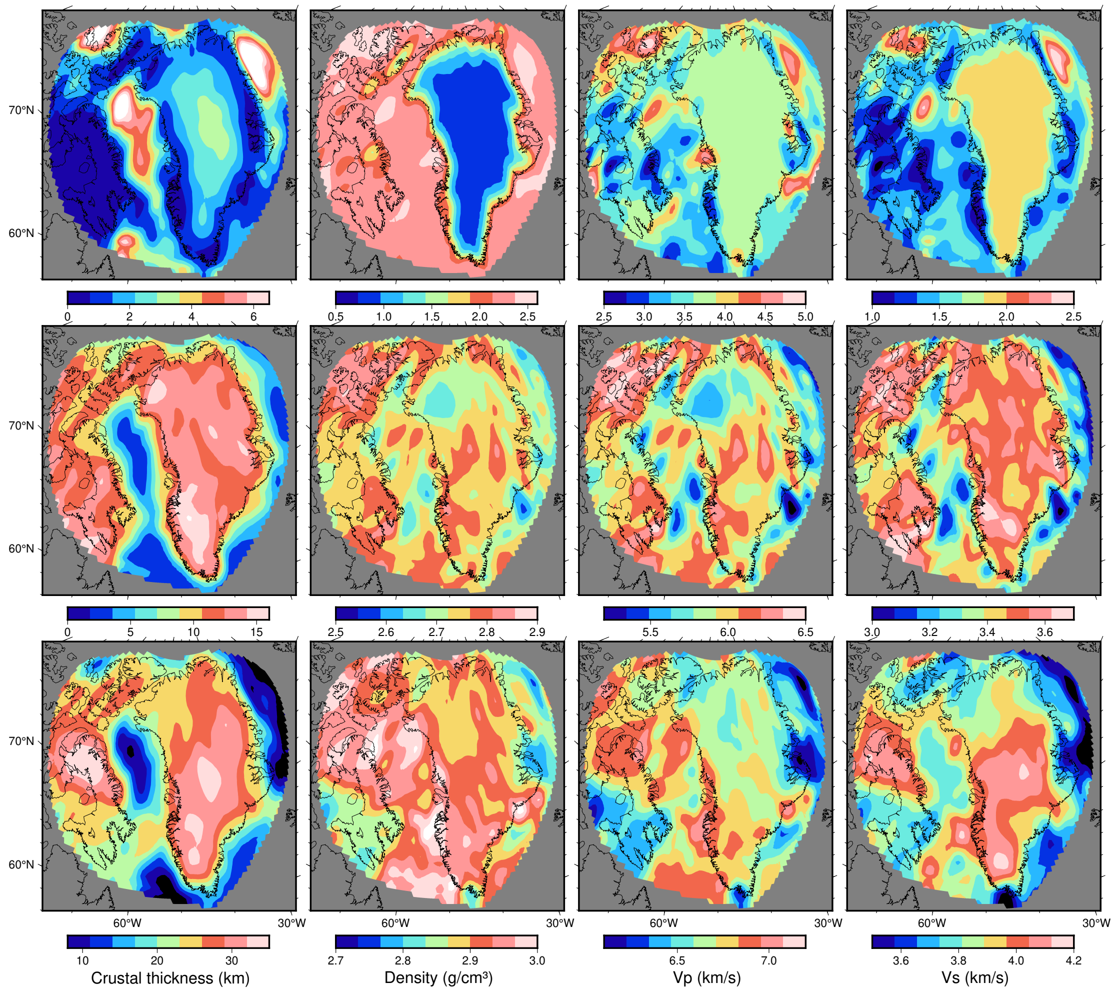

Figure A3.4: Crustal properties resulting from the inversion. Left to right: crustal thickness, density, Vp and Vs. Top to bottom: crustal layer 1, layer 2, and layer 3.

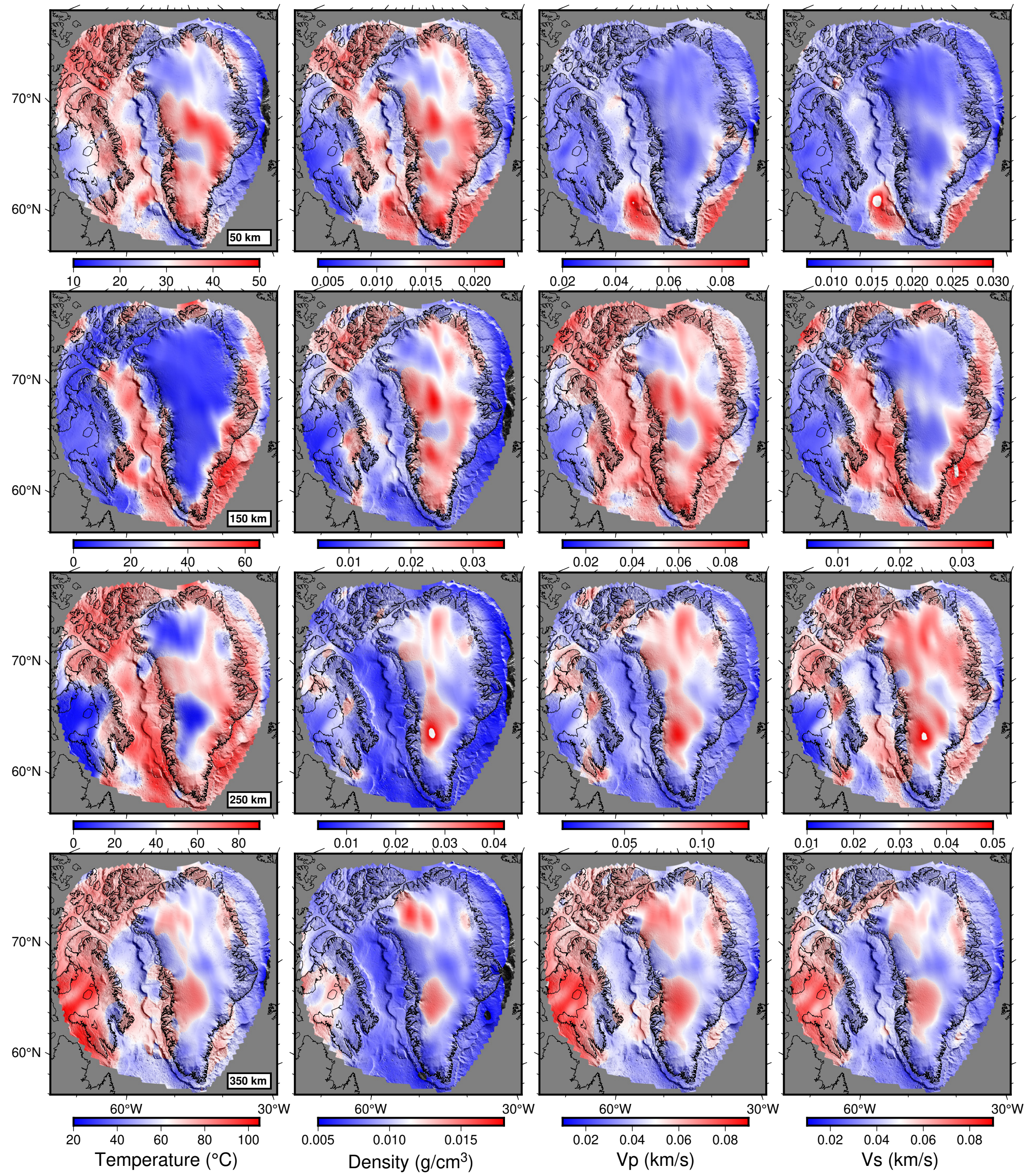

Figure A3.5: Uncertainties of shallow mantle properties at different depths. Left to right: temperature, density, Vp, and Vs. Top to bottom: depths of 50 km, 150 km, 250 km, and 350 km.

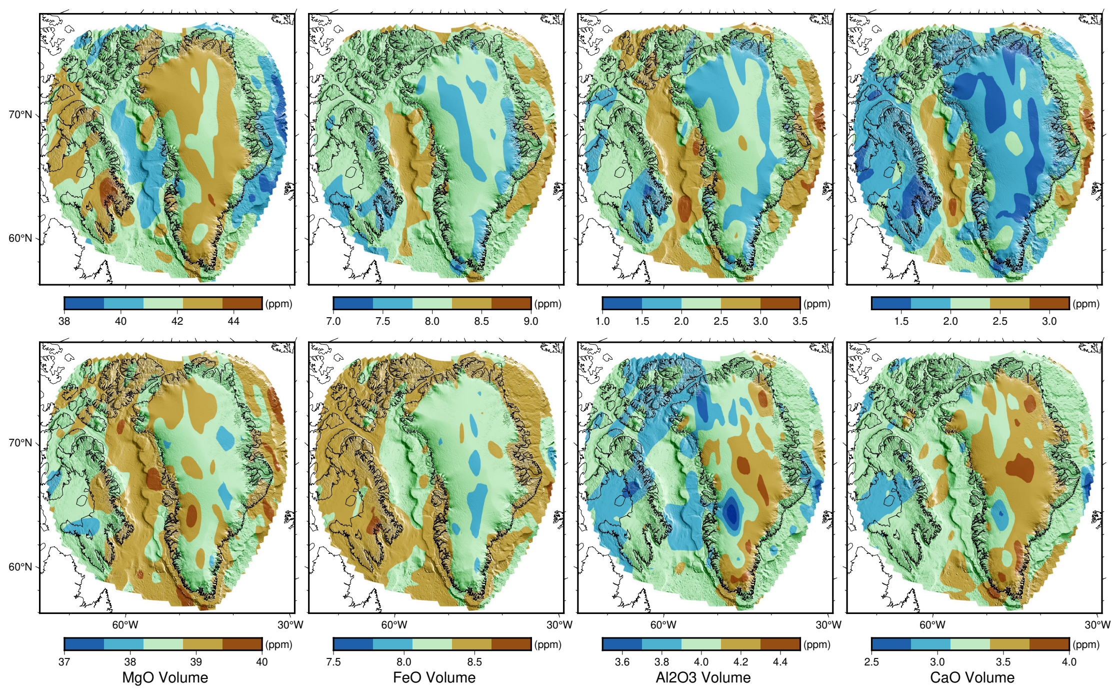

Figure A3.6: Depth-averaged major element spatial distributions in the lithosphere (first row) and asthenosphere (second row). From left to right: MgO, FeO, Al_2O_3, CaO.

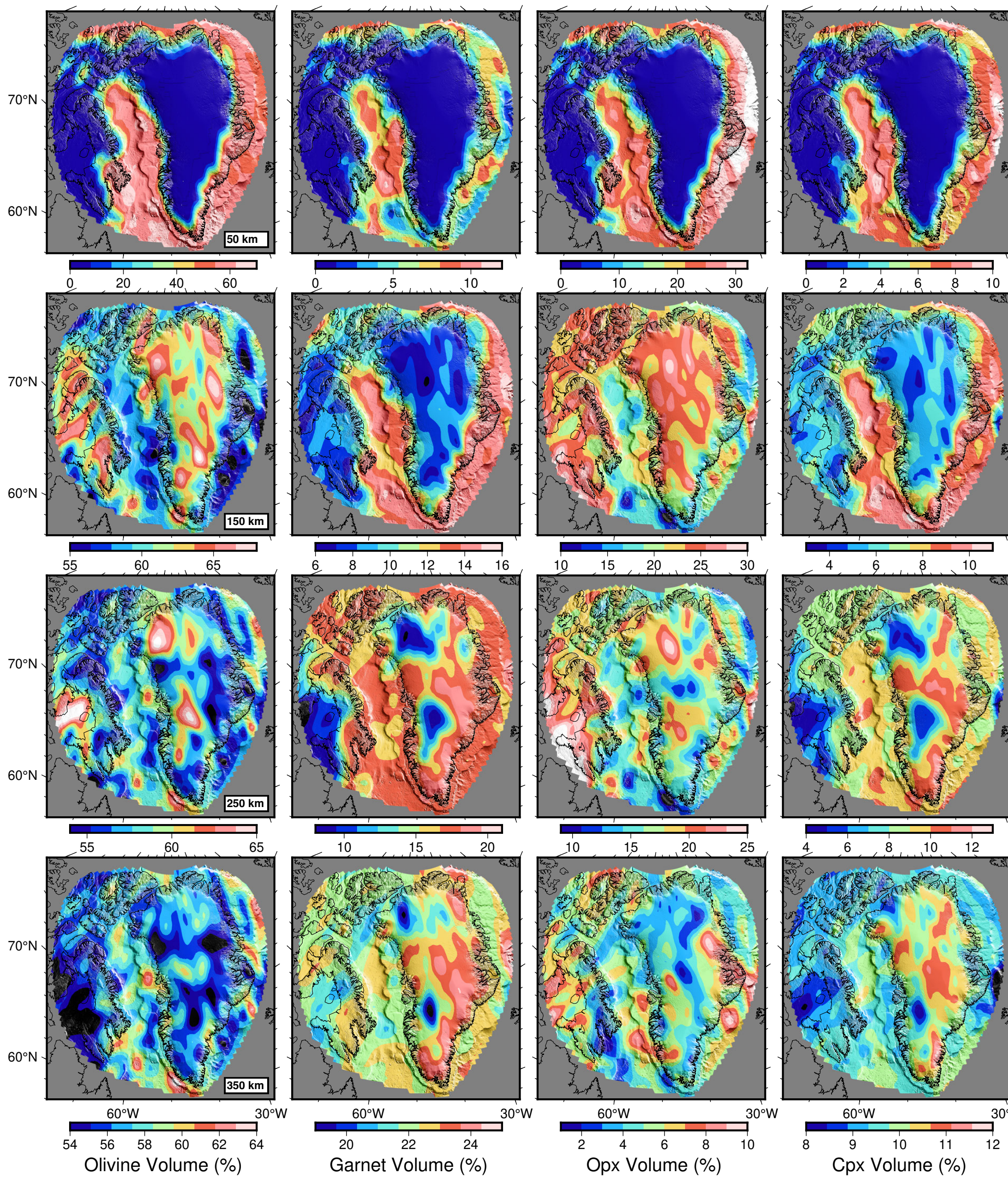

Figure A3.7: Distribution of mantle minerals at different depths. Left to right: Olivine, garnet, opx, and cpx. Top to bottom: depths of 50 km, 150 km, 250 km, and 350 km.

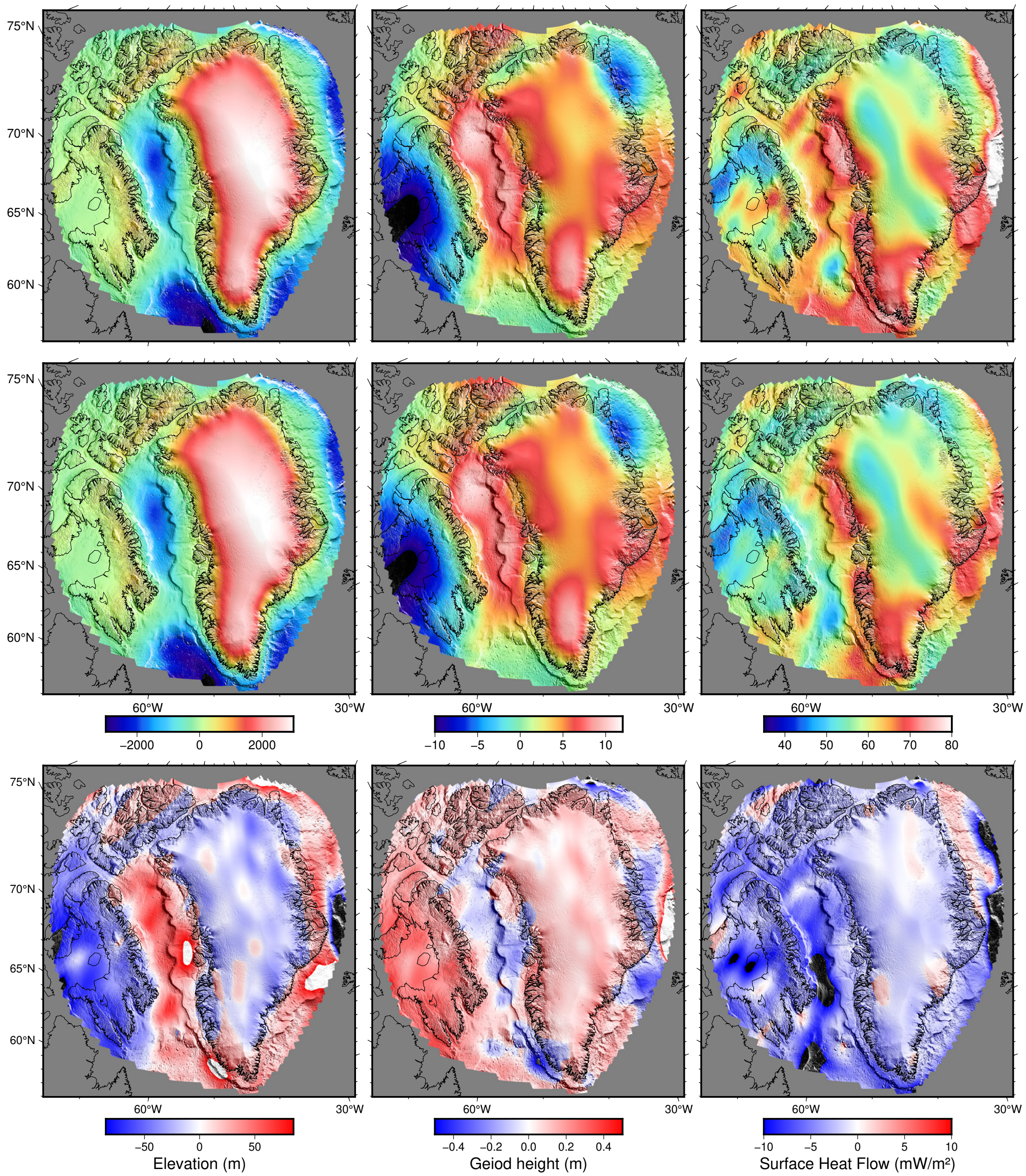

Figure A3.8: Observed (first row), modeled (mean value, second row), and the difference (modeled minus observed, third row) for (left to right): elevation, geoid height, and surface heat flow (SHF).

Chapter 4

The Influence of Lateral Earth Structure on Glacial Isostatic Adjustment in Greenland

4.1 Introduction

The evolution of the GrIS is influenced by solid Earth deformation, which depends on the rheological properties of the underlying crust and mantle. Quantifying bedrock deformation or the isostatic response is also necessary to interpret geological observations of relative sea-level change (Tarasov and Richard Peltier, 2002; Fleming and Lambeck, 2004; Lecavalier et al., 2014) and present-day vertical land motion (Dietrich et al., 2007; Khan et al., 2016; Berg et al., 2024) for understanding ice balance changes and Earth rheology (viscosity) structure. A common assumption in most of these studies is that a spherically-symmetric Earth model with radial variations in viscosity structure is sufficiently accurate for the Greenland region, which is dominated by low temperatures and thus relatively thick lithosphere and high viscosity mantle material. Recent work (noted in previous chapters) has challenged this assumption, particularly in regions influenced by the Iceland hotspot, which is supported by anomalously high VLM rates associated with past ice mass changes (Khan et al., 2016).

Lecavalier et al. (2014) considered a broad range of Earth model parameters and inferred a 120 km thick lithosphere, 5×10^{20} Pas upper mantle viscosity (UMV), and 2×10^{21} Pas lower mantle viscosity (LMV) in Greenland. This model provided a relatively accurate fit to paleo RSL dataset except for southern and northwestern Greenland, where the model underestimates RSL in the Early Holocene (in both regions). The RSL data-model misfits in northwestern Greenland were largely resolved by implementing an improved temperature forcing for this sector of the GrIS (Lecavalier et al., 2017). Although, the revised ice sheet model provides better fits to RSL data in this region, the lack of more precise RSL observations is a limiting factor in testing and improving GIA models for northwest Greenland. The RSL discrepancies in southern Greenland remain a challenge to explain (e.g., Milne et al., 2018). Steffen et al. (2020) proposed the glacially-triggered faulting hypothesis in which the oldest RSL data were moved upward due to the brittle failure of crustal rocks in the early Holocene.

In 2016, Khan et al. (2016) generated a new VLM dataset based on GNSS measurements. This database separated the VLM signal associated with contemporary ice thickness changes (during the GNSS monitoring period) to that due to ice sheet changes prior to this period (associated with GIA). Their investigation highlighted large VLM data-model misfits associated with GIA, especially in the southeast of Greenland. The GIA-related VLM rates show large spatial variations with higher VLM rates compared to model rates. Milne et al. (2018) investigated the influence of lateral Earth structure on Greenland GIA. However, incorporating lateral variability in Earth structure did not significantly improve the VLM data-model fits. By incorporating recent ice sheet change associated with the Little Ice Age (LIA) and a low viscosity Earth model, Adhikari et al. (2021) succeeded in fitting the VLM data. However, the low viscosity values obtained are not supported by RSL data spanning millennial timescales (for which higher viscosity values are preferred). Therefore, a transient rheology hypothesis was introduced to explain the viscosity change through time (Adhikari et al., 2021), which is supported by seismic results and mineral physics considerations (Paxman et al., 2023). Pan et al. (2024) introduced an alternative explanation by considering a thin low viscosity layer at the base of the lithosphere. Introducing such a layer makes it possible to fit both the paleo RSL and VLM data sets. However, there has not been any independent evidence supporting a thin low viscosity layer in seismic tomography models (Ajourlou et al., 2023; Celli et al., 2021).

Since the rheological properties of the crust and mantle are strongly controlled by temperature (Ranalli, 1995; Karato et al., 2008), we utilize the thermal structure model for the Greenland lithosphere and upper mantle from Chapter 3 to develop an ensemble of 3-D viscosity structures. The impact of these structures on the interpretation of both RSL and VLM datasets is investigated with respect to the recent studies outlined above to determine if they have a significant influence on the GIA model fits to RSL and VLM data (Adhikari et al., 2021; Paxman et al., 2023; Pan et al., 2024). Furthermore, we investigate the impact of recent ice loading (e.g., LIA and peripheral glaciers) on the present VLM rates. Finally, we quantify the RSL and VLM rate uncertainties associated with lateral variations in Earth viscosity structure.

4.2 Data and Methodology

4.2.1 Paleo RSL and Contemporary VLM Data

Holocene RSL data points used in this project are taken from Lecavalier et al. (2014), but with some new data added (Sarah Woodroffe, personal communication). RSL height at a specific time is measured in different locations, and data are grouped into 60 sites (Fig. 4.1-A). These sites are mostly concentrated in western and eastern Greenland with two distinctive spatial gaps in northwestern and southeastern Greenland. The temporal and height distribution of RSL points is illustrated in Fig. 4.1-B and comprises 123 SLIPs, 741 marine limiting points, and 172 terrestrial limiting points (see Section 1.5.3), mainly spanning the Holocene ($\sim$10 kyr BP to present). Based on Fig. 4.1-B, the relative sea level in Greenland experienced a rapid fall following the onset of major regional deglaciation in the Early Holocene ($\sim$ 12 kyr BP). Most sea level changes occurred between the Early and Mid-Holocene ($\sim$10-4 kyr BP), and since then, the amplitude of RSL change has been relatively low. In the Early Holocene, SLIP heights vary by more than 100 m, demonstrating significant spatial variations in RSL around Greenland. RSL data points were pre-processed before being utilized in a data-model misfit analysis (Sec. 4.2.4).

The contemporary VLM data are calculated from Greenland's GNSS Network (GNET). As noted above, these VLM data include signals associated with surface loading on different timescales (e.g., deglacial, LIA, contemporary changes) within Greenland and further afield (Berg et al., 2024). The VLM rates are estimated at 58 GNET stations (Fig. 4.2) over a decade (2010-2022) to ensure the rates are not significantly affected by short timescale (interannual to annual) processes. The VLM rates are corrected for the present-day elastic solid Earth response (due to the contemporary ice loading change) to remove the non-GIA signal (more details in Berg et al. (2024)). Most VLM rates are around 0 to 4 mm/yr except for the high VLM rates in southeastern Greenland and low VLM rates in southwestern Greenland.

In this study, we did not consider RSL and VLM data from sites in northwestern Greenland (Figs. 4.1-A and 4.2) given that the adopted ice model (Huy3) is known to be inaccurate in this region (Lecavalier et al., 2017).

4.2.2 Generation of 3D viscosity models

To model RSL and VLM associated with GIA, a global model of Earth viscosity structure is required. We construct such a model by combining estimates of regional viscosity structure (using results from Chapter 3) with global models determined using seismic velocity models. Since

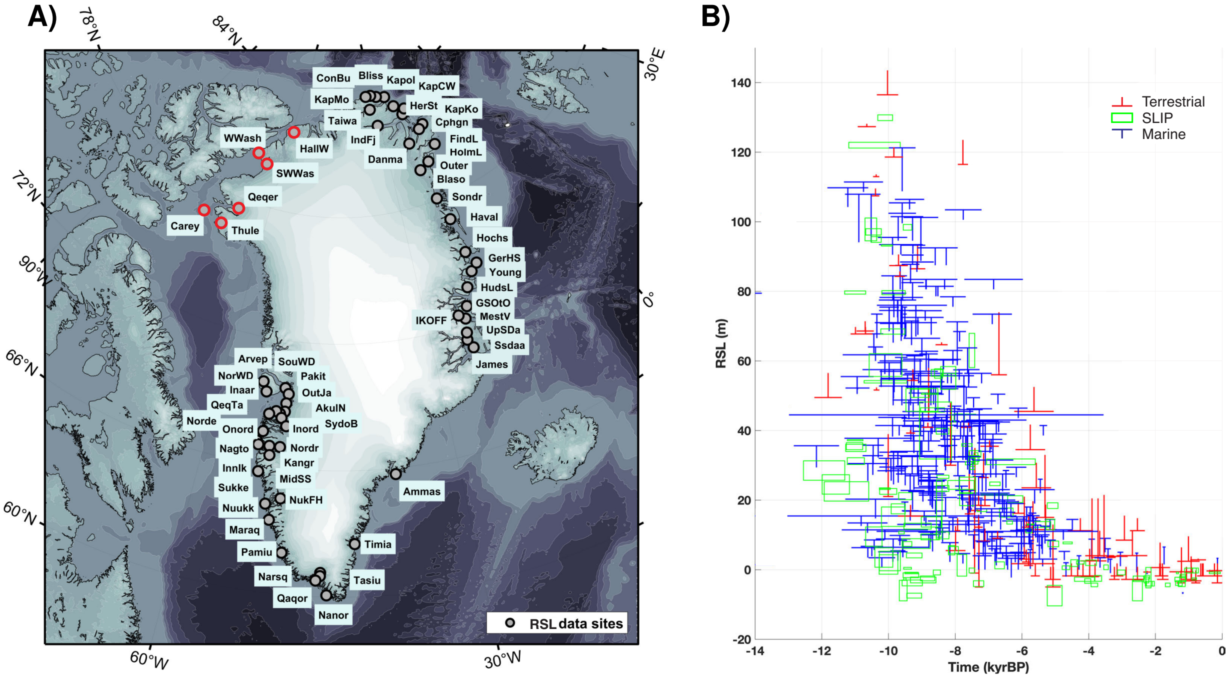

Figure 4.1: **A)** The spatial distribution of RSL data sites across Greenland (Table A4.1). Sites circled in red were not used in the data-model comparisons due to a known bias in the ice model in this region (Lecavalier et al., 2017). **B)** RSL reconstructions for all sites, including three types of RSL data (see key). The height and width of the RSL data points represents 1σ uncertainty in RSL height and time. Following convention, only half of the 1-sigma range is shown for limiting data points ('top' half for terrestrial and 'bottom' half for marine).

we are using the Seakon 3D GIA model in this analysis, we adopt the following relationships to calculate perturbations in viscosity structure from perturbations in shear wave velocity structure (Latychev et al., 2005):

$$\delta \ln \rho \, (r, \theta, \phi) = \frac{\partial \ln \rho}{\partial \ln V_s} \, (r) \, \delta \ln V_s \, (r, \theta, \phi), \tag{4.1a}$$

$$\delta T \, (r, \theta, \phi) = -\frac{1}{\alpha(r)} \, \delta \ln \rho \, (r, \theta, \phi), \tag{4.1b}$$

$$\delta \eta \, (r, \theta, \phi) = \exp \left(-\epsilon \, \delta T \, (r, \theta, \phi) \right), \tag{4.1c}$$

where V_s, ρ, and δT are the perturbations in shear wave velocity, density, and temperature, re-

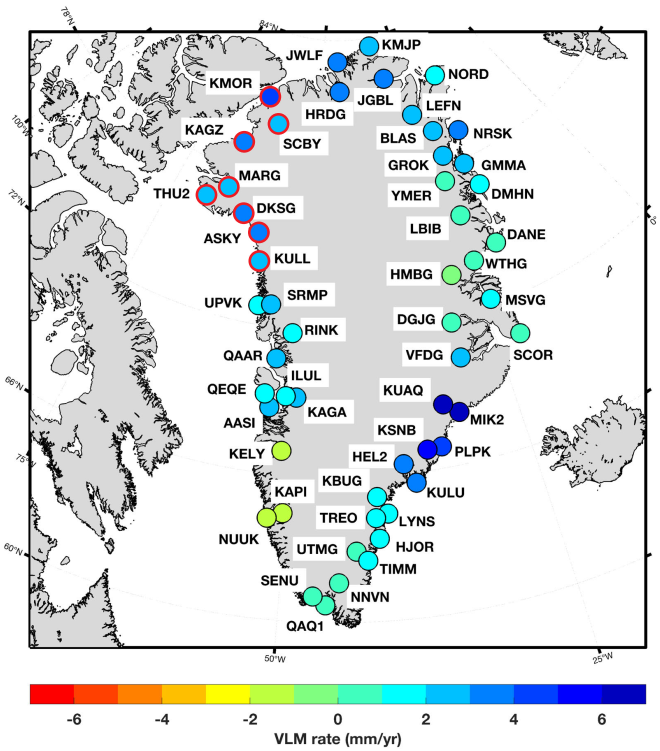

Figure 4.2: The 58 GNET stations used in this chapter. Colored circles show the VLM rates at each site. Sites circled in red were not used in the data-model comparisons due to a known bias in the ice model in this region (Lecavalier et al., 2017).

spectively. $\delta\eta$ ($= \eta/\eta_0$) is the relative viscosity, indicating the viscosity perturbation from the reference viscosity. $\frac{\partial \ln \rho}{\partial \ln V_s}$ and ϵ are scaling factors, α is the coefficient of thermal expansion, r, θ, and ϕ are the radius, colatitude, and east longitude. The coefficient of thermal expansion (α) is depth-dependent and is estimated based on laboratory experiments performed under high temperature and high pressure conditions (Chopelas and Boehler, 1992). The viscosity scaling factor (ϵ) determines the contribution of temperature perturbations to lateral viscosity variations. We adopt two values for ϵ (0.02 and 0.04 °C^{-1}) to crudely account for uncertainty in this value.

4.2.2.1 Regional Earth Model

Global seismic models and, therefore, global viscosity models determined from them have limited spatial resolution and so are unable to capture structures less than a few hundred km in spatial scale. To improve previous work that consider global models only (Milne et al., 2018), we develop regional models of 3D Earth structure using the temperature models determined in Chapter 3 (Fig. 3.10). Therefore, we skip Eq. 4.1a-b and scale the inferred temperature perturbations to viscosity perturbations (Eq. 4.1c). The regional viscosity model is on a 1°× 1°

grid, covers Greenland and northeastern Canada, and extends down to mid upper mantle depths (∼400 km).

LitMod temperature output is provided as a posterior PDF (Chapter 3). However, investigating the whole PDF is not practical due to the computational expense of 3D GIA modelling. Therefore, the mean value of the posterior PDF (based on the assumption of a Normal distribution) is used to estimate the mean lateral viscosity variations. Fig. 4.3 illustrates the viscosity models at different depths using two scaling factors ($\epsilon = 0.02\ ^{\circ}\mathrm{C}^{-1}$ and $\epsilon = 0.04\ ^{\circ}\mathrm{C}^{-1}$). The viscosity models in Fig. 4.3 illustrate large spatial variations within and peripheral to Greenland (∼6 orders in top left panel). The lowest viscosity values appear in oceanic regions (e.g., Baffin Bay, the Labrador Sea, and the Greenland Sea). Some continental regions also show relatively low viscosity values, notably eastern and southern Greenland. Whereas, the highest viscosity values exist in thick and cold cratonic regions (e.g., western Baffin Island and northwestern/centersouthern Greenland).

Similar to global viscosity models, global lithosphere thickness models are generated on a coarse grid with relatively low spatial resolution. Therefore, we use our results of depth to the LAB in Chapter 3 (Fig. 3.9) as the regional high-resolution lithospheric thickness (LT) model. The regional LT model in Chapter 3 is defined as the depth to the 1250 °C isotherm and reveals high lateral variations in Greenland. The highest variations of LT are captured in eastern, southern, and northwestern Greenland. Eastern Greenland has the lowest LT because of the proximity to the Iceland hotspot and the likely passage of this hotspot under eastern Greenland in the geologically recent past. High LT represents deep and cold cratonic features in central south and northwestern Greenland. As for the regional viscosity model, the regional LT model needs to be included within a global model to be implemented in the GIA modelling.

4.2.2.2 Global Viscosity Model

We applied the S40RTS (Ritsema et al., 2011) and SL2013 (Schaeffer and Lebedev, 2013) seismic tomography models to generate lateral viscosity perturbations. The global shear wave velocity perturbation in SL2013 extends to 1000 km depth, whereas S40RTS covers the whole mantle. We combine these two models such that SL2013 defines structure in the upper mantle and S40RTS the lower mantle. To avoid numerical artifacts, the velocity perturbations were linearly interpolated over a depth range of several hundred km in the shallow lower mantle. The scaling relationships defined in Eq. 4.1, were used to convert the resulting global shear wave perturbations to global viscosity models. As noted above, two epsilon values were used in the last step to convert temperature variations to viscosity variations. The final viscosity model is determined by patching the regional viscosity model into this global model (Fig. 4.4). We adopted an interpolation procedure to avoid edge effects where the two models are joined. An example

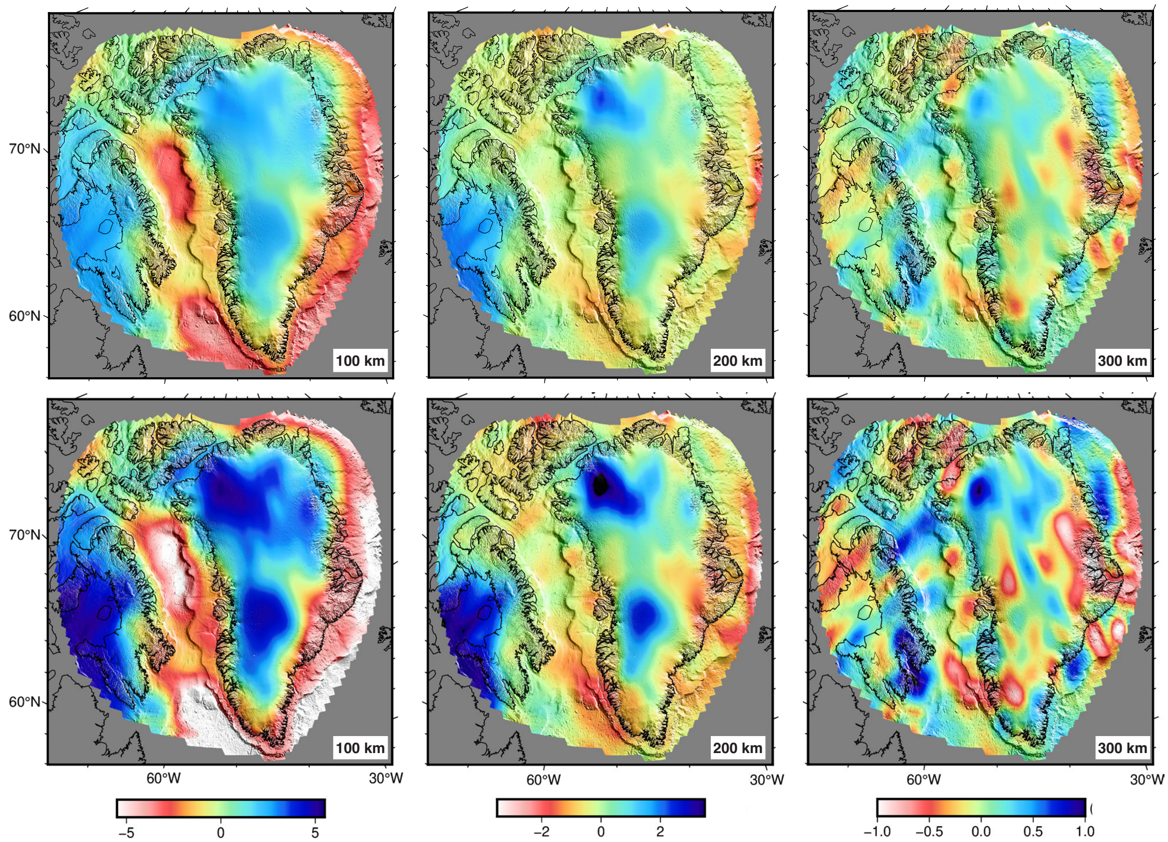

Figure 4.3: Relative viscosity models ($\log(\eta/\eta_0)$) determined from the mean of the temperature posterior PDF with $\epsilon = 0.02\ ^\circ\mathrm{C}^{-1}$ in the first row and $\epsilon = 0.04\ ^\circ\mathrm{C}^{-1}$ in the second row.

viscosity model (Fig. 4.4-A) illustrates the viscosity perturbations with respect to a reference (radial) viscosity profile (Section 4.2.4).

We used the global lithosphere model presented in Afonso et al. (2019) (called LithoRef18), which is defined on a 2°× 2° grid. LithoRef18 is constructed from multiple geophysical data sets used in a joint inversion approach. LAB depth in LithoRef18 is defined as the depth to the 1300 °C isotherm. So, to make the global and regional LT models compatible, we created a revised version of LithoRef18 by using the 1250 °C isotherm from the inferred temperature profiles to define LAB depth. Note that the final LT model is scaled to give a global mean that is compatible with the optimal radial model (Section 4.2.4).

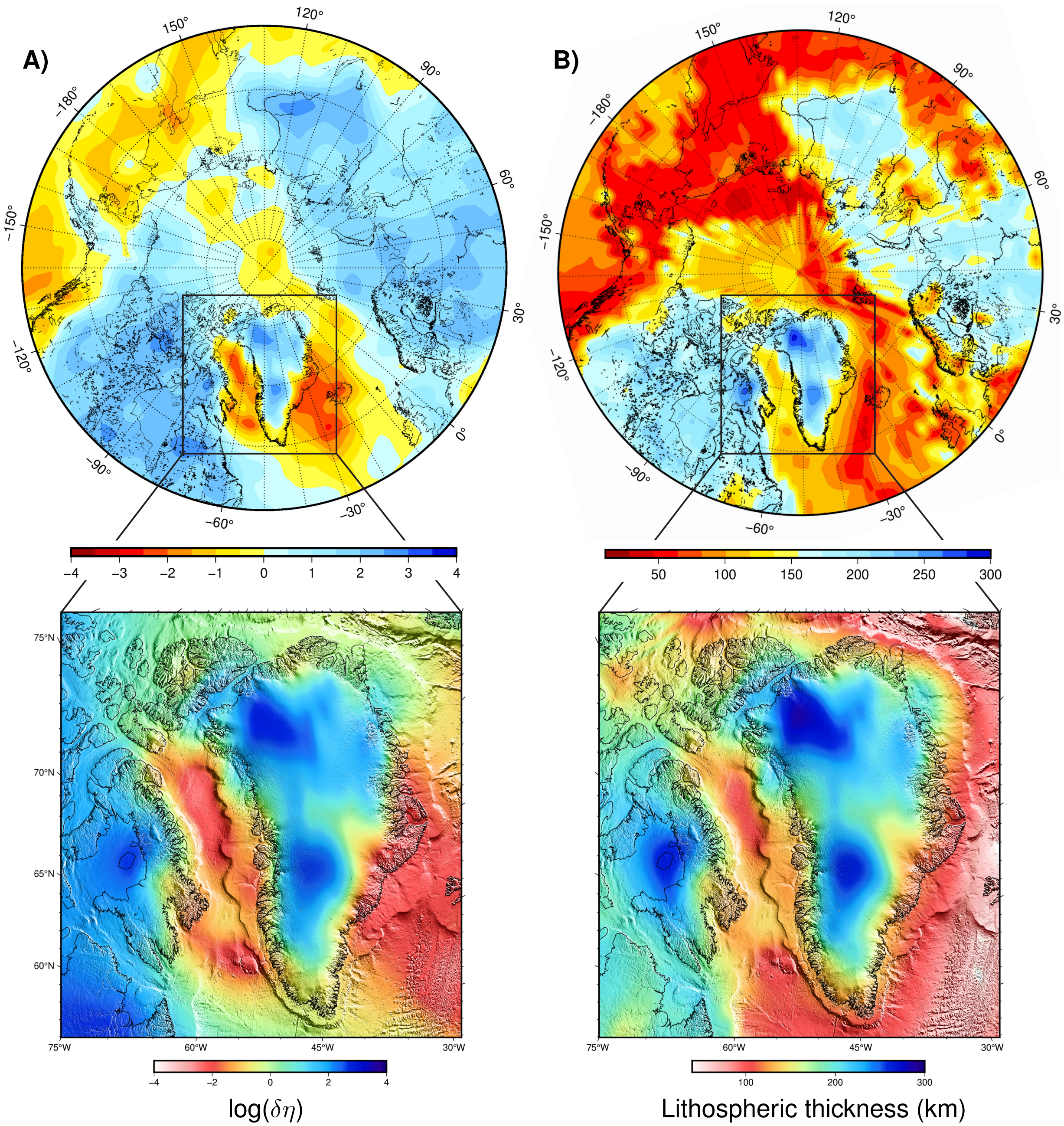

Figure 4.4: Final Earth models. **A)** Lateral viscosity variations at depth 120 km from the combination of regional viscosity and global models (SL2013 and S40RTS). **B)** Lithospheric thickness from the combination of our regional model (Chapter 3) and a global model based on the results of Afonso et al. (2019). Lower panels show results for our study region only.

4.2.2.3 Viscosity Model Uncertainty

Quantifying uncertainty is one of the key aspects of this chapter. However, there is no direct (analytical) approach to estimating GIA uncertainty from temperature uncertainty. Therefore, multiple 3D GIA realizations are used to estimate the uncertainty. The 3-D temperature models resulting from the LitMod inversion were used to determine a sub-ensemble of 3-D viscosity models for GIA simulations of deglacial RSL and present-day VLM. Given the high computational expense of the 3-D Earth GIA model, we chose to limit the sub-ensemble to 50 viscosity models. We chose 25 temperature models that accurately capture the mean of the ensemble and represent a high variance subset such that uncertainty is well represented in the sub-ensemble (Figure 4.5). The 25 temperature models were used to define lateral variability in viscosity (relative to an average, depth varying, profile) via an exponential dependence of viscosity on temperature (Eq. 4.1c). Uncertainty in the parameter that defines the strength of this dependence (ϵ in Eq. 4.1c) was accounted for by considering plausible end-member values for this value, 0.02 $°C^{-1}$ and 0.04 $°C^{-1}$, giving a total of 50 laterally variable viscosity models. The same approach was applied to generate the lithospheric thickness sub-ensemble from sampled temperature profiles. These 50 Earth models, spanning the area of interest and extending to a depth of ~400 km, were patched into the global Earth model described above (Sec. 4.2.2.2).

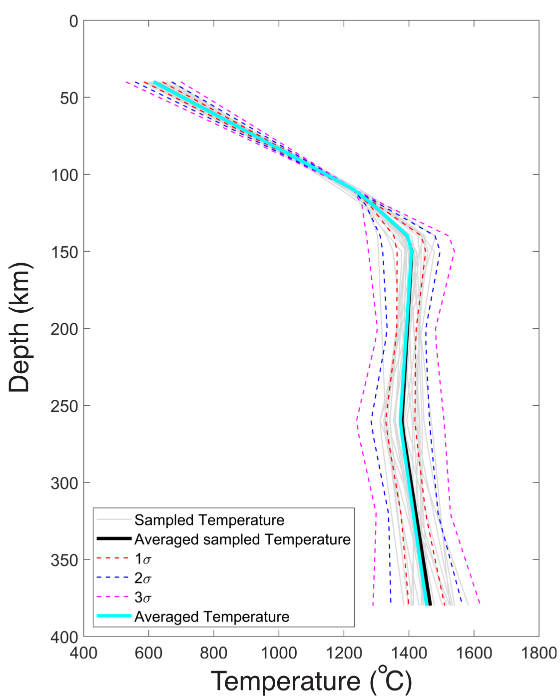

Figure 4.5: Sampled temperature profiles from the posterior PDF at a grid node in eastern Greenland. The averaged temperature (cyan line) is the mean value of the posterior PDF, whereas the averaged sampled temperature (black line) is the average of the sampled temperature profiles (gray lines). Dashed lines represent 1-3 sigma uncertainties of the temperature posterior PDF (see key).

4.2.3 GIA modelling

The solid Earth response of a compressible, self-gravitating, viscoelastic Earth to an ice loading history is calculated from a numerical finite-volume approach via a forward modelling method (Latychev et al., 2005). In this approach, the solid Earth deformation is calculated on a multi-layered triangulated (spherical tetrahedral) grid, and the outputs are changes in gravity and horizontal and vertical surface motion. Physical properties such as viscosity, density, and elastic parameters are assigned to each tetrahedron vertex (grid node). Grid resolution varies with depth because the Earth's lateral variation in the lithosphere is higher compared to the relatively homogeneous mantle. The defined grid size (radially and spatially) is $\sim$15 km near the surface and increases to $\sim$50 km at the CMB. Sea-level changes (ocean loading) is computed by solving the sea level equation (Clark et al., 1978) which accounts for coastline evolution (Mitrovica and Milne, 2003; Kendall et al., 2005) (see Section 1.5.2). The influence of Earth rotation on GIA model output is also included (Milne and Mitrovica, 1998; Mitrovica et al., 2005).

The Earth and ice models are the two key model inputs required to solve the sea level equation. The input ice model provides information about ice thickness and extent at different times. We used the Huy3 ice model (Lecavalier et al., 2014) for the deglacial period, specifically constrained to reconstruct the GrIS evolution from the LGM to the present. This ice model is the most recent reconstruction of deglacial GrIS changes based on fitting GIA-related (RSL) observations. As discussed above, the Huy3 model is known to underestimate ice thinning in NW Greenland during the Holocene (Lecavalier et al., 2017). Therefore, we exclude this region from the RSL and VLM interpretations in this analysis. For the interpretation of present-day VLM rates, we also consider the more recent ice sheet loading during and following the Little Ice Age (Kjeldsen et al., 2015), as well as changes in peripheral glaciers (PG) during the 20th century (Khan et al., 2022).

The input 3D Earth models are defined in Section 4.2.2. As noted above, we impose the lateral viscosity structure onto a 1D (radial) viscosity model. The 1D reference viscosity profile is defined as a uniform viscosity within the upper and lower mantle. This model assigns one viscosity value below the lithosphere down to 670 km and one below 670 km down to CMB. An optimum 1D reference model is achieved by examining a combination of different LT-UMV-LMV values and comparing the resulting model output to RSL data. Lecavalier et al. (2014) determined an optimal 1D reference model with an LT of 120 km, 5×10^{21} (Pas) for UMV and 2×10^{22} (Pas) for LMV. Past 3D modelling work (Milne et al., 2018) assumed this optimal 1D 3-layer model (LT-UMV-LMV). However, this 1D model is likely biased due to ignoring the influence of lateral Earth structure. Therefore, in this study, we explicitly infer a 1D structure that optimises the fit of our average (mean) 3D model with the RSL dataset (Section 4.2.4).

4.2.4 Estimation of Earth Model Parameters

The quality of a given model parameter set is determined by comparing model output to the reconstructed RSL data (Fig. 4.1). The optimum applied Earth viscosity model has the lowest data-model misfit. The data-model misfit is calculated based on the minimum distance (L2-norm or Euclidean distance) between each SLIP and the modelled RSL. The misfit for SLIP data is calculated via (Mitrovica et al., 2000):

$$\delta_{SLIP} = \frac{1}{N}\sqrt{\sum_{n=1}^{N} ((\frac{\Delta}{\sigma})^2_{RSL,n} + (\frac{\Delta}{\sigma})^2_{t,n})}, \tag{4.2}$$

where $\Delta_{RSL,n}$ and $\Delta_{t,n}$ are the observed and modelled RSL difference for the nth observation in height and time, respectively. $\sigma_{RSL,n}$ and $\sigma_{t,n}$ are the RSL height and time uncertainties, respectively, and N is the total number of SLIP data at each site.

Since the RSL limiting data constrain height in one direction only, it is difficult to determine the closest point on the model curve to each data point. Therefore, in this case, a simplified approach is taken where the misfit is calculated based on equation Eq. **??** in cases where the model curve sits on the 'wrong' side of the limiting data point (e.g., below a marine limiting point). Also, since the limiting data points constrain RSL in only one direction, the resulting misfit is weighted at 50% compared to SLIPs (Eq. **??**):

$$\delta_{Lim} = \frac{1}{N}\sqrt{\sum_{n=1}^{N} (\frac{\Delta}{\sigma})^2_{RSL,n}}, \tag{4.3a}$$

$$\delta_{Total} = \delta_{SLIP} + 0.5 \times \delta_{Lim}. \tag{4.3b}$$

The RSL data in Greenland is not distributed uniformly, and so the data-model misfit can be biased toward regions and time periods with a high density of RSL data (Briggs and Tarasov, 2013). Therefore, spatio-temporal weighting is applied such that higher weights are assigned in regions with low data distribution in space and time. To account for spatial variations in data density, we divided the entire region into five sub-regions (northwestern, northeastern, eastern, western, and southern Greenland), and the RSL uncertainty is scaled by $\alpha = \sqrt{n/N}$, where n is the number of RSL points in each sub-region and N is the total number of Greenland-wide RSL points. To account for variations in temporal data density in a given sub-region, the data

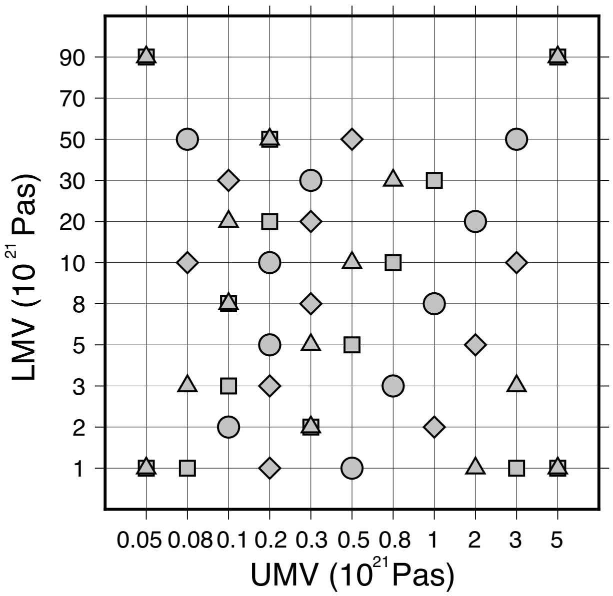

Figure 4.6: Sampled LT-UMV-LMV parameter space: 48 parameter vectors from a total of 484 are selected to generate model output used to train the emulator. Squares, circles, diamonds, and triangles represent 46, 71, 96, and 120 km LT values, respectively.

were divided into four time bins ([0-3 ka], [3-6 ka], [6-9 ka], [9+ ka]), and similarly, the time uncertainty is scaled by α.

To quantify the impact of lateral variability in Earth structure on RSL and VLM, it is necessary to define a radial (1D) viscosity model on which to superimpose the lateral variations and compare output from this 3D Earth model to that from a more traditional 1D Earth model. To ensure a valid comparison, we used a leading deglacial ice sheet reconstruction (Lecavalier et al., 2014) and determined optimal values for a three-parameter radial model (specifically, LT-UMV-LMV) using both 3D and 1D Earth models. These parameter values were optimized based on minimizing data-model misfit to the RSL dataset (Fig. 4.1). For the 1D case, optimal parameters are a 120 km lithosphere, an upper mantle viscosity of $5{\times}10^{20}$ Pas, and a lower mantle viscosity of 10^{21} Pas. Finding an the optimal parameter set for the 3D case is more challenging due to the high computational expense of a single model run, making it impractical to search the parameter space.

We adopted a newly developed 3D GIA emulator (Love et al., 2024) to search the parameter space. In this approach, we selected 48 Earth model parameter sets (from a possible 484) to generate model output with which to train the emulator (Fig. 4.6). The trained emulator is then used to predict RSL for the rest of Earth model parameter sets. The emulated RSL values are compared to RSL data to find the best 1D reference Earth model for our lateral viscosity model.

4.3 Results and Discussion

4.3.1 Inference of optimal 1D reference

The total misfit between the emulator's output and paleo RSL data for selected Earth parameter sets is shown in Fig. 4.7. Relatively low viscosity values in the upper mantle produce larger

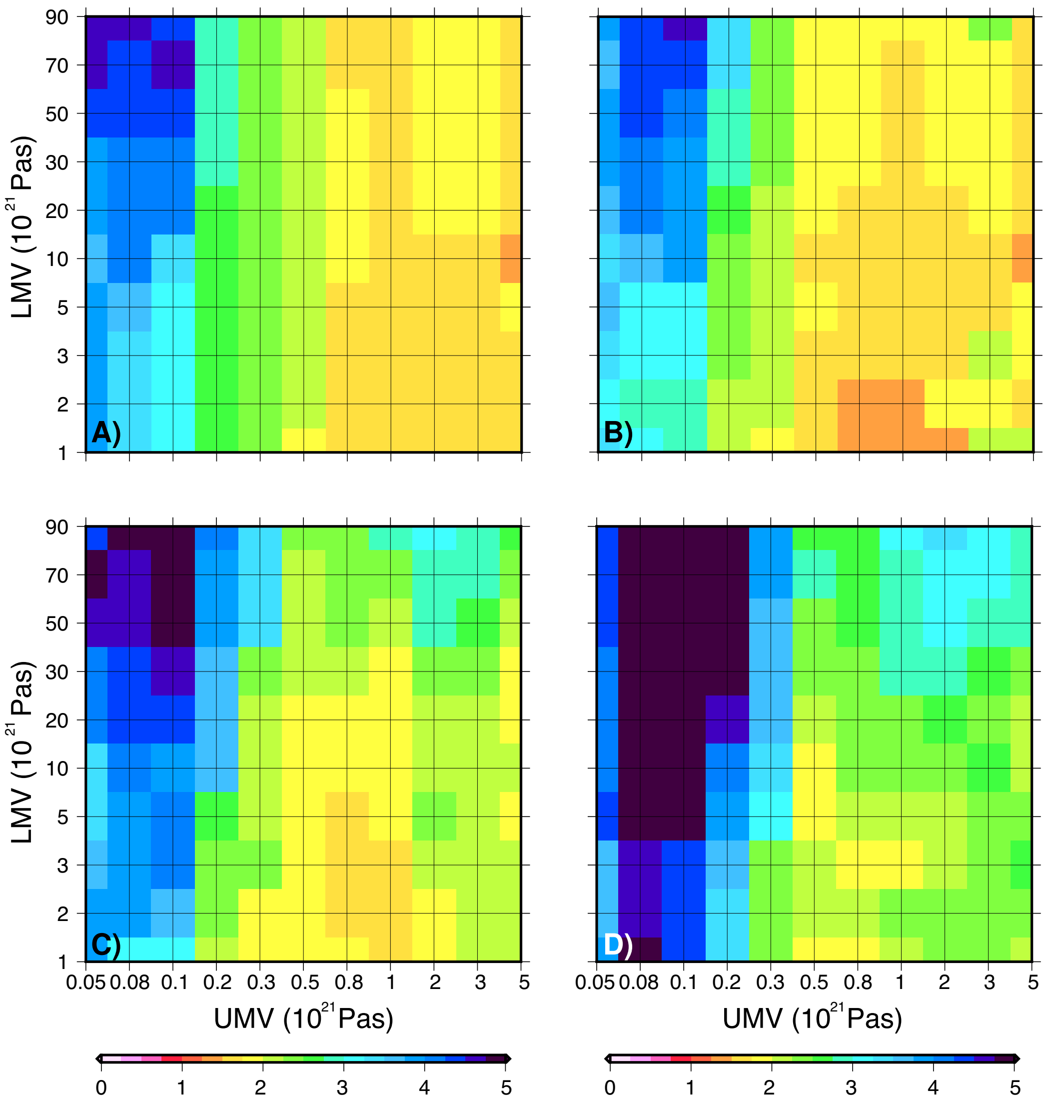

Figure 4.7: Total data-model misfit for emulated RSL using the average lateral viscosity model and different radial viscosity models. Each frame shows results for a different lithosphere thickness value: **A)** 46 km, **B)** 71 km, **C)** 96 km, and **D)** 120 km.

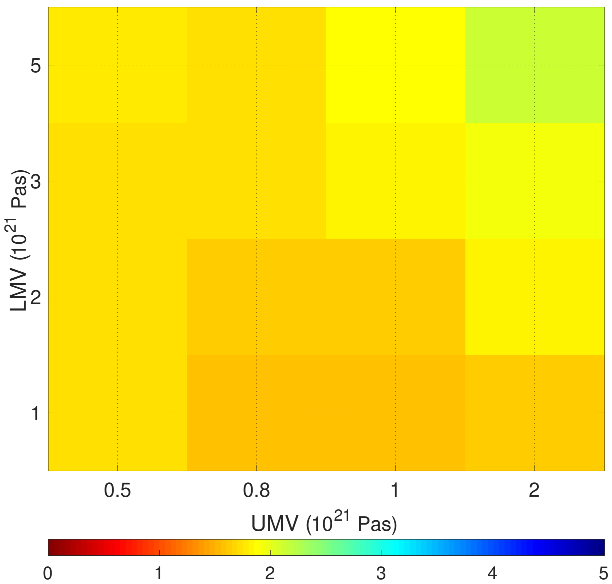

Figure 4.8: Total data-model misfit for a sub-set of 16 UMV-LMV parameter sets and an LT of 71 km.

misfits, and larger viscosity values in the upper mantle generally decrease the misfit. Conversely, relatively low viscosity values in the lower mantle generally produce smaller misfits, although this is a more subtle feature. Among the four LT values, 71 km generates the lowest misfits; specifically, the lowest misfit is obtained with 8×10^{20} Pas for the upper mantle and 1×10^{21} Pas for the lower mantle.

Although the emulator predictions are sufficiently accurate (Love et al., 2024), we used the emulator results (Fig. 4.7) to inform a more detailed search using the Seakon model. That is, we selected a region of UMV-LMV space with low data-model misfits and used Seakon to find the optimum 1D reference Earth model produced the minimum data-model misfit using the average laterally variable viscosity model. Based on the results in Fig. 4.7, we considered the following parameter ranges: 71 km LT, upper mantle viscosity values between 0.5-2 $\times10^{21}$ Pas, and lower mantle viscosity values between 1-5 $\times10^{21}$ Pas. In Fig. 4.8, the total data-model misfit for these 16 LT-UMV-LMV parameter sets is shown, and 1 $\times10^{21}$ Pas for both UMV and LMV produced the lowest misfit. The optimal 1D reference model determined from the Seakon runs is only one increment away from the optimal model inferred from the emulator, which shows the robustness and accuracy of the employed emulator. The lateral variations in viscosity were superimposed on the inferred optimal reference 1D Earth model to generate model output of RSL and VLM for this optimum parameter set.

4.3.2 Paleo relative sea level

The modelled RSL signal at 8 ka shows the typical pattern of high sea levels in areas characterized by ice retreat and negative values adjacent to these regions (Fig. 4.9-A&B). For the 1D case (Fig. 4.9-A), the ice history model largely governs the spatial pattern. The pattern of RSL change based on the optimal 3D viscosity model (Fig. 4.9-B) has a similar spatial structure compared to that for the optimal 1D model but the amplitudes are significantly different. This reflects the substantial lateral variations in temperature/viscosity (Fig. 4.3), which are neglected in the 1D model, as well as the different radial viscosity profiles in each case. The 3D model generally produces lower RSL values around the Greenland coast (except for southern Greenland) and by as much as 20 m in some locations (i.e., a similar magnitude to the total signal). Modelled RSL curves for the 1D and 3D cases also show large variations and different patterns around the Greenland coast (Fig. 4.9-D and Fig. A4.1). The magnitude of difference between the 3D and 1D RSL models is also temporally and spatially variable. The differences between the optimal 3D and 1D viscosity models is significant, especially in southern Greenland, where the modelled RSL is larger by a factor of 2-3 in the Early Holocene.

In northern Greenland (e.g., ConBu site; Fig. 4.9-D), modelled RSL suggests deglaciation was gradual since the Early Holocene and slower than other regions where a rapid RSL fall was experienced. Adding 3D viscosity variations produces a smaller magnitude RSL signal at this location and improves the data-model fit around 8 ka. However, the modelled curve sits too high for most of the Holocene (for both 1D and 3D Earth models) and does not follow the paleo RSL data, especially after 6 ka. These RSL data-model discrepancies around 10 ka and after 6 ka suggest that a later and faster deglaciation is required in this region to accommodate most of this misfit.

The high temperatures in central eastern Greenland also result in a more rapid RSL fall (e.g., MestV and Ammas; Fig. 4.9-D). At the MestV site, a modification to the deglaciation chronology (later deglaciation) would produce a significantly better fit compared to the 1D model. At Ammas, the 3D results fit the paleo data better than the 1D results. Some of the highest quality RSL data are found in southern Greenland (e.g., Pamiu and Nanor; Fig. 4.9-D). Past work has indicated difficulty in matching the RSL amplitude and rate of fall at these sites (Lecavalier et al., 2014; Woodroffe et al., 2015), which has led to the suggestion of glacially-triggered faulting (Steffen et al., 2020). Our new 3D model indicates relatively high temperatures in this region, resulting in a larger amplitude RSL response than the 1D model (Fig. 4.9-D; sites Nanor and Pamiu). However, this also leads to a poorer fit due to the modelled curve sitting too high for most of the Holocene. An earlier deglaciation of this region (Fig. 4.10) accommodates most of this misfit and exploring this idea will be necessary to further test the faulting hypothesis .

High-quality RSL data are also available in western Greenland (e.g., SouWD; Fig. 4.9-D).

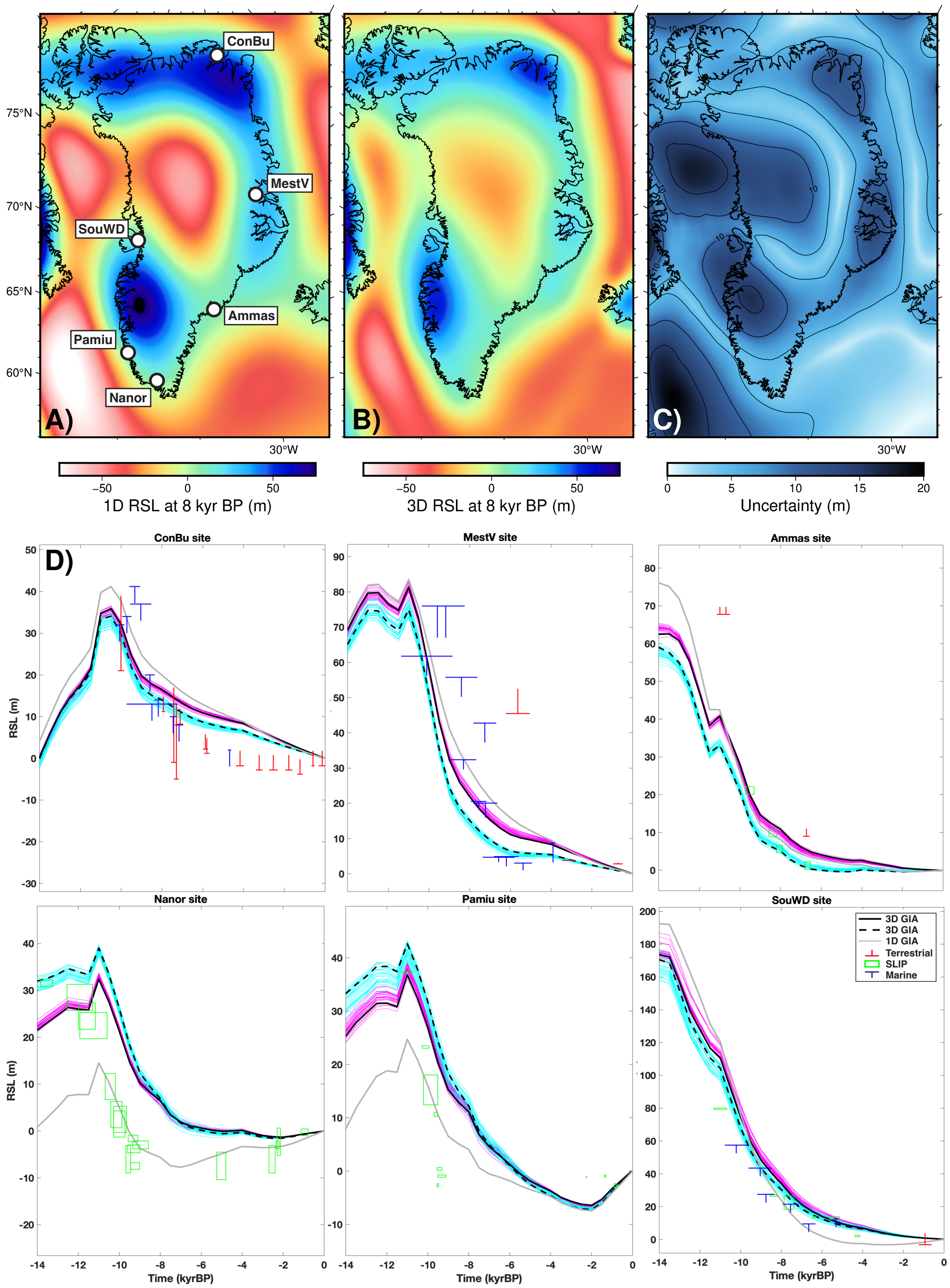

Figure 4.9: Modelled and observed RSL changes. **A)** Modelled RSL for the best 1D reference model (LT = 120 km, UMV = 5×10^{21}, and UMV = 1×10^{22}), and **B)** for the optimum 3D Earth models (using the 1D reference model (LT = 71 km, UMV and UMV = 1×10^{22}) and the mean of the 50 model sub-ensemble with ϵ = 0.02 and 0.04 °C^{-1}). **C)** Uncertainty of the 3D RSL signal, and **D)** RSL data-model comparison for 1D and the 50 model sub-ensemble of 3D Earth models at six sites. Green boxes and blue and red markers are SLIP, marine, and terrestrial limiting points, respectively. RSL for the best 1D viscosity model is shown by the gray line. RSL for the 3D models are shown as cyan and magenta lines, for ϵ = 0.02 and 0.04 °C^{-1}, respectively (solid and dashed black lines are the average of these sub-ensembles).

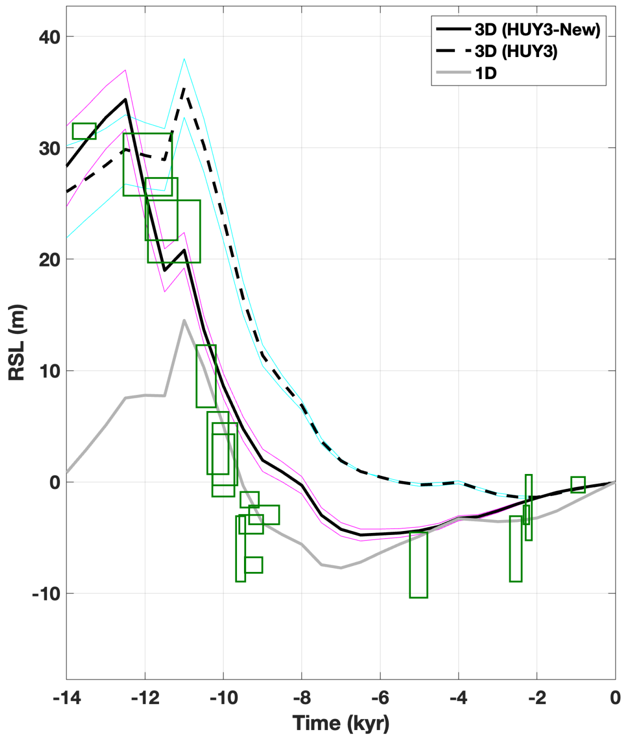

Figure 4.10: RSL data-model comparison in southern Greenland for 1D GIA using HUY3 ice model (gray line) and the laterally variable Earth model using HUY3 (dashed black line) and revised HUY3 ice model with 1.5 ka earlier deglaciation (solid black line). Green boxes are SLIPs. The 3D RSL shown in solid and dashed black lines are the average of the Earth models with $\epsilon = 0.02$ and 0.04 $°C^{-1}$, which are shown in cyan and magenta color for HUY3 and revised HUY3 ice models, respectively.

Our 3D Earth model shows relatively low temperatures in this region, leading to a higher viscosity and smaller amplitude RSL response compared to the 1D model. As a result, the 3D model better captures the SLIPs at this location, particularly in the mid-Holocene (8-5 ka). An important implication of thicker lithosphere and lower viscosities in this region is that the modelled RSL curve no longer goes to negative values in the late Holocene, which is a feature of the observations in this region and is related to peripheral bugle effects from North American ice loading as well as re-advance of the GrIS in southwest Greenland since ∼4 ka (e.g., Simpson et al., 2009). Again, this suggests that further work on the ice model will be necessary to address this issue. Overall, the optimized 3D Earth model better fits the data set considered here (Fig. 4.9-D). As indicated above, further improvements to the model fits can be achieved by making changes to the ice sheet reconstruction.

There is also considerable uncertainty in the signal associated with lateral Earth structure (Fig. 4.9-C), reaching amplitudes exceeding 10-15 m in many areas. The uncertainty corresponds to the spread in modelled RSL caused only by the uncertainty in lateral Earth model viscosity structure (and so will be an underestimate of the uncertainty associated with the full 3D structure). The RSL spread is temporally and spatially variable around Greenland (Fig. 4.9-C&D), and it can accommodate the majority of RSL data at some sites (e.g., SouWD, Ammas;

Fig. 4.9-D). The spread in RSL is generally greatest before 10 ka, but there are exceptions (e.g., ConBu, MestV).

4.3.3 Present-day vertical land motion

Results for present-day VLM using the optimum 1D Earth model (Fig. 4.11-A) indicate the highest rates in northeastern Greenland, while southwestern Greenland shows the greatest subsidence. These results generally indicate an uplift in north and eastern Greenland, while the rest of Greenland subsides. Compared to the GNSS VLM rates, there is a high correlation in northeastern Greenland. However, the data-model misfit is large in the rest of Greenland, especially in southeastern Greenland, where the difference reaches ∼8 mm/yr (Fig. 4.11-E). The 1D model results show relatively poor fits to the observed VLM rates at most GNSS stations as highlighted in recent work (Milne et al., 2018; Adhikari et al., 2021).

Results for the 3D model VLM indicate a large signal associated with lateral viscosity structure (compare frames A & B in Fig. 4.11). Compared to the 1D model, the 3D results show an increase in uplift rates at most locations. Where a large area of western and southern Greenland is predicted to be experiencing subsidence using the 1D model (Fig. 4.11-A), those based on the 3D model (Fig. 4.11-B) indicate uplift in all coastal areas except for parts of southwestern and northwestern Greenland. In most coastal areas, the increase in uplift rate amplitude reflects the thinner lithosphere in these regions in the 3D Earth model compared to the 1D model (Fig. 4.4).

The contribution of lateral structure results in an improved fit to the observed VLM at most GNET sites (Fig. 4.11-B&E, pink bars). While the fit is markedly improved compared to 3D modelling results based on global seismic velocity models and an older generation of lithosphere thickness models (Milne et al., 2018), a considerable underestimate remains in central eastern Greenland. As discussed above, many studies (including this one) indicate that the Iceland hotspot was located beneath this part of Greenland in the past. Therefore, rock temperatures in this region remain relatively high, resulting in low viscosities and a thinner lithosphere (Fig. 4.4). VLM in such regions is highly sensitive to ice thickness changes on century-to-decadal timescales (e.g., Adhikari et al., 2021), and so we considered the influence of ice thickness variations on shorter timescales that are not accurately captured in the Huy3 model. Specifically, Little Ice Age (LIA) changes associated with the ice sheet (Kjeldsen et al., 2015) and 20th century changes in peripheral glaciers (Khan et al., 2022) were incorporated. There is considerable uncertainty in our knowledge of both ice sheet and glacier changes leading to and following the LIA maximum (Kjaer et al., 2022; Khan et al., 2022). For this reason, we considered a range of plausible chronologies for the ice sheet changes and a ±20% range in the total amplitude of thickness change from the LIA maximum to the present in the ice sheet and peripheral glacier models.

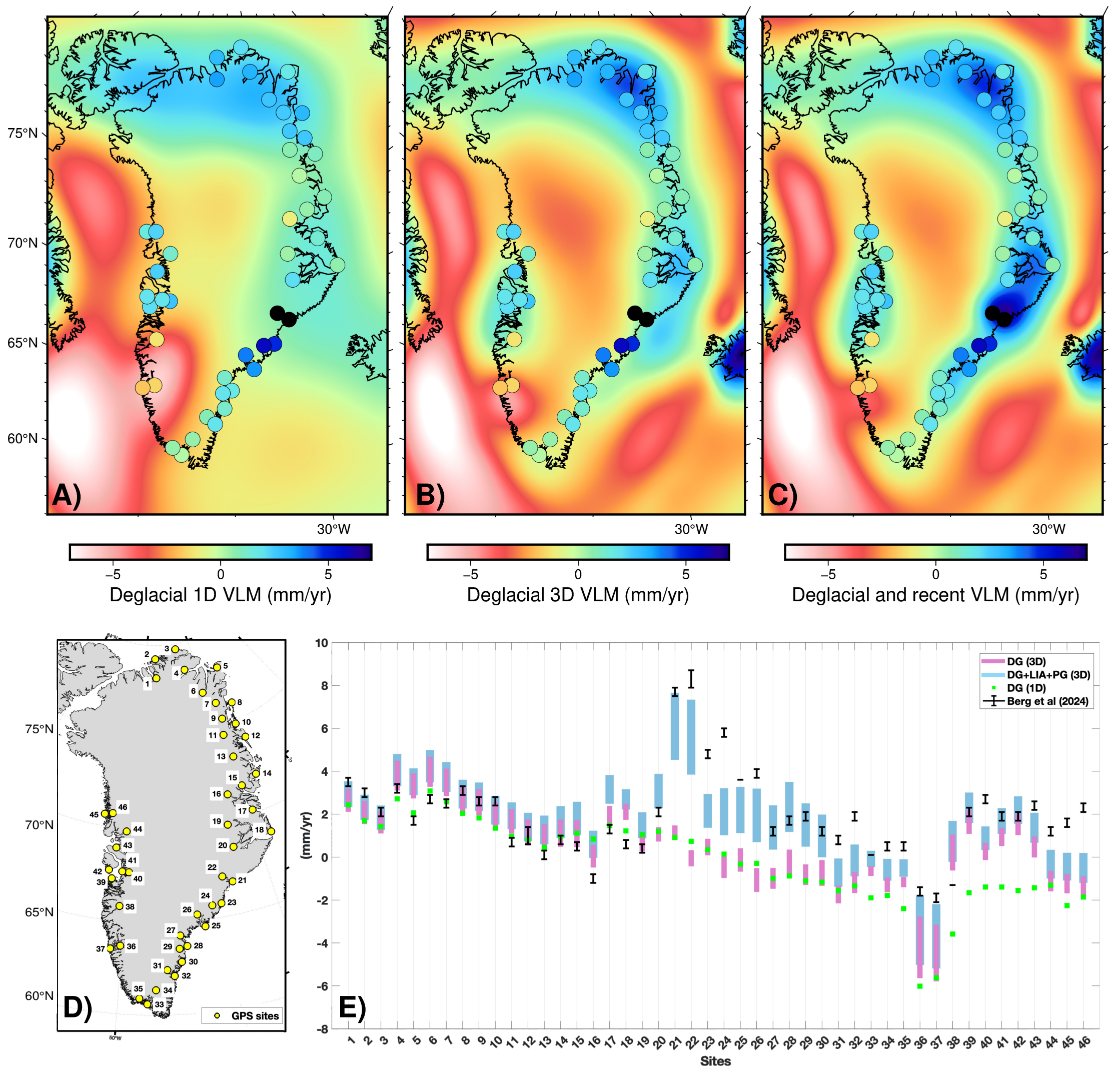

Figure 4.11: Modelled and observed VLM. **A)** Modelled deglacial VLM with the 1D Earth model, and **B)** the 3D Earth model. **C)** As in (B) but including more recent loading signals associated with the ice sheet and peripheral glaciers (see text for details). **D)** The location of the GNET stations, and **E)** modelled and observed VLM, shown in (A-C), in sites mentioned in (D).

Present-day VLM, including deglacial and more recent changes in the ice sheet and peripheral glaciers, is illustrated in Fig. 4.11-C. The recent loading history corresponds to ice thickness changes on century to decadal timescales, including post-Little Ice Age changes in the ice sheet (Kjeldsen et al., 2015) and changes in peripheral glaciers (Khan et al., 2022). Based on

Fig. 4.11-B, C & E, the contribution of the ice sheet and glacier changes are most significant in central eastern Greenland. Compared to the deglacial loading results, where eastern Greenland is predicted to be experiencing spatially constant uplift, the ice sheet signal is larger at most sites and much more spatially variable. The blue bars in Fig. 4.11-E show the impact of adding the recent loading signals to the VLM model output - the fit is dramatically improved in central eastern Greenland. Overall, the quality of fit is remarkable given that no model parameters were tuned to match the VLM rates. Among the sites with largest data-model misfit, prior to considering more recent loading changes (20-37), the misfits at sites 21 and 22 are resolved. Despite a general improvement in eastern Greenland, there remain sites where the model does not capture the observations: 23-26, 31-32, and 34-35. Also, the modelled VLM rates in WNW Greenland (sites 44-46) do not fit the data to within the estimated uncertainty. Unfortunately, there are no RSL data at these sites (44-46) to evaluate ice model accuracy.

While there remain some stations where the model does not capture the observed VLM rates, these can be explained by uncertainties in the ice-loading models. One notable simplification of our LIA and PG models is that the extent of changes was assumed to be synchronous across Greenland. Such a scenario is unlikely given the spatial variation in atmosphere and ocean forcing factors and variations in the sensitivity of the ice sheet and PGs to these factors. An important outcome of this chapter is demonstrating that improved decadal- to century-scale ice chronology models are required to accurately interpret the observed VLM rates in central eastern Greenland.

4.3.4 General Discussion

In some previous 3D GIA studies, including the lateral variation in viscosity structure generated a poorer fit compared to the 1D model (e.g., Yousefi et al., 2018). In many previous studies, the viscosity perturbations were added to a pre-defined optimum 1D model. However, our results indicate that the optimal 1D radial Earth model can change significantly when lateral variations are considered, indicating the best 3D model is not built upon the best 1D model (Love et al., 2024). Previous studies inferred a thick LT (120 km) and different viscosity values for upper and lower mantle (UMV = 5×10^{20} and LMV = 2×10^{21}) (Lecavalier et al., 2014), while we found a thinner LT (71 km) and identical viscosity for upper and lower mantle (UMV and LMV = 1×10^{21}) when lateral viscosity structure is included. The optimal reference 1D Earth model is slightly different from the best emulated 1D Earth model (1×10^{21} Pas instead of 0.8×10^{21} Pas), indicating the accuracy of the emulator in predicting the 3D GIA model in near fields (Love et al., 2024).

The Earth model realizations applied in this study generate a large spread in modelled GIA, indicating the significant influence of Earth model uncertainty on determining RSL and VLM.

The uncertainty in modelled RSL and VLM vary temporally and geographically and explain data-model misfit entirely in some regions. As noted above, Earth model uncertainty associated with lateral structure is considered in this analysis and so further work is required to include uncertainty in the radial component. In addition, the Earth model realizations are based on a sub-sample of 25 high variant temperature profiles from the temperature posterior PDF. Although the average values of sub-sample and posterior PDF are highly coherent, a proper uncertainty estimation would required full uncertainty propagation using the posterior PDF.

The paleo RSL data considered here is improved compared to previous work (Lecavalier et al., 2014) with better temporal and spatial coverage. However, the absence of data in south-eastern and northwestern Greenland hampers the accuracy of Earth model estimation that is valid for Greenland. The optimum Earth model is determined based on the paleo RSL data and the same Earth model is used to estimate the present-day VLM rates. Therefore, regions with no paleo RSL data could result in modelled VLM rates that are not reliable in these regions. For instance, the VLM data-model misfits in northwestern and southeastern Greenland may originate from this issue. In addition, good quality paleo RSL data are distributed mostly in southern and western Greenland, while eastern and northeastern Greenland have only RSL limiting points. Although, we adjusted the weights of data points in the misfit calculation based on the spatial and temporal data distributions, the final results might still be biased toward the locations with the highest density of SLIPs.

The ability of our GIA model to produce quality fits to both paleo RSL data and contemporary VLM rate observations has relevance for recent work that has identified and sought to explain why models tuned to fit one of these data sets provide very poor fits to the other (Milne et al., 2018). Current hypotheses include the contribution of a transient component in the solid Earth deformation (Adhikari et al., 2021; Paxman et al., 2023) and the existence of a thin asthenosphere layer resulting in a large response to the LIA ice sheet signal but with little impact on the deglacial RSL signal (Pan et al., 2024). Regarding the former, our results do not rule out the existence of a transient response, but they do suggest it is of a smaller amplitude. As for the latter, our temperature inversions do not indicate a relatively hot and thin layer in the asthenosphere.

4.4 Conclusion

In this study we present the effect of lateral variability of Earth structure and its uncertainty on modelling the GIA in Greenland, focusing on RSL and VLM. Our main results and their implications are summarized in the following.

- The influence of laterally variable viscosity on RSL predictions is significant compared to

1D model results and varies across Greenland. The 3D model generally produces lower RSL by as much as 20 m except for southern Greenland where the 3D model is larger by a factor of 2-3 in the Early Holocene. Overall, the total data-model misfit for the optimized 3D model is lower and so fits the paleo data better than the optimal 1D Earth model. Although modelled RSL curves follow the paleo data in most regions, further improvement is possible by revising the deglacial ice model.

- RSL data in southern Greenland are poorly fit. Our new 3D model explains the high RSL amplitude in this region due to the high regional temperature, but it leads to a poorer fit due to the modelled curve sitting too high for most of the Holocene. An earlier deglaciation could reduce the misfit, and this should be explored in future work to further test the hypothesis of glacially-triggered faulting in this region.

- Our predicted VLM rates driven by deglacial and recent loading significantly improve and extend previous results. While the deglacial 3D VLM data-model fit improved compared to previous 3D modelling results based on global seismic and lithosphere models, VLM rates in central eastern Greenland are underestimated. Due to the proximity of Iceland and the possibility of plume passage in this region, the temperatures are relatively high (resulting in low viscosities) which makes this region sensitive to ice thickness changes on century-to-decadal timescales. Incorporating these recent and shorter-term changes with the Huy3 deglacial model improved the VLM data-model fit significantly in eastern Greenland. Despite an overall improved fit, there remain some stations with significant data-model residuals. We propose that these can be accommodated by ice model uncertainty and better constraints on ice sheet and glacier changes during and following the LIA.

Our GIA model produces quality fits to both paleo RSL data and contemporary VLM rate observations, indicating the contribution of a transient component in the solid Earth deformation might be less important that previously suggested (Adhikari et al., 2021; Paxman et al., 2023) and the existence of a thin asthenosphere layer (Pan et al., 2024) is not required.

4.5 Appendix A4

This supplementary material presents additional information to support the primary text.

- Text and Table A4.1. List of RSL data sites.

- Text and Fig. A4.1. RSL data-model comparison.

Text A4.1 (Table). List of RSL data sites including geographical coordination, acronym and full names.

Text A4.1 (Figure). RSL data-model comparison at sites shown in Fig.4.1-a. The sites at north-western Greenland is excluded due to the inaccuracy of Huy3 ice model. Fig. A4.1 illustrates modelled RSL with 1D (radial) and the laterally variable Earth model for 50 realizations with ϵ = 0.02 and 0.04 $°C^{-1}$. RSL data include SLIPs (Green boxes), marine limiting point (blue markers), and terrestrial limiting points (red markers).

Table A4.1: List of RSL data sites

ID	Latitude	Longitude	Sites	ID	Latitude	Longitude	Sites
James	70.843	-24.1278	Jameson Land	Carey	76.722	-73.1646	Carey Øer
Ssdaa	71.278	-24.6515	Southern Schuchert Dal and area	Thule	76.543	-68.8396	Thule
UpSDa	71.606	-24.3872	Upper Schuchert Dal	NorWD	69.919	-54.3866	Northwest Disko Island
MestV	72.254	-23.9043	Mesters Vig	SouWD	69.469	-53.7562	Southwest Disko Island
IKOFF	72.495	-24.8010	Inner Kong Oscars Fjord	Arvep	69.758	-51.2708	Arveprinsen Ejland
GSOtO	72.791	-23.0707	Geographical Society O/Traill O	Pakit	69.496	-50.7331	Pakitsoq
HudsL	73.622	-21.9171	Hudson Land	OutJa	69.045	-50.9047	Outer Jakobshavn
Young	74.255	-20.2412	Young Sound	AkulN	68.647	-50.9664	Akulliit/Nuuk
GerHS	74.539	-18.8429	Germania Haven So	SydoB	68.523	-51.5628	Sydosbugten
Hochs	75.206	-19.9475	Hochstetter Foreland	Inaar	68.618	-52.0872	Inaarsuit
Haval	76.913	-20.1779	Havalrosodden	QeqTa	68.449	-52.9469	Qeqertarsiatsuaq
Sondr	78.062	-21.2030	Sondre Mellemland	Norde	68.332	-51.2966	Nordenskiold
Blaso	79.590	-22.4380	Blaso	Inord	67.969	-50.5781	Inner Nordre Stromfjord
Outer	79.834	-19.6252	Outer Nioghalvfierdsfjorden	Onord	67.590	-53.3707	Outer Nordre Stromfjord
HolmL	80.459	-15.9623	Holm Land	Nordr	67.100	-53.9219	Nordre Isortoq
Danma	80.953	-22.7483	Danmark Fjord	Nagto	66.936	-53.6840	Nagtoralingquaq
Cphgn	81.565	-16.5661	Denmark	InnIk	66.944	-52.3324	Inner Ikertoq
KapKo	82.374	-21.3665	Kap Kobenhavn	Kangr	66.954	-51.0404	Kangerlussuaq
HerSt	82.600	-20.0329	Herlufsholm Strand	MidSS	66.510	-52.1721	Mid Sondre Stromfjord
IndFj	82.188	-30.9059	Independence Fjord	Sukke	65.677	-53.2013	Sukkertoppen
KapCW	82.882	-23.4500	Kap Clarence Wyckoff	NukFH	64.533	-50.3135	Nuuk Fjord Head
Taiwa	83.009	-32.5470	Taiwan	Nuukk	64.199	-51.8991	Nuuk
Kapol	83.432	-25.7299	Kap Ole Chiewitz	Maraq	63.462	-51.2866	Marraq
Bliss	83.543	-29.0035	Bliss Bugt	Pamiu	61.974	-49.6212	Paamiut
ConBu	83.655	-31.2688	Constable Bugt	Tasiu	61.136	-45.6588	Tasiusaq
KapMo	83.646	-33.2704	Kap Morris Jesup	Narsq	60.984	-45.6770	Narssaq
HallW	81.754	-59.4412	Hall Land/W Nyeboe Land	Qaqor	60.764	-46.0954	Qaqortoq
WWash	80.279	-67.3915	W Washington Land	Nanor	60.078	-45.0035	Nanortalik
SWWas	79.942	-64.1774	SW Washington Land	Timia	62.519	-42.2132	Timmiarmiut
Qeqer	77.501	-66.6720	Qeqertat	Ammas	65.720	-37.3062	Ammassalik

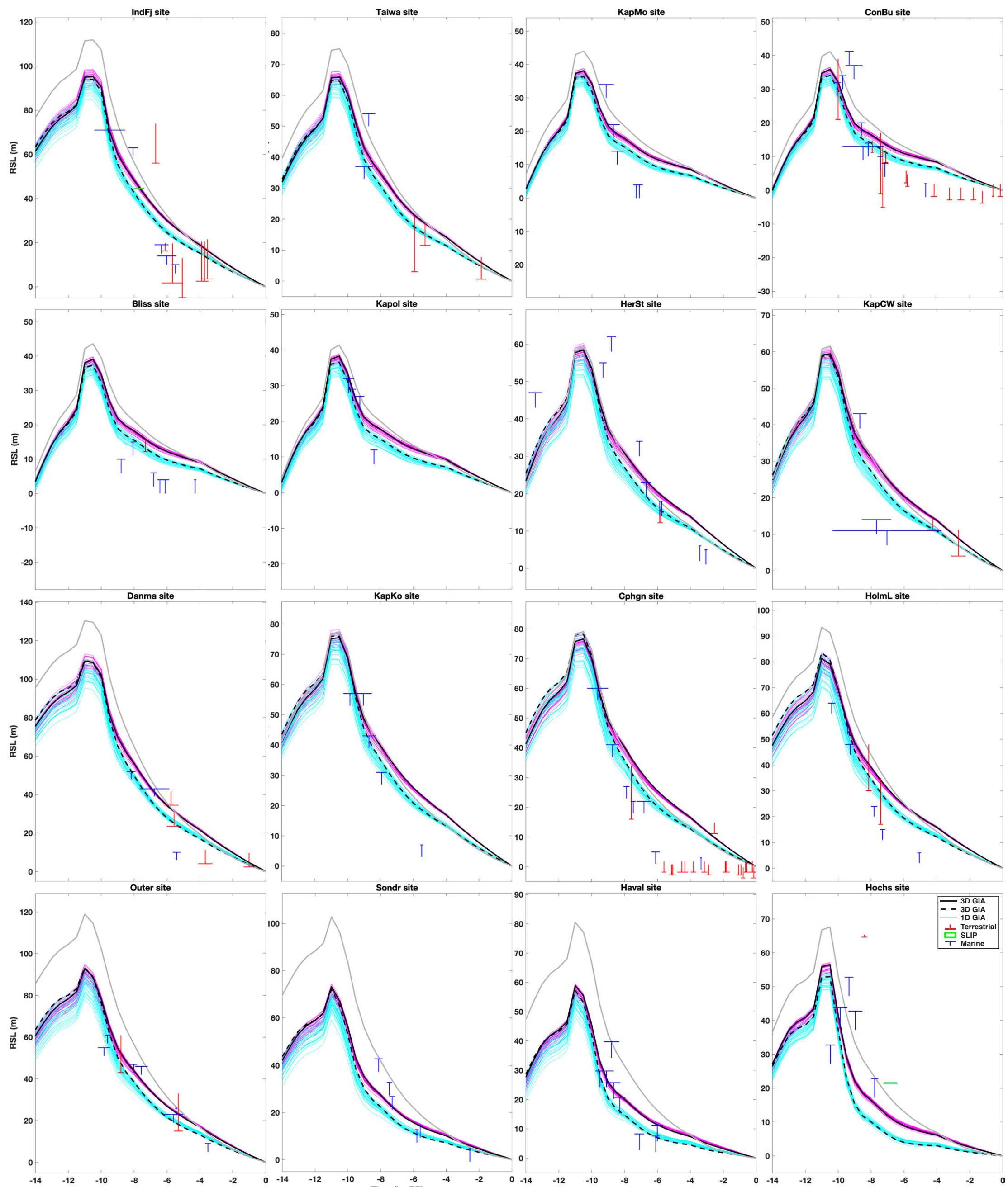

Figure A4.1: RSL data-model comparison for 1D and the laterally variable Earth model at sites shown in Fig.4.1-a and Table A4.1. Green boxes, blue markers, and red markers are SLIP, marine, and terrestrial limiting points, respectively. RSL for best 1D viscosity model is shown in gray line, and 3D RSL is shown in solid and dashed black lines as an average of the Earth models ensemble with $\epsilon = 0.02$ and $0.04\ ^{\circ}\mathrm{C}^{-1}$, which are shown in cyan and magenta color, respectively.

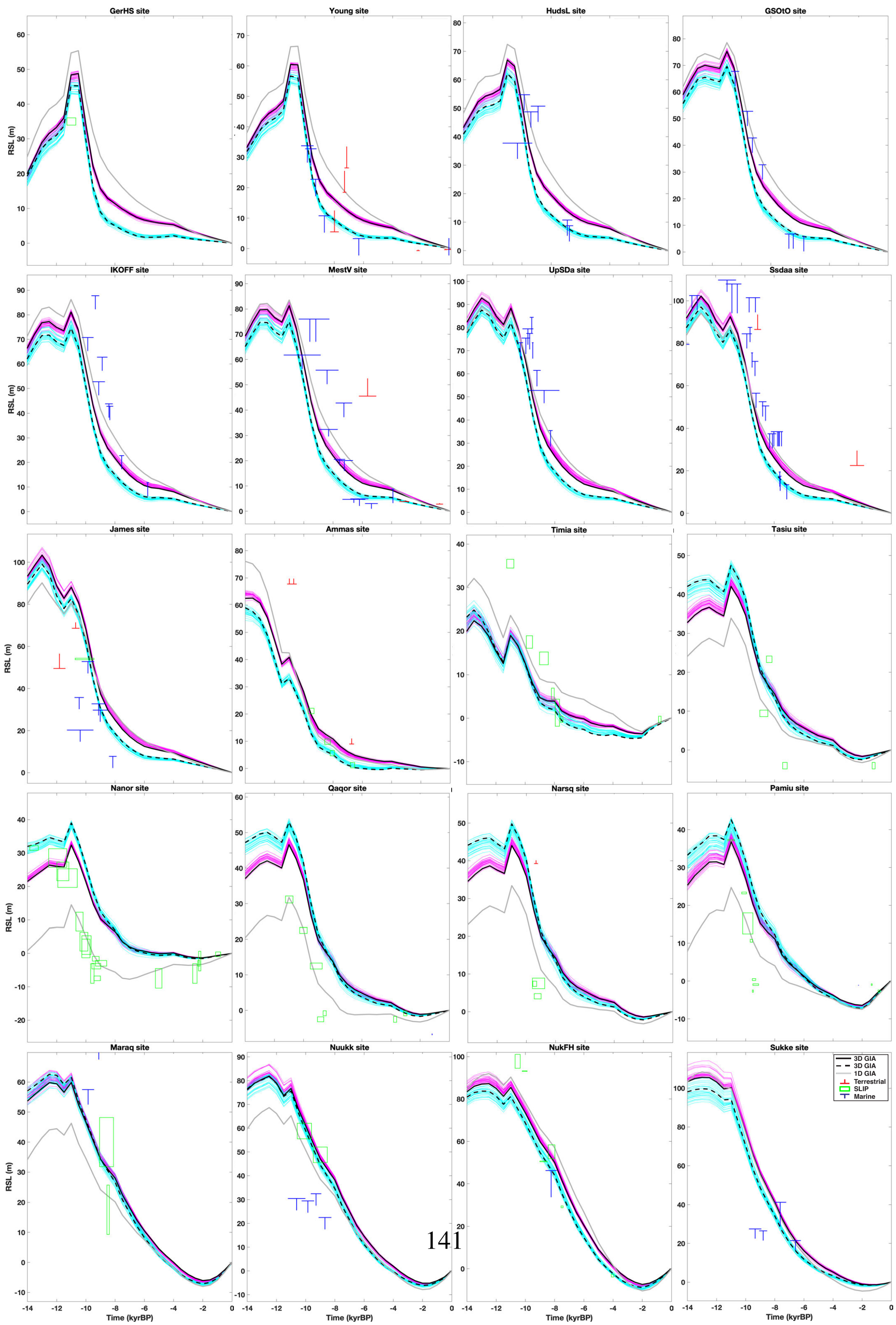

Figure A4.1: (*continued*)

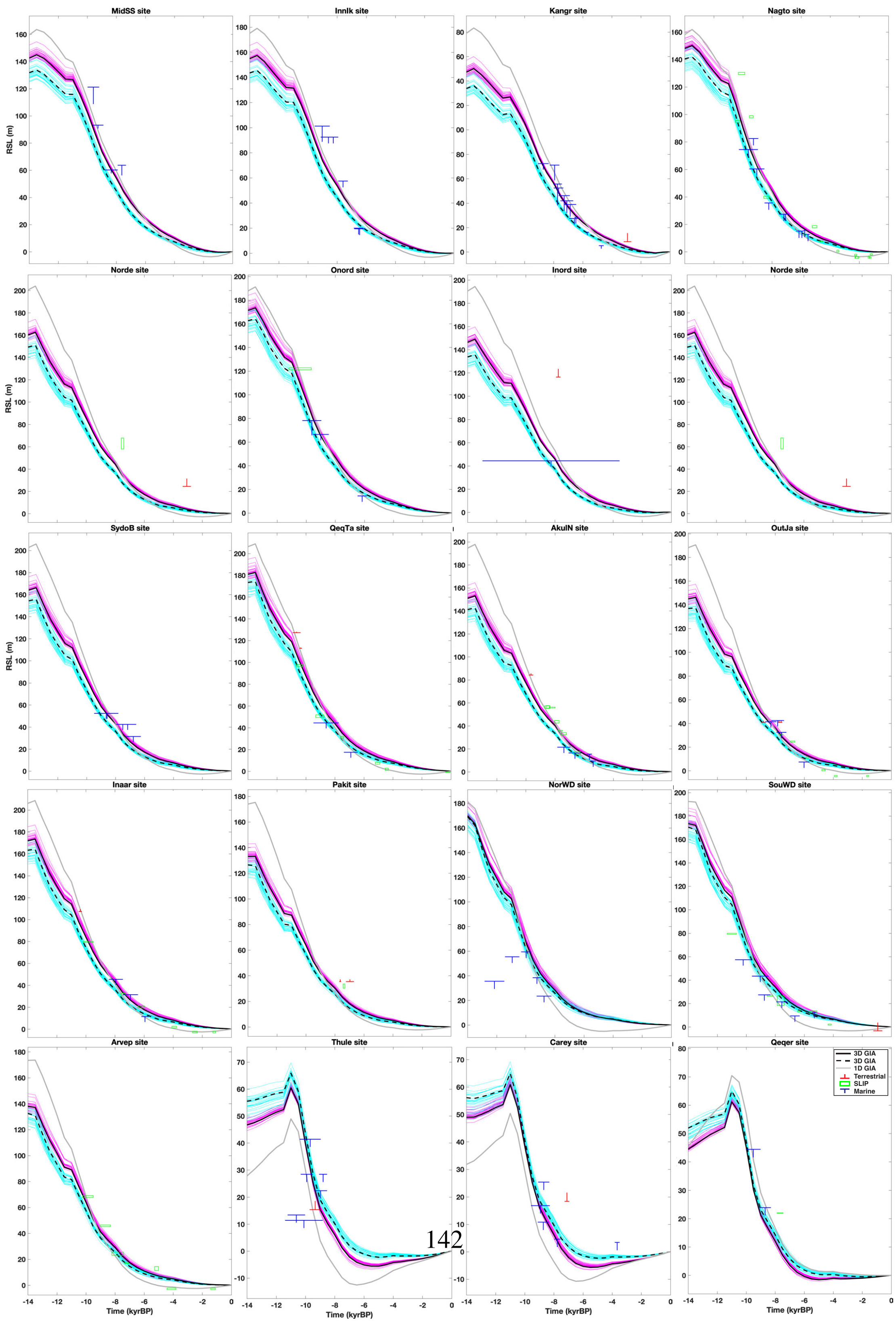

Figure A4.1: (*continued*)

Chapter 5

Conclusions and Future Research Directions

Projections of future sea-level rise depend strongly on the contribution of the Greenland ice sheet (GrIS) as one of the few remaining ice sheets on Earth. The accuracy of GrIS projections depends on our knowledge of the underlying Earth processes and properties. For example, GrIS projections depend on the rate and amplitude of the isostatic response, which impacts surface mass balance and can influence ice sheet dynamics. The main objective of my PhD thesis was to enhance our knowledge of Earth structure and composition beneath Greenland and the surrounding region. Improving Earth structure and composition constraints are important to understand and separate the evolution of ice sheet change and solid Earth response signals. In addition, it provides valuable information about the tectonic evolution and mantle dynamics of this region. My PhD thesis is divided into three research projects that are linked together in a way that the output of each step (chapter) is used as an input to the next step (chapter). The details of each project are discussed in Chapters 2-4. This chapter presents some of the main findings and their implications, and recommendations for future work are outlined.

In Chapter 2, we generated a new, regional, high-resolution Rayleigh wave phase velocity model for Greenland and the surrounding region using the teleseismic two-station interferometry technique. We used 48 permanent seismograph stations with seismic records from the vertical component of teleseismic events spanning over two decades in Greenland (on/offshore), northeastern Canada and western Europe to improve constraints on Earth structure. The new phase velocity map improved existing constraints on the velocity structure of the crust and the shallow upper mantle. Rayleigh wave phase velocity maps and azimuthal anisotropy provided valuable insight into the geologic evolution and lattice-preferred orientation (LPO)/mantle flow of the study region. Significant heterogeneity was observed in our results, and we found a strong correlation between inferred geological features and isotropic and anisotropic velocities. The inferred PVDCs used in the joint inversion are the most important dataset to constrain the thermochemical structure of the crust and shallow mantle because of the high sensitivity of these data to this structure and the improved spatial resolution compared to other data sets.

We adopted newly installed seismograph stations over the past 10-15 years, specifically in Greenland's central and southern parts and northeastern Canada. Additionally, we improved the resolution around the coast and continental shelf by broadening the aperture of the network used in our study by adding stations from beyond these regions. Despite the significant improvement in phase velocity map resolution and tectonic structure constraints, some limitations can be considered for potential avenues to improve the current findings. With the growing number of seismograph stations in Greenland, ray path density is poorest in northern Greenland and the Canadian Arctic. Therefore, installing new seismograph stations in regions such as the Canadian Arctic and northern/central Greenland should be a priority. In addition, depth-dependent anisotropy is not included in the currently used inversion method, and as a result, some types of geologic features are ignored. There is no fully developed inversion method to estimate anisotropy with depth.

In Chapter 3, we constrained the thermochemical properties of the shallow upper mantle (to $\sim$400 km depth) beneath Greenland and the surrounding regions. We adopted the LitMod software, which applies the Bayesian probabilistic approach to multiple geophysical data sets to invert for radial thermochemical structure of the lithosphere and shallow mantle. Specifically, we combined the regional, high-resolution surface wave data from Chapter 2 with various other data sets to perform a joint inversion for temperature and composition, from which properties such as viscosity can be determined. We solved for radial thermochemical properties beneath Greenland, Baffin Bay, and northeastern Canada, where the ice sheet was located during the LGM. Our results improve upon past studies by extending geographic coverage and spatial resolution and indicate large LAB-depth variations across Greenland. LAB-depth estimation varies greatly ($\sim$100-300 km) across Greenland, reflecting multiple geologic structures and thermal processes. While there are some agreements between our LAB-depth result and past studies (Steinberger et al., 2019; Steffen et al., 2018; Lebedev et al., 2018), significant differences are observed across Greenland, reflecting the importance of multiple input data types such as seismic, topography, and geoid height. Our LAB-depth result supports a W-E passage of the Iceland hotspot with the inferred thinner lithosphere in the mid-section of Greenland. A major lithospheric erosion event is supported by the exposed volcanic rocks of the North Atlantic igneous Province (NAIP) in east and west Greenland, which is inferred to extend beneath central Greenland. Despite the elevated SHF and high RHP concentrations in the NW-SE direction, we do not see any correlation with our LAB-depth result, and so we conclude that a W-E Iceland plume track over Greenland is more likely.

On average, 25-30 % of the model simulations are accepted to form the posterior probability distribution functions (PDFs) for different Earth properties (such as temperature). The estimated uncertainty for thermochemical structure is depth-dependent and spatially variable for each parameter, reflecting the importance of the input data quality and the sensitivity of model output to the parameters being inverted. Among Litmod's many outputs, we use only mantle temperature for our GIA analysis in Chapter 4. Overall, the quality of the inversion results in Chapter 3 were high, and we inferred large variations in the thermal structure of the mantle beneath Greenland, which is in good agreement with past studies. However, the results presented here can be extended by several recommendations. The current methodology ignores thermal processes such as volcanism and heat transfer by advection, which greatly affect the geothermal reconstruction where these processes are active. New data constraints would strengthen the inversion quality, including seismic (Vp, Vs, ambient noise, and receiver functions) and non-seismic (magnetorelluric and petrological) data. Performing a 3D inversion (compared to the series of 1D inversions performed here) would improve coherence over larger spatial scales which would be useful for exploring largescale processes such as tectonic evolution and mantle dynamics.

In Chapter 4, we examined the impact of lateral variations in Earth viscosity on the GIA model fits to observations of paleo RSL and present-day VLM rates. We used the new 3D temperature model developed in Chapter 3 to generate an ensemble of 3-D viscosity structures of Greenland's lithosphere and upper mantle. To more efficiently search the parameter space of the Earth viscosity model, we adopted a machine learning technique to emulate the 3D GIA simulation (Love et al., 2024). A sub-ensemble (25 samples) of inferred regional temperature models from Chapter 3 was adopted to quantify uncertainty in the GIA model output. The inferred uncertainty was determined from the 25 3D Earth models using two different values to scale temperature to viscosity. The resulting 50 viscosity models were used with ice loading models spanning millennial to central-to-decadal timescales to generate the most accurate model constraints on RSL and VLM, and their corresponding uncertainty, to date.

In many previous 3D GIA studies, the lateral variation in viscosity structure was superimposed on a previously determined, optimal, 1D Earth model. In many cases, the resulting 3D model generated a poorer fit compared to the 1D model (Yousefi et al., 2018). However, our results indicate that the optimal 1D radial Earth model can change significantly when lateral variations are considered, indicating the best 3D model is not built upon the best 1D model (Love et al., 2024). Our 3D model indicates the significant influence of laterally variable viscosity on RSL predictions compared to 1D model results. Overall, the total data-model misfit for the optimized 3D model is lower than that for the optimised 1D Earth model. Our results also indicate that changes in the deglacial ice model can improve the RSL data-model fit in many regions. For instance, our 3D model fits the high amplitude RSL in southern Greenland, which has not be achieved with a 1D Earth model, leading to the hypothesis of glacially-triggered faulting during the early Holocene in this part of Greenland (Steffen et al., 2020). While our model does not disprove this hypothesis, it reveals a path to testing it further via the exploration of regional deglaciation scenarios.

Our predicted VLM rates indicate large variations across Greenland and, compared to previous studies, better fit the VLM data. Milne et al. (2018) illustrated that the best 1D Earth model (based on paleo RSL data) fit well only in northeastern Greenland, with large discrepancies in the rest of Greenland. Adhikari et al. (2021) succeeded in fitting the VLM data using a loading model of ice sheet changes during and following the Little Ice Age. However, the inferred, optimal, upper mantle viscosity value is an order of magnitude lower than that determined from the deglacial RSL constraints. This finding led to the transient rheology hypothesis in this region, in which the viscosity depends on the timescale (frequency) of the loading. Our results successfully fit the RSL paleo and contemporary VLM rate data simultaneously without invoking transient rheology in the region. Due to the proximity of Iceland, low viscosity in eastern Greenland increases the sensitivity to shorter timescale loading change and, therefore, results in higher VLM rates compared to the 1D model. Incorporating recent and short-term changes with the Huy3 deglacial model greatly improved the VLM data-model fit in eastern Greenland. There remain some data-model residuals and a clear next step in addressing these is to develop improved models of LIA to 20th century changes in the ice sheet and peripheral glaciers.

Our results show that the contribution of Earth model uncertainty to simulating both RSL and VLM is significant. RSL uncertainty is large, especially in the Early Holocene when the amplitude reaches several 10s of meters and spatially correlates with modelled RSL amplitude in northeastern and southwestern Greenland. Uncertainty in VLM rates also varies across Greenland and is largest in southwestern Greenland with an amplitude of $\sim$2 mm/yr. Overall, the quantified uncertainty explained data-model residuals at many sites.

Our uncertainty analysis is limited in several respects. First, we considered only the contribution from lateral structure and ignored that associated with radial structure. Furthermore, we used only a small sub-ensemble of the temperature posterior PDFs to quantify the uncertainty associated with lateral viscosity structure. Second, we only considered uncertainty associated with recent ice sheet and glacier loading for predicting VLM rates. Also, this was limited to a small number of chronologies and simple scaling for different amplitudes of ice thickness changes. There is also considerable uncertainty associated with the deglaciation model (Huy3) and this was not considered here. Addressing these limitations of our uncertainty analysis are an obvious target for future work. Recent developments in the field, including the use of machine learning to emulate 3D GIA model output (Love et al., 2024) and the application of adjoint methods (Crawford et al., 2018; Lloyd et al., 2020) show good potential for building on the work described in Chapter 4.

References

Adhikari, S., Milne, G. A., Caron, L., Khan, S. A., Kjeldsen, K. K., Nilsson, J., Larour, E., and Ivins, E. R. (2021). Decadal to centennial timescale mantle viscosity inferred from modern crustal uplift rates in greenland. *Geophysical Research Letters*, 48(19):e2021GL094040. e2021GL094040 2021GL094040. 2, 20, 23, 117, 133, 136, 137, 146

Afonso, J. C., Ben-Mansour, W., O'Reilly, S., Griffin, W., Salajegheh, F., Foley, S., Begg, G., Selway, K., Macdonald, A., Januszczak, N., Fomin, I., Nyblade, A., and Yang, Y. (2022). Thermochemical structure and evolution of cratonic lithosphere in central and southern Africa. *Nature Geoscience*, 15:1–6. 3, 73, 77, 81

Afonso, J. C., Fernàndez, M., Ranalli, G., Griffin, W. L., and Connolly, J. A. D. (2008). Integrated geophysical-petrological modeling of the lithosphere and sublithospheric upper mantle: Methodology and applications. *Geochemistry, Geophysics, Geosystems*, 9(5). 76, 78

Afonso, J. C., Fullea, J., Griffin, W. L., Yang, Y., Jones, A. G., D. Connolly, J. A., and O'Reilly, S. Y. (2013a). 3-D multiobservable probabilistic inversion for the compositional and thermal structure of the lithosphere and upper mantle. I: a priori petrological information and geophysical observables. *Journal of Geophysical Research: Solid Earth*, 118(5):2586–2617. 3, 4, 10, 11, 12, 23, 73, 74, 75, 76, 77, 78, 79, 81, 82, 83, 91, 98

Afonso, J. C., Fullea, J., Yang, Y., Connolly, J., and Jones, A. (2013b). 3-D multi-observable probabilistic inversion for the compositional and thermal structure of the lithosphere and upper mantle. II: General methodology and resolution analysis. *Journal of Geophysical Research: Solid Earth*, 118(4):1650–1676. 3, 4, 10, 12, 13, 14, 23, 73, 75, 76, 81, 91, 98

Afonso, J. C., Ranalli, G., Fernàndez, M., Griffin, W. L., O'Reilly, S. Y., and Faul, U. (2010). On the Vp/Vs–Mg correlation in mantle peridotites: Implications for the identification of thermal and compositional anomalies in the upper mantle. *Earth and Planetary Science Letters*, 289(3):606–618. 76, 91

Afonso, J. C., Rawlinson, N., Yang, Y., Schutt, D. L., Jones, A. G., Fullea, J., and Griffin, W. L. (2016). 3-d multiobservable probabilistic inversion for the compositional and thermal structure of the lithosphere and upper mantle: Iii. thermochemical tomography in the western-central u.s. *Journal of Geophysical Research: Solid Earth*, 121(10):7337–7370. 3, 13, 73, 74, 75, 81, 82, 83

Afonso, J. C., Salajegheh, F., Szwillus, W., Ebbing, J., and Gaina, C. (2019). A global reference model of the lithosphere and upper mantle from joint inversion and analysis of multiple data sets. *Geophysical Journal International*, 217(3):1602–1628. 3, 22, 71, 79, 98, 122, 123

Afonso, J. C. and Zlotnik, S. (2011). *The Subductability of Continental Lithosphere: The Before and After Story*, pages 53–86. Springer Berlin Heidelberg, Berlin, Heidelberg. 76

Ajourlou, P., Darbyshire, F., Audet, P., and Milne, G. A. (2023). Seismic anisotropy of the crust and upper mantle in Greenland and northeastern Canada: Insights from Rayleigh-wave tomography. *Geophysical Journal International*, 217(3):1602–1628. 72, 73, 76, 77, 85, 91, 93, 117

Albers, M. and Christensen, U. R. (2001). Channeling of plume flow beneath mid-ocean ridges. *Earth and Planetary Science Letters*, 187(1-2):207–220. 53

Albuquerque Seismological Laboratory/USGS (2014). Global Seismograph Network (GSN - IRIS/USGS) [Data set]. International Federation of Digital Seismograph Networks. 28

Artemieva, I. M. (2019). Lithosphere thermal thickness and geothermal heat flux in greenland from a new thermal isostasy method. *Earth-Science Reviews*, 188:469–481. 3, 22, 23, 46, 71, 98, 99, 100

Bagherpur Mojaver, O. and Darbyshire, F. (2022). Crustal structure beneath the northern appalachians and the eastern grenville province. *Journal of Geophysical Research: Solid Earth*, 127(1):e2021JB023246. e2021JB023246 2021JB023246. 9

Ballmer, M., van Hunen, J., Tackley, P., and Ito, G. (2011). Spatial and temporal variability in hawaiian hotspot volcanism induced by small-scale convection. *Nature Geoscience - NAT GEOSCI*, 4:457–460. 76

Bamber, J. L., Layberry, R. L., and Gogineni, S. P. (2001). A new ice thickness and bed data set for the Greenland ice sheet: 1. Measurement, data reduction, and errors. *Journal of Geophysical Research: Atmospheres*, 106(D24):33773–33780. 3, 22, 71

Bastow, I., Thompson, D., Kendall, J.-M., Helffrich, G., Wookey, J., Snyder, D., Eaton, D., and Darbyshire, F. (2011). Precambrian Plate Tectonics: Seismic Evidence from Northern Hudson Bay. *Geology*, 39:91–94. 27, 51

Bedrosian, P. (2007). Mt+, integrating magnetotellurics to determine earth structure, physical state, and processes. *Surveys in Geophysics*, 28:121–167. 103

Berg, D., Barletta, V. R., Hassan, J., Lippert, E. Y. H., Colgan, W., Bevis, M., Steffen, R., and Khan, S. A. (2024). Vertical land motion due to present-day ice loss from greenland's and canada's peripheral glaciers. *Geophysical Research Letters*, 51(2):e2023GL104851. e2023GL104851 2023GL104851. 21, 116, 118

Biegler, L., Biros, G., Ghattas, O., Heinkenschloss, M., Keyes, D., Mallick, B., Marzouk, Y., Waanders, B., and Willcox, K. (2011). Large-scale inverse problems and quantification of uncertainty. 12

Boyce, A., Bastow, I. D., Darbyshire, F. A., Ellwood, A. G., Gilligan, A., Levin, V., and Menke, W. (2016). Subduction beneath Laurentia modified the eastern North American cratonic edge: Evidence from P wave and S wave tomography. *Journal of Geophysical Research: Solid Earth*, 121(7):5013–5030. 33

Briggs, R. D. and Tarasov, L. (2013). How to evaluate model-derived deglaciation chronologies: a case study using antarctica. *Quaternary Science Reviews*, 63:109–127. 126

British Geological Survey (1970). Great Britain Seismograph Network [Data set]. International Federation of Digital Seismograph Networks. 28

Brocher, T. M. (2005). Empirical Relations between Elastic Wavespeeds and Density in the Earth's Crust. *Bulletin of the Seismological Society of America*, 95(6):2081–2092. 82

Brocher, T. M. and Christensen, N. I. (1990). Seismic anisotropy due to preferred mineral orientation observed in shallow crustal rocks in southern Alaska. *Geology*, 18(8):737–740. 47

Brooks, C. K. (2011). The East Greenland rifted volcanic margin. *GEUS Bulletin*, 24:1–96. 3, 22, 24, 71

Brunsvik, B. R., Eilon, Z. C., and Lynner, C. (2021). Mantle Structure and Flow Across the Continent-Ocean Transition of the Eastern North American Margin: Anisotropic S-Wave Tomography. *Geochemistry, Geophysics, Geosystems*, 22(12):e2021GC010084. e2021GC010084 2021GC010084. 51

Cao, Y., Jónsson, S., and Hreinsdóttir, S. (2023). Iceland kinematics from insar. *Journal of Geophysical Research: Solid Earth*, 128(3):e2022JB025546. e2022JB025546 2022JB025546. 21

Celli, N. L., Lebedev, S., Schaeffer, A. J., and Gaina, C. (2021). The tilted iceland plume and its effect on the north atlantic evolution and magmatism. *Earth and Planetary Science Letters*, 569:117048. 41, 47, 72, 77, 93, 100, 117

Chalmers, J. A. and Pulvertaft, T. (2001). Development of the continental margins of the Labrador Sea: a review. *Geological Society, London, Special Publications*, 187(1):77–105. 24

Chase, C., Libarkin, J., and Sussman, A. (2010). Colorado plateau: Geoid and means of isostatic support. *International Geology Review*, July 2002:575–587. 79

Chase, C. G. (1985). The geological significance of the geoid. *Annual Review of Earth and Planetary Sciences*, 13(1):97–117. 79

Chen, Y. and Niu, F. (2016). Joint inversion of receiver functions and surface waves with enhanced preconditioning on densely distributed cndsn stations: Crustal and upper mantle structure beneath china. *Journal of Geophysical Research: Solid Earth*, 121(2):743–766. 74

Chopelas, A. and Boehler, R. (1992). Thermal expansivity in the lower mantle. *Geophysical Research Letters - GEOPHYS RES LETT*, 19:1983–1986. 120

Clark, J., Farrell, W., and Peltier, W. (1978). Global Changes in Postglacial Sea Level: A Numerical Calculation. *Quaternary Research*, 9:265–287. 125

Colli, L., Ghelichkhan, S., Bunge, H.-P., and Oeser, J. (2018). Retrodictions of Mid Paleogene mantle flow and dynamic topography in the Atlantic region from compressible high resolution adjoint mantle convection models: Sensitivity to deep mantle viscosity and tomographic input model. *Gondwana Research*, 53:252–272. 53

Congdon, P. (2002). Bayesian statistical modeling. *Measurement Science and Technology*, 13:643. 12

Connolly, J. (2005). Computation of phase equilibria by linear programming: A tool for geodynamic modeling and its application to subduction zone decarbonation. *Earth and Planetary Science Letters*, 236(1):524–541. 82

Constable, A., Harper, S., Dawson, J., Holsman, K., Mustonen, T., Piepenburg, D., and Rost, B. (2022). *Cross-Chapter Paper 6: Polar Regions*, pages 2319–2368. Cambridge University Press, Cambridge, UK and New York, USA. 1

Cox, A. and Hart, R. (1986). *Plate Tectonics: How It Works*. 102

Crawford, O., Al-Attar, D., Tromp, J., Mitrovica, J. X., Austermann, J., and Lau, H. C. P. (2018). Quantifying the sensitivity of post-glacial sea level change to laterally varying viscosity. *Geophysical Journal International*, 214(2):1324–1363. 146

Dahl-Jensen, T., Larsen, T. B., Woelbern, I., Bach, T., Hanka, W., Kind, R., Gregersen, S., Mosegaard, K., Voss, P., and Gudmundsson, O. (2003). Depth to Moho in Greenland: receiver-function analysis suggests two Proterozoic blocks in Greenland. *Earth and Planetary Science Letters*, 205(3):379–393. 26, 41

Danish Seismological Network (1976). GEUS Geological Survey of Denmark and Greenland, Denmark. 28

Darbyshire, F. (2005). Upper mantle structure of Arctic Canada from Rayleigh wave dispersion. *Tectonophysics*, 405:1–23. 26

Darbyshire, F. A. (2003). Crustal structure across the Canadian High Arctic region from teleseismic receiver function analysis. *Geophysical Journal International*, 152(2):372–391. 3, 22, 71

Darbyshire, F. A., Dahl-Jensen, T., Larsen, T. B., Voss, P. H., and Joyal, G. (2017). Crust and uppermost-mantle structure of Greenland and the Northwest Atlantic from Rayleigh wave group velocity tomography. *Geophysical Journal International*, 212(3):1546–1569. 3, 7, 9, 10, 22, 26, 27, 41, 50, 71, 72, 100

Darbyshire, F. A. and Eaton, D. W. (2010). The lithospheric root beneath Hudson Bay, Canada from Rayleigh wave dispersion: No clear seismological distinction between Archean and Proterozoic mantle. *Lithos*, 120(1):144–159. The lithosphere/asthenosphere boundary: Nature, formation and evolution. 9

Darbyshire, F. A., Eaton, D. W., and Bastow, I. D. (2013). Seismic imaging of the lithosphere beneath Hudson Bay: Episodic growth of the Laurentian mantle keel. *Earth and Planetary Science Letters*, 373:179–193. 27, 43, 49, 51

Darbyshire, F. A., Larsen, T. B., Mosegaard, K., Dahl-Jensen, T., Gudmundsson, O., Bach, T., Gregersen, S., Pedersen, H. A., and Hanka, W. (2004). A first detailed look at the Greenland lithosphere and upper mantle, using Rayleigh wave tomography. *Geophysical Journal International*, 158(1):267–286. 7, 26, 45, 72, 100

Darbyshire, F. A. and Lebedev, S. (2009). Rayleigh wave phase-velocity heterogeneity and multilayered azimuthal anisotropy of the Superior Craton, Ontario. *Geophysical Journal International*, 176(1):215–234. 9, 30, 32, 33

Dawes, P. R. (2009). The bedrock geology under the Inland Ice: the next major challenge for Greenland mapping. *GEUS Bulletin*, 17:57–60. 3, 22, 23, 25, 40, 41, 43, 71, 102

Deschamps, F., Lebedev, S., Meier, T., and Trampert, J. (2008). Azimuthal anisotropy of Rayleigh-wave phase velocities in the east-central United States. *Geophysical Journal International*, 173(3):827–843. 30, 31, 33

Dietrich, R., Maas, H.-G., Baessler, M., Rülke, A., Richter, A., Schwalbe, E., and Westfeld, P. (2007). Jakobshavn isbræ, west greenland: Flow velocities and tidal interaction of the front area from 2004 field observations. *Journal of Geophysical Research: Earth Surface*, 112(F3). 116

Dodman, D., Hayward, B., Pelling, M., Castan Broto, V., Chow, W., Chu, E., Dawson, R., Khirfan, L., McPhearson, T., Prakash, A., Zheng, Y., and Ziervogel, G. (2022). *Cities, Settlements and Key Infrastructure*, pages 907–1040. Cambridge University Press, Cambridge, UK and New York, USA. 1

Doin, M.-P., Fleitout, L., and McKenzie, D. (1996). Geoid anomalies and the structure of continental and oceanic lithospheres. *Journal of Geophysical Research: Solid Earth*, 101(B7):16119–16135. 79

Doubrovine, P. V., Steinberger, B., and Torsvik, T. H. (2012). Absolute plate motions in a reference frame defined by moving hot spots in the pacific, atlantic, and indian oceans. *Journal of Geophysical Research: Solid Earth*, 117(B9). 102

Dube, J.-M., Darbyshire, F. A., Liddell, M. V., Stephenson, R., and Oakey, G. (2020). Seismic anisotropy of the Canadian High Arctic: Evidence from shear-wave splitting. *Tectonophysics*, 789:228524. 26, 27

Eaton, D. and Darbyshire, F. (2010). Lithospheric architecture and crustal evolution of the Hudson Bay region. *Tectonophysics*, 480:1–22. 40

Eaton, D., Frederiksen, A., and Miong, S.-K. (2004). Shear-wave splitting observations in the lower Great Lakes region: Evidence for regional anisotropic domains and keel-modified asthenospheric flow. *Geophysical Research Letters*, 31(7). 51

Eaton, D. W., Darbyshire, F., Evans, R. L., Grütter, H., Jones, A. G., and Yuan, X. (2009). The elusive lithosphere–asthenosphere boundary (lab) beneath cratons. *Lithos*, 109(1):1–22. Continental Lithospheric Mantle: The Petro-Geophysical Approach. 98, 100

Edwards, T. L., Nowicki, S., Marzeion, B., Hock, R., Goelzer, H., Seroussi, H., Jourdain, N. C., Slater, D. A., Turner, F. E., Smith, C. J., McKenna, C. M., Simon, E., Abe-Ouchi, A., Gregory, J. M., Larour, E., Lipscomb, W. H., Payne, A. J., Shepherd, A., Agosta, C., Alexander, P., Albrecht, T., Anderson, B., Asay-Davis, X., Aschwanden, A., Barthel, A., Bliss, A., Calov, R., Chambers, C., Champollion, N., Choi, Y., Cullather, R., Cuzzone, J., Dumas, C., Felikson, D., Fettweis, X., Fujita, K., Galton-Fenzi, B. K., Gladstone, R., Golledge, N. R., Greve, R., Hattermann, T., Hoffman, M. J., Humbert, A., Huss, M., Huybrechts, P., Immerzeel, W., Kleiner, T., Kraaijenbrink, P., Le clec'h, S., Lee, V., Leguy, G. R., Little, C. M., Lowry, D. P., Malles, J.-H., Martin, D. F., Maussion, F., Morlighem, M., O'Neill, J. F., Nias, I., Pattyn, F., Pelle, T., Price, S. F., Quiquet, A., Radić, V., Reese, R., Rounce, D. R., Rückamp, M., Sakai, A., Shafer, C., Schlegel, N.-J., Shannon, S., Smith, R. S., Straneo, F., Sun, S., Tarasov, L., Trusel, L. D., Van Breedam, J., van de Wal, R., van den Broeke, M., Winkelmann, R., Zekollari, H., Zhao, C., Zhang, T., and Zwinger, T. (2021). Projected land ice contributions to twenty-first-century sea level rise. *Nature (London)*, 593(7857). 23, 72

Ekström, G. (2011). A global model of Love and Rayleigh surface wave dispersion and anisotropy, 25-250 s. *Geophysical Journal International*, 187(3):1668–1686. 26, 72

Engelhart, Simon E, H. B. P. D. B. C. P. W. R. T. T. E. (2009). Spatial variability of late Holocene and 20th century sea-level rise along the Atlantic coast of the United States. *Geology*, 37. 2

Evans, M. S., Kendall, J.-M., and Willemann, R. J. (2006). Automated SKS splitting and upper-mantle anisotropy beneath Canadian seismic stations. *Geophysical Journal International*, 165(3):931–942. 26

Farinotti, D., Huss, M., Fürst, J., Landmann, J., Machguth, H., Maussion, F., and Pandit, A. (2019). A consensus estimate for the ice thickness distribution of all glaciers on earth. *Nature Geoscience*, 12. 81

Farrell, W. E. and Clark, J. A. (1976). On Postglacial Sea Level. *Geophysical Journal International*, 46(3):647–667. 2, 17

Faure, N. (2022). GIA modelling of Greenland using an ice history from the last glacial cycle to present day with lateral varying viscosity profiles on a spherical Earth. Master's thesis, TU Delft. 23

Fleming, K. and Lambeck, K. (2004). Constraints on the greenland ice sheet since the last glacial maximum from sea-level observations and glacial-rebound models. *Quaternary Science Reviews*, 23(9):1053–1077. 116

Fletcher, W. (2018). Determining the Shear Wave Velocity structure of Shallow Marine Sediments utilizing the MASW method [Data set]. International Federation of Digital Seismograph Networks. 28

Foster, A., Darbyshire, F., and Schaeffer, A. (2020). Anisotropic structure of the central North American Craton surrounding the Mid-Continent Rift: Evidence from Rayleigh waves. *Precambrian Research*, 342:105662. 33, 49

Foster, A., Ekström, G., and Nettles, M. (2014). Surface wave phase velocities of the western united states from a two-station method. *Geophysical Journal International*, 196:1189–1206. 28

Fouch, M. J., Fischer, K. M., Parmentier, E. M., Wysession, M. E., and Clarke, T. J. (2000). Shear wave splitting, continental keels, and patterns of mantle flow. *Journal of Geophysical Research: Solid Earth*, 105(B3):6255–6275. 51

Fouch, M. J. and Rondenay, S. (2006). Seismic anisotropy beneath stable continental interiors. *Physics of the Earth and Planetary Interiors*, 158(2):292–320. Continental Anisotropy. 51

Frederiksen, A., Ferguson, I., Eaton, D., Miong, S.-K., and Gowan, E. (2006). Mantle fabric at multiple scales across an Archean–Proterozoic boundary, Grenville Front, Canada. *Physics of the Earth and Planetary Interiors*, 158(2):240–263. Continental Anisotropy. 51

Fullea, J., Afonso, J. C., Connolly, J. A. D., Fernàndez, M., García-Castellanos, D., and Zeyen, H. (2009). Litmod3d: An interactive 3-d software to model the thermal, compositional, density, seismological, and rheological structure of the lithosphere and sublithospheric upper mantle. *Geochemistry, Geophysics, Geosystems*, 10(8). 3, 81, 82

Funck, T., Ögmundur Erlendsson, Geissler, W. H., Gradmann, S., Kimbell, G. S., McDermott, K., and Petersen, U. K. (2017). A review of the ne atlantic conjugate margins based on seismic refraction data. *Geological Society, London, Special Publications*, 447(1):171–205. 81

Funder, S. and Hansen, L. (1996). The greenland ice sheet - a model for its culmination and decay during and after the last glacial maximum. *Bulletin of the Geological Society of Denmark*, 42. 2

GEOFON Data Centre (1993). GEOFON Seismic Network [Data set]. Deutsches Geo-ForschungsZentrum GFZ. 28

Gerya, T. (2010). *Introduction to numerical geodynamic modelling*. Cambridge University Press. 76

Gilligan, A., Bastow, I. D., and Darbyshire, F. A. (2016). Seismological structure of the 1.8 Ga Trans-Hudson Orogen of North America. *Geochemistry, Geophysics, Geosystems*, 17:2421–2433. 41

Gradmann, S., Ebbing, J., and Fullea, J. (2013). Integrated geophysical modelling of a lateral transition zone in the lithospheric mantle under Norway and Sweden. *Geophysical Journal International*, 194(3):1358–1373. 73

Griffin, W., O'Reilly, S. Y., Doyle, B., Pearson, N., Coopersmith, H., Kivi, K., Malkovets, V., and Pokhilenko, N. (2004). Lithosphere mapping beneath the north american plate. *Lithos*, 77(1):873–922. Selected Papers from the Eighth International Kimberlite Conference. Volume 2: The J. Barry Hawthorne Volume. 97, 98

Guo, Z., Afonso, J. C., Qashqai, M. T., Yang, Y., and Chen, Y. J. (2016). Thermochemical structure of the north china craton from multi-observable probabilistic inversion: Extent and causes of cratonic lithosphere modification. *Gondwana Research*, 37:252–265. 74, 75, 79

Haario, H., Laine, M., Mira, A., and Saksman, E. (2006). Dram: efficient adaptive mcmc. *Statistics and Computing*, 16:339–354. 74

Haines, A. (2003). Climate Change 2001: The Scientific Basis. Contribution of Working Group 1 to the Third Assessment report of the Intergovernmental Panel on Climate Change.: JT Houghton, Y Ding, DJ Griggs, M Noguer, PJ van der Winden, X Dai. Cambridge: Cambridge University Press, 2001, pp. 881, £34.95 (HB) ISBN: 0-21-01495-6; £90.00 (HB) ISBN: 0-521-80767-0. *International Journal of Epidemiology*, 32(2):321–321. 22

Hanna, E., Pattyn, F., Navarro, F., Favier, V., Goelzer, H., van den Broeke, M. R., Vizcaino, M., Whitehouse, P. L., Ritz, C., Bulthuis, K., and Smith, B. (2020). Mass balance of the ice sheets and glaciers – progress since ar5 and challenges. *Earth-Science Reviews*, 201:102976. 1

Haskell, N. A. (1953). The dispersion of surface waves on multilayered media. *Bulletin of the Seismological Society of America*, 43(1):17–34. 83

Henriksen, N., Chalmers, J., and Friend, C. (2008). *Geological History of Greenland: Four Billion Years of Earth Evolution*. Geological Survey of Denmark and Greenland. 23, 24

Henriksen, N., Higgins, A., Kalsbeek, F., and Pulvertaft, T. C. R. (2009). Greenland from Archaean to Quaternary. Descriptive text to the 1995 Geological map of Greenland, 1:2 500 000. 2nd edition. *GEUS Bulletin*, 18:1–126. 23, 24, 44, 49, 52

Herrmann, R. B. (2013). Computer Programs in Seismology: An Evolving Tool for Instruction and Research. *Seismological Research Letters*, 84(6):1081–1088. 83

Hodges, K. (2016). Crustal Decoupling in Collisional Orogenesis: Examples from the East Greenland Caledonides and Himalaya. *Annual Review of Earth and Planetary Sciences*, 44:685–708. 44, 49

Holbrook, W., Larsen, H., Korenaga, J., Dahl-Jensen, T., Reid, I., Kelemen, P., Hopper, J., Kent, G., Lizarralde, D., Bernstein, S., and Detrick, R. (2001). Mantle thermal structure and active upwelling during continental breakup in the North Atlantic. *Earth and Planetary Science Letters*, 190(3):251–266. 24, 45

Hopper, J. R., Dahl-Jensen, T., Holbrook, W. S., Larsen, H. C., Lizarralde, D., Korenaga, J., Kent, G. M., and Kelemen, P. B. (2003). Structure of the SE Greenland margin from seismic reflection and refraction data: Implications for nascent spreading center subsidence and asymmetric crustal accretion during North Atlantic opening. *Journal of Geophysical Research: Solid Earth*, 108(B5). 24

Horowitz, M., Jauhar, S., Natesan, S., Murray, R., and Taylor, D. (2021). A method for tapering antipsychotic treatment that may minimize the risk of relapse. *Schizophrenia Bulletin*, 47. 78

IMBIE, T. (2019). Mass balance of the greenland ice sheet from 1992 to 2018. 579. 1

Institut de physique du globe de Paris (IPGP), & École et Observatoire des Sciences de la Terre de Strasbourg (EOST) (1982). GEOSCOPE, French Global Network of broad band seismic stations. Institut de physique du globe de Paris (IPGP), Université de Paris. 28

IRIS HQ (DC) (2012). Greenland Ice Sheet Monitoring Network [Data set]. International Federation of Digital Seismograph Networks. 28

Ito, G., Dunn, R., Li, A., Wolfe, C. J., Gallego, A., and Fu, Y. (2014). Seismic anisotropy and shear wave splitting associated with mantle plume-plate interaction. *Journal of Geophysical Research: Solid Earth*, 119(6):4923–4937. 53

Ito, G., Lin, J., and Graham, D. (2003). Observational and theoretical studies of the dynamics of mantle plume–mid-ocean ridge interaction. *Reviews of Geophysics*, 41(4). 53

Jackson, I. and Faul, U. H. (2010). Grainsize-sensitive viscoelastic relaxation in olivine: Towards a robust laboratory-based model for seismological application. *Physics of the Earth and Planetary Interiors*, 183(1):151–163. Special Issue on Deep Slab and Mantle Dynamics. 83

Jason Morgan, W. (1983). Hotspot tracks and the early rifting of the Atlantic. *Tectonophysics*, 94(1):123–139. Processes of Continental Rifting. 102

Joyce, J. (2021). Bayes' Theorem. In Zalta, E. N., editor, *The Stanford Encyclopedia of Philosophy*. Metaphysics Research Lab, Stanford University, Fall 2021 edition. 11

Karato, S.-i., Jung, H., Katayama, I., and Skemer, P. (2008). Geodynamic Significance of Seismic Anisotropy of the Upper Mantle: New Insights from Laboratory Studies. *Annual Review of Earth and Planetary Sciences*, 36(1):59–95. 19, 47, 82, 117

Keilis-Borok, V., Yanovskaya, T., Levshin, A., Its, E., Lander, A., Bukchin, B., Barmin, M., and Ratnikova, L. (2012). *Seismic Surface Waves in a Laterally Inhomogeneous Earth*. Modern Approaches in Geophysics. Springer Netherlands. 40

Kendall, R., Mitrovica, J., and Milne, G. (2005). On post-glacial sea level - ii. numerical formulation and comparative results on spherically symmetric models. *Geophysical Journal International - GEOPHYS J INT*, 161:679–706. 125

Kennett, B. L. N., Engdahl, E. R., and Buland, R. (1995). Constraints on seismic velocities in the Earth from traveltimes. *Geophysical Journal International*, 122(1):108–124. 29

Khan, S. A., Colgan, W., Neumann, T. A., van den Broeke, M. R., Brunt, K. M., Noël, B., Bamber, J. L., Hassan, J., and Bjørk, A. A. (2022). Accelerating ice loss from peripheral glaciers in north greenland. *Geophysical Research Letters*, 49(12):e2022GL098915. e2022GL098915 2022GL098915. 21, 125, 133, 134

Khan, S. A., Sasgen, I., Bevis, M., van Dam, T., Bamber, J. L., Wahr, J., Willis, M., Kjær, K. H., Wouters, B., Helm, V., Csatho, B., Fleming, K., Bjørk, A. A., Aschwanden, A., Knudsen, P., and Munneke, P. K. (2016). Geodetic measurements reveal similarities between post–Last

Glacial Maximum and present-day mass loss from the Greenland ice sheet. *Science Advances*, 2(9). 2, 21, 23, 116, 117

Kjaer, K. H., Bjørk, A. A., Kjeldsen, K. K., Hansen, E. S., Andresen, C. S., Siggaard-Andersen, M.-L., Khan, S. A., Søndergaard, A. S., Colgan, W., Schomacker, A., Woodroffe, S., Funder, S., Rouillard, A., Jensen, J. F., and Larsen, N. K. (2022). Glacier response to the little ice age during the neoglacial cooling in greenland. *Earth-Science Reviews*, 227:103984. 133

Kjeldsen, K., Korsgaard, N., Bjørk, A., Khan, S., Box, J., Funder, S., Larsen, N., Bamber, J., Colgan, W., Van den Broeke, M., Siggaard-Andersen, M.-L., Nuth, C., Schomacker, A., Andresen, C., Willerslev, E., and Kjaer, K. (2015). Spatial and temporal distribution of mass loss from the greenland ice sheet since ad 1900. *Nature*, 528:396–400. 125, 133, 134

Kumar, A., Fernàndez, M., Jiménez-Munt, I., Torne, M., Vergés, J., and Afonso, J. C. (2020). Litmod2d_2.0: An improved integrated geophysical-petrological modeling tool for the physical interpretation of upper mantle anomalies. *Geochemistry, Geophysics, Geosystems*, 21(3):e2019GC008777. e2019GC008777 2019GC008777. 81

Kumar, P., Kind, R., Priestley, K., and Dahl-Jensen, T. (2007). Crustal structure of Iceland and Greenland from receiver function studies. *Journal of Geophysical Research: Solid Earth*, 112(B3). 89

Lambeck, K., Purcell, A., and Zhao, S. (2017). The north american late wisconsin ice sheet and mantle viscosity from glacial rebound analyses. *Quaternary Science Reviews*, 158:172–210. 19

Larsen, L. and Pedersen, A. (2009). Petrology of the paleocene picrites and flood basalts on disko and nuussuaq, west greenland. *Journal of Petrology - J PETROL*, 50:1667–1711. 98

Larson, E. and Ekström, G. (2001). Global Models of Surface Wave Group Velocity. *Pure and Applied Geophysics*, 158:1377–1399. 26, 72

Laske, G., Masters, G., Ma, Z., and Pasyanos, M. (2013). Update on CRUST1.0 - A 1-degree global model of Earth's crust. *Abstract EGU2013-2658 presented at 2013 Geophys. Res. Abstracts 15*, 15:2658–. 44, 80, 81

Latychev, K., Mitrovica, J., Tromp, J., Tamisiea, M., Komatitsch, D., and Christara, C. (2005). Glacial isostatic adjustment on 3-d earth models: A finite-volume formulation. *Geophysical Journal International - GEOPHYS J INT*, 161:421–444. 119, 125

Lau, H. C. P. and Holtzman, B. K. (2019). "measures of dissipation in viscoelastic media" extended: Toward continuous characterization across very broad geophysical time scales. *Geophysical Research Letters*, 46(16):9544–9553. 19

Lawver, L. A. and Muller, R. D. (1994). Iceland hotspot track. *Geology*, 22(4):311–314. 102

Lebedev, S., Schaeffer, A. J., Fullea, J., and Pease, V. (2018). Seismic tomography of the Arctic region: inferences for the thermal structure and evolution of the lithosphere. *Geological Society, London, Special Publications*, 460(1):419–440. 3, 22, 23, 26, 41, 46, 71, 72, 91, 95, 96, 99, 100, 102, 144

Lebedev, S. and Van Der Hilst, R. D. (2008). Global upper-mantle tomography with the automated multimode inversion of surface and S-wave forms. *Geophysical Journal International*, 173(2):505–518. 10, 31

Lebedeva-Ivanova, N., Gaina, C., Minakov, A., and Kashubin, S. (2019). Arccrust: Arctic crustal thickness from 3-d gravity inversion. *Geochemistry, Geophysics, Geosystems*, 20(7):3225–3247. 46, 81, 98

Lecavalier, B. S., Fisher, D. A., Milne, G. A., Vinther, B. M., Tarasov, L., Huybrechts, P., Lacelle, D., Main, B., Zheng, J., Bourgeois, J., and Dyke, A. S. (2017). High arctic holocene temperature record from the agassiz ice cap and greenland ice sheet evolution. *Proceedings of the National Academy of Sciences*, 114(23):5952–5957. 117, 118, 119, 120, 125

Lecavalier, B. S., Milne, G. A., Simpson, M. J., Wake, L., Huybrechts, P., Tarasov, L., Kjeldsen, K. K., Funder, S., Long, A. J., Woodroffe, S., Dyke, A. S., and Larsen, N. K. (2014). A model of Greenland ice sheet deglaciation constrained by observations of relative sea level and ice extent. *Quaternary Science Reviews*, 102:54–84. 2, 3, 23, 72, 116, 118, 125, 127, 130, 135, 136

Levshin, A., Ritzwoller, M., Barmin, M., Villaseñor, A., and Padgett, C. (2001). New constraints on the arctic crust and uppermost mantle: surface wave group velocities, Pn, and Sn. *Physics of the Earth and Planetary Interiors*, 123(2):185–204. Tomographic Imagining of 3-D Velocity Structure and Accurate Earthquake Location,. 26, 27, 50, 72

Li, T., Wu, P., Steffen, H., and Wang, H. (2018). In search of laterally heterogeneous viscosity models of glacial isostatic adjustment with the ICE-6G_C global ice history model. *Geophysical Journal International*, 214(2):1191–1205. 19

Liddell, M. V., Bastow, I., Darbyshire, F., Gilligan, A., and Pugh, S. (2017). The formation of laurentia: Evidence from shear wave splitting. *Earth and Planetary Science Letters*, 479:170–178. 27, 51, 52

Lloyd, A. J., Wiens, D. A., Zhu, H., Tromp, J., Nyblade, A. A., Aster, R. C., Hansen, S. E., Dalziel, I. W. D., Wilson, T., Ivins, E. R., and O'Donnell, J. P. (2020). Seismic structure of the antarctic upper mantle imaged with adjoint tomography. *Journal of Geophysical Research: Solid Earth*, 125(3). 146

Love, R., Milne, G. A., Ajourlou, P., Parang, S., Tarasov, L., and Latychev, K. (2024). A fast surrogate model for 3d-earth glacial isostatic adjustment using tensorflow (v2.8.10) artificial neural networks. *EGUsphere*, 2024:1–25. 5, 127, 129, 135, 145, 146

Lu, C., Forte, A. M., Simmons, N. A., Grand, S. P., Kajan, M. N., Lai, H., and Garnero, E. J. (2020). The Sensitivity of Joint Inversions of Seismic and Geodynamic Data to Mantle Viscosity. *Geochemistry, Geophysics, Geosystems*, 21(4):e2019GC008648. 53

Lucazeau, F. (2019). Analysis and mapping of an updated terrestrial heat flow data set. *Geochemistry, Geophysics, Geosystems*, 20(8):4001–4024. 79, 80, 107

MacGregor, J. A., Colgan, W. T., Paxman, G. J., Tinto, K. J., Csathó, B., Darbyshire, F. A., Fahnestock, M. A., Kokfelt, T. F., MacKie, E. J., Morlighem, M., et al. (2024). Geologic provinces beneath the Greenland Ice Sheet constrained by geophysical data synthesis. *Geophysical Research Letters*, 51(8):e2023GL107357. 40, 41, 43, 44, 49

Marianne Karplus, . G. K. (2017). Lemon Creek Glacier - UTEP [Data set]. International Federation of Digital Seismograph Networks. 28

Marquart, G., Schmeling, H., and Čadek, O. (2007). Dynamic models for mantle flow and seismic anisotropy in the North Atlantic region and comparison with observations. *Geochemistry, Geophysics, Geosystems*, 8(2). 53

Martos, Y. M., Jordan, T. A., Catalán, M., Jordan, T. M., Bamber, J. L., and Vaughan, D. G. (2018). Geothermal Heat Flux Reveals the Iceland Hotspot Track Underneath Greenland. *Geophysical Research Letters*, 45(16):8214–8222. 3, 43, 47, 79, 80, 91, 101, 102, 107

Meier, T., Dietrich, K., Stöckhert, B., and Harjes, H.-P. (2004). One-dimensional models of shear wave velocity for the eastern Mediterranean obtained from the inversion of Rayleigh wave phase velocities and tectonic implications. *Geophysical Journal International*, 156(1):45–58. 9, 28, 76

Meltzer, A. and Christensen, N. (2001). Nanga Parbat crustal anisotropy: Implications for interpretation of crustal velocity structure and shear-wave splitting. *Geophysical Research Letters*, 28(10):2129–2132. 47

Meyer, B., Chulliat, A., and Saltus, R. (2017). Derivation and error analysis of the earth magnetic anomaly grid at 2 arc min resolution version 3 (EMAG2v3). *Geochemistry, Geophysics, Geosystems*, 18(12):4522–4537. 49, 52

Milne, Glenn, A. and Mitrovica, Jerry, X. (1998). Postglacial sea-level change on a rotating earth. *Geophysical Journal International*, 133(1):1–19. 2, 17, 125

Milne, G. and Shennan, I. (2013). Isostasy: glaciation-induced sea-level change. In *Encyclopedia of Quaternary Science*, volume 3, page 452–459. Elsevier, Oxford. 2

Milne, G. A., Latychev, K., Schaeffer, A., Crowley, J. W., Lecavalier, B. S., and Audette, A. (2018). The influence of lateral Earth structure on glacial isostatic adjustment in Greenland. *Geophysical Journal International*, 214(2):1252–1266. 2, 117, 120, 125, 133, 136, 146

Milne, G. A., Mitrovica, J. X., and Davis, J. L. (1999). Near-field hydro-isostasy: the implementation of a revised sea-level equation. *Geophysical Journal International*, 139(2):464–482. 17

Mira, A. (2001). On metropolis-hastings algorithms with delayed rejection. *Metron*, 59. 74

Mitrovica, J. and Milne, G. (2002). On the origin of late Holocene sea-level highstands within equatorial ocean basins. *Quaternary Science Reviews*, 21(20):2179–2190. 17

Mitrovica, J. and Milne, G. (2003). On post-glacial sea level: I. general theory. *Geophysical Journal International - GEOPHYS J INT*, 154:253–267. 125

Mitrovica, J. X., Forte, A. M., and Simons, M. (2000). A reappraisal of postglacial decay times from Richmond Gulf and James Bay, Canada. *Geophysical Journal International*, 142(3):783–800. 126

Mitrovica, J. X. and Peltier, W. R. (1991). On postglacial geoid subsidence over the equatorial oceans. *Journal of Geophysical Research: Solid Earth*, 96(B12):20053–20071. 19

Mitrovica, J. X. and Wahr, J. (2011). Ice age earth rotation*. *Annual Review of Earth and Planetary Sciences*, 39(Volume 39, 2011):577–616. 14

Mitrovica, J. X., Wahr, J., Matsuyama, I., and Paulson, A. (2005). The rotational stability of an ice-age earth. *Geophysical Journal International*, 161(2):491–506. 125

Mjelde, R., Aurvåg, R., Kodaira, S., Shimamura, H., Gunnarsson, K., Nakanishi, A., and Shiobara, H. (2002). Vp/vs-ratios from the central kolbeinsey ridge to the jan mayen basin, north atlantic; implications for lithology, porosity and present-day stress field. *Marine Geophysical Researches*, 23:123–145. 89

Montagner, J.-P. and Anderson, D. L. (1989). Petrological constraints on seismic anisotropy. *Physics of the Earth and Planetary Interiors*, 54(1):82–105. 31, 37

Mordret, A. (2018). Uncovering the Iceland Hot Spot Track Beneath Greenland. *Journal of Geophysical Research: Solid Earth*, 123(6):4922–4941. 3, 7, 22, 23, 26, 41, 71, 72, 95, 102

Morlighem, M. e. a. (2022). Icebridge bedmachine greenland, version 5. 81

Muller, R. D., Royer, J.-Y., and Lawver, L. A. (1993). Revised plate motions relative to the hotspots from combined Atlantic and Indian Ocean hotspot tracks. *Geology*, 21(3):275–278. 102

Nathan, E. M., Hariharan, A., Florez, D., and Fischer, K. M. (2021). Multi-Layer Seismic Anisotropy Beneath Greenland. *Geochemistry, Geophysics, Geosystems*, 22(5):e2020GC009512. e2020GC009512 2020GC009512. 26, 27, 50, 52, 53

Natural Resources Canada (1975). Canadian National Seismograph Network [Data set]. International Federation of Digital Seismograph Networks. 28

Nicolas, A. and Christensen, N. I. (1987). *Formation of Anisotropy in Upper Mantle Peridotites - A Review*, pages 111–123. American Geophysical Union (AGU). 9

Nolet, G. (1993). Solving large linearized tomographic problems. *Seismic tomography: theory and practice*, pages 227–247. 33

Norsar (1971). NORSAR Station Network [Data set]. NORSAR. 28

Oakey, G. N. and Stephenson, R. (2008). Crustal structure of the Innuitian region of Arctic Canada and Greenland from gravity modelling: implications for the Palaeogene Eurekan orogen. *Geophysical Journal International*, 173:1039–1063. 24

ONeill, C., Müller, D., and Steinberger, B. (2005). On the uncertainties in hot spot reconstructions and the significance of moving hot spot reference frames. *Geochemistry, Geophysics, Geosystems*, 6(4). 102

Oppenheimer, M., Glavovic, B., Hinkel, J., van de Wal, R., Magnan, A., Abd-Elgawad, A., Cai, R., Cifuentes-Jara, M., DeConto, R., Ghosh, T., Hay, J., Isla, F., Marzeion, B., Meyssignac, B., and Sebesvari, Z. (2019). Sea level rise and implications for low-lying islands, coasts and communities. *IPCC Special Report on the Ocean and Cryosphere in a Changing Climate*. 15

O'Reilly, S. and Griffin, W. (2006). Imaging global chemical and thermal heterogeneity in the subcontinental lithospheric mantle with garnets and xenoliths: Geophysical implications. *Tectonophysics*, 416(1):289–309. The Heterogeneous Mantle. 97, 98

Paige, C. C. and Saunders, M. A. (1982). LSQR: An Algorithm for Sparse Linear Equations and Sparse Least Squares. *ACM Trans. Math. Softw.*, 8(1):43–71. 31

Pail, R., Fecher, T., Barnes, D., Factor, J. F., Holmes, S. A., Gruber, T., and Zingerle, P. (2018). Short note: the experimental geopotential model xgm2016. *Journal of Geodesy*, 92:443–451. 78, 80

Pan, L., Mitrovica, J. X., Milne, G. A., Hoggard, M. J., and Woodroffe, S. A. (2024). Timescales of glacial isostatic adjustment in Greenland: is transient rheology required? *Geophysical Journal International*, 237(2):989–995. 117, 136, 137

Pattyn, F., Ritz, C., Hanna, E., Asay-Davis, X., DeConto, R., Durand, G., Favier, L., Fettweis, X., Goelzer, H., Golledge, N., Munneke, P., Lenaerts, J., Nowicki, S., Payne, A., Robinson, A., Seroussi, H., Trusel, L., and Van den Broeke, M. (2018). The greenland and antarctic ice sheets under 1.5 °c global warming. *Nature Climate Change*, 8. 1

Paxman, G. J. G., Lau, H. C. P., Austermann, J., Holtzman, B. K., and Havlin, C. (2023). Inference of the timescale-dependent apparent viscosity structure in the upper mantle beneath greenland. *AGU Advances*, 4(2):e2022AV000751. e2022AV000751 2022AV000751. 2, 20, 24, 117, 136, 137

Pedersen, H. (2006). Impacts of non-plane waves on two-station measurements of phase velocities. *Geophysical Journal International*, 165:279–287. 28

Pedersen, H., Boué, P., Poli, P., and Colombi, A. (2015). Arrival angle anomalies of rayleigh waves observed at a broadband array: A systematic study based on earthquake data, full waveform simulations and noise correlations. *Geophysical Journal International*, 203:1626–1641. 28

Peltier, W. R., Argus, D. F., and Drummond, R. (2015). Space geodesy constrains ice age terminal deglaciation: The global ice-6g_c (vm5a) model. *Journal of Geophysical Research: Solid Earth*, 120(1):450–487. 19

Petrescu, L., Darbyshire, F., Bastow, I., Totten, E., and Gilligan, A. (2017). Seismic anisotropy of Precambrian lithosphere: Insights from Rayleigh wave tomography of the eastern Superior Craton. *Journal of Geophysical Research: Solid Earth*, 122(5):3754–3775. 9, 49

Petrov, O., Morozov, A., Shokalsky, S., Kashubin, S., Artemieva, I. M., Sobolev, N., Petrov, E., Ernst, R. E., Sergeev, S., and Smelror, M. (2016). Crustal structure and tectonic model of the Arctic region. *Earth-Science Reviews*, 154:29–71. 44, 81

Pilidou, S., Priestley, K., Gudmundsson, O., and Debayle, E. (2004). Upper mantle S-wave speed heterogeneity and anisotropy beneath the North Atlantic from regional surface wave tomography: the Iceland and Azores plumes. *Geophysical Journal International*, 159(3):1057–1076. 27, 50

Pourpoint, M., Anandakrishnan, S., Ammon, C., and Alley, R. (2018a). Lithospheric structure of greenland from ambient noise and earthquake surface wave tomography. *Journal of Geophysical Research: Solid Earth*, 123. 7, 26, 41, 72

Pourpoint, M., Anandakrishnan, S., and Ammon, C. J. (2018b). High-Resolution Rayleigh Wave Group Velocity Variation Beneath Greenland. *Journal of Geophysical Research: Solid Earth*, 123(2):1516–1539. 3, 7, 22, 26, 41, 71, 72

Pörtner, H.-O., Roberts, D., Adams, H., Adelekan, I., Adler, C., Adrian, R., Aldunce, P., Ali, E., Begum, R. A., Friedl, B. B., Kerr, R. B., Biesbroek, R., Birkmann, J., Bowen, K., Caretta, M., Carnicer, J., Castellanos, E., Cheong, T., Chow, W., G. Cissé, G. C., and Ibrahim, Z. Z. (2022). *Climate Change 2022: Impacts, Adaptation and Vulnerability*. Technical Summary. Cambridge University Press, Cambridge, UK and New York, USA. 1

Ranalli, G. (1995). *Rheology of the Earth*. Springer Netherlands. 15, 16, 117

Rickers, F., Fichtner, A., and Trampert, J. (2013). The Iceland–Jan Mayen plume system and its impact on mantle dynamics in the North Atlantic region: Evidence from full-waveform inversion. *Earth and Planetary Science Letters*, 367:39–51. 26

Ritsema, J., Deuss, A., van Heijst, H. J., and Woodhouse, J. H. (2011). S40RTS: a degree-40 shear-velocity model for the mantle from new Rayleigh wave dispersion, teleseismic traveltime and normal-mode splitting function measurements. *Geophysical Journal International*, 184(3):1223–1236. 121

Ritzwoller, M. H., Shapiro, N. M., Barmin, M. P., and Levshin, A. L. (2002). Global surface wave diffraction tomography. *Journal of Geophysical Research: Solid Earth*, 107(B12):ESE 4–1–ESE 4–13. 26, 72

Ritzwoller, M. H., Shapiro, N. M., Levshin, A. L., and Leahy, G. M. (2001). Crustal and upper mantle structure beneath Antarctica and surrounding oceans. *Journal of Geophysical Research: Solid Earth*, 106(B12):30645–30670. 26, 72

Rogozhina, I., Petrunin, A., Vaughan, A., Steinberger, B., Johnson, J., Kaban, M., Calov, R., Rickers, F., Thomas, M., and Koulakov, I. (2016). Melting at the base of the Greenland Ice Sheet explained by Iceland hotspot history. *Nature Geoscience*, 9. 3, 22, 43, 44, 47, 71, 72, 91, 93, 101, 102

S. Zlotnik, J.C. Afonso, P. D. and Fernández, M. (2008). Small-scale gravitational instabilities under the oceans: Implications for the evolution of oceanic lithosphere and its expression in geophysical observables. *Philosophical Magazine*, 88(28-29):3197–3217. 76

Schaeffer, A. and Lebedev, S. (2014). Imaging the North American continent using waveform inversion of global and USArray data. *Earth and Planetary Science Letters*, 402:26–41. 3, 22, 71

Schaeffer, A., Lebedev, S., and Becker, T. (2016). Azimuthal seismic anisotropy in the Earth's upper mantle and the thickness of tectonic plates. *Geophysical Journal International*, 207(2):901–933. 3, 22, 27, 53, 71, 72, 96

Schaeffer, A. J. and Lebedev, S. (2013). Global shear speed structure of the upper mantle and transition zone. *Geophysical Journal International*, 194(1):417–449. 26, 33, 45, 72, 96, 100, 121

Schiffer, C., Balling, N., Jacobsen, B. H., Stephenson, R. A., and Nielsen, S. B. (2014). Seismological evidence for a fossil subduction zone in the East Greenland Caledonides. *Geology*, 42(4):311–314. 49

Schiffer, C., Peace, A. L., Jess, S., and Rondenay, S. (2022). The crustal structure in the Northwest Atlantic region from receiver function inversion – Implications for basin dynamics and magmatism. *Tectonophysics*, 825:229235. 3, 22, 71

Schmidt-Aursch, M. C. and Jokat, W. (2005). The crustal structure of central East Greenland—I: From the Caledonian orogen to the Tertiary igneous province. *Geophysical Journal International*, 160(2):736–752. 24

Schutt, D. L. and Lesher, C. E. (2010). Compositional trends among kaapvaal craton garnet peridotite xenoliths and their effects on seismic velocity and density. *Earth and Planetary Science Letters*, 300(3):367–373. 96

Scripps Institution of Oceanography (1986). Global Seismograph Network - IRIS/IDA [Data set]. International Federation of Digital Seismograph Networks. 28

Shackleton, N. J. and Opdyke, N. D. (1973). Oxygen isotope and palaeomagnetic stratigraphy of equatorial pacific core v28-238: Oxygen isotope temperatures and ice volumes on a 105 year and 106 year scale. *Quaternary Research*, 3(1):39–55. 13

Shan, B., Afonso, J. C., Yang, Y., Grose, C. J., Zheng, Y., Xiong, X., and Zhou, L. (2014). The thermochemical structure of the lithosphere and upper mantle beneath south china: Results from multiobservable probabilistic inversion. *Journal of Geophysical Research: Solid Earth*, 119(11):8417–8441. 3, 74, 75, 79, 82

Shearer, P. M. (2019). *Introduction to Seismology*. Cambridge University Press, 3 edition. 6, 8

Shennan, I. (2015). *Handbook of Sea-Level Research*, pages 3–25. 20

Shepherd, A., Ivins, E. R., A, G., Barletta, V. R., Bentley, M. J., Bettadpur, S., Briggs, K. H., Bromwich, D. H., Forsberg, R., Galin, N., Horwath, M., Jacobs, S., Joughin, I., King, M. A., Lenaerts, J. T. M., Li, J., Ligtenberg, S. R. M., Luckman, A., Luthcke, S. B., McMillan, M., Meister, R., Milne, G., Mouginot, J., Muir, A., Nicolas, J. P., Paden, J., Payne, A. J., Pritchard, H., Rignot, E., Rott, H., Sørensen, L. S., Scambos, T. A., Scheuchl, B., Schrama, E. J. O., Smith, B., Sundal, A. V., van Angelen, J. H., van de Berg, W. J., van den Broeke, M. R., Vaughan, D. G., Velicogna, I., Wahr, J., Whitehouse, P. L., Wingham, D. J., Yi, D., Young, D., and Zwally, H. J. (2012). A Reconciled Estimate of Ice-Sheet Mass Balance. *Science*, 338(6111):1183–1189. 2

Shulgin, A. and Artemieva, I. M. (2019). Thermochemical heterogeneity and density of continental and oceanic upper mantle in the european-north atlantic region. *Journal of Geophysical Research: Solid Earth*, 124(8):9280–9312. 96

Silver, P. G. and Chan, W. W. (1988). Implications for continental structure and evolution from seismic anisotropy. *Nature*, 335:34–39. 47

Silver, P. G. and Chan, W. W. (1991). Shear wave splitting and subcontinental mantle deformation. *Journal of Geophysical Research: Solid Earth*, 96(B10):16429–16454. 47

Simmons, N. A., Forte, A. M., Boschi, L., and Grand, S. P. (2010). Gypsum: A joint tomographic model of mantle density and seismic wave speeds. *Journal of Geophysical Research: Solid Earth*, 115(B12). 53, 72, 77, 96

Simon, K., James, T., Henton, J., and Dyke, A. (2016). A glacial isostatic adjustment model for the central and northern laurentide ice sheet based on relative sea-level and gps measurements. *Geophysical Journal International*, 205:ggw103. 19

Simpson, M. J., Milne, G. A., Huybrechts, P., and Long, A. J. (2009). Calibrating a glaciological model of the greenland ice sheet from the last glacial maximum to present-day using field observations of relative sea level and ice extent. *Quaternary Science Reviews*, 28(17):1631–1657. Quaternary Ice Sheet-Ocean Interactions and Landscape Responses. 132

Smith, M. L. and Dahlen, F. A. (1973). The azimuthal dependence of Love and Rayleigh wave propagation in a slightly anisotropic medium. *Journal of Geophysical Research*, 78:3321–3333. 31

Snyder, D., Berman, R., Kendall, J.-M., and Sanborn-Barrie, M. (2013). Seismic anisotropy and mantle structure of the Rae craton, central Canada, from joint interpretation of SKS splitting and receiver functions. *Precambrian Research*, 232:189–208. 27, 51, 52

Sokos, E. (2015). Lefkada temporary network [Data set]. International Federation of Digital Seismograph Networks. 28

St-Onge, M., Searle, M., and Wodicka, N. (2006). Trans-Hudson Orogen of North America and Himalaya-Karakoram-Tibetan Orogen of Asia: Structural and thermal characteristics of the lower and upper plates. *Tectonics*, 25:TC4006. 24

St-Onge, M. R., Gool, J. A. M. V., Garde, A. A., and Scott, D. J. (2009). Correlation of Archaean and Palaeoproterozoic units between northeastern Canada and western Greenland: constraining the pre-collisional upper plate accretionary history of the Trans-Hudson orogen. *Geological Society, London, Special Publications*, 318(1):193–235. 23, 24, 27, 40, 41, 43, 45

Steffen, R., Audet, P., and Lund, B. (2018). Weakened Lithosphere Beneath Greenland Inferred From Effective Elastic Thickness: A Hot Spot Effect? *Geophysical Research Letters*, 45(10):4733–4742. 3, 22, 46, 71, 72, 98, 99, 100, 144

Steffen, R., Steffen, H., Weiss, R., Lecavalier, B. S., Milne, G. A., Woodroffe, S. A., and Bennike, O. (2020). Early holocene greenland-ice mass loss likely triggered earthquakes and tsunami. *Earth and Planetary Science Letters*, 546:116443. 117, 130, 146

Steffen, R., Strykowski, G., and Lund, B. (2017). High-resolution Moho model for Greenland from EIGEN-6C4 gravity data. *Tectonophysics*, 706-707:206–220. 3, 22, 71, 102

Stein, S. and Wysession, M. (1991). *An Introduction to Seismology, Earthquakes, and Earth Structure*. Wiley-Blackwell, 1 edition. 7

Steinberger, B., Bredow, E., Lebedev, S., and Schaeffer, A. (2019). Widespread volcanism in the greenland–north atlantic region explained by the iceland plume. *Nature Geoscience*, 12. 3, 46, 52, 72, 91, 98, 99, 100, 102, 144

Steinberger, B., Sutherland, R., and O'Connell, R. (2004). Prediction of emperor-hawaii seamount locations from a revised model of plate motion and mantle flow. *Nature*, 430:167–73. 101, 102

Stephen, R. (2005). Hole 1256D VSP [Data set]. International Federation of Digital Seismograph Networks. 28

Stixrude, L. and Lithgow-Bertelloni, C. (2011). Thermodynamics of mantle minerals - II. Phase equilibria. *Geophysical Journal International*, 184(3):1180–1213. 83

Straume, E. O., Gaina, C., Medvedev, S., Hochmuth, K., Gohl, K., Whittaker, J. M., Abdul Fattah, R., Doornenbal, J. C., and Hopper, J. R. (2019). Globsed: Updated total sediment thickness in the world's oceans. *Geochemistry, Geophysics, Geosystems*, 20(4):1756–1772. 81

Suckro, S. K., Gohl, K., Funck, T., Heyde, I., Schreckenberger, B., Gerlings, J., and Damm, V. (2013). The Davis Strait crust: a transform margin between two oceanic basins. *Geophysical Journal International*, 193:78–97. 45

Szwillus, W., Afonso, J. C., Ebbing, J., and Mooney, W. D. (2019). Global crustal thickness and velocity structure from geostatistical analysis of seismic data. *Journal of Geophysical Research: Solid Earth*, 124(2):1626–1652. 81

Takam Takougang, E., Harris, B., Kepic, A., and Le, C. (2015). Cooperative joint inversion of 3d seismic and magnetotelluric data: With application in a mineral province. *GEOPHYSICS*, 80:R175–R187. 103

Tarantola, A. (2005). *Inverse Problem Theory and Methods for Model Parameter Estimation*. Society for Industrial and Applied Mathematics. 11, 12, 73, 74

Tarasov, L., Dyke, A. S., Neal, R. M., and Peltier, W. (2012). A data-calibrated distribution of deglacial chronologies for the north american ice complex from glaciological modeling. *Earth and Planetary Science Letters*, 315-316:30–40. Sea Level and Ice Sheet Evolution: A PALSEA Special Edition. 19

Tarasov, L. and Peltier, W. (2004). A geophysically constrained large ensemble analysis of the deglacial history of the North American ice-sheet complex. *Quaternary Science Reviews*, 23(3):359–388. Climate system history and dynamics: the Canadian Program in Eart h System Evolution. 2

Tarasov, L. and Richard Peltier, W. (2002). Greenland glacial history and local geodynamic consequences. *Geophysical Journal International*, 150(1):198–229. 116

Tegner, C., Storey, M., Holm, P., Thorarinsson, S., Zhao, X., Lo, C.-H., and Knudsen, M. (2011). Magmatism and eurekan deformation in the high arctic large igneous province: 40ar–39ar age of kap washington group volcanics, north greenland. *Earth and Planetary Science Letters*, 303(3):203–214. 98

Tork Qashqai, M., Afonso, J. C., and Yang, Y. (2018). Physical state and structure of the crust beneath the western-central united states from multiobservable probabilistic inversion. *Tectonics*, 37(9):3117–3147. 3, 73, 74, 79

Tork Qashqai, M., Carlos Afonso, J., and Yang, Y. (2016). The crustal structure of the arizona transition zone and southern colorado plateau from multiobservable probabilistic inversion. *Geochemistry, Geophysics, Geosystems*, 17(11):4308–4332. 3, 73, 74, 75, 77

Torsvik, T. H., Carlos, D., Mosar, J., Cocks, L. R. M., and Malme, T. N. (2002). *Global reconstructions and North Atlantic paleogeography 440 Ma to recent. BATLAS–Mid Norway Plate Reconstruction Atlas with Global and Atlantic Perspectives*. Geological Survey of Norway, Trondheim. 24

Toyokuni, G., Matsuno, T., and Zhao, D. (2020). P wave tomography beneath greenland and surrounding regions: 1. crust and upper mantle. *Journal of Geophysical Research: Solid Earth*, 125(12):e2020JB019837. e2020JB019837 2020JB019837. 3, 7, 22, 26, 71, 72

Toyokuni, G. and Zhao, D. (2021). P-Wave Tomography for 3-D Radial and Azimuthal Anisotropy Beneath Greenland and Surrounding Regions. *Earth and Space Science*, 8(12):e2021EA001800. e2021EA001800 2021EA001800. 26

Ucisik, N., Gudmundsson, Ó., Priestley, K., and Larsen, T. B. (2005). Seismic anisotropy beneath east Greenland revealed by shear wave splitting. *Geophysical Research Letters*, 32(8):L08315. 50

Ucisik, N., Ólafur Gudmundsson, Hanka, W., Dahl-Jensen, T., Mosegaard, K., and Priestley, K. (2008). Variations of shear-wave splitting in Greenland: Mantle anisotropy and possible impact of the Iceland plume. *Tectonophysics*, 462(1):137–148. Seismic Anisotropy and Geodynamics of the Lithosphere-Asthenosphere System. 26, 50

Uieda, L., Tian, D., Leong, W. J., Schlitzer, W., Grund, M., Jones, M., Fröhlich, Y., Toney, L., Yao, J., Magen, Y., Tong, J.-H., Materna, K., Belem, A., Newton, T., Anant, A., Ziebarth, M., Quinn, J., and Wessel, P. (2023). *PyGMT: A Python interface for the Generic Mapping Tools*. 56

University of Bergen (1982). University of Bergen Seismic Network [Data set]. International Federation of Digital Seismograph Networks. 28

van Gool, J. A., Connelly, J. N., Marker, M., and Mengel, F. C. (2002). The Nagssugtoqidian Orogen of West Greenland: tectonic evolution and regional correlations from a West Greenland perspective. *Canadian Journal of Earth Sciences*, 39(5):665–686. 3, 22, 24, 52, 71

van Wijk, J., Baldridge, W., van Hunen, J., Goes, S., Aster, R., Coblentz, D., Grand, S., and Ni, J. (2010). Small-scale convection at the edge of the Colorado Plateau: Implications for topography, magmatism, and evolution of Proterozoic lithosphere. *Geology*, 38(7):611–614. 76

Vauchez, A. and Nicolas, A. (1991). Mountain building: strike-parallel motion and mantle anisotropy. *Tectonophysics*, 185(3):183–201. 47

Vervaet, F. and Darbyshire, F. (2022). Crustal structure around the margins of the eastern Superior craton, Canada, from receiver function analysis. *Precambrian Research*, 368:106506. 41

Voss, M. and Jokat, W. (2007). Continent-ocean transition and voluminous magmatic underplating derived from P-wave velocity modelling of the East Greenland continental margin. *Geophysical Journal International*, 170(2):580–604. 22, 24, 71

Voss, M., Schmidt-Aursch, M. C., and Jokat, W. (2009). Variations in magmatic processes along the East Greenland volcanic margin. *Geophysical Journal International*, 177(2):755–782. 22, 24, 71

Wake, L., Lecavalier, B., and Bevis, M. (2016). Glacial isostatic adjustment (gia) in greenland: a review. *Current Climate Change Reports*, 2. 23, 72

Wang, C.-Y., Lin, Y. N., Hwang, C., and Shum, C. K. (2024). Observing glacial isostatic adjustment by psinsar in southern hudson bay. *Remote Sensing of Environment*, 304:114023. 21

Wang, Z. and Dahlen, F. A. (1995). Spherical-spline parameterization of three-dimensional earth models. *Geophysical Research Letters*, 22(22):3099–3102. 31

Whitehouse, P. L. (2018). Glacial isostatic adjustment modelling: historical perspectives, recent advances, and future directions. *Earth Surface Dynamics*, 6(2):401–429. 14

Whitehouse, P. L., Bentley, M. J., and Le Brocq, A. M. (2012). A deglacial model for Antarctica: geological constraints and glaciological modelling as a basis for a new model of Antarctic glacial isostatic adjustment. *Quaternary Science Reviews*, 32:1–24. 3

Won Sang Lee, . Y. P. (2013). Korea Polar Observation Network [Data set]. International Federation of Digital Seismograph Networks. 28

Woodroffe, S. A., Long, A. J., Punwong, P., Selby, K., Bryant, C. L., and Marchant, R. (2015). Radiocarbon dating of mangrove sediments to constrain holocene relative sea-level change on zanzibar in the southwest indian ocean. *The Holocene*, 25(5):820–831. 130

Wouters, B., Bamber, J., Van den Broeke, M., Lenaerts, J., and Sasgen, I. (2013). Limits in detecting acceleration of ice sheet mass loss due to climate variability. *Nature Geosci*, advance online publication. 2, 3, 19, 71

Yang, X., Li, Y., Afonso, J. C., Yang, Y., and Zhang, A. (2021). Thermochemical state of the upper mantle beneath south china from multi-observable probabilistic inversion. *Journal of Geophysical Research: Solid Earth*, 126(5):e2020JB021114. e2020JB021114 2020JB021114. 3, 73, 74, 81, 98

Yousefi, M., Milne, G., Love, R., and Tarasov, L. (2018). Glacial isostatic adjustment along the Pacific coast of central North America. *Quaternary Science Reviews*, 193:288–311. 135, 145

Zeitz, M., Haacker, J. M., Donges, J. F., Albrecht, T., and Winkelmann, R. (2022). Dynamic regimes of the greenland ice sheet emerging from interacting melt–elevation and glacial isostatic adjustment feedbacks. *Earth System Dynamics*, 13(3):1077–1096. 1, 72

Zhang, A., Afonso, J. C., Xu, Y., Wu, S., Yang, Y., and Yang, B. (2019). The deep lithospheric structure of the junggar terrane, nw china: Implications for its origin and tectonic evolution. *Journal of Geophysical Research: Solid Earth*, 124(11):11615–11638. 74, 79, 91

Zhang, A., Guo, Z., Afonso, J. C., Handley, H., Dai, H., Yang, Y., and Chen, Y. J. (2021). Lithosphere–asthenosphere interactions beneath northeast China and the origin of its intraplate volcanism. *Geology*, 50(2):210–215. 81